The Design and Control of an Actively Restrained Passive Mechatronic System for Safety Critical Applications

by

Lucian Marian Lacraru

BSc

A thesis

submitted in partial fulfilment of the requirements

for the award of

The Degree of Doctor of Philosophy of Loughborough University

5th July 2005

Abstract

Development of manipulators that interact closely with humans has been a focus of research in fields such as robot-assisted surgery and haptic interfaces for many years. Recent introduction of powered surgical-assistant devices into the operating theatre has meant that robot manipulators have been required to interact with both patients and surgeons. Most of these manipulators are modified industrial robots. However, the use of high-powered mechanisms in the operating theatre could compromise safety of the patient, surgeon, and operating room staff. As a solution to the safety problem, the use of actively restrained passive arms has been proposed. Clutches or brakes at each joint are used to restrict the motion of the end-effector to restrain it to a pre-defined region or path. However, these devices have only had limited success in following pre-defined paths under human guidance.

In this research, three major limitations of existing passive devices actively restrained are addressed. Improvements on all three areas of research have significantly contributed to the knowledge in areas of passive robotic devices, actuators technology and control. Firstly, the kinematic configuration is significantly improved so that the path following definition is more accurate and much easier to implement in practice. Secondly, the actuator and transmission technology are improved by proposing a piezo-actuator and a compact clutching method to produce the frictional torque. Finally, a control strategy able to compensate for stick-slip friction at very low velocities has been developed, which allows smooth and accurate motion control.

In order to ensure safety, the proposed joint is based on an electromechanical friction clutch. The proposed joint's control system demonstrates smooth position control and high positional accuracy despite the inherent stick-slip characteristic of the clutch mechanism. A sliding mode controller (SMC) has been developed to overcome such nonlinearity at low velocities. Stick-slip reduction by almost 90% is achieved using a SMC. A combination of PD control and SMC is also shown to efficiently regulate the motion for a wide range of sliding velocities.

Based on the prototype actively restrained passive joint a two-DOF polar manipulator is proposed as a potential configuration for an actively restrained passive system. A task-interpreter algorithm has been developed, which allows a two-DOF manipulator to successfully reach a pre-specified position; follow a predefined trajectory; and stay within a safe envelope.

Acknowledgements

This work was conducted in Wolfson School of Mechanical and Manufacturing Engineering at Loughborough University. The author gratefully acknowledges the support of the School, and is thankful for the financial support provided.

The research was supervised by Dr K. Bouazza-Marouf and I would like to thank him for his support and guidance. I also like to thank my friends and colleagues during the completion of this research for continual support and encouragement.

I would like to express my sincerest thanks to my wife, brother, mother *(in memoriam)* and father for all unconditional support throughout my journey up to now.

Dedication

To my mother (in memoriam)

Thank you for all of your patience, understanding and support.

In Romanian

Dedic aceasta teza mamei mele.

Multumesc pentru rabdarea, intelegerea si suportul tau. D-zeu sa te odihneasca in pace.

Table of Contents

Table of Figures

List of Tables

Notation

A	area of the contact between the brake pad and brake disc
A_{lever}	area of a rectangular shape of the mechanical lever
b	viscous friction coefficient in the motor
C_d	viscous damping coefficient in the clutch system
$e(t)$	position error
f	SMC gain
F_a	actuation force
F_c	dynamic friction
F_{DC}	the force provided by the motor-lever assembly
F_f	frictional force
F_N	normal force onto the braking disc
F_{piezo}	force provided by the piezoactuator
F_{system}	reaction force provided by the system
F_u	user-input force or the reaction force due to the mass M for the experimental setup
$F_{u,\,min}$	vector of a minimum predefined value for user-input force
F_s	static friction
F_v	viscous friction
g	gravitational acceleration
h	height of the rectangular part of the brake pad
i_a	armature current
I	system's mass moment of inertia
I_{shaft}	shaft's mass moment of inertia
I_{disc}	brake disc's mass moment of inertia
I_{pulley}	pulley's mass moment of inertia
J	experimental set-up total mass moment of inertia
J_T	actuation assembly mass moment of inertia
k_p or k_{piezo}	the stiffness of the piezoactuator

k_s or k_{system}	the stiffness of the system
K	positive constant for CTC law
K_d	derivative gain
K_e	back emf constant
K_{COF}	constant of the coefficient of friction
K_{kal}	design parameter for Kalman filtering
K_p	proportional gain
K_{region}	is a positive defined constant set to enhance the feeling of the user
K_t	motor torque constant
L	width of the friction pad
L_a	armature inductance
m_θ	gradient of the revolute joint position
m_r	gradient of the prismatic joint posiiton
M	mass released on pulley
$P_d(x_d, y_d)$	vector that defines the desired path in Cartesian space
P_v	predefined value for the control strategy to avoid stick-slip
$p(t)$	applied pressure
$Q_d(r_d, \theta_d)$	vector that defines the desired path in joint space or polar space
r	defines the translation of the prismatic joint
r_c	distance between centre of the motor shaft and contact point on the disc.
r_i	inner radius of the brake pad
r_o	outer radius of the brake pad which is equal to the radius of the brake disc.
R_a	armature resistance
R_L	length of the virtual joint link
R_p	pulley radius
t	time
T	sampling time
T_{DC}	dc motor output torque
T_f	frictional torque
T_u	external driving torque produced by the user-input force or pulley-weight system

$u(t)$	control law
$v_a(t)$	armature voltage of the dc motor(+/- 5V)
v_b	back emf voltage of the dc motor
$V_{piezo}(t)$	input voltage in the piezodriver (+/- 10V)
x_p	stroke of the piezoactuator
x_s	displacement of the mechanics activated by the piezoactuator
δ	Stribeck coefficient
$\theta(t)$	is the actual position of the revolute joint (is also the shaft angular position of the experimental setup)
$\dot{\theta}$	revolute joint velocity
$\ddot{\theta}$	revolute joint acceleration
θ_d	the desired position of the revolute joint (is also the shaft angular position of the experimental setup)
$\dot{\theta}_d$	the desired velocity of the revolute joint
$\dot{\theta}_s$	Stribeck velocity
θ_{DC}	dc motor's shaft position
$\dot{\theta}_{DC}$	dc motor's shaft velocity
$\ddot{\theta}_{DC}$	dc motor's shaft acceleration
γ	angle of a segment of an annular brake pad
λ	distance between the boundary and actual position
μ	coefficient of friction
μ_d	dynamic friction coefficient
μ_s	static friction coefficient
$\sigma(\chi)$	sliding surface for the sliding mode controller
τ	control input function
ε	is the thickness of the boundary layer used for saturation

Chapter 1
Introduction

1.1 Background

Development of manipulators that interact closely with humans is increasingly a focus of research in fields such as medical robots, assembly tasks and material handling in the manufacturing industry. Robotic devices have been introduced into the operating theatre to assist surgeons performing complex surgical procedures with a higher degree of accuracy and reliability than would otherwise be possible with more traditional methods. The general strength, advantages and potential of robots are thoroughly presented by the National Horizon Scanning Centre, UK [1]. Briefly, they are:

- reduction of tremor and fatigue;
- exact movements can be pre-programmed, enabling achievement of pre-planned procedure with greater precision and accuracy;
- consistent performance;
- reduction in time taken for routine operations as well as reduction in staff requirements, improving productivity of staff;
- systems are potentially immune to radiation;
- increase utilisation and productivity;
- quick financial payback, reduced healthcare delivery cost.

A wide variety of surgical operations have benefited from the introduction of a robotic assistant. For example minimally invasive surgery, orthopaedics, neurology, cardiac, and cosmetical procedures have all been enhanced by robotic assistance. However,

many of the robotic devices currently in use are based on modified industrial manipulators and have typically been designed for high speed, high torque applications. The accuracy of such devices is unsurpassed but in an operating theatre, the use of large powered mechanisms has the potential to compromise the safety of patient, surgeon, and the operating room staff. In the limited space of an operating room, the use of a bulky heavy wheel-based robot may be perceived as alien, intimidating, and the robot may even become out of control, as was the case with industrial robots.

Alternatives to these high-powered robots have included custom-built manipulators specially built for surgical environments, which can work together with the surgeon in order to perform a surgical task. However, the accuracy of these systems while tracking a predefined path is not yet proven to be entirely satisfactory. Furthermore, most of these systems use electrical motors to directly resist the surgeon's motion. This can be a potential threat for both surgeons and patients as in case of motor failure uncontrollable movements can occur. Substitutions to these motorised robots are manipulators that are not able to generate motion on their own (i.e. the only motion in the system is provided by the human operator), but are capable of restraining the operator in order to follow a predetermined trajectory, as is required in most complex surgical procedures. These systems are to be called *actively restrained passive mechatronic systems.* The only driving force in the system is under direct control of the surgeon him/herself. These systems require the surgeon to grasp a control handle mounted on or near the manipulator end-effector and provide the motive force. Computer controlled clutches or brakes limit the range of motion of the end-effector to restrain the tool to remain on a pre-defined path or within a pre-defined safe working region. Although current devices have proved relatively successful in creating a satisfactory man-machine interface, they have only had limited success in restraining the tool to remain along a pre-defined path as may be required by more complex machining processes such as bone milling, and sawing and cutting involved in modern surgical procedures.

1.2 Aims of the Research

This research aims to develop a safe manipulator that interacts closely with humans so that safety critical applications such as surgical procedures could be performed. Safety is paramount when introducing new technologies to the operating theatre. To guarantee that patient safety is not compromised, only increased, it is essential that the surgeon be maintained within the decision-making loop of the system. This important safety issue suggests the design of a guiding system that works together with the surgeon in order to achieve a surgical goal. In addition, to maximize the safety of those interacting with the system, a mechatronic device that is unable to produce motion by itself is preferred. A passive rather than an active effector arm greatly reduces the inherent risk, removing the requirement for a safety critical control system.

By critically reviewing current developments in the field of surgical assistant devices it is possible to identify solutions to current difficulties in the areas of safety and control. Therefore, the main aim of this research is to design a prototype joint mechanism based on which a device that could aid the surgeon performing orthopaedic procedures could be produced. The prototype joint should be incapable of producing motion on its own, but able to restrict the surgeon's motion in order to (1) reach a specified position, (2) follow a predefined trajectory, and (3) stay within a safety envelope. The prototype joint's associated control system should demonstrate greater positional accuracy than is possible using traditional methods by surgeons. The proposed system should be designed to assist a human operator to perform both precise positioning and accurate path following. This multitasking capability of the system would make it capable of assisting surgeon in performing a variety of orthopaedic procedures where it is required to drill and screw into the bone, as well as sawing, cutting and milling bones. Examples of such procedures are implantation of knee and shoulder prostheses, total hip replacement (THR), tibial and femur osteotomies, and repair of femoral fractures. To illustrate the outcome of this research, Total Knee Replacement (TKR) is chosen as a typical procedure.

The aim of this research is to develop an inherently safe mechatronic system able to assist in safety critical applications such as orthopaedics surgery. The manipulator will be passive (i.e. not able to drive the human operator) and will have the capability to guide the surgeon so that complex surgical procedures may be performed. To this end the following seven objectives are defined:

Objective 1: The mechatronic system should not be able to move on its own, but only under the direct control of a human operator.

Objective 2: The mechatronic system must be able to be moved completely free. This is important when the operator wants to move and track the position of an instrument or of a sensor.

Objective 3: The mechatronic system must be able to physically guide the operator so that a predefined position can be reached. This is useful in applications such as neurosurgery and orthopaedics, in order to insert a drill bit, a needle, or an electrode; After the desired position is reached, the manipulator's joint are locked and the surgeon may then manually execute the surgical task.

Objective 4: The mechatronic system must be able to guide the operator so that a predefined trajectory can be followed. Such a mode of operation is useful when the surgical act is complex, or when the access towards the surgical goal is delicate because of the surrounding anatomic structures. This mode is often necessary for plastic and reconstructive surgery.

Objective 5: The manipulator's end-effector must stay within a pre-specified envelope or safety region. Inside the region any motion is free while on the border some of the motions are forbidden (e.g. motions that will take the tip of the manipulator beyond the safety region). This approach is suitable for

resection operations, or osteotomies. It also enables anatomic obstacles to be defined so that they can be avoided. It is particularly suitable for Total Knee Replacement.

Objective 6: The control algorithms and strategies employed should be robust against external disturbances such as the user-input force or from the mechanical properties of the device itself.

Objective 7: The manipulator must be easy to use with little or no training.

The above objectives have been fulfilled by undertaking the following work. By employing a friction clutch mechanism as a mechatronic joint to restrain the user-input force, the manipulator would not be able to move on its own but only under direct control of a human operator, thus accomplishing objective 1. The proposed electromechanical friction clutch is not able to introduce motion in the system but only to restrain the motion by dissipating the user-supplied energy. Therefore, if no control is provided to the joints, the manipulator can be moved freely, thus satisfying the objective 2 of this research.

This thesis has identified the limitations of existing actively restrained passive devices such as PADyC, PTER and COBOT. The limitations of the manipulator kinematics for trajectory following tasks as well as the limitations of the control strategy of such passive systems are discussed. As a solution to these limitations, a two-DOF polar manipulator has been proposed. It has been demonstrated that for the latter kinematic architecture, the path planning and path tracking issues are simpler, and complex tasks can be achieved more effectively. Furthermore, the operators do not have to 'feel' their way along a narrow corridor, bouncing from wall to wall, as is the case for PTER and PADyC. This kinematic configuration also reduces the need for training, thus satisfying objective 7.

As a result of this preliminary work an alternative joint mechanism has been designed. Besides the fact that the proposed electromechanical friction clutch satisfies objective 1, it has been shown that it can also smoothly and effectively control the joint's motion so that objectives 3, 4, and 5 are satisfied.

1.3 Total Knee Replacement Surgery

The knee is a particularly complex joint, with large rolling surfaces and an elaborate system of ligaments precisely configured to constrain lateral motion. Furthermore, orthopaedic surgery to replace injured or damaged knee joints is a complicated process requiring accurate alignment of surfaces of prosthetic implant components and their accurate positioning within the knee in order to recuperate normal leg functions. The mechanical axis of the knee that corresponds to ideal positioning within the knee is presented in Figure 1-1.

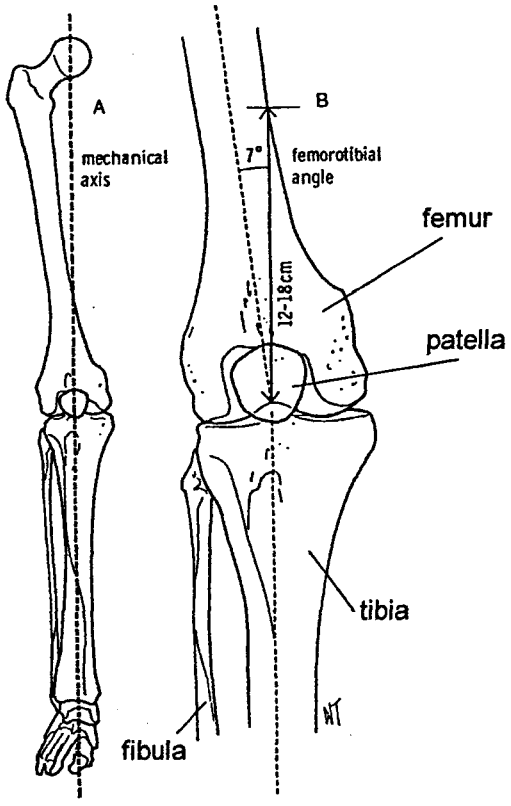

Figure 1-1. The mechanical axis of the knee corresponded to the right leg [2]

Total Knee Replacement (TKR) surgery is a procedure in which the surgeon is required to cut a series of plane profiles into the surface of the tibia and femur in such a way that a prosthetic knee joint may be fitted. The complete cutting sequence is shown in Figure 1-2a. Accurate alignment and position of the prosthetic components is crucial to the success of the operation (i.e. painless and improved leg-motion for the patient). Misalignment or poor fitting of the prosthesis can also reduce the longevity of the replacement joint. The operation is particularly made difficult because of the jigs and oscillating saw that the surgeon is required to use. The components of total knee replacement procedure are shown in Figure 1-2b.

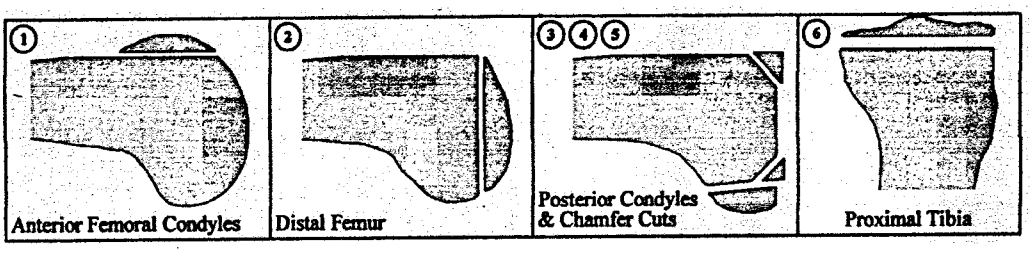

a)

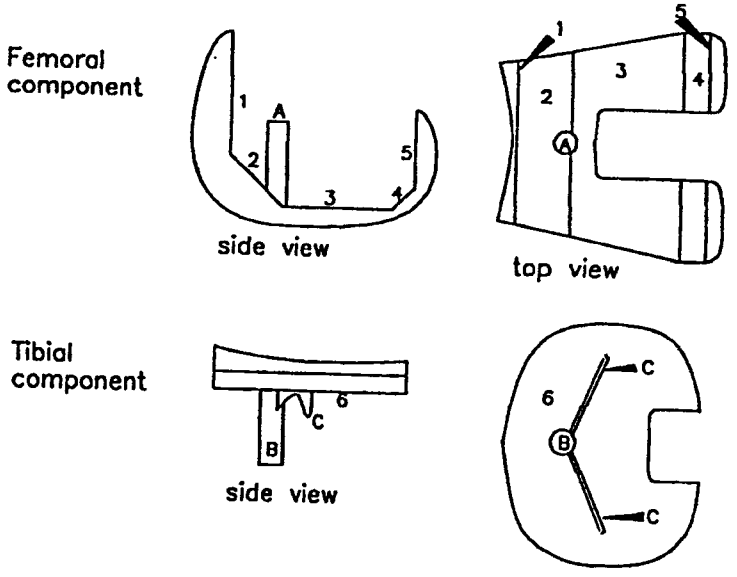

b)

Figure 1-2. TKR procedure a) TKR cuts [3], b) TKR prostheses [4]

The femoral component, shown in Figure 1-2b, typically consists of a metal cap shaped approximately like a normal bone on the outside surfaces. The inner surfaces consist of five flat planes and a locating pillar. These five planes should match with the five planes cut into the bone. The locating pillar prevents any sideways movement. The tibial component, also shown in Figure 1-2b, consists of a metal plate that holds a plastic insert. This insert forms a low-friction bearing surface for the femoral component. A number of interchangeable inserts are available depending on the distance required between the bones. The underside of the metal plate consists of a locating pillar and two stabilisation vanes. These prevent lateral and rotational movement respectively. A third component is used to replace the patella.

In traditional TKR, the surgeon uses a system of jigs and rods to approximate the axis of the leg and to suitably align the prosthetic components. A jig placement is based on presurgical X-ray images. Due to the lack of intraoperative information, reports suggest that a sizeable fraction of current manual procedures result in clinically significant inaccuracies, and up to 40% of the patients are left with leg pain or limited flexion after conventional TKR surgery [5]. The alignment of the femur and tibia and the location of ligament attachments are crucial; small displacement (i.e. 2.5 mm) of the femoral component have been shown to alter the range of motion by as much as 20 degrees [6].

There are several surgical techniques considered by surgeons in performing TKR [2]. A traditional TKR procedure is briefly described in Appendix A1. To overcome inaccuracies introduced by the traditional methods, the use of computers and robots to assist surgeons in knee surgery has been proposed [7]. Several computer/robotic-assisted TKR have been developed to increase the accuracy of the prosthetic alignment. For example, *computer integrated instrumentation* incorporates highly accurate measurement devices to locate joint centres, to track surgical tools, and to visually assist the surgeon to align prosthetic components; *image guided knee replacement* provides a three-dimensional preoperative plan that guides the placement of the cutting blocks and prosthetic components; and *robot assisted knee replacement* allows for the machining of bones accurately without the use of standard cutting blocks.

At the Praxim Company, in Grenoble, France [8] a *computer integrated instrument* has been developed. The use of computer-integrated instruments introduces two novel stages to the surgical procedure. The first stage determines the mechanical axis of the femur and tibia. Reference frames are fixed to the iliac crest, distal femur, proximal tibia, and foot with custom designed screws. The hip is rotated through a range of motions, and the position and orientation of the reference frames are used to locate the hip centre. The centre of the knee and ankle is obtained through a similar procedure. Next the mechanical axis of the femur and tibia is calculated. In the second stage of the procedure, the surgeon secures reference frames to the cutting blocks, whose position relative to the desired position is displayed on a computer. Once a jig is oriented properly, it is secured in position and the cuts are made with a standard oscillating saw.

A group at Nortwestern University developed an *image guided knee replacement* [4]. The procedure begins with preoperative planning. To create the preoperative plan, three-dimensional (3D) computer models of the patient's femur and tibia are constructed from computerised tomography (CT) data. Next, planning software orients the tibial and femoral components and calculates bone resections that align the mechanical axis of the limb and produce the intended implant contact. An intraoperative system determines the position and orientation of the patient's femur and tibia and guides the placement of the cutting jigs onto the bones so that the resection determined in the preoperative plan can be made. The major advantage of this method is the fact that at the end of the operation the difference between the preoperative plan and the actual surgery can be measured. This difference quantifies the actual success/failure rate, which aid to increasing the performances of further developments.

Several groups have implemented prototypes of *robot assisted knee replacement* based on industrial robots to improve the accuracy and precision of bone resections. A typical robotic sequence of the TKR procedure is presented in Appendix A2. The use of a robot generally results in a greater precision in implementing the computer simulated preoperative plan than the surgeon can achieve unaided. Matsen *et al.* [9] implemented a system for distal femoral arthroplasty, but their test on plastic bone models did not show promising results. The authors stressed the difficulty of using an industrial system

such as a PUMA manipulator in the operating room, because of its well-known limitations on kinematic accuracy, controllability due to excessive friction, and programmability. Fadda and Marcacci *et al.* [10, 11] linked a sophisticated preoperative planning system to a standard industrial robot to allow placement of cutting blocks and machining of the bones. The experimental tests carried out in their laboratory showed promising results, but the concerns regarding the intrinsic safety of the manipulator in the operating theatre were not assessable. Another robot capable of assisting in TKR is Robodoc® [12]. Initially designed for total hip replacement (THR), Robodoc performed the first world wide robotic TKR in year 2000 [13]. Robodoc is a fully automatic robot capable of performing a surgical task without the help of the surgeon. The description and functionality are described in the next section. The main drawbacks of the system are related to the lack of physical interaction with the surgeon. Furthermore, the procedure did not prove any of the advantages hoped such as: shorter surgical time, less post operation blood loss, and greater leg range of motion. Due to these issues several authors [14] indicated that the Integrated Surgical Systems' Robodoc has generally been 'mothballed'.

Davies *et al.* [15, 16] designed a special purpose robot for knee surgery. This active constraint robot (ACROBOT^{TM}) uses a force control handle near the tip of the robot to interact with a surgeon in order to improve the surgeon's input. The surgeon holds the motor of a rotary cutter attached to the end of a robot arm and moves the arm under force control. The actively restrained motorised joints prevent the robot from moving out of a predefined 'safe regions' in the cutting plane. The control scheme used is a modified damping approach, which implies that when reaching the predefined constraint the stiffness of the system increases (by changing the motor control parameters) and the surgeon experiences a high resistance when trying to move the cutter outside these safe regions. Thus, the robot prevents access to regions that include ligaments, nerves, and vasculature. The robot can also provide a virtual cutting block that constraints the rotary cutter to cut various shapes, such as a series of planes suitable for mounting the implant. Consequently, the robot can provide accuracy and constraints while the surgeon can feel the forces exerted on the bone and use his/her judgment to slow down or take a lighter cut when a hard region of bone is encountered. However,

because the system is actually driving against any input force to return the robot to the safe region, it is still capable of producing uncontrollable motion and thus the safety of the system is still questionable.

Van Ham *et al.* [17] developed a similar robotic system. Designed for TKR, the system is capable of cutting bones with great accuracy and surface flatness. Just as the ACROBOT system, this system needs the surgeon force in order to move the end-effector, which is under force control. However, the constraints in this case are based on an alternative method for force control using a hybrid force-velocity control scheme. Thus, specifying the desired force (or velocity) and the desired moment (or angular velocity) along every axis of the task frame, the system is capable of constraining the surgeon to stay in a pre-defined cutting plane and cannot move out of this plane. Although, the system shows a high degree of accuracy for the surface flatness, it does not prove it can follow a predefined trajectory, as it is required by most of the surgical procedures.

Another system capable of constraining the surgeon force in order to follow a predefined trajectory for TKR has been developed by Reedman and Bouazza-Marouf [18]. The system is based on a novel revolute joint, which allows motion only if two worms, associated with each joint and driven by DC servomotors, are controlled simultaneously. To ensure a smooth and accurate following of a trajectory, the authors generate the velocity command from the user-input force. The results so far are promising, however, the system is just in its launching stage and much research needs to be carried out regarding the manipulator kinematics and the control system in order to accurately follow any predefined trajectory and stay in a predetermined safety region. A detail description of these robotic devices is presented in the next chapter.

1.4 Shortfalls of Current Procedures

Every year thousands of patients suffering from joint disabilities such as rheumatoid arthritis or osteoarthritis undergo total knee replacement (TKR) in order to return to a

more active and pain-free lifestyle. Currently, in order to implant prosthetic knee components a complex jig system of cutting blocks and alignment rods is used to help the surgeon to approximate the geometry of the femur and tibia bones and select the appropriate size and location of the components. This process, which relies heavily on the surgeon's experience with a given jig system, has prompted the search for a more accurate and repeatable system for the placement of total knee prosthetic components.

Using the *existing jig systems*, components are oriented within two or three degrees of the desired "natural" position. These jig systems introduce several sources of inaccuracy in alignment of the prosthetic components. One major source of error is that only the very ends of the involved bones are exposed during surgery, forcing the surgeon to make decisions regarding the alignment of the femur and tibia bones based on very limited information. The preoperative X-rays can help, but these still represents only a two-dimensional projection of a complex three-dimensional structures. A second source of error is the jig system itself, which represents a physical embodiment of a component placement algorithm preferred by the system's designer. Optimal placement of components may not be achieved when the configuration of an individual patient's bones differs from those of the generalized model assumed by the jig system, or if the algorithm on which the system is based is sub-optimal or outdated. Furthermore, the existing jig systems, by necessity, direct a set of cuts in the bones based largely on local topography. It is hoped that these cuts will lead to the proper placement of the components. A preferable approach would be to visualize the correct placement of the prosthesis, based on the overall geometry of the leg, and then determine the proper cuts required to achieve optimal placement.

Computer integrated instruments that combine standard cutting guides with highly accurate measurements are a natural extension of current techniques and offer several potential advantages (i.e. potential to reduce surgical errors). However, there are several shortcomings for these systems. Firstly, the current method of obtaining the mechanical axis of the femur and tibia requires the installation of surgical screws into the iliac crest, distal femur, proximal tibia and foot. Secondly, although the computation of the mechanical axes of the femur and tibia can improve the alignment accuracy, not all of

the degrees of freedom are controlled by the current alignment procedure. Finally, the inaccuracy of the guide itself still influences the overall accuracy of the operation.

Image guided knee replacement allows one to measure actual placement of the implants relative to the planned placement. This provides the possibility to perform studies that compare the accuracy of mechanical instruments to computer-based instruments. It also provides the possibility to study the effects of alignment on implant wear and patient outcome. However, the system does not offer any help regarding physically restraining the surgeon if he/she is about to cut in a forbidden area such as vasculature, nerves and ligaments around the joint.

The *robot assisted knee replacement* also has advantages and disadvantages. Similar to the image guided knee replacement, the robot assisted knee replacement has the advantages of preoperative imaging, modelling and planning. In addition, the machining capability of a robot may provide a more accurate fit between the prosthesis and the bone, making the use of cement unnecessary in some cases. A robot is also capable of imposing physical constraints, unlike the surgeon holding an image guided surgical tool. However, the existing robots are powered by electrical actuators in order to drive the manipulator or resist the surgeons' input. This makes them capable of uncontrollable motions in case of a software or hardware failure, which may endanger the safety of those interacting with the operating environment

Another critical aspect for the success of a TKR procedure is that of surface quality of the final cuts. This is particularly important in the implant of a cementless prosthetic component, where the bone is required to grow into the prosthesis in order to help maintain its position. A very common problem during the removal of bone is that even with jigs as a guide, the thin saw deflects away from the bone during cutting. One solution to the problem of surface roughness and inaccuracy caused by the oscillating saw has been the introduction of milling tools. However, hand-held milling tools are very difficult to use, because of the way in which the cutting force is transferred to the user. Even with jigs and guides the milling tool can 'bite' into the bone, causing the surgeon's hand to be suddenly jolted. This can cause irreparable damage to the bone and

surrounding tissue. Therefore, in order to increase the accuracy with which the operation is performed robotic devices with milling tools mounted on the end-effector have been an attractive solution to these problems.

1.5 Organization of the Thesis

A review of the literature regarding medical robots and computer-assisted surgery devices is presented in the next chapter. It addresses the issue of safety of those interacting with the operating environment, and presents a classification of surgical assistant devices from the safety point of view. The current state of the art in terms of the solutions currently being developed and the procedures that are performed using existing devices is also given.

In Chapter 3, the existing actively restrained passive mechatronic systems are discussed in detail. The chapter aims to highlight the limitations of these devices with respect to mechanical design and control strategy. The proposed actively restrained passive mechatronic system is introduced in order to identify a solution to the existing limitations. A novel joint mechanism is proposed and its development is descried at the end of the chapter.

Because dry friction plays an important role in the control of the proposed joint mechanism, friction modelling and friction compensation techniques for control are reviewed in Chapter 4. The aim of this investigation is to identify the most suitable friction model for the proposed mechanism, and also to identify the most appropriate method of compensating friction-related effects such as stick-slip.

In Chapter 5 an experimental test-bed was designed and built to gain more knowledge of friction in the system. The conclusions draw from the study of the friction within the proposed clutch mechanism enables proper estimation of friction model parameters. The compensation techniques selected to overcome the stick-slip effect are developed and evaluated in Chapter 6. The results demonstrate the effectiveness of the sliding-mode

control and the potential of a computed-torque control for the position regulation at low velocities. Furthermore, the mathematical model derived is validated, which enables further analyses with the proposed electromechanical friction clutch, without building another prototype.

Chapter 7 describes the development of an efficient control strategy to smoothly and accurately regulate the position of an actively restrained passive revolute joint. Simulation and experimental results are presented, which confirm the stability, and robustness of the developed control system. In Chapter 8 the strategy developed for a revolute joint is extended to a two degree-of-freedom (DOF) actively restrained passive mechatronic system. Simulation analysis is presented, and it is shown that based on the same principle as the one-DOF, a two-DOF can also perform motion control in a smooth and accurate manner. The conclusions of the research, as well as the recommendations for future work are stated in Chapter 9.

Chapter 2
Literature Survey

2.1 Introduction

Over the last twenty years, robots have started to be introduced in the operating rooms. Robotic technology is now regularly used to aim endoscopes in laparoscopy and minimally invasive surgery [19-23]; and to guide instruments to tumours in brain surgery [23-25]. The use of a robot to shape bones in hip replacement surgery was one of the first groundbreaking applications [26]. However, today there are surgical robots controlled by the surgeons while they are physically separated from the surgical site, called telemanipulator systems [20-22]. Furthermore, robotic systems that are physically interacting with the surgeon in order to perform a surgical task are under development [16-18]. These synergistic systems aim at the surgeon and the robot to share the control of the end-effector. In this way is taken advantage of both robot accuracy and surgeon's feeling and judgment. The current state of the art in guiding systems for Medical Robotics and Computer Assisted Surgery (MRCAS) is presented in this chapter. Firstly, a discussion on the issue of safety of robotic systems is introduced. This is followed by a classification of the guiding systems for MRCAS with respect to safety and man-machine interface. Next, several robotic and computer assisted surgery systems described in the literature are discussed. The systems relevant to this research are also presented and critically reviewed. At the end of the chapter, the research objectives are outlined.

2.2 Safety of Robotic Devices in Medicine

Most of the robotic devices that are currently used to assist surgeons performing surgical tasks have been based on modified industrial manipulators. Industrial robots have typically been designed for high speed and high torque applications making them an inappropriate choice for use in the operating environment without the introduction of complex safety strategies. The manufacturers of industrial robot systems generally recommend the manipulator to be enclosed in its own cell, thus, protecting the human workers from the threat of injury by means of an interlocked safeguarding boundary [27]. Such safety measures are not feasible for safety-critical applications such as orthopaedic surgery. However, with the introduction of complex safety strategies, to ensure that unauthorised motion cannot be made, industrial robots have been allowed in the operating environment. In order to introduce a robotic system into the operating environment, Taylor et al. [28] defined four safety requirements. These are:

1). The robot must never "run away";

2). The robot must never exert excessive force on the patient;

3). The robot's cutter must stay within a pre-specified positional envelope relative to the volume being cut;

4). The surgeon must be in charge at all times.

It is generally recognised that even where safety is of principal importance (i.e. medical robots, Space Shuttle or Airplanes), there is no such thing as 100% safety and errors in software and failures of hardware do occur, despite duplications of systems and redundant instrumentation. This is the case for any robotic system that is able to move on its own. One solution of increasing safety of robotic systems has been to design a special-purpose robot for a particular surgical procedure.

Associated with this concept is that of a mechanical constraint that physically prevents motion outside a limited area. A further implication of this approach is that, where possible, axes should be moved sequentially, one at a time rather than in parallel, to minimize the volume of space that can be swept out by an unforeseen motion. This implies that complex shapes resulting from the interaction of many axes of motion may

need to be approximated by a series of simple shapes, resulting from a sequence of single axis motion. Related to these special-purpose robots are robotic systems that physically interact with the surgeon (work together or in synergy). These systems aim to improve even more safety and increase acceptance of these robotic systems by surgeons and patients, as the surgeon shares the control with a robotic system. The surgeon is required to hold an instrumented handle and provide the motive force, while the system uses motorised joints to resist the surgeon's motion and keep him/her on the pre-defined path. The main problem of these systems is that they still use electrical motors that are capable of driving the robot. Thus, they are still capable of making uncontrollable movements, if there were a motor failure and injure the humans in the robot's proximity.

As stated by Taylor et al. [28] *"the most obvious way to prevent a robotic device from making an undesirable motion is to make it incapable of moving of its own accord"*. Motor-less manipulators have been implemented, in which joint encoders are used to provide feedback to the surgeon on where his/her instruments are relative to the image-based surgical plan. One important limitation of this approach is that it provides only positional feedback and, therefore, cannot help the surgeon to execute a complex pre-computed trajectory. Thus, a system that is incapable of moving on its own accord, but which is capable of physically guiding the surgeon in order to follow a pre-defined trajectory is the most suitable mechatronic system to assist in the operating environment. This is the area of medical robots that the current research targets, and the proposed manipulator is introduced in the next chapter.

2.3 Classification of Guiding Systems for MRCAS

Many guiding systems have been developed for a variety of different surgical procedures, but until recently a classification of these aids appears to be somewhat of a grey area. Davies [27] proposed a hierarchy of systems for holding and manipulating surgical tools in terms of passive and active to describe a system's interaction with the patient and the way in which the tools are used. A powered robotic manipulator is used

in a passive manner if it is implemented to align a mechanical guide or to place surgical jigs. In this case the robot is relied upon for positional accuracy but the tool interaction is controlled and applied by the surgeon. Conversely, Davies states that a manipulator is used in an active manner if the robot makes physical contact with the patient, i.e. cutting bone with a milling tool or removing tissue with a probe.

Cinquin et. al. [29] used the terms passive, semi-active and active to describe the way in which the surgeon interacts with the system. Cinquin's classification of surgical aids stretches further than just robots. A *passive system* is considered a powered robotic manipulator if it is implemented to align a mechanical guide or to place surgical jigs, just as Davies stated [27]. Furthermore, Cinquin et. al described a passive system as a system in which the surgeon guides the tools, while the tools offer position measurements and can be visualized. Unpowered articulated manipulators that register position, hand-held instruments that are located by visual, ultrasonic and electro-magnetic techniques fall under this category. Augmented Reality (AR) systems, in which video, Computed Tomography (CT) or Magnetic Resonance Imaging (MRI) data is enhanced through computer graphics techniques, are used to display intraoperative data and aid in tool guidance are also classified as passive.

A *semi-active system* is described as a system in which the surgeon is guided through a procedure aided by mechanical jigs or laser guidance. The jigs or laser could possibly be controlled by a powered robot. In the same category falls the systems that use mechanical constraints to limit the workspace of the robot, enabling the surgeon to move the robot around freely within a predefined region, but it cannot go beyond the safety region. As the end-effector approaches the boundary surface, freedom of motion in certain directions is either reduced or eliminated completely. The term *active* describes an autonomous system that can perform a whole surgical operation without the surgeon's help. The surgeon only has a supervisory role.

Like Cinquin et. al., DiGioia, Jaramz and Colgan [30] also divide the guidance systems for MRCAS into three groups: passive, semi-active and active systems. The meaning of each of the terms is stated in relation to the way in which the surgeon physically

interacts with the system. Later, Davies adopted DiGioia's classification system and replaced the notion of 'semi-active' systems with synergistic systems, and added one further term: telemanipulator systems [31]. A synergistic system is one in which the surgeon physically interacts with the robot. By grasping a control handle mounted on the robot end-effector, the surgeon applies a force to move the manipulator. A computer controls the actuators of the manipulator in order to force the surgeon to remain within a pre-defined region or along a pre-defined path. A telemanipulator, on the other hand, is a manipulator that is remotely controlled by the surgeon. The surgeon uses a joystick-like mechanism to command the motion of the robot, which executes the surgical procedure. Based on the safety issues, and on the interaction between surgeon and the guiding system, a new categorisation of guiding systems for Medical Robotics and Computer Assisted Surgery is proposed. A flowchart is displayed in Figure 2-1.

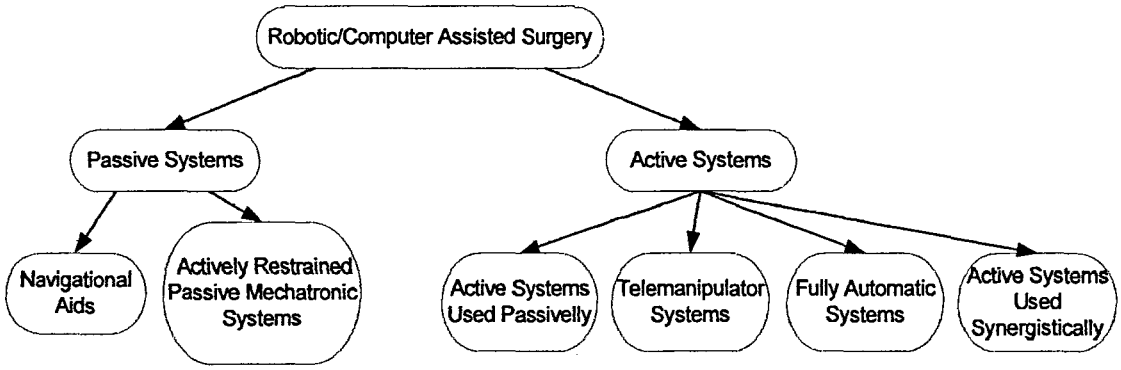

Figure 2-1. Classification of guiding device for MRCAS

As can be seen from Figure 2-1, the guiding systems for Robotic- and Computer-Assisted Surgery are divided into two categories: *passive systems* and *active systems*. Each of these systems is subdivided into further groups. Note that this classification is a snapshot of robotic/computer assisted surgery devices at the beginning of the 21st century. This classification is expected to suffer changes in the years to come, as technology evolves and human awareness of such devices increases.

The term *passive systems* define that category of systems that cannot produce motion on their own. Therefore, they cannot harm anybody who interacts with them. These systems are completely safe, without any risk of injuries to the patient or the surgeon.

The passive systems can be both non-invasive and invasive. The non-invasive ones are called *navigational aids*, and the invasive ones are called *actively restrained passive mechatronic systems*.

The *navigational aids* consist of computer-integrated instrumentation and image guided surgery. Thus, they are used only to display real-time information allowing the surgeon to localise a surgical instrument relatively to the anatomical structures and to compare the executed strategy with the planned one. The surgeon is totally in charge of the execution of the surgical action. On the other hand, the *actively restrained passive mechatronic systems* are capable of guiding the surgeons in order to improve accuracy, efficiency and reliability of surgical procedures. They can be used as both precise positioning systems and trajectory following systems. Such systems are intended to combine the advantages of both passive and active systems: the complexity of tasks potentially achieved by an active system with the limited risk involved by a passive one.

The term *active systems* defines those manipulators that are activated by actuators such as electrical motors and that are able to move on their own accord. Thus, there is a potential risk of injuries due to the fact that at anytime the manipulators could make uncontrollable movements. These systems can also be non-invasive and invasive. The non-invasive ones are usually precise positioning systems and are called *active systems used passively.* The invasive systems are usually precise trajectory following systems and include *telemanipulator systems*, *fully automatic robotic systems*, and *active systems used synergistically.*

The *active systems used passively* are used to aid tool guidance in a surgical environment. After actively positioning the robot at the desired position, brakes are applied and the robot is switched off, so that no uncontrollable motion can occur. After the positioning is completed and the robot switched off, the surgeon is totally in charge of the operation. Davies, Cinquin and DiGioia [27, 29-31] classify these types of robotic devices as passive systems because they do not physically interact with the patient. However, in terms of the above definitions for passive and active systems, as long as a system is capable of moving on its own it is an active system. For example, while

performing active positioning, before the robot has been switched off, software or hardware failure can occur, which could result in harm to people in close proximity.

Telemanipulator systems are those systems where the surgeon is in charge of the operation through a master-slave principal. The master is usually mounted separately from the slave and may consist of a simple joystick input system or a kinematic imitator of the slave robot. The slave robot comes into contact with the patient and is a robotic system able to move on its own. In this case, the distance between the surgeon and the operating theatre is of no importance.

The *fully automatic robotic systems* are used to perform a part of a surgical operation without the surgeon's help. In this case the surgeon only has a supervisory role. The last group of active systems are the *active systems used synergistically.* In this case the surgeon physically interacts with the robot in order to perform a surgical procedure. Electrical motors are used to restrain the surgeon's motion, but they are still capable of driving the robot. In the following subchapters, each of these groups is discussed in more detail, offering examples of systems from the existing literature.

2.4 Passive Systems

2.4.1 Navigational aids

A surgical assistant shall be described as a *navigational aid* if the system has no control over the position of the tool. The tool is guided under the power and judgement of the surgeon alone. The assistant system merely monitors and displays the tool position and may offer advice on a preferred procedure. These systems can be used to move the tool to a pre-determined position, as displayed on the screen, but require a lot of training. Furthermore, these systems are not suitable for trajectory following.

Leitner *et. al.* [8] developed a computer-assistant for total knee replacement (TKR) surgery. The system is based on the use of an Aesculap ancillary for total knee

prosthesis and a 3D localizer (Optotrack^{TM}), which localizes infra-red diodes within the surgical field. Rigid bodies constructed by assembling at least three infra-red diodes, are fixed to the iliac crest, the distal femur, the proximal tibia, and the foot in order to determine the mechanical axis of the leg. After a calibration procedure, a palpator (i.e. a rigid body fixed to a stem) permits measurement of positions of 3D points with accuracy and precision. Once the surgeon has calibrated the patient's leg and the cutting planes of cutting guides, the system can compute the angles between the cutting plane of a cutting guide and the mechanical axis. These angles can then be displayed in real time using a graphical interface. Once a jig is oriented properly, it is secured in position and cuts are made with a standard oscillating saw.

DiGioia and co-workers [30, 32, 33] have developed a navigational aid for accurate placement of the acetabular cup implant in total hip replacement (THR). The system is a computer assisted and image guided clinical system that provides surgeons with the tools to place the cup precisely within the pelvis and measure its relative orientation. The system includes a pre-operative planner, a range of motion simulator, and an intra-operative display tool. The pre-operative planner allows the surgeon to determine the appropriate implant size and placement of the acetabular component within the pelvis based upon pre-operative computerised tomography (CT) images. The range of the motion simulator determines the femoral range of motion based on the implant placement parameters provided by the pre-operative planner. Feedback provided by the simulator can aid the surgeon in determining optimal, patient-specific acetabular implant placement. The system allows the surgeon to determine where the pelvis and acetabulum are in 'operating room coordinates' at all times during surgery using a non-invasive technique. As opposed to the registration method presented by Leitner, who is using an optical tracking camera, which is tracking the position of fiducial pins (special light emitting diodes (LED's)) surgically implanted into bone, DiGioia and co-workers use surface geometry to perform the registration. Using this technique, it is necessary to sense multiple points on the surface of the bone with a digitizing probe during surgery. These intraoperative data points are then matched to a geometric description of the bony surface of the patient derived from the CT images used to plan the surgery.

A combination of the two registration techniques is used by Julliard, Lavalle and Dessenne [34], who proposed a navigational aid for reconstruction of the anterior cruciate ligament. The system consisting of a computer and a 3D optical sensor is proposed to help the surgeon to control the placement of a graft. This system can be used to minimize anisometry of the graft and avoid notch impingement. Three-dimensional data are collected intraoperativelly using the optical localizer. During the operation two optical rigid bodies are attached to the femur and the tibia that define the reference coordinate system for the femur and the tibia. For various knee positions the surgeon records the location of the optical rigid bodies. The surgeon then uses a palpator to digitize in 3D fifty to a hundred data points by pushing the tip in contact with the bone surface and pressing a foot switch for each point. Next, using an arthroscope the surgeon digitises the femoral notch and the tibial plateau in the area of natural insertion. After data acquisition, the computer reconstructs notch and tibial surfaces by approximating the points that have been digitized. At this stage, the system enables the surgeon to navigate on the real knee surfaces, and to visualize the position of the palpator on the arthroscopic image and on the 3D views of the virtual model, which are displayed on the computer screen.

Another system based on 'shape registration' (that does not uses artificial fiducial markers before the scanning process) was developed by Merloz *et al.* [35]. The system is a computer assisted spine surgical system used for pedicle screw placement. A user interface enables the surgeon to plan the trajectory of the pedicle screw using preoperative CT images of the chosen vertebrae. A 3D pointer equipped with LEDs, together with a 3D optical localizer, collects point coordinates on the visible back part of the vertebra. To track and compensate for all motions caused by respiration and bone manipulation, a dynamic frame rigid body is attached to each vertebra to be operated on. Anatomic landmarks are selected on CT images and digitised during surgery, such that a registration algorithm is used to match intraoperative data with the CT model of the vertebra. A computer based guiding system together with a 3D optical localizer is used to perform the planned trajectory, using diodes mounted on a standard surgical drill guide.

Phillips and Viant *et al.* [36, 37] proposed a computer assisted orthopaedic system. The prototype system is used to implement a straight-line trajectory typical of drilling operations such as distal locking of intramedullary nails and fixation of hip fractures. The system comprises three parts: a smart image intensifier able to take distortion-free X-ray images; a trajectory planner that describes the required drilling trajectory in 3D space; and a braked passive manipulator, which translates this trajectory into a physical position. Once the X-ray images have been taken the trajectory planner is used to decide upon a trajectory for the drill bit. Then, the surgeon moves the manipulator end-effector (a guiding cannula) to the required position with the aid of the graphical display, which shows continuously the deviation of the end-effector from the optimal trajectory. The surgeon is expected to align two cross hairs on the computer screen to position the guiding cannula along the desired drilling trajectory. Once the desired position has been achieved the brakes on the passive arm are applied.

Another computer-integrated orthopaedic system is described by Joscowicz *et al.* [38]. Design to assist surgeons performing alignment and positioning of bone fragments, nail insertion, and distal screw locking, the system is composed of a standard fluoroscopic C-arm, a real-time optical position tracking system, a computer workstation with data processing and visualisation software, and an adjustable drill guide device for assisting the surgeon in distal locking. The system displays 3D bone models created from preoperative CT and tracked intraoperativelly in real time. Fluoroscopic images are used to register the bone models to the intraoperative situation and to verify that the registration is maintained. The position-tracking unit provides accurate, real-time 3D positions with optical cameras following infrared LEDs rigidly mounted on the surgical instruments and attached to the bone via bone screws. The computer workstation is used preoperatively for modelling and planning, and intraoperativelly for data fusion and display. The adjustable drill guide is a passive positioning device that attaches to the nail head to assist the surgeon in drilling the distal holes.

Tonetti *et al.* [39] describe the application of an image-guided system for iliosacral screw placement for repairing pelvic fractures. The novel use of an ultra-sound scanner to register patient position to pre-operative CT data is the focus point. An optical

localiser tracks the position of the scanner and sixty ultra-sound images scanner positions are recorded. Commercially available surface based registration software is used to relate the two types of data. The graphical user interface (GUI) displays two cross hairs to the surgeon. One cross hair represents the position of the end of the drill bit, while the second corresponds to alignment. Two small, concentric target circles are also shown to indicate the desired trajectory. The goal for the surgeon is to align the drill bit so that the two cross hairs are in the centre of the smallest circle. Once this has been accomplished the surgeon can start the drilling procedure. During the operation the surgeon keeps track of performance via the cross hairs to ensure that trajectory stays true.

Langlotz *et al.* [40] also demonstrates that an image guided system can be used to perform pelvic osteotomies for the treatment of dysplastic hips. System registration is performed in a more common manner than is accomplished by Tonetti [39]. The operation cannot be performed in a non-invasive manner, therefore the surgeon has visual and physical access to the bone so that it can be probed and matched to the CT model resulting in the registration of the system. Again, a custom GUI is used to guide the surgeon through the operation.

Augmented Reality (AR) is a new technique for surgical data visualisation. It is a method that involves combining information from the real world with computer generated graphics. Blackwell, Morgan and DiGioia [41] discuss the techniques that they used to implement a Three-Dimensional Image Overlay System at Carnegie Mellon University. In a similar manner to some of the systems that have been discussed so far, an optical localiser is used to track tools, jigs and equipment. However, in this case the surgeon, wearing a pair of polarised glasses, views the patient through a semi-transparent "window" (a half-silvered mirror) onto which the computer-generated image is projected. The type of data that is typically displayed on such a screen is the desired tool position, 3D images of the bone structure under the surface of the skin and tool penetration depth. To ensure that the surgeon's view of the patient and the projected images match up, the localiser must track the position of the surgeon with respect to the patient and the view screen.

2.4.2 Actively restrained passive mechatronic systems

Systems of this type are usually found in the literature included under different headings. Some authors include these systems in a *semi-active systems* group [29, 30], and others include them under the heading of *synergistic systems* [31, 42]. However, both of these terms do not fully describe these systems and are rather confusing. The term "*actively restrained passive mechatronic system*" was introduced by the author, because it is believed that it describes more accurately such a system from both a safety and control points of view. Generally, it refers to manipulators that are not able to move on their own, yet are able to restrict the surgeon's motions in some manner. The surgeon provides the motive force for the tool, while computer controlled brakes or clutches restrain the motion. The actuators cannot impart a force to move the tool, but can only resist motion in some manner. Common examples of actuators for this genre of manipulators are electromechanical, pneumatic and hydraulic clutches and brakes.

A manipulator of this type is PADyC (Passive Arm with Dynamic Constraints) [42-44]. The prototype PADyC is a SCARA manipulator with two-DOF. Figure 2-2 shows a schematic of one joint of the system. For each joint, the classical actuator is replaced by a system that allows for four possible functions, F1 to F4: F1- the joint can be moved in the + and – directions; F2- the joint can be moved in + direction but cannot be moved in the – direction; F3- the joint can be moved in the – direction but cannot be moved in the + direction; F4- the joint cannot be moved.

The manipulator joint consists of a pair of motors that drive two overrunning clutches, shown in Figure 2-2. The motors drive the clutch wheels through a worm gear to prevent the surgeon from back-driving the mechanism. The clutches are computer-controlled to allow the surgeon to move the manipulator in four different modes: (1) completely free movement of the arm, (2) reach a pre-defined position, (3) follow a pre-defined trajectory and (4) stay in a pre-defined safety region [43, 44].

In order to constrain the motion of the end-effector according to a given task, the clutches will engage or disengage a pair of freewheels independently. Each motor is electronically constrained to rotate in a single direction. The velocity of each joint directly depends on the end-effector velocity produced by the user. Referring to Figure 2-2, which shows the joint mechanism, one clutch controls clockwise rotation while the other one restrains motion in an opposite direction. The speed at which a clutch is driven determines the maximum velocity in that direction. Thus, the surgeon can move the arm in either direction if the joint velocity is kept less than the velocity of the motors; the surgeon can only move the arm in one direction, if one of the motors is stopped; and the arm cannot be moved at all, while both motors are stopped. In 1993, Lavalee and Trocaz obtained a European patent for the system joint [45], and in 1995, a US one [46].

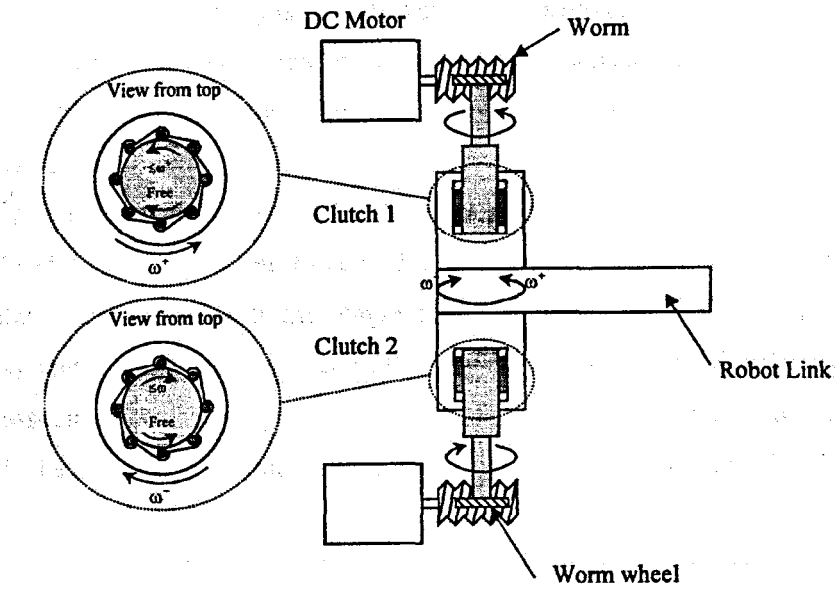

Figure 2-2. PADyC joint mechanism [18]

Although, the system is entirely safe, the two-DOF prototype has insufficient positional accuracy [43, 44]. The end-effector positional error was reported as being as high as a few millimetres. The inaccuracy of the system was attributed to the flexion in the axes between the freewheels and the link, flexion in the freewheels, backlash in the worm-gear drives, and hysteresis of the freewheels. Experiments show that the error amplitude

of the two-DOF prototype arm can reach 10 mm for an end-effector force of 10N and 20 mm for an input force of 20N. More recently, a 6-DOF system based on the PADyC prototype has been proposed for cardiac puncturing and used only to help the surgeons reach a position in space [47]. The six-axis system is used to attain the desired line of the trajectory so that the surgeon can accurately insert a surgical needle. The system has not been used for trajectory following because of the drawbacks of the joint mechanism and control difficulties. These issues are explored in detail in the next chapter.

2.5 Active Systems

An active system is defined as a system that is able to perform position and trajectory tasks under its own power. The active systems are motorised manipulators, similar to industrial robots, which can carry out a part of a surgical task by themselves. As shown in section 2.3, this class of robotic systems is divided further into four subclasses. These subclasses will be presented in more detail in the following sections.

2.5.1 Active systems used passively

These systems are usually non-invasive systems used for precise positioning of surgical tools in the operating environment. After positioning the robot is locked in position and switched off, leaving the surgeon in charge of the operation. Kwoh and co-workers proposed the first active robotic system used in a passive way [48, 49]. The authors used an industrial robot, a "PUMA 560", to suspend a fixture close to the patient's head to fix a biopsy tool for neurosurgery. The robot helped the surgeon to orientate drills and biopsy tools, which were inserted manually into the patient skull. A three-dimensional model of the brain and tumour was completed based on pre-operative CT scans. Then, registration of the robot to the patient was performed. Next, the robot was moved to the desired position and locked with all power disconnected, thus making it safer. After the surgeon completed the operation, the robot was switched on and removed from the

patient. The preliminary results demonstrated that, compared with a conventional stereotactic frame, a robot could perform this kind of operation in neurosurgery automatically and more precisely. However, due to the safety concerns implicated by using an industrial robot, the project had to be abandoned.

"PinPoint ™" system [50, 51] is a robotic system used to mechanically guide biopsy. Developed by Marconi Medical Systems, PinPoint is a frameless stereotactic arm for use in planning CT guided biopsies. The arm is direction encoded so that the intervention path can be visualised on CT and evaluated. Once the optimum biopsy needle path is determined the PinPoint arm can be locked, thus serving as a motionless guide to needle placement.

Recently, a special commercial purpose-robot called "NeuroMate™" has been developed by Integrated Surgical Systems (ISS) [24]. "NeuroMate™" is an image-directed robotic assistant for stereotactic brain surgery, orienting and positioning surgical tools. The system consists of a robotic arm assembly and a PC-based positioning system. The system is primarily used passively (i.e. locked in position whilst a surgeon uses surgical instruments manually) but has the capacity for active surgical applications.

Bouazza-Marouf, Browbank and Hewit [52], developed a system for internal fixation of femoral fractures. It incorporates a prototype manipulator, a PC based controller and a machine vision sub-system interfaced to a standard C-arm X-ray unit. Once intra-operative registration is established and the drilling trajectory defined by the surgeon, the machine vision sub-system outputs the trajectory data to the controller allowing automatic positioning of a drill holder unit. All the robot's joints, except the drill-holder feed joint, are locked in position before the drilling is initiated by the surgeon. In addition to the safety related problems introduced by this type of systems, the surgeon is helpless in controlling the tools in motion as is required by complex surgical procedures such as TKR.

2.5.2 Telemanipulator systems

Telemanipulator systems are usually developed to assist surgeons in minimal invasive surgery such as laparoscopy, heart surgery, and microsurgery in a number of specialties such as vascular, gynaecological, neurological, and ophthalmological surgery. The first telemanipulator system available on the market was "AESOP®" (Automated Endoscope System for Optimal Positioning) manufactured by Computer Motion [22]. The computer-controlled robot holds a laparoscope and moves under the direction of the surgeon by means of a foot, a hand or a voice controller.

From the "AESOP®" system, two very well known master-slave systems are derived. The "da Vinci™" surgical system developed by Intuitive Surgical Incorporated [21] and the "Zeus™" system of Computer Motion [22, 54]. Both systems consist of an invasive three-arm manipulator and a console that helps the surgeon to perform a surgical procedure with great precision and without tremor. A robotic arm carries an endoscope (AESOP) that feeds back an image of the operative site to the monitor, while two other manipulator arms carry interchangeable tools, such as scissors and grippers. The console displays the surgical field and the surgeon can see the ends of the robotic arms as they move under his direction. The system also provides the surgeon with force feedback, gained by using haptic technology, to reproduce the contact forces of the surgery. Beside the three arms and the console, the "da Vinci™" system has an "EndoWrist™" fitted to the manipulator arms, which carry the tools. The "EndoWrist™" is a key component of the Intuitive system. It has seven-DOF for each hand and gives the surgeon the ability to reach around, beyond, and behind delicate body structures. It is connected to the rest of the system by a mechanical cable transmission and its motion is monitored so that the control algorithms can translate the surgeon's motion to the robot's wrist. "Zeus™" uses a voice-controlled endoscope. The surgeon console consists of a monitor and a seated station whereby the surgeon can control the positioner robots via handles resembling traditional laparoscopic instruments. During surgery, the motions of the instrument-holding robots are controlled by the surgeon while seated at the console. The left and right master mechanisms each have five-DOF that mimics the motion of a laparoscopic instrument.

Each Zeus positioner is a geared, servomotor-driven mechanism that attaches to the rail of the surgical table. The scale of movement between master and slave can be adjusted so that high precision can be achieved. The main drawbacks of these systems are the reduced feeling for surgeons and mediocre patient safety.

Another telerobotic system used to help the surgeons in microsurgery is RAMS (The Robot Assisted MicroSurgery) [55, 56]. The system allows the surgeon to command motions for a surgical instrument using a master input device (similar to a joystick) that precisely measures its handle position in six degrees of freedom. The system overview is shown in Figure 2-3. The software on the servo-control boards, position the joints of the slave arm and determines the torque at the joints of the master arm. The system is able to scale down the surgeon's hand motion and to filter out the surgeon's tremor.

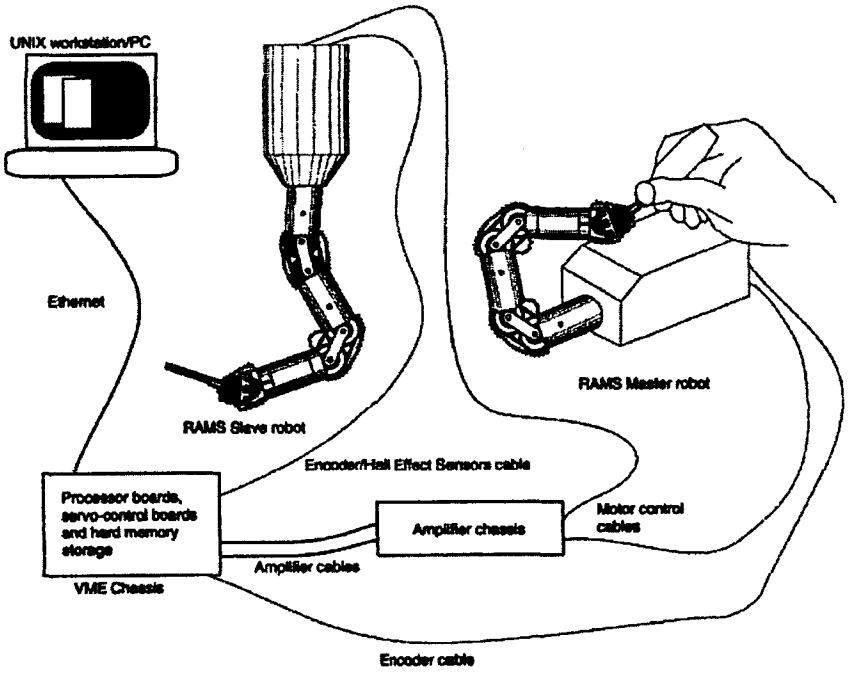

Figure 2-3. RAMS system overview [55]

Another telemanipulator system available on the market is "EndoAssist™" developed by Armstrong Healthcare [23]. EndoAssist is a robotic system that holds a conventional laparoscopic telescope and camera co-ordinated by the surgeon's head movements using a headband pointer. The camera is moved only when a footswitch has been pressed, which allows freedom of movement for the surgeon all the time. The robot has assisted

in cholecystectomy, hernia repairs, appendectomy, hemicolectomy, sympathectomy, hysterectomy, and gynaecological laparoscopy.

Kobayashi *et al.* [57] describes a new type of laparoscopic manipulator system. It consists of a five-bar linkage mechanism, an optical zoom, and a man-machine interface. This system's major characteristics are the capability of achieving intrinsic safety due to limitations in the range of movement, and high reliability because of the simplicity of both its mechanism and its software. The five-bar linkage mechanism, shown in Figure 2-4, has two-DOF and its movement determines the angle of the laparoscope. By changing the angles of two active joints, using electrical motors (A and B in Figure 2-4), the top link can be moved in the X-Y plane, as shown in Figure 2-4. An optical zoom is used to substitute for the normal back-and-forth movements of the laparoscope. A man-machine interface that consists of a gyro sensor mounted on the surgeon's head, a knee switch, and an indicator, is used to control the motion of the laparoscope manipulator.

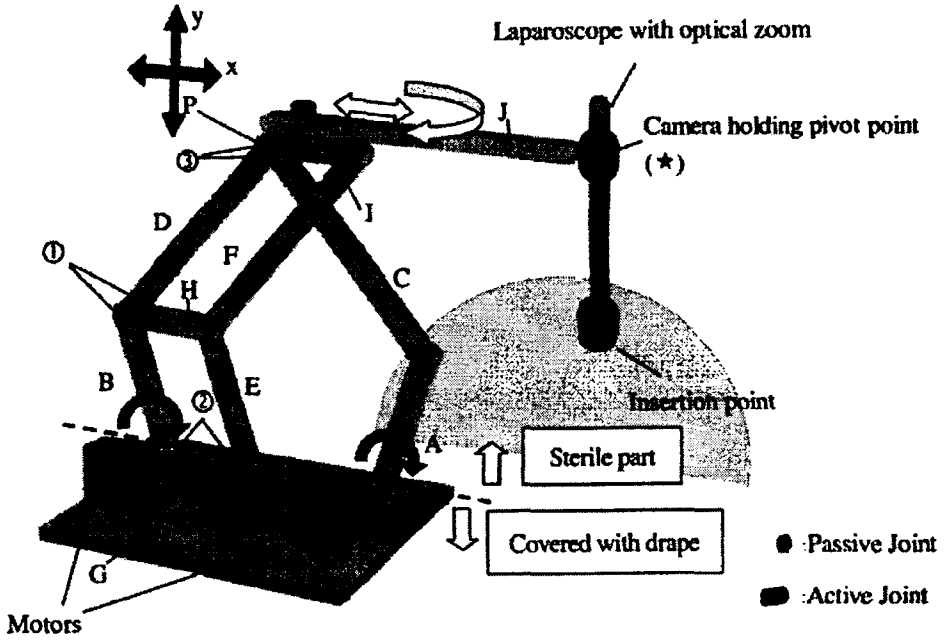

Figure 2-4. Five-bar linkage manipulator mechanism [57]

Even though the system is intrinsically safe and has good reliability due to its simplicity of software and mechanism, it does not offer the flexibility required when following

predefined trajectories, and does not restrain the motion of the end-effector in order to avoid going into forbidden areas such as nerves and blood vessels.

2.5.3 Fully automatic robotic systems

A well-known system of this category is "Robodoc®" produced by the Integrated Surgical System [21, 58-60]. Designed to perform cementless total hip replacement, the system consists of a pre-operative planning computer workstation, named Orthodoc, and a five-axis robotic arm, called Robodoc. The robotic arm has a high-speed rotary cutter as an end-effector, which can accurately ream out the femoral cavity for the stem of a particular implant. The system is illustrated in Figure 2-5.

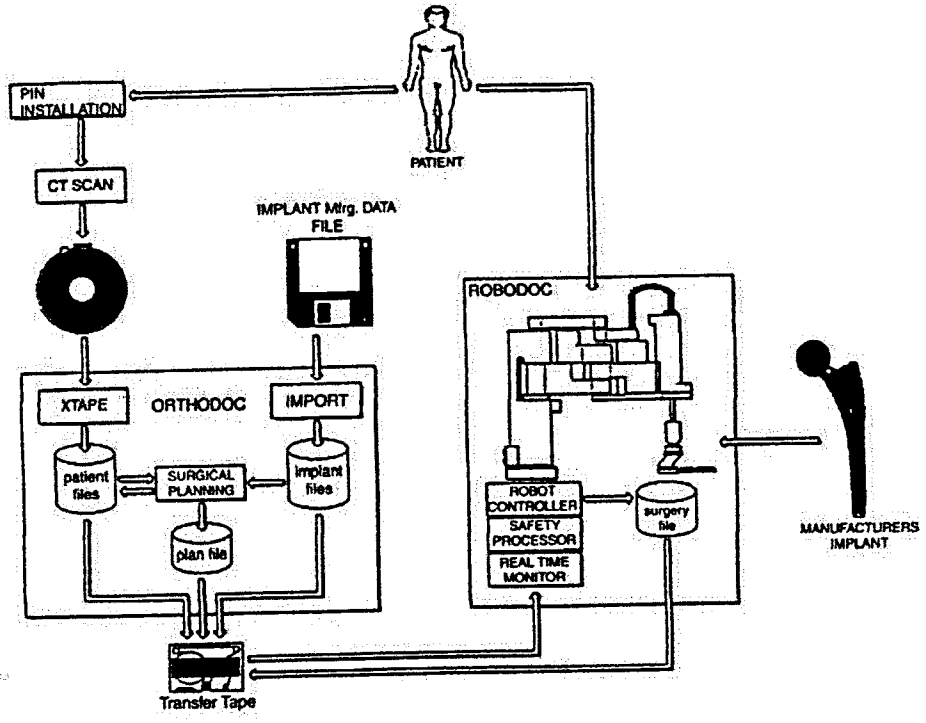

a)

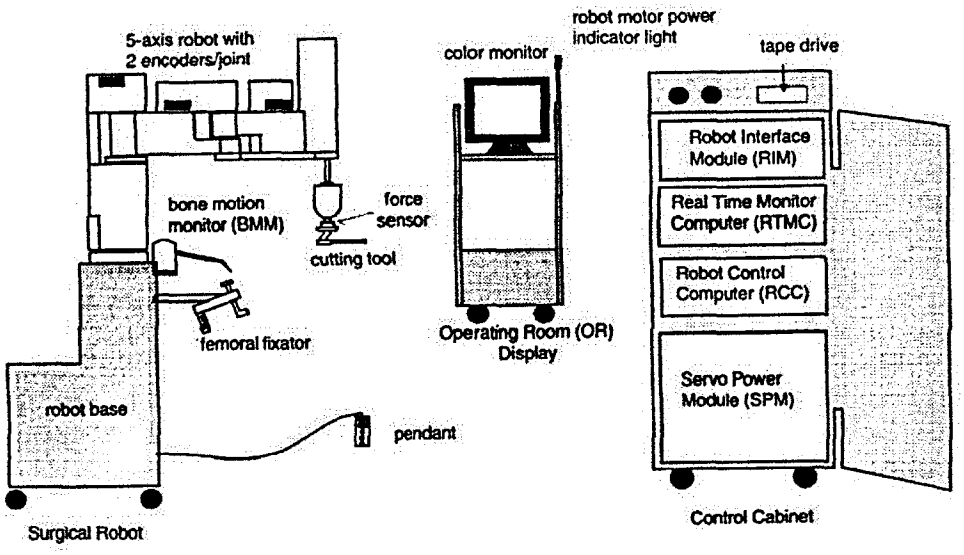

b)

Figure 2-5. ROBODOC [58], a) system procedural flow; b) surgical assistant

The pre-operative planning computer allows a computerised model of the suitable size and shape of implant to be placed over a three-dimensional model of the hip, built from a series of CT scans. Once the pre-operative planning has been finished, the intraoperative phase begins with the patient's leg being clamped to a rigid framework mounted on the robot. In this way the working area is treated as a static object, in which the predefined motion (planned pre-operatively) can be executed. The procedural flow is shown in Figure 2-5a. This strategy gives input to the computer-controlled robot. Once the patient is clamped, the surgeon 'opens the hip' and the femoral head is removed as in a traditional operation. At this point the robot tip, carrying a high-speed rotary cutter mounted on a force sensor, is moved into position and then the sequence of motion required to resect the appropriate shape for mounting the implant stem starts.

For safety reasons the robot, shown in Figure 2-5b, contains a series of safety-related modifications. They are a dedicated safety processor, hardware sensors and software routines [61]. A redundant motion monitoring subsystem is used during the cutting phase to check that the cutter tip never strays more than a pre-specified amount outside of the defined implant volume. It also monitors strain gauges that can detect possible shifts of the bone relative to the fixation device. The safety processor ensures that the

robot operates within a set of safety limits. It has a direct hardware interface to all safety-related hardware components, including the redundant encoders, force sensor and bone motion monitor, cutter control relay, and robot motor power relay. The system is automatically stopped in case one of the linked subsystems exceeds its safety limit.

The main disadvantages of Robodoc are its large dimensions, excessive weight, and lack of physical interaction with the surgeon. In addition, the time for the procedure was proved to be longer than in conventional surgery, resulting in increased anaesthesia times and increased blood loss.

Another fully automatic robot able to assists surgeons in orthopaedic surgery is "CASPAR" (Computer Assisted Surgical Planning And Robotics) [62]. Produced by OrtoMAQUET in Germany, the system utilizes a robot based on an anthropomorphic Staubli-Automation industrial clean-robot, which has been fundamentally modified for orthopaedic surgery. Similar with Robodoc, based on patient data, the placement of a hip prosthesis is simulated. All contours for a perfect fit are milled to high precision under surgeon's supervision. The drawbacks of this system are similar to those mentioned for ROBODOC, such as large dimensions, heavy weight and lack of physical interaction with the surgeon.

Another fully automatic robot used for THR is "CRIGOS", developed at the Aachen University of Technology, Germany [63]. The main difference of this system when comparing it with the others used for THR is a compact parallel robot configuration (closed kinematic chains). This kinematic architecture has a couple of properties, which can be advantageous in a surgical application. Due to the high nominal load/weight ratio, the surgical robot can be very light. Moreover, because these types of manipulators usually have a smaller workspace and less dexterity they can be much safer than serial manipulators. Depending on the complexity of the surgical intervention, the active system "CRIGOS" supports two modes of execution: (1) it can be used passively or (2) fully automatic. In the first mode the robot is used to position tool-guides. After the desired position is achieved the robot is switched off, allowing the surgeon to work on the bone by inserting and moving the surgical instrument in the tool

guide. When 3D milling is required (preparing a femoral cavity of a hip prosthesis), the fully automatic mode is employed.

A further example of a fully automatic robot system is the "Minerva" system, developed by the Laboratory of Microengineering at the Swiss Federal Institute of Technology in Lausanne, Switzerland [25, 64-66]. The system has been applied clinically for neurosurgical applications and is able to independently perform skin incisions, drilling of the cranium, perforating of meninges and manipulation of stereotactic instruments under the supervision of a surgeon. The robot, in association with a CT imaging system, employs a series of special tools, located on a rotary carousel, each of which can then be locked into position on a single axis travel. This single axis then advances the tool linearly into the region of the patient's head, which is datumed to a stereotactic frame. The robot's positional accuracy is just under 1mm. However, the authors admitted that two of the operations were considered as failures. The first was attributed to the head of the patient being fixed too low in the stereotactic frame, thus making it impossible for the robot to reach the target area. The second operation failed because the robot retrieved tissue from around the tumour rather than tissue from the tumour itself [65, 66]. It is well known, that operating on the brain is an extremely delicate procedure and that robot failure could seriously injure or kill the patient.

All of these systems work without the surgeons' help, the surgeon having only a supervisory role. Even though most of these systems are available commercially and few of them operate in the surgical environment, not many medical centres have purchase these systems as there are still many questions regarding safety of those who interact with the system, the surgeon's input and the size and shape of the systems.

2.5.4 Active systems used synergistically

The active systems used synergistically are also invasive systems, but the surgeon works together (in synergy) with the robot in order to perform a complex surgical task.

Thus the surgeon's skills and judgement are considered at all times. One well-known system that belongs to this category is ACROBOT (Active Constraint Robot), developed by Davies et al. at Imperial College, London [15, 16, 67]. The system has been designed to perform operations such as prosthetic implant in Total Knee Replacement (TKR) surgery. ACROBOT allows a surgeon to hold a force-controlled handle placed on the tip of the manipulator. The surgeon can move a cutter through the bone but the system prevents him from either cutting too much bone or moving out of a pre-defined region. Each robotic joint is motorised. As the user pushes on the control handle, the motors are back-driven to a new position. By varying the control parameters used to power the motors, the stiffness of the system can be varied. If the surgeon tries to move outside the edge of the safety envelope the motors become extremely stiff, resisting the surgeon's efforts. The stiffness can be programmed with a smooth transition so that the surgeon has a tactile sense of his position within the safe region.

The control strategy is based on creating an artificial region with different levels of resistance of the surgeon efforts, as shown in Figure 2-6. Inside this region the surgeon can freely move the robot to the desired position, but at the edge of that defined area, the surgeon can only move the robot along, but not beyond, the boundary. Region I is a permitted zone and only a low-force is necessary to move the robot arm. Region III is a completely restricted region, requiring high forces to move into it, while region II is an intermediate zone in which the system progressively increases the resistance of the motors since region III is very close. To constrain the robot to a particular region, the motor control parameters have to be adjusted depending on the position of the end-effector. The velocity of the manipulator is chosen proportional to the user-input force [68]. This concept is called by the authors 'active constraints' and is meant to increase safety and accuracy of the cutting process. In spite of the fact that the system is custom-built, it is very similar in nature to an industrial system due to the need for powerful motors that resist the surgeon's input-force. Beside the 'region' control shown above, the system was not demonstrated for either position or trajectory control. Furthermore, because the system is actually driving against any input force to return the robot to the safe region, both the surgeon and the patient are at risk.

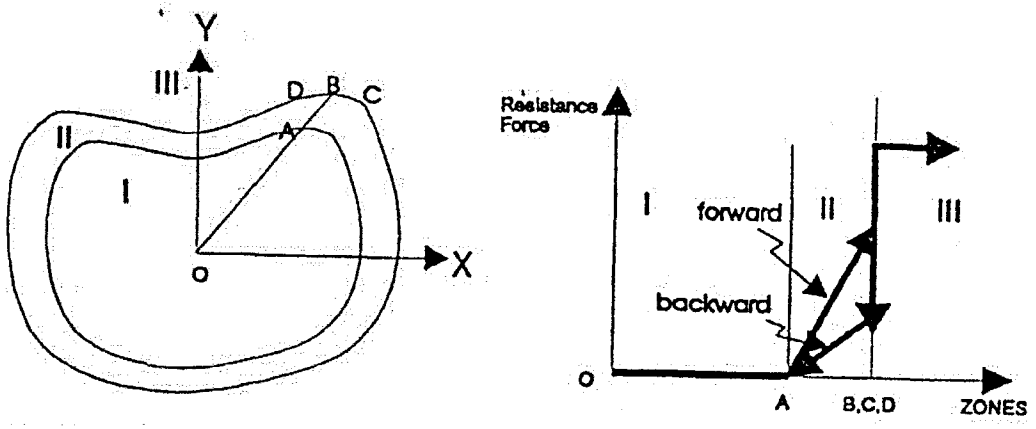

Figure 2-6. Resistance force in different zones and different directions of motion constraint [68]

Van Ham *et al.* [17] proposed another active system that is able to work together with a surgeon in order to achieve a surgical task. Designed for tibial knee implant, the system uses a hybrid force-velocity control scheme to constrain the end-effector to stay in a predefined plan. By specifying the desired force (or velocity) and the desired moment (or angular velocity) along every axis of the task frame, the system is capable of constraining the surgeon to stay in a pre-defined cutting plane and cannot move out of this plane. An end mill, mounted on the robot's end-effector, is used to cut the bone surfaces, instead of a saw as in the conventional operation, to diminish the influence of the flexibility of the tool. Although, the system shows a high degree of accuracy for the surface flatness and that it can stay within a specified plane, it does not prove it can follow a predefined trajectory. In addition, the system is not capable of constraining the motion within the specified cutting plane. Thus, in the cutting plane the safety of critical regions such as nerves and blood vessels is only guaranteed by the supervision of the surgeon.

Reedman and Bouazza-Marouf [18] developed a two-DOF SCARA manipulator (RR) able to follow a trajectory under a user-input force. The proposed joint mechanism is shown in Figure 2-7, and consists of two worms driven by a low power DC servomotor. The two worms follow a worm wheel that is fixed to the robot link. The user provides a force on the end-effector and motion is allowed by controlling the two worms simultaneously. The non-backdriveability of the worm is achieved by the choice of the

lead angle, which is less than the angle of friction. The high gear ratio chosen contribute to the manipulator safe in case of a failure. The joint torque is measured using strain gauges, and the control strategy adopted is computed-torque control. To ensure sufficient smoothness of the desired position the velocity command is generated from the user-input force. Although, the control strategy is more focused on cancelling backlash, trajectory following is performed with high accuracy. However, just a few analyses have been presented and it seems that the manipulator cannot track a trajectory with low velocity due to a vibrating motion excited by both the interaction with the user and oscillations generated from overall system stiffness. Moreover, due to manipulator configuration, the velocity demand may suddenly change from zero to a larger value, requiring large torque from the motors. Thus, the system lurches, resulting in large errors.

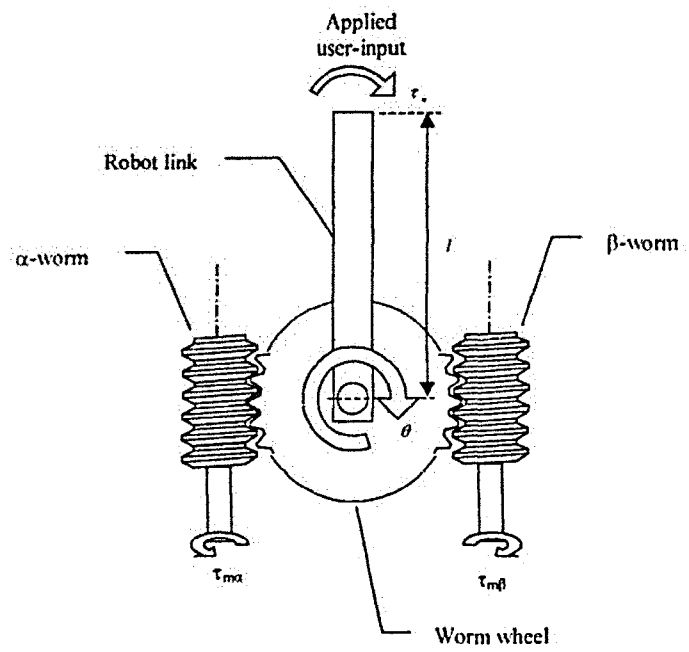

Figure 2-7. Dual-worm drive joint [18]

Even though these systems require an input from the surgeon in order to perform a surgical task, they are still the subject of research referring to safety and accuracy while path tracking. Furthermore, more research needs to be done in order to keep the tip of the manipulator inside a safety envelope while restraining it from going beyond the

predefined boundary, in order to avoid certain anatomical obstacles (i.e. blood vesels, or ligaments).

2.6 Other Relevant Works

An area of interest in terms of using mechatronic systems for physical interaction with humans is that of haptic devices. Haptic devices are mechanisms that provide tactile feedback to a user while helping him/her complete a task accurately. As with surgical systems, many of the research devices have used modified industrial manipulators to provide this feedback. Much of the research has involved making the end-effector behave like a different object, for example a tennis ball or a spring. However, in machining processes and in guiding devices it is more important that the system is capable of following a pre-define trajectory. There are two particularly interesting projects in the field of haptic displays that are relevant in the context of this research. These are PTER (Passive Trajectory Enhancing Robot), developed by a group at the Georgia Institute of Technology, US [69, 70], and COBOT (Collaborative Robot) designed by Colgate and Peshkin at LIMPS Atlanta, US [71, 72].

2.6.1 PTER (Passive Trajectory Enhancing Robot)

PTER is a passive system that instead of using actuators to add energy into the system utilizes actuators that dissipate user-supplied energy. The system, shown in Figure 2-8, uses brakes and clutches to dissipate user-supplied energy in order to simulate virtual boundaries [69]. The robot is based on a motorized active haptic display known as HURBIRT [70]. The main difference between the two robots is that PTER uses four clutches and a differential gearbox to dynamically link the rotational velocities between successive revolute joints (i.e. by varying the braking force of the clutches). The end-effector of the linkage consists of a handle instrumented with a force sensor. PTER uses

four electromagnetic clutches to control motion. The joint coupling mechanism is shown in Figure 2-9. Two of the clutches connect each of the two controllable joints to a zero velocity source acting like a brake (clutches 1 and 2 in Figure 2-9a). A third clutch is controlled to couple or release the rotation of both links that rotate in the same direction. The fourth clutch connects the rotation of the two links in the opposite direction through a gear train, as depicted in Figure 2-8b. This principle was patented in 1998 in the US by Book and Charles [73].

Although many control strategies have been employed on PTER [74-77] the manipulator is not able to track a trajectory any closer than about 4mm. It was also found that in order to achieve acceptable performance, the clutches needed to be switched on and off very quickly, which caused undesirable discontinuous motion of the manipulator.

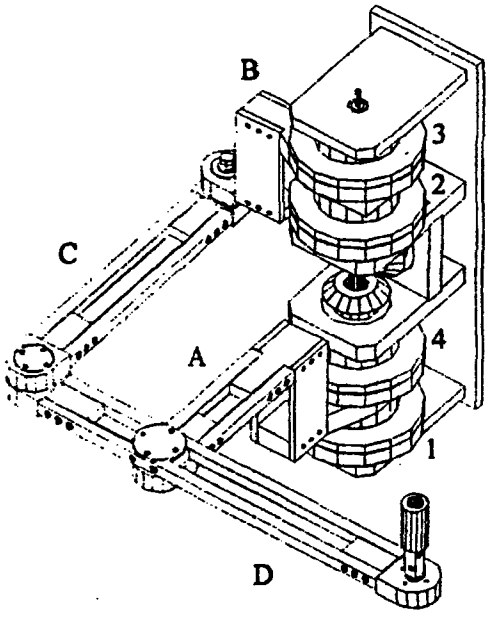

Figure 2-8. PTER system [69]

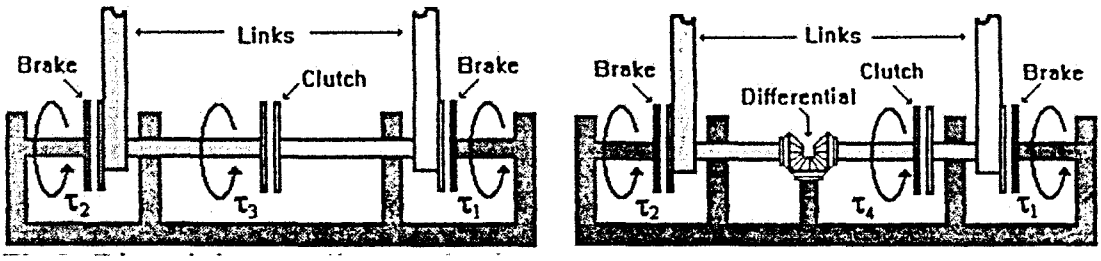

a) b)

Figure 2-9. Joint coupling mechanism, a) Direct, b) Inverting [69]

2.6.2 COBOT (COllaborative RoBOT)

Another example of a passive haptic device is COBOT developed by Colgate and Peshkin [71, 72]. The principle of COBOT is to implement the constraints by redirecting the operator's input. Thus, the active part of the system is a steering mechanism. The prototype COBOT is a single steering wheel, running on a plane surface, supported by a passive two-DOF Cartesian frame, as shown in Figure 2-10. The user moves the end-effector via a control handle mounted on the x-y frame. The direction of motion is controlled by sensing the force perpendicular to the direction of wheel rotation and controlling the direction of the wheel by a servomotor and gear train. Colgate et al. [79] describe two modes of operation: virtual caster and virtual wall. In virtual caster mode the steering behaves in a fashion that follows the direction of the input force. The motorised wheel is steered to minimize the forces perpendicular to the wheel. However, in the virtual wall model, as the user approaches a predefined boundary, the direction of travel is controlled to constrain the motion by steering the wheel perpendicular on the direction it is pushed, prohibiting movement beyond the boundary and moving tangential to the constraint.

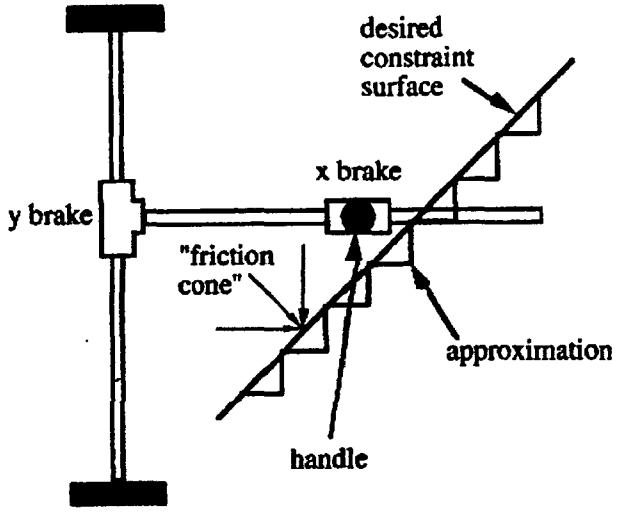

Figure 2-10. COBOT's concept [79]

There are two types of continuous variable transmissions (CVTs) used in the construction of cobots [80]. The first type is a single steered wheel rolling on a planar surface. This *translational* CVT (simply called the wheel) constrains a pair of linear speeds. The ratio of these speeds is defined by the heading of the wheel; it is the allowed direction of motion on the rolling surface. Forces perpendicular to the rolling direction are supported by constraint forces. The second type of CVT relates two angular speeds. This *rotational* CVT (or simply CVT) is composed of a sphere caged between two drive rollers and two steering rollers. The CVT constrains the drive roller speeds. The ratio of these angular speeds is defined by the common angular displacement of the steering rollers. Thus, the joints of the manipulator are kinematically linked, that is if the user forces motion of one joint the rest of the joints are forced to move in a direction that generates motion along the desired path. However, although this passive device promises trajectory tracking, the size of the CVT mechanism is large compared to the maximum force that they can resist. The robot is only expected to be able to withstand 13N of force (in its worst configuration) at the end-effector before the drive rollers in the CVT slip and the robot loses its ability to maintain the current position.

The COBOT was originally designed to provide physical feedback for virtual environments, but the potential of these collaborative robots in other safety-critical settings was quickly noted but only mentioned briefly. However, in reality the problem (certainly in the surgical environment) will be to ensure that the wheels do not slide on, or lose contact with the surface of the plane that they work on.

2.7 Discussion

Among the systems presented above, several surgical robot systems are in clinical trials in the UK and Europe whilst others including Robodoc, EndoAssist and AESOP are in the early stages of diffusion. However, the number of robotic systems remains low and many are being used for research, even if approved. It seems that it is difficult to introduce such motorised devices into the operating rooms due to the risks associated with them. Most medical robotic devices achieve safety by means of their software system. For example, most of the "active systems used passively" and "fully active systems" are based on complex software routines in order to achieve a goal. In addition, some systems, which are able to work together with a surgeon such as ACROBOT and Van Ham's manipulator, share similar disadvantages. The assurance of safety of a robotic mechanism is especially important under conditions of possible malfunction and/or accidental misdirection by the surgeon. An unexpected movement of the surgeon's hands could initiate an incorrect command input and the man-machine interface will respond in an unforeseen manner. Thus, it is preferable for the robot to be mechanically safe, rather than to have its safety attained only through the use of complicated software systems.

There are several custom-built systems that have been designed to increase safety. For example, some fully automatic systems have been designed with limited motion and forces, adequate for specific tasks in order to avoid severe injuries of patients if there were a failure. Kobayashi's laparoscope and CRIGOS system have been built to limit the robot's workspace by choosing a suitable kinematic solution. However, these systems often lack dexterity, and have difficulties following predefined trajectories.

There are some reports in which the safety of a device was achieved by virtue of a mechanism as in the case of PADyC, Reedman's manipulator, COBOT, and PTER. These concepts show the potential for future medical robots, but there is considerable room for improvement of kinematic solutions, actuator and transmission technology in order to accurately satisfy the surgical requirements. This is the subject of this research and an improved kinematic solution and actuator and transmission technology is proposed to overcome the drawbacks of existing systems in order to ease the introduction of these devices into the operating environment.

As it can be seen from the literature, safety is of the utmost importance. This highlights the concerns of using modified industrial or custom-built active systems no matter how advanced the measures taken to prevent unauthorised motion. It is believed that an actively restrained passive mechatronic system is the best solution for assisting in an operating environment as it combines the advantages of both passive and active systems: the complexity of task potentially achieved by an active system with the limited risk involved by a passive one.

Chapter 3
Actively Restrained Passive Mechatronic Systems

3.1 Introduction

This chapter describes in more details the existing systems similar in principle to the proposed actively restrained passive mechatronic system. Their drawbacks and limitations are presented, and a solution to overcome these is proposed. It is shown that for the existing actively restrained passive mechatronic devices a user is required to have a deep understanding of the mechanism in order to perform computer-controlled path following tasks in a smooth manner. The limitations of the manipulator kinematic configuration are also shown for trajectory following tasks, as well as the limitation of the control strategy in such passive systems. As a solution to these limitations, a polar manipulator is proposed as an actively restrained passive mechatronic system. It is shown that for this kinematic architecture, the path planning and path tracking issues are much simpler. Furthermore, a suitable joint mechanism was developed in order to overcome some of the drawbacks of the existing joint mechanisms and to improve the overall response of the proposed actively restrained passive mechatronic system.

3.2 Existing Actively Restrained Passive Mechatronic Devices

From the literature it can be seen that PADyC is the only actively restrained passive mechatronic system developed to assist in medical procedures. However, there are two other devices that make use of passivity to ensure user safety. These two devices, PTER

(Passive Trajectory Enhancing Robot) and COBOT (Collaborative Robot) provide a very different approach to that of PADyC by forcing a kinematic relationship between the joints, such that any user-input force in the general direction of the path will generate motion of the system along the path. These three mechatronic systems are discussed in this section, and the mechanical design (i.e. the kinematic configuration of the two-DOF system and the joint mechanism) and the control strategy adopted are highlighted.

3.2.1 PADyC

The PADyC system was introduced in section 2.4.2. The prototype is a two-DOF SCARA manipulator (RR) incapable of producing motion of its own, but capable of guiding the surgeon to achieve certain surgical tasks [42-44]. At every joint, PADyC has a pair of over-running clutches, each running on a separate motor driven hub. By controlling the speed of each motor, one clutch limits the maximum allowable speed in one direction, while the second clutch restricts speed in the opposite direction. Consequently, the operator can use any of four modes. The user can: freely move the arm, reach a pre-defined position, follow a pre-defined trajectory, and stay in a pre-defined region.

In the *'free' mode,* all the freewheels are disengaged; the authorised maximum velocity of each joint is constant and chosen sufficiently high to give the operator the feeling of free motion. The arm behaves as a classical passive one unless the operator tries to move the arm faster than the motor speed. Thus, the operator is constrained to stay below the pre-defined limit of the rotational speed.

In the *'position' mode,* a goal position may be defined in Cartesian space or in joint space. In the former case, a position of the end-effector is transformed into a finite set of goal configurations $Q(t)=(\theta_1, \theta_2)$ of the arm. At an instant time, t, a constraint vector C(t) (which describes the clutching status of each of the freewheels) is selected, which

corresponds to the smallest generalised rectangle that contains the segment between the initial and final position [Q_i, Q_f], as shown in Figure 3-1. The authorised speed of both joints is proportional to the error distance (difference between desired position and actual position). After the position is reached, all the freewheels are locked (i.e. C(t) = (1, 1, 1, 1)) in order to keep the position stable.

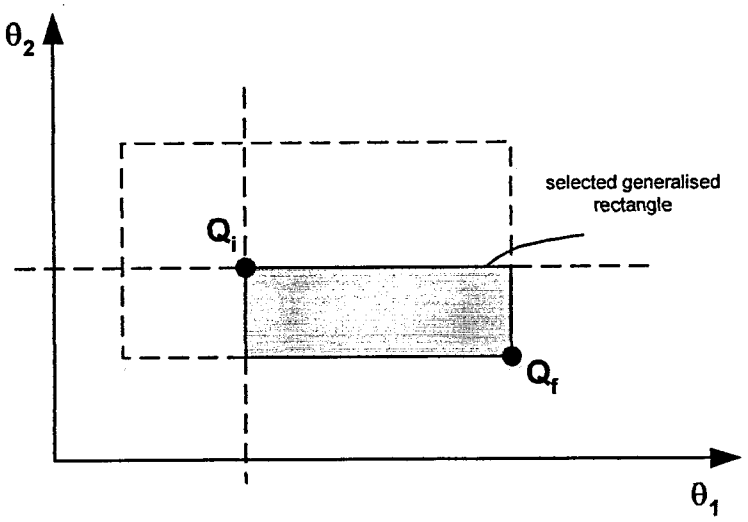

Figure 3-1. Position mode [43]

In the *'trajectory' mode,* a set of positions has to be reached. The trajectory is planned as a continuous curve (interpolation of sets of recorded configurations) associated to its corridor. Several methods have been tested to compute the motors' speed [43]. The method chosen by the authors searches for the largest rectangle completely included in the corridor associated with the trajectory, and which determines the right direction, as shown in Figure 3-2. The motors' speed is deduced from the rectangle dimensions.

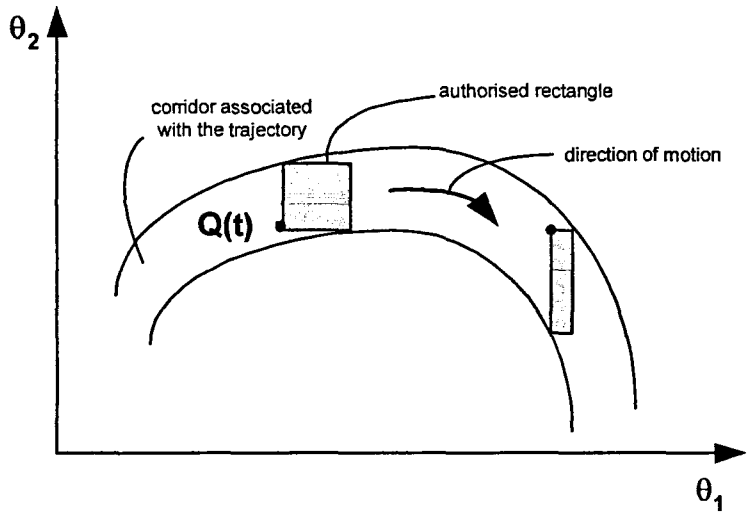

Figure 3-2. Trajectory following [43]

Further analysis of the algorithm that is used to implement the path following mode reveals some interesting problems. Consider the circular path, p(x, y), in Cartesian coordinates, as shown in Figure 3-3a, and its joint space representation, $Q(\theta_1, \theta_2)$, as shown in Figure 3-3b. The method employed to control PADyC involves approximating the joint-space path with a straight line. By considering a new point, a joint-space distance ΔQ further along the path, the amount that each joint needs to be moved to reach the new point can be calculated. Using this method, it is possible to generate an authorised rectangle (a region of allowable motion) as shown in Figure 3-3b. Figure 3-3a shows the authorised region, which is the mapped rectangle from joint-space into the task space. The authorised region is calculated by the computer in real-time and is continually adjusted to compensate for the current position of the manipulator. It can be seen that if the choice of ΔQ is very small, the robot may follow the path with some small degree of error, i.e. guiding the user down a narrow corridor.

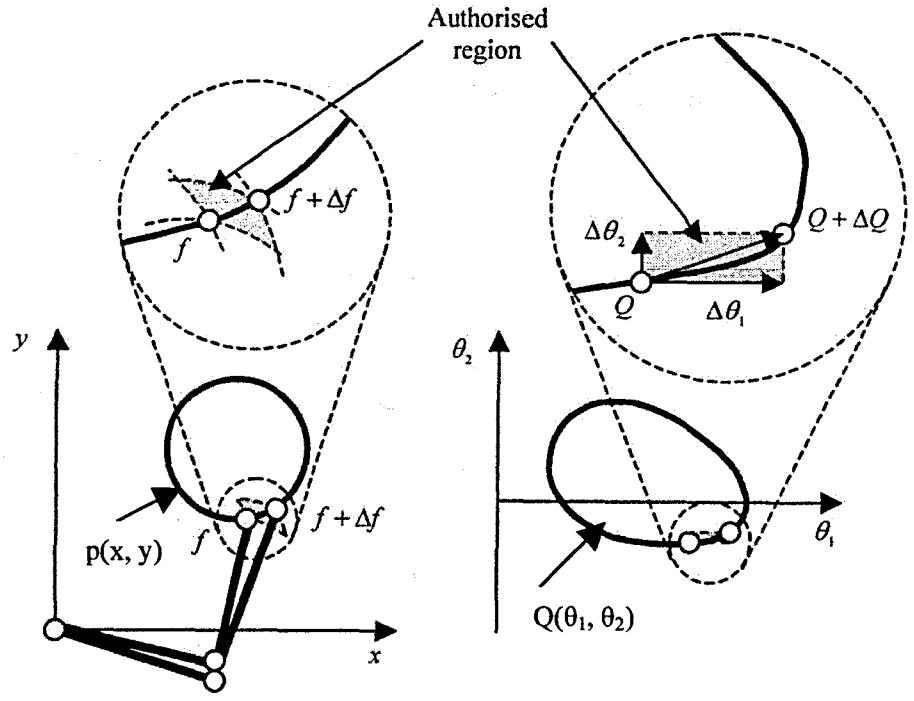

a) b)

Figure 3-3. PADyC-trajectory following [18]

Furthermore, for the robot's end-effector to trace the desired path the motorised clutches must impart a resistive force at one or more joints. In this case, if the user tries to exceed the maximum allowable speed of a given joint, the clutch suddenly engages and constraints the joint to remain at the given angular velocity. Any resistance to motion radically (and in this case instantaneously) changes the dynamic behaviour of the system transmitting an irregular 'feel' to the motion. The user is required to compensate for these changes and needs to adjust the direction that the driving force is applied in order to follow the path. In other words, the user is expected to 'feel' his way along a narrow corridor; bouncing from wall to wall. In addition, some tasks, for example using milling tool to machine bone or making an incision with a scalpel, require a smooth constrained motion to obtain the best results and much training would be required for the user to learn to operate the manipulator adequately.

In the *'region' mode,* the tip of the arm is constrained to stay in a pre-defined region. Inside the region, any motion is free, whilst over a border it is completely forbidden. A

region defined in the configuration space is considered, as shown in Figure 3-4. As in the trajectory mode, the problem is to find an authorised rectangle around the current position. The authors' choice of the authorised rectangle is to maximise the area of the possible position at the next sample time without favouring any particular quadrant [43]. For each of the four quadrants, the rectangle with the maximum area is computed. This rectangle is limited by the quadrant and by the region's border. Then, for each direction of rotation, the smallest side of the rectangles is retained to form the final authorised rectangle drawn in Figure 3-4. Given the final rectangle size and the sample time, the motor speeds are computed.

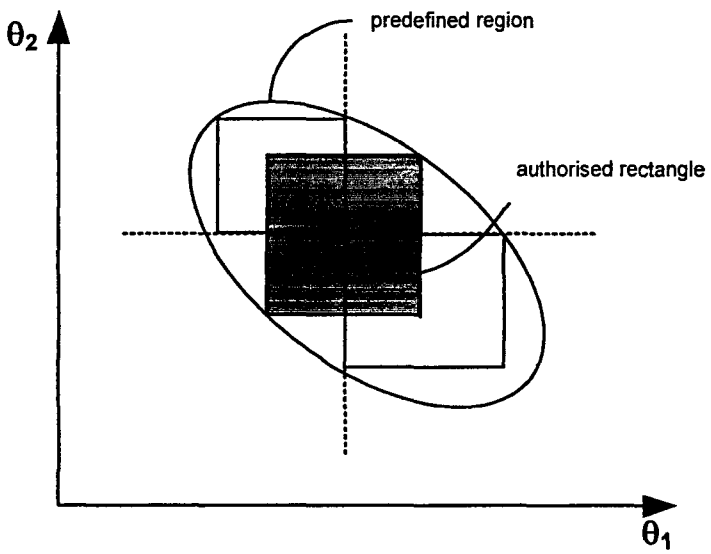

Figure 3-4. Region mode [43]

It is clear that it takes a certain time to make the constraint fully effective, i.e. to obtain the computed speed of the motors. The authors determined that the maximum delay to stop one motor at full deceleration is 15 ms. Because of this delay, the actual position of the end-effector when the constraints are effective is no longer the read position and the use of the given algorithms could result in the setting of a constraint no longer compatible with the current position. This could lead to authorisation of a motion, which is no longer compatible with the task. This algorithm proved to be very difficult to implement in practice and the authors are currently investigating new control strategies. Experiments show that the error amplitude of the two-DOF prototype arm can reach 10 mm for an end-effector force of 10N and 20 mm for an input force of 20N.

More recently, a 6-DOFsystem based on the PADyC prototype has been proposed for cardiac puncturing [47]. However, the manipulator is used only to help the surgeons reach a position in space and has not been used for trajectory following because of the above-explained drawbacks of the joint mechanism and control strategy.

3.2.2 PTER

As shown in section 2.6.1, PTER is a controlled five-bar linkage system overactuated (two-DOF and four actuators) that uses clutches and brakes to dissipate user-supplied energy [69, 70]. Two of the clutches connect each of the two controllable joints to a zero velocity source, transforming them in brakes. A third clutch couples the rotation of these two joints in one direction, while a fourth clutch connects the rotation of the two joints in the opposite direction through a gear train. It is proposed that when the user applies an input force to the control handle, the voltages supplied to the clutches could be varied in order to allow motion in a given direction. PTER uses the clutches to dynamically generate forces/torques that regulate the joint velocities in an attempt to make a kinematic coupling between the joints. By controlling the clutches, each joint of PTER is coupled to all others kinematically. That is if the user forces motion of one joint, the rest of the joints are also forced, using the coupling clutches, to move in a direction that generates motion of the end-effector along the desired path. The trajectory is planned as a corridor of acceptable positions surrounding the ideal path. Using position and force measurements, the system's control strategy is as follows [69]:

- Trajectory control is performed inside a predefined corridor;
- The system does not allow motion that will take the end-effector further away;
- The system does not provide control if the force is bringing the end-effector back inside the corridor.

Both trajectory planning and trajectory tracking are similar to PADyC's and thus it shares similar disadvantages such as the discontinuous feel transmitted to the motion of the end-effector. Furthermore, it was reported that when the tip of the device crosses a boundary and the clutches are locked, there would be a small amount of slippage at the

clutch interface before the manipulator is restricted [69]. Depending on the velocity at the end-effector it was reported that the system can slip as much as 4mm into the forbidden area. In an attempt to improve the control performance, a new actuator based on piezoelectricity was proposed [77, 78]. However, because of the limitations of the piezodriver the authors have not been able to improve their initial results.

3.2.3 COBOT

As described in section 2.6.2, a "COBOT" is defined as a robotic device that manipulates objects in collaboration with a human operator. It provides assistance to the human operator by settling up virtual surfaces, which can be used to constrain and guide motion. COBOT is also known as a programmable constraint machine (PCM), it does not use servo devices to implement constraint, but instead employs steerable nonholonomic joints (nonholonomic meaning that the steering wheel is path-dependent, and it does not guarantee return to the original system position).

COBOT use a steering mechanism to guide the user along a desired path. A unicycle cobot was described in section 2.6.2. A three-wheeled COBOT known as Scooter was designed and implemented to assist in material handling applications such as loading and unloading of vehicle doors in an automotive assembly line [81-82]. The vehicle door is loaded onto Scooter at a loading bay. The operator then moves the COBOT in the general direction of the target area. A computer, controlling the steering mechanism, is used to guide the user to the correct target point where the door is fixed to the vehicle. The COBOT concept was further developed and a continuously variable transmission (CVT) was designed [80]. It was proposed that the CVT could be used in a revolute joint to control the relationship between joint velocities. The proposed method is particularly interesting in the way that each joint is coupled to the next by a drive shaft. A serial manipulator with two rotational CVT is shown in Figure 3-5. By controlling two rubber steering wheels, the CVT gives the correct velocity coupling between the input shafts (to joint 1 and 2 in Figure 3-5). By using a CVT at each joint the user can

be constrained to follow a path. The joints of the robot are mechanically constrained to give the kinematic solution for the required motion, i.e. by inducing motion in one joint the user forces the desired motion of other joints. The full description of the cobot's control is described by Gillespie *et al.* [83]. Although, there were developed both translational and rotational CVT, the PCM device has a significant disadvantage, because of the sliding possibility between the wheel and surface when a relatively large force is applied at the end-effector. Excessive wear of the rubber steering and drive rollers during normal operation is also of concern. Furthermore, the authors did not evaluate the rotational CVT in either the 'position' mode or the 'trajectory' mode. Therefore, it is really hard to evaluate the performance of the proposed device.

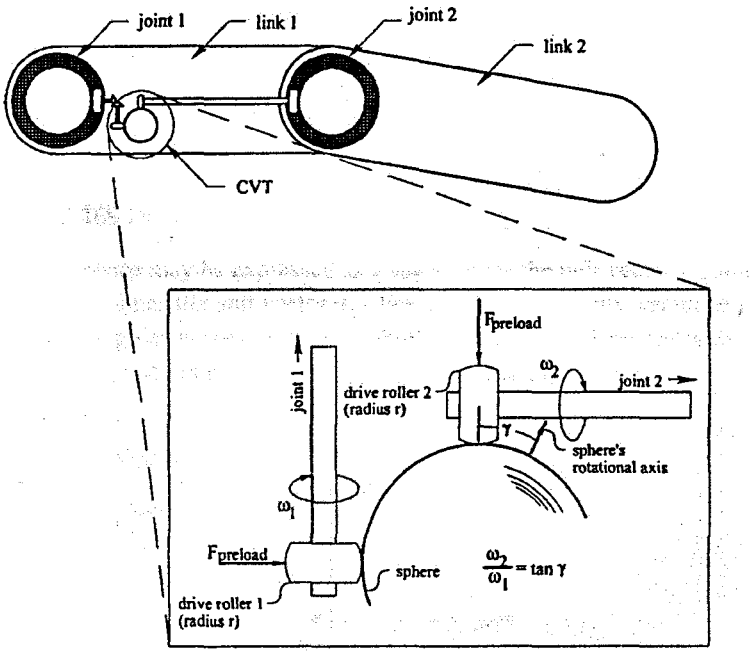

Figure 3-5. Serial PCM [80]

3.2.4 Evaluation of the existing actively restrained devices

Although there has been considerable research in this particular field, the success of trajectory following of actively restrained manipulators has been limited. The COBOT's principle gives a potential decent tracking performance for the translational motion.

However, the ability to resist input forces normal to the path is limited, i.e. application of large input forces can lead to the end-effector leaving the path. On the other hand, while the clutch mechanism of PADyC and PTER provide sufficient holding torque, satisfactory tracking performance and smooth operation has not been adequately demonstrated. The performance of PTER is degraded by the stick-slip problems associated with clutch/brake systems along with dynamics of the manipulator itself. The PADyC system exhibited mechanical problems attributed to backlash and flexibility inherent in the clutches of the prototype. Moreover, there are issues regarding the implementation of the desired trajectory. PADyC and PTER implement the path as a corridor of acceptable positions, thus the accuracy of the system depends on how narrow that corridor is and usually means that the user bounces from wall to wall in order to stay in the predefined corridor.

There are also issues regarding the ease of use for trajectory planning applications. For example, the users of the PADyC and PTER prototypes are expected to 'feel' their way along a narrow corridor; bouncing from wall to wall. Both systems would benefit from the user being shown the direction of the applied force as introduced by Reedman and Bouazza-Marouf [84].

In order to achieve good tactile feedback, the motion of the manipulator should be as free as possible inside a safety region, and as the control point (usually the tip of the manipulator) moves near the region border the manipulator's speed should decrease. Thus, informing the operator of approaching a forbidden area. Neither of the above mentioned devices is capable of this.

In the next section, an analysis of a two-DOF polar manipulator is undertaken. It is shown that for this configuration of an actively restrained passive manipulator, the path can be implemented easier and more accurately. Moreover, for a polar manipulator there are no geometrical conditions on the direction of the user-input force that should be applied in order to follow a predefined path. Using a suitable control strategy, it is shown that the manipulator can effectively guide the user in order to follow a specified path without complex gear and clutch systems or CVTs that impose a kinematic

relationship between each of the joints. Furthermore, in order to improve the tactile feedback when the tip of the manipulator approaches a pre-specified boundary, which defines a safety region, a strategy based on a combination of force control and velocity control is proposed. The chapter concludes with the development of the proposed joint mechanism, whose performance is demonstrated later in the thesis, and is shown to be more accurate than that of the existing joint mechanisms.

3.3 Analysis of a Two-DOF Polar Manipulator

As defined in section 2.8, the proposed actively restrained passive mechatronic system should be able to (1) reach a pre-specified position, (2) follow a pre-defined trajectory, and (3) stay within a pre-programmed region. These three requirements are seen as three different modes in which the proposed manipulator operates. Consequently, to reach a pre-specified position, in order to insert a drill bit, a needle, or an electrode, the manipulator is controlled in the '*position*' mode; to follow a pre-defined trajectory, as it is required by more complex surgical procedures, the system is controlled in the '*trajectory*' mode; and to stay within a pre-programmed region, in order to avoid certain anatomical obstacles (i.e. blood vessels or ligaments), the manipulator is controlled in the '*region*' mode.

Consider the two-DOF polar manipulator (RP) shown in Figure 3-6. The end-effector is required to track a desired path $P_d(x_d, y_d)$ while the user applies a force $\mathbf{F_u} = (F_{u,\varphi}\ F_{u,r})^T$, where $F_{u,\varphi}$ and $F_{u,r}$ are the tangential and radial components of the user-input force as shown in Figure 3-6. The desired path $P_d(x_d, y_d)$ can be defined in either Cartesian (x, y) or polar coordinates (θ, r) and the control of the manipulator is performed in joint coordinates.

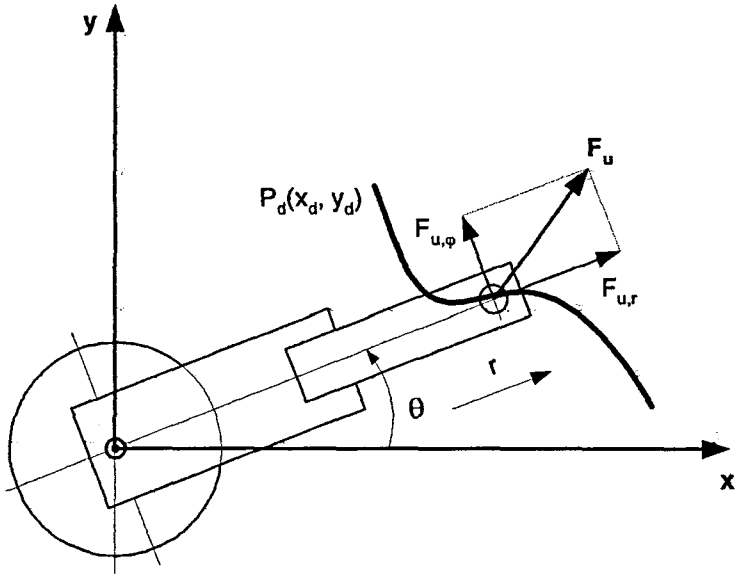

Figure 3-6. Trajectory following using a passive polar manipulator

For the '*position*' and '*trajectory*' modes, a position control strategy in joint space is chosen, using an independent controller for each joint. For the *'region'* mode, a combination of velocity control and force control strategy is adopted. These modes of operation are fully described in Chapter 8.

In general, polynomial functions describe the position of each Cartesian variable with respect to time. This allows the velocity and acceleration along the path to be specified. For this application, however, only the path itself is predefined. A 'task interpreter algorithm' is used to specify the velocity on the path so that the position of the manipulator is regulated effectively.

The desired tasks (i.e. position, trajectory or region mode) are defined in polar coordinate as a set of position points $Q_i(\theta_i, r_i)$. The method employed to control the proposed manipulator involves approximating the joint-space path with a set of straight lines. By considering a new point, a joint-space distance ΔQ further along the path, the amount that each joint needs to be moved to reach the new point can be calculated. In this way the velocity of each joint can be specified so that the position of each joint is reached at the same time. It can be seen that this method is much simpler than the

method employed by PADyC, as the velocity of the joints can directly be computed from the known data without any intermediary operations such as constructing an authorised rectangle. Furthermore, the specified path passes right through the predefined position points and it does not need a pre-specified corridor of positions, as in the case of PADyC and PTER. This method is described in more details in Chapter 8.

As previously mentioned, the end-effector is required to track a path $Q_d(\theta_d, r_d)$, where $\theta_d = [\theta_1, \theta_2, \ldots \theta_n]$, and $r_d = [r_1, r_2, \ldots r_n]$ are the predefined position points, while the user applies a force F_u. Due to the actuator limited output torque/force, (i.e. limited frictional torque), a maximum magnitude of user-input force needs to be specified, as above this force the system cannot be controlled. Furthermore, a minimum driving force needs to be specified in order to avoid undesired movements caused by the user when s/he does not desire to move the end-effector while holding the control handle. Thus, in order to effectively control the manipulator in all three modes certain conditions apply as shown in Figure 3-7. It can be seen that dependending on the user-input force three situations are distinguished:

1. If the user-input force is less than a minimum pre-defined magnitude, the system will not permit motion (i.e. if $|\mathbf{F_u}| \leq |\mathbf{F_{u\ min}}|$ no motion is allowed, where $F_u = (F_{u,\varphi}, F_{u,r})^T$, and $F_{u\ min} = (F_{u,\varphi\ min}, F_{u,r\ min})^T$);

2. If only one component of the user-input force is greater than a minimum pre-defined magnitude than the motion will depend on the desired path and the kinematic configuration of the arm as defined below:

   2.1. if $|F_{u,\varphi}| > |F_{u,\varphi\ min}|$ and $|F_{u,r}| \leq |F_{u,r\ min}|$ the control system will not allow motion in the r direction but will allow motion in the θ direction so long as the orientation of the desired path coincides with the θ direction;

   2.2. if $|F_{u,r}| > |F_{u,r\ min}|$ and $|F_{u,\varphi}| \leq |F_{u,\varphi\ min}|$ the control system will not allow motion in the θ direction but will allow motion in the r direction so long as the orientation of the desired path coincides with the r direction;

3. If the user-input force is greater than the minimum pre-defined magnitude the motion is allowed on both axes (i.e. if $|\mathbf{F_u}| > |\mathbf{F_{u\ min}}|$ motion is allowed).

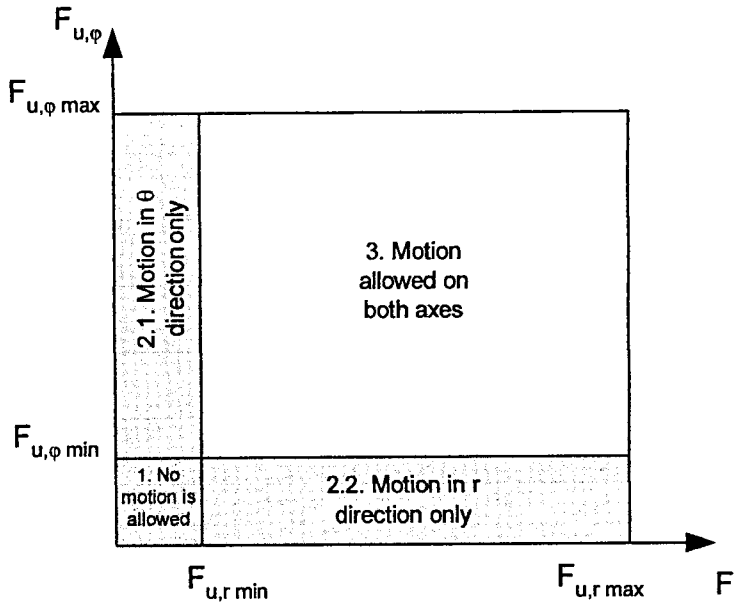

Figure 3-7. Diagram of the control strategy for path following

For the implementation and control of the *'region'* mode a rectangular region is defined by the surgeon. By selecting a minimum of four position points the surgeon can limit the manipulator's workspace to a 'safety' region so that a desired task can be achieved without damaging the surrounding surfaces. This is shown in Figure 3-8 for the vertical cut in the Total Knee Replacement procedure.

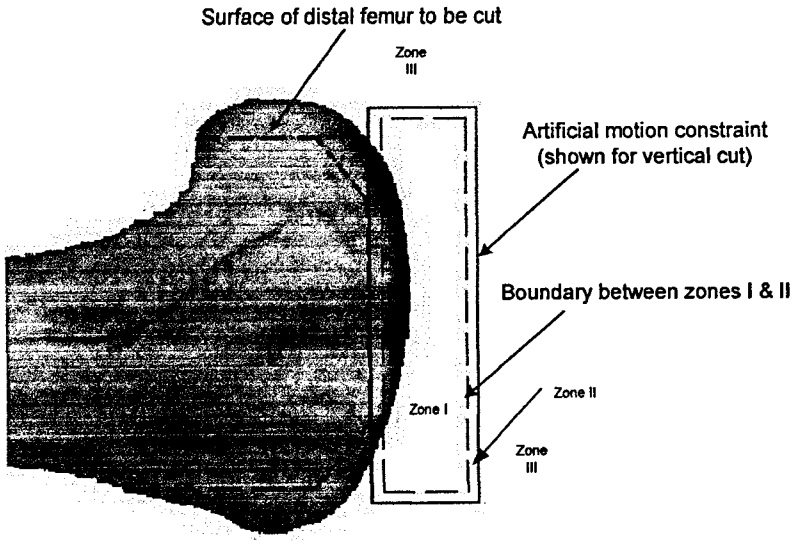

Figure 3-8. Concept used for the *'region'* mode: implementation and control

The control strategy to keep the tip of the manipulator inside the predefined 'safety' region is based on creating another region inside of this 'safety' region (i.e. an 'intermediate' region) with different levels of resistance of the surgeon efforts, as shown in Figure 3-9b. Inside the 'intermediate' region the user can move freely as there is no control action to restrain the motion (or the user-input force). As soon as the user approaches the boundary of the 'intermediate' region, point A in Figure 3-9a, the control system starts restraining the user-input force warning the surgeon about the fact that the boundary of the 'intermediate' region was reached and that s/he is going towards the border of the 'safety' region. If the surgeon continues pushing toward the safety region the control system allows the surgeon to move the end-effector along, but not beyond, the boundary, to points C or D in Figure 3-9 depending on the direction of the user-input force.

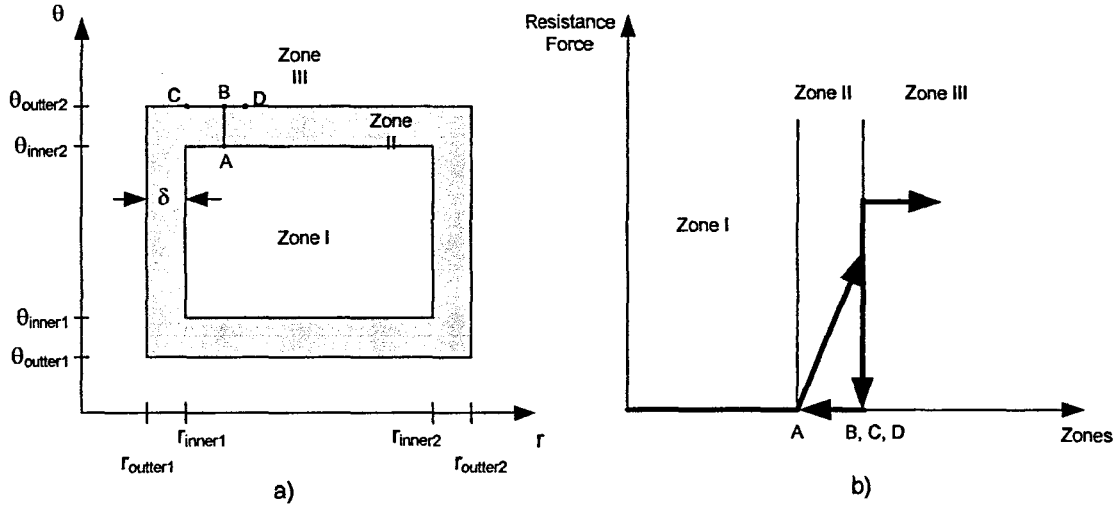

Figure 3-9. Resistance force in the *'region'* mode

From Figure 3-9 it can be seen that the strategy for the 'region' mode is divided in three regions or zones. Region I is a permitted zone and only a low-force is necessary to move the robot arm. Region III is a completely restricted region, requiring high forces to move into it, while region II is an intermediate zone in which the system progressively decreases the velocity of the tip of the manipulator. Thus, the resistance of the surgeon efforts is increased, since region III is very close. As shown in Figure 3-9b

the end-effector can be easily moved to point A and with higher resistance force to a point on the safety border, for example point B. Further movement into zone III would now require very high force, whilst going along the boundary to point C or D would be easier. All other movements towards zone I are unrestricted.

The above described principle is called 'active constraints' and has also been applied by the authors of Acrobot, described in section 2.5.4. With respect to the control strategy in the 'region' mode, both systems consider the user-input force magnitude, the current position and the direction of motion. The authors of Acrobot [68, 176] use the above information to regulate the velocity of the motorised robot joints (i.e. desired variable stiffness for the robot). However, in this work the user-input force magnitude, the current position and the direction of motion are used to define the velocity of the joint via a clutch system. The amount of restraint needed is obtained from a friction clutch, and not directly from an electrical motor at each joint. This method is described in Chapter 8.

In order to achieve accurate and smooth control of the manipulator while following predefined paths, a suitable joint mechanism needs to be developed. The drawbacks of the existing joint mechanisms were shown, hence a joint mechanism that can overcome these inconveniences is highly desirable. In the next section the proposed joint mechanism is introduced and its advantages with respect to the other systems are explained.

3.4 The Proposed Joint Mechanism: Concept Development

It has been shown that the mechanical design of a joint mechanism and the choice of the actuators are critical for the performance of the manipulator as a whole. The drawbacks regarding the geometric dimensions, weight and positional accuracy of the existing actively restrained passive mechatronic systems can be overcome by using an appropriate mechanical design and selecting suitable actuators. It has been shown that there are serious control issues in the use of complex gear train mechanisms. PADyC's

joint flexibility, backlash and hysteresis are the reason why this concept cannot accurately follow a predefined path. Similarly, the gear train used by PTER introduces compliance, which, together with the stick-slip friction in the clutch, is the motivation for rapidly switching the electromagnetic clutches on and off, thus causing undesirable discontinuous motion of the manipulator and large positional errors. However, the use of brakes and clutches for a joint mechanism has the potential to assist safety critical applications. Nonetheless, the control is very challenging, and the actuator and transmission technology needs to be improved. This research aims to develop a new joint mechanism for actively restrained passive mechatronic systems, which, even though is based on brakes/clutches similar to PADyC and PTER systems, shows a great improvement from both control and kinematics point of views. In order to overcome the drawbacks of the existing systems an in-depth analysis of the classical brake and clutch characteristics was completed, and is shown in Appendix B2.

A classification of existing brake systems has been done by Childs [85], and is illustrated in Figure 3-10. It can be seen that a brake system can be separated into two parts: the method of activation (actuation), and the method of braking/clutching. Furthermore, the method of braking/clutching can be divided into mechanical friction and electromagnetic reaction.

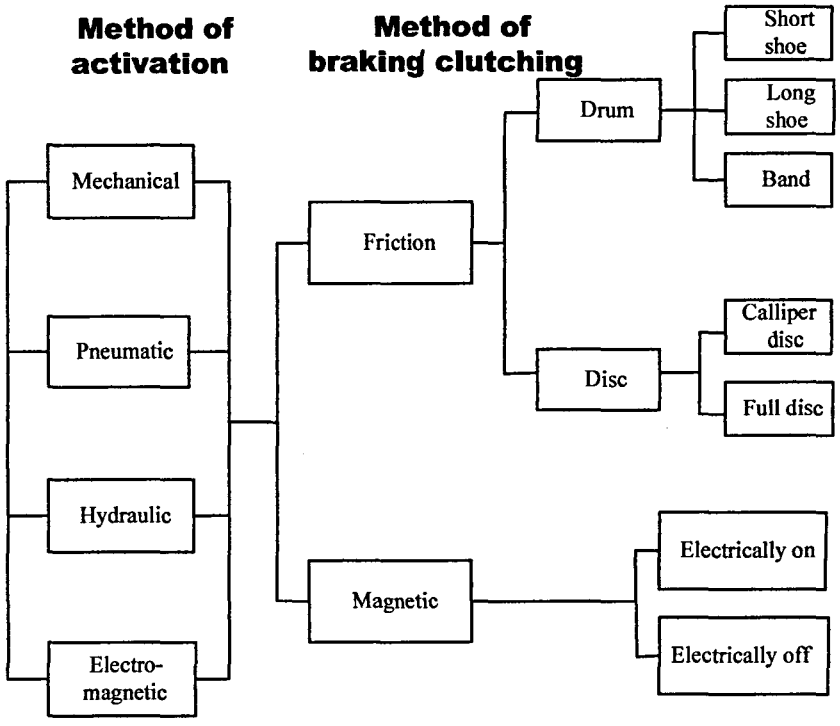

Figure 3-10. Brake systems classification [85]

By analysing the existing braking/clutching methods more closely, as shown in Appendix B2, it was discovered that none of the already existent brakes/clutches could accomplish all the requirements for the proposed brake/clutch. For example, the mechanically activated brakes/clutches are not precise and not suitable for motion control. The pneumatic and hydraulic brakes/clutches introduce an alien fluid into the workspace. This may not be acceptable for applications where a relatively clean environment must be kept. The electromagnetic brakes/clutches are difficult to accurately control because of their complex dynamics [69]. This also affects their stability. The other clutches based on an electromagnetic reaction such as the magnetic particle brake/clutch, hysteresis brake/clutch, and eddy-current brake/clutch, do not have wearing parts, yet they show great disadvantages from the control point of view. The magnetic particle brake/clutch is required to occasionally turn a full revolution to keep the particles evenly distributed, and does not perform a back and forth motion through a narrow angle as good as a robotic joint is required to do. The hysteresis brake/clutch was not selected because of the cogging phenomenon and hysteresis characteristic of applied current versus torque. The eddy-current clutch-brake cannot

deliver torque at low slip speeds, thus making it inappropriate for the operating environment.

An electromechanical friction brake/clutch is proposed as a joint mechanism for the proposed actively restrained passive joint used for safety critical applications. The joint's components are (1) a friction brake/clutch (defined as the contact interface between two bodies) responsible for creating the sliding friction, and (2) the actuator, accountable for supplying a normal force F_N onto a brake disc. In order to overcome the difficulties shown by the existing systems the joint components have to fulfil several requirements. These are:

a) The friction brake/clutch must have:

- Good stability and simplicity, in order to have a reliable joint mechanism that is easy to control and maintain;
- High link stiffness so that little or no compliance is allowed, thus an increase in the overall joint accuracy is obtained, as well as diminishing the stick-slip friction effect;
- The materials selected should have a high coefficient of friction, thus providing a larger braking force/torque, and contributing to the compactness of the mechanism;
- The materials of the bodies in contact need to have a minimum difference between static and dynamic coefficient of friction, which diminishes the stick-slip effect, thus contributing to smooth motion control of the system;
- High heat dissipation, to avoid high temperature problems that may arise;
- High wear resistance for the materials in contact, to prolong the operational life of the system, making it more reliable for longer time and less expensive to maintain.

b) The actuator needs to:

- Provide sufficient actuation force to produce a large braking force/torque;
- Be fast and precise;
- Have high stability;

- Have high rigidity, so that it does not allow flexibility, backlash and physical deformations;
- Be easily and accurately controllable.

3.4.1 The friction brake/clutch

In order to design the friction brake/clutch, three aspects were taken into consideration:

- Finding the most suitable method of braking/clutching in order to obtain great rigidity and compactness for the novel joint;
- Material selection: in order to have a high coefficient of friction; a small difference between the static and dynamic coefficient of friction; and high value of hardness. The material selection ensures that a large braking force/torque can be obtained with good friction characteristics, and a low wear;
- Hard coatings of materials, due to the possibility of increasing the hardness, thus the resistance to wear of materials.

3.4.1.1 The method of braking/clutching

Different frictional brakes are presented in Figure 3-11, and a comparison of braking/clutching methods is given in Appendix B2. Because of its simplicity and high stability, and due to the self-cleaning characteristic and uniform wear across the surface in contact, the calliper disk braking/clutching method was found to be the most suitable for the proposed brake/clutch. The calliper disk is very compact and does not require as many components as the drum brakes for example. Their main disadvantage is that they require a larger activation force than is required for the drums brakes because they produce no friction moment. The proposed calliper disk brake/clutch was chosen with a segment pad as shown in Figure 3-12.

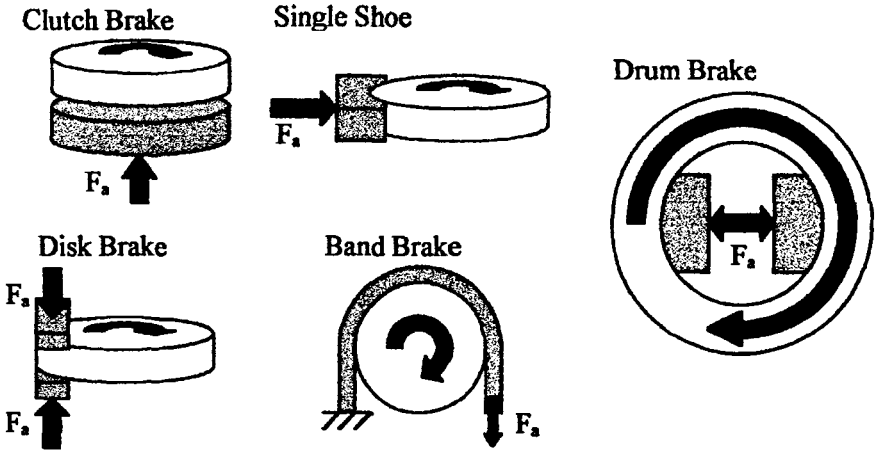

Figure 3-11. Friction brake systems [91]

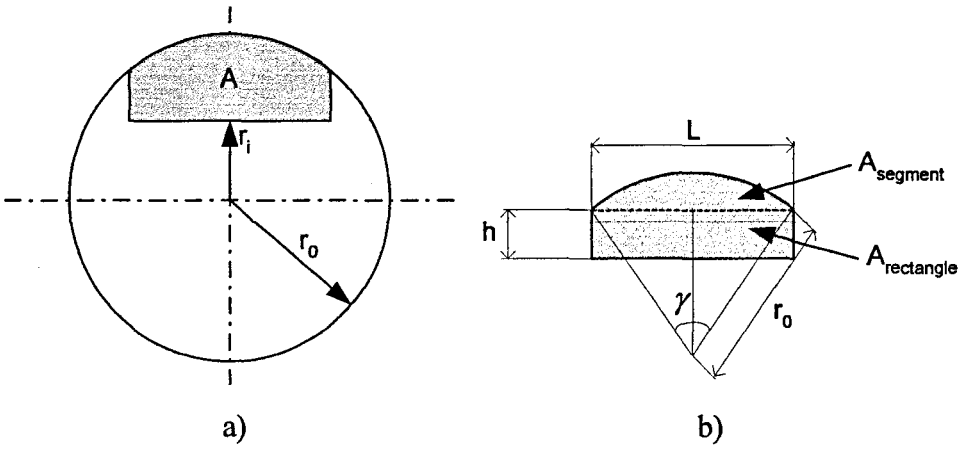

Figure 3-12. Segment covered by the brake pad: a) Brake contact, b) Explicit diagram for calculus of the contact area

The resulting frictional torque can be obtained using one of the two assumptions: either uniform wear of the frictional material or uniform pressure across the surfaces in contact. The uniform wear assumption is used, which supposes that the thickness of the lining material removed, δ, is proportional to the applied pressure p, and relative speed v [86]. Thus, it can be written

$$\delta = k p r_0 \qquad (3\text{-}1)$$

where k is a constant of proportionality, and r_0 denotes the outer radius of the disc. Whenever this condition holds, it implies that the pressure increases as the radius decreases, so that the maximum pressure p_{max} is found at the inner radius r_i. Thus,

$$\delta = k\, p_{max}\, r_i \qquad (3\text{-}2)$$

Elimination of k and δ from equation (3-1) and (3-2) yields

$$p = p_{\max} \frac{r_i}{r_0} \tag{3-3}$$

The area of the surface in contact, A, is shown in Figure 3-12a, and is calculated as $A = A_{rectangle} + A_{segment}$, shown in Figure 3-12b. Thus, the area of the contact between the brake disc and the brake pad is obtained as:

$$A = (L \cdot h) + \left(\frac{\gamma \cdot r_o^2}{2} - \frac{L}{2} \sqrt{r_o^2 - \frac{L^2}{4}} \right) \tag{3-4}$$

where, L represents the width of the friction pad, h denotes the height of the rectangle and γ is the angle between the ends of the 'segment' shown in Figure 3-12b. The values of the brake pad are given in Appendix D1.

The resulting frictional torque is given by

$$T_f(\dot{\theta}) = \mu(\dot{\theta}) \cdot p \cdot r_0 \cdot A \tag{3-5}$$

where $\mu(\dot{\theta})$ is the coefficient of friction between the materials in contact.

Substituting equation (3-3) into equation (3-5), the maximum frictional torque yields

$$(T_f(\dot{\theta}))_{\max} = \mu(\dot{\theta}) \cdot p_{\max} \cdot r_i \cdot A \tag{3-6}$$

3.4.1.2 Material selection

In order to produce a large friction coefficient with comparable dynamic and static coefficient of friction, a proper selection of materials for both brake disk and brake pad was completed. From the literature it was observed that among metals, steel on steel contact produces one of the largest friction coefficients. Several ceramics and polymers were reported to have a greater friction coefficient than metals [87]. However, results regarding the dynamic and static coefficient of ceramics or polymers in contact have not yet been reported. This area of materials properties is of great importance in developing a brake/clutch that can outperform existing systems. It is strongly recommended that for further developments of the brake/clutch proposed in this research, new materials need

to be considered and investigated. The static and dynamic coefficients of friction of several materials in direct contact are presented in Table 3-1 [88]. Note that the values in the table seem rather high.

Table 3-1. Coefficient of friction for different materials in contact

Materials in contact	Static coefficient of friction	Dynamic coefficient of friction
Steel on Steel	0.74	0.57
Aluminum on Steel	0.61	0.47
Copper on Steel	0.53	0.36
Rubber on Concrete	1.0	0.8
Wood on Wood	0.25 - 0.5	0.2
Glass on Glass	0.94	0.4
Waxed wood on Wet snow	0.14	0.1
Metal on Metal (lubricated)	0.15	0.06
Teflon on Teflon	0.04	0.04

3.4.1.3 Wear-resistant surfaces and coatings

Hard coatings of materials are also an important factor in selecting suitable materials for brakes and clutches. This is because hard coatings increase the materials hardness improving the resistance to wear. This prolongs the operational life of the brake making it more reliable for a longer time, which is an important issue for safety critical devices, in particular of those working in an operating environment. In consequence, the materials chosen initially for the bodies in direct contact have the possibility to be coated. Information about different methods of hard coating can be found in Lansdown and Price [89].

Table 3-2. UNS S20100-Physical properties

Properties	Value
Static coefficient of friction	0.3
Modulus of Elasticity	210[GPa]
Compressive yield strength	441[MPa]
Tensile strength yield	678[MPa]
Tensile strength ultimate	902[MPa]
Hardness Rockwell C	28.5
Density	7.86[g/cc]

3.4.2 The actuator

In order to design an efficient electromechanical brake/clutch the actuator needs to fulfil several requirements as presented at the beginning of the section. The classical types of actuators such as mechanical, electrical, pneumatic, hydraulic, and electromagnetic were analysed. Buerbaumer [91] made a comparison between these actuators, however a more complete one is presented in Appendix B1.

Analysing the traditional actuators, it can be seen that there is no actuator able to satisfactorily accomplish all the requirements for the proposed brake/clutch. Mechanical actuators such as cams, gears, belts and pulleys can hardly be controlled in a close-loop manner and their accuracy is constrained by the machining limitations. Pneumatic and hydraulic actuators have limited accuracy, require back-up service and there is the possibility of leaking. The electromagnetic actuators suffer from complex dynamics, difficulties in control, and low stability. The electrical actuators provide limited force/torque, and in combination with a gearbox introduce flexibility and backlash.

In order to eliminate the flexibility and backlash inherent in the PADyC system, and to diminish the compliance in the transmission presented on PTER, a new type of actuator has been proposed. Based on the piezoelectricity effect, the piezoelectric actuator has

high rigidity and stability, is fast and precise, and is easy to control. It is also able to provide large actuation forces under special conditions. These properties make it ideal for use in the proposed electromechanical brake/clutch. However, the piezoactuator provides little displacement and the actuation force is strictly related with the amount the piezostacks moves. Force generation is always coupled with a reduction in displacement. The maximum force (blocked force) a piezoactuator (PZT) can generate depends on its stiffness and maximum displacement [93].

$$F_{max} = k_p \cdot \Delta l_{max} \qquad \textbf{(3-7)}$$

where, Δl_{max} = max. displacement without external force or restraint, and k_p is the PZT actuator's stiffness. In actual applications the load spring constant can be larger or smaller than the PZT spring constant. Therefore, the effective force $F_{max\ eff}$ generated by the PZT is given by:

$$F_{max\ eff} \approx \left(\frac{k_p \cdot k_s}{k_p + k_s} \right) \cdot \Delta l_{max} \qquad \textbf{(3-8)}$$

where, k_s is the stiffness of the system. The piezoelectric actuator model is derived in Appendix E1. The actuator proposed is a high voltage from Piezomechanik Gmbh [92], version PSt 1000/16/40 whose properties are tabulated in Table 3-3. The relationship between force and displacement for input voltages U_{max} and $U_{max}/2$ is presented in Figure 3-13.

Table 3-3. Piezoactuator PSt 1000/16/40 VS20 properties

Properties	Value
Max. Compressive Load	15000 N
Max. Force Generated	12000 N
Stroke	55 μm
Length	36 mm
Capacitance	360 nF
Compression Stiffness	200 N/μm
Unloaded Resonance frequency	25 kHz
Loaded Resonance frequency	400 Hz

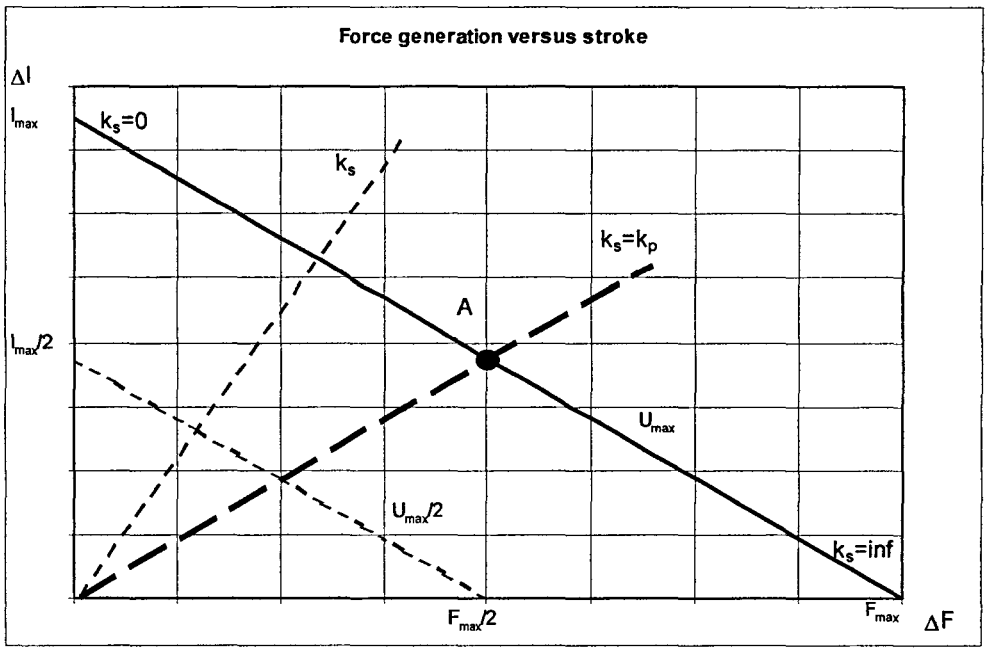

Figure 3-13. Force Generation v Stroke for input voltages U_{max} and $U_{max}/2$

The operating point A of the actuator, shown in Figure 3-13, represents the achievable force and stroke obtained from the intersection of actuator characteristic line l_{max}-F_{max} with the stiffness line of the attached mechanics k_s. This force-stroke diagram shows three cases: (1) k_s=0, represents a negligible stiffness of the actuated system compared to actuator's stiffness. In this case the stroke is maximum while the generated force is zero; (2) k_s=inf, denotes an infinitely stiff clamping of the actuator. This is the blocking condition. Actuator cannot produce a stroke, but only a force. However, this force can never be reached in real systems because of the limited stiffness of natural materials; (3) $k_s = k_p$ is the case for a well matched actuator system with maximum transfer of physical work from actuator to the attached system. The achieved stroke is half of the maximum stroke l_{max}, and the resulting force is half of the maximum blocking force F_{max}. Consequently, in order to take maximum advantage of the generated force, the mechanism needs to be machined with micrometer precision. More information about piezoelectricity and piezoactuators is presented in Appendix C.

Because the acquisition of the proposed piezoactuator and its required piezodriver proved to be a couple of times higher than the budget allocated for this research, it was

decided to prove the concept of an electromechanical friction clutch as an actively restrained passive joint, with a much cheaper actuator. Thus, the research aims at investigating the potential of an electromechanical friction clutch as a joint mechanism for an actively restrained passive mechatronic system, and not at developing a manipulator that can actually sustain the force of a human user.

An electric actuator such as a DC motor was considered as an alternative actuator for the proposed brake/clutch. Contrary to the others electric actuators such as stepper motors and AC motors, the DC motor offers continuous control over a wide range of velocities/torque and has greater efficiency. In addition, the DC motors technology offers simplified speed/torque control and a linear speed/torque relationship. Furthermore, a brushless DC motor was preferred due to enhanced efficiency, and significantly longer rated life times, because there is no power loss in the brushes. However, the DC motor provides a much smaller activation torque/force than it could have been obtained from a piezoactuator. This limitation does not allow for control of a user-input torque/force larger than a rather small value, as it is shown in Chapter 5. The performance specifications of the DC motor considered are presented in Appendix D2, and the mathematical model of a DC motor is derived in Appendix E2.

3.5 Conclusions

In analysing the existing actively restrained passive mechatronic devices in more detail, it was observed that there are several issues regarding (1) kinematics, (2) actuators and transmission technology, and (3) control strategy that needs to be improved in order to introduce these devices into the operating environment. Because of the kinematic configuration, the performance of existing actively restrained passive mechatronic systems is seriously affected when they assist in following predefined trajectories. For example, the path planning is defined as a corridor of acceptable positions around the desired path, as in the case of PADyC and PTER. This can be a major disadvantage when surgical tasks with sub millimetre accuracy are required, such as in TKR. Furthermore, the control strategy to follow a trajectory has yet to prove that it can do so

in a smooth and accurate manner. The authors of PTER reported a maximum error of 4mm, while the PADyC's authors reported a maximum error of 20mm. This is partly because of the proposed joint mechanisms: PADyC motorised clutch mechanisms suffers from flexibility, backlash in the worm-gear drives and hysteresis of the freewheels; PTER choice of brakes and clutches introduces undesired dynamic behaviour due to the friction-related effects such as stick-slip; and COBOT's steering wheel slips and leaves the desired trajectory when a relatively large amount of torque is provided. The concepts presented above, together with the kinematics configuration selected, contribute to large geometrical dimensions of these systems, which may look intimidating and out of control, even though they are not. In addition, the control algorithms developed lacks smoothness (e.g. the user is required to 'feel' his/her way along a narrow corridor bouncing from wall to wall) and are troublesome to implement in practice.

The joint mechanisms presented above are believed to have the potential to assist surgery. However, with all the drawbacks explained, there is much room for improvement. The kinematic configuration, actuator and transmission technology, and control strategies can all be improved in order to ease the access of these devices into operating environment. This is the aim of this research, and a two-DOF polar manipulator has been proposed. A suitable kinematics configuration has been selected that allows a much easier and accurate implementation of the desired path. Furthermore, a much smoother task definition strategy was developed in order to improve the interaction between the manipulator and the human operator. In addition, the control system does not require complex calculations keeping the computer specification to a minimum, and the mechanical configuration does not need special linkages keeping the geometrical dimensions and weight to a minimum.

In order to achieve an accurate and smooth control of the manipulator, while performing surgical tasks, a suitable joint mechanism was developed. An electromechanical friction clutch is proposed to accomplish this task. The challenges with such a mechanism are similar to those of PTER, such as friction-related effects (i.e. stick-slip). One difference between these two systems is that while PTER concept uses electromagnetic brakes,

which are known for their problems in accurate control and for their low stability, the proposed system uses friction brake/clutch activated by an electrical actuator, (e.g. a piezoactuator or a DC motor). The electromechanical friction clutch proposed uses an easy to control and precise actuator to provide the force onto a brake disc, and uses a rigid and compact friction mechanism to provide the frictional torque. Another difference between these two systems is the path planning and path tracking problems. On one hand PTER's authors choose a trajectory associated to a corridor of acceptable position points, while, the proposed system takes advantage of the polar kinematic configuration to define the path right through the predefined position points.

The control strategy for the *'region'* mode is however, the largest difference between these two systems. The proposed control strategy for the *'region'* mode is based on both velocity control and force control. Thus, the control system considers the magnitude and direction of the force applied by the user, and, dependent on the position of the tip of the manipulator with respect to the region's border, the motion of the arm is restrained accordingly. Still, the main issue of this actively restrained passive mechatronic system is the smooth control of the joint clutch, which usually exhibit stick-slip while tracking at low velocities. This issue is tackled in the following chapters.

Chapter 4
Modelling and Compensation Techniques for Control of Machines with Friction

4.1 Introduction

The proposed joint mechanism makes use of dry friction to dissipate the extra energy provided to the system. The actively restrained passive mechatronic joint proposed is based on an electromechanical friction clutch and consists of a controllable actuator and a friction clutch. The concept is that a human operator externally produces the driving torque and the computer-controlled clutch is used to restrain the motion so that various tasks can be performed. Thus, the motion control of a machine with dry friction is considered. In this chapter, the literature regarding friction modelling and friction compensation techniques for control is investigated. Firstly, a review of the existing modelling solutions and compensation techniques is given followed by some conclusions. Secondly, for the proposed joint mechanism, the method used for modelling the friction, as well as the techniques employed for friction compensation are identified.

4.2 Background

Friction is commonly studied, as it always appears when there is a contact between two bodies. Although, friction may be a desirable property, as it is for brakes and clutches, it

is generally an impediment for servo control. The literature relevant to friction modelling and control is very widely spread.

Tribology is the science of rubbing contacts, and its aim is to understand the physical processes of sliding machine contacts: bearings, transmission elements, seals, etc. For the control engineer, it is frictional dynamics which is of greatest interest. Thus, this research focuses more on friction dynamics, rather than surface chemistry and physics. More particularly, the relationship between the friction and velocity is of utmost importance to this research, as the control system of the proposed joint is required to regulate the position at very low position rates (i.e. velocity).

There are four dynamic regimes of friction in a lubricated system: static friction, boundary lubrication, partial fluid lubrication and full fluid lubrication. Figure 4-1 is known as the Stribeck curve and illustrates these regimes. All of these four regimes contribute to the dynamic that a controller confronts as the machine accelerates away from zero velocity.

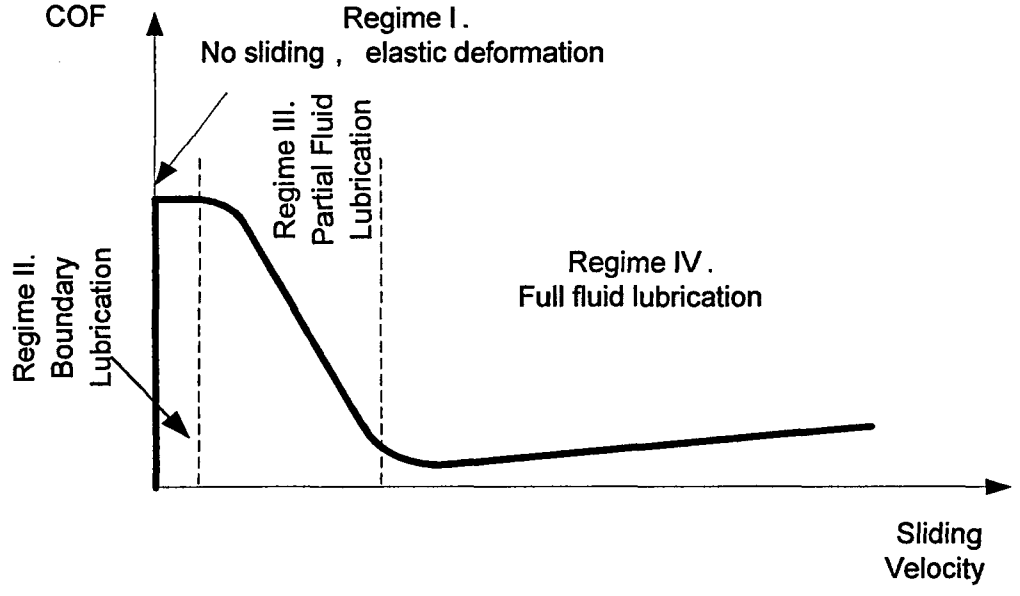

Figure 4-1. The generalized Stribeck curve, showing friction as a function of velocity for low velocities [94]

The first regime, *static friction and presliding displacement*, occurs at asperity junctions, as shown in Figure 4-2. These asperities have two important behaviours: they deform elastically, giving rise to presliding displacement; and the asperities deform plastically, giving rise to rising static friction, both are discussed later in the chapter. The elasticity of asperities suggests that when forces are applied the asperities will deform, but recover when the force is removed, as does a spring. This observation is accurate if the force applied is less than the break-away friction, as demonstrated in [95-97].

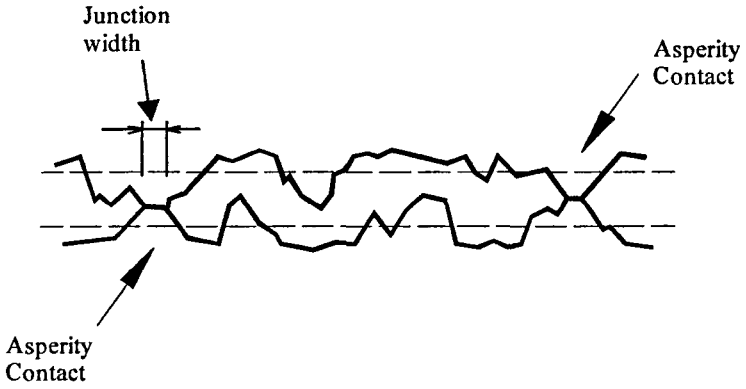

Figure 4-2. Part-to-part contact occurs at asperities, the small surface features

The second regime is the *boundary lubrication* and is characteristic of surface-to-surface contact at very low sliding velocities. In this regime fluid lubrication is not important as the velocity is not adequate to build a fluid film between the surfaces, as demonstrated in [98]. This regime is the most difficult to model and the sliding velocity is practically impossible to control smoothly.

The third regime, *partial fluid lubrication*, is the process by which lubricant is drawn into the contact area, but some solid-to-solid contact also takes place. When the fluid film is sufficiently thick, separation is complete and the friction moves into the *full fluid lubrication* regime. This fourth regime is also called Hydrodynamic or Elasto-Hydrodynamic Lubrication (EHL). In this research, 'dry friction' is considered to be the

metal-to-metal contact, fluid free. The friction in the proposed clutch is experimentally shown in the next chapter.

Due to the friction high nonlinearity and inconsistency, there are great difficulties in both modelling and developing control strategies to overcome them [99]. At low-velocities, a periodic process of sticking and slipping can be observed. This phenomenon is known as stick-slip effect. Stick-slip friction is present to some degree in almost all mechanisms and is often responsible for performance limitations. The effect often results in undesirable unstable dynamic behaviour. Precise position control tasks, such as those found in robotic applications [100-106], or in machine tools [107-111], are examples of systems affected by this phenomenon. Stick-slip friction puts a lower bound on the performance that can be extracted from a mechanism, such as minimum velocity achievable and persistent steady state errors. Symptoms of this phenomenon in mechanisms can be anything from jerky motion or limit cycles, to catastrophic instability.

In the next section, friction modelling is addressed. Results, from a range of experiments reported in tribology, mechanism, physics and controls literature are presented and assimilated. In section 4.4, friction simulation is introduced as an analysis tool, in order to develop and investigate different friction compensation techniques. In section 4.5 compensation methods for machine with friction are presented. Here the control literature is investigated. At the end of the chapter a friction model is chosen, which is used to develop a control strategy that overcomes the friction effects. The compensation methods that are going to be investigated on the prototype joint mechanism, in an attempt to diminish or completely overcome the stick-slip effect, are also selected.

4.3 Friction Modelling

The factors affecting friction between any two materials are very complex [114-126]. The most important are the normal force on the bodies, the length of time at which they

have been at rest (i.e. rising static friction), a phase lag between a change in velocity and the corresponding change in friction (i.e. frictional memory), the relative velocity, the history of velocity, and the history of normal load. Consequently, the task of modelling friction characteristics between bodies in contact, moving relative to each other, is very challenging.

The classic model of friction force is proportional to load, opposes the motion, and is independent of contact area. This was known to Leonardo Da Vinci (112), but remained hidden in his notebooks for centuries. Da Vinci's friction model was rediscovered by Amontons [113] and analysed in more detail by Coulomb [114]. The Coulomb friction force F_c is proportional to the normal force and it is independent of the absolute value of velocity. The friction model based solely on the Coulomb friction is described as:

$$F_f = F_c \, \mathrm{sgn}(\dot{x}) = \mu |F_N| \, \mathrm{sgn}(\dot{x}) \qquad \textbf{(4-1)}$$

where, the signum function is mathematically defined as:

$$\mathrm{sgn}(\dot{x}) = \begin{cases} +1, \ldots \dot{x} > 0 \\ 0, \ldots\ldots \dot{x} = 0 \\ -1, \ldots \dot{x} < 0 \end{cases} \qquad \textbf{(4-2)}$$

It was observed that the friction characteristic of rigid bodies moving relative to each other at substantial speed is rather linear. As the velocity of the bodies in contact decreases, the frictional effects that the mechanism experiences become highly non-linear, and is not well understood. When the bodies in contact are at rest, there is an opposing frictional force proportional to the force applied on the bodies. This force is called sticking force F_s, and prevents any motion until the applied force can overcome the maximum stiction level inherent between the materials in contact. Thus, at zero velocity it can be stated that the function is discontinuous, and is consequently modelled using a signum function, shown in equation (4-2). This model represents the static and the Coulomb friction, model given by equation (4-3), which is commonly used in engineering.

$$F_f = \begin{cases} F_c \, \mathrm{sgn}(\dot{x}), \ldots\ldots\ldots\ldots if \rightarrow \dot{x} \neq 0 \\ F_a, \ldots\ldots\ldots\ldots\ldots\ldots if \rightarrow \dot{x} = 0, |F_a| < F_s \\ F_s \, \mathrm{sgn}(F_a), \ldots\ldots if \rightarrow \dot{x} = 0, |F_a| \geq F_s \end{cases} \qquad \textbf{(4-3)}$$

where, F_a represents the force applied, F_s is the sticking force, and F_c denotes the Coulomb friction force. However, due to the fact that the friction force is not dependent on the slip velocity this classical friction model is not adequate for simulation analysis or development of control strategies for friction compensation, when the velocity is in close proximity of zero.

The classical friction components can be combined in different ways as shown in Figures 4-3a, 4-3b, and 4-3c. These models have components that are either linear in velocity or constant. Stribeck [115] observed that near zero velocity the friction force does not decrease discontinuously as in Figure 4-3c, but that the velocity-friction force dependence is continuous as shown in Figure 4-1 and Figure 4-3d. As this phenomenon becomes recognised by the friction community several authors [94, 116, 117] have developed friction models that can illustrate this effect.

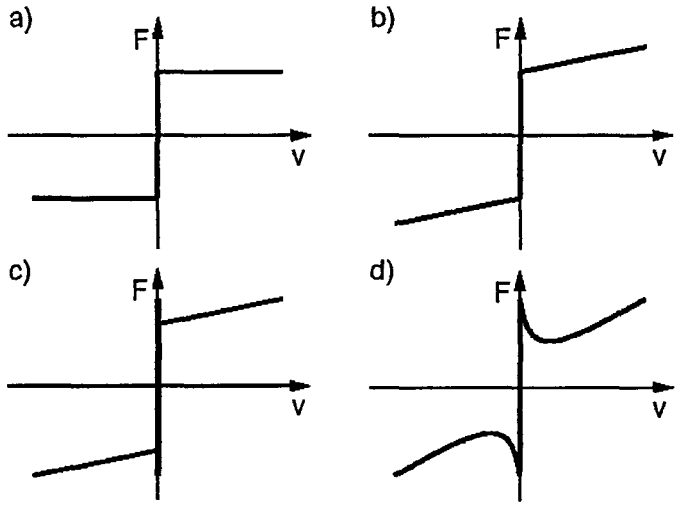

Figure 4-3. Friction models: a) Coulomb friction, b) Viscous friction, c) Coulomb + static friction + viscous friction, d) Coulomb + static friction + viscous friction + Stribeck friction [94]

Friction models capable of displaying the Stribeck effect are those developed by Hess and Soom [116], Bo and Pavelescu [117], and Armstrong-Helouvry [94]. Hess and Soom [116] employed a model of the form:

$$F(\dot{x}) = F_c + \frac{(F_s - F_c)}{1+(\dot{x}/\dot{x}_s)^2} + F_v\dot{x} \qquad \textbf{(4-4)}$$

while Bo and Pavelescu [117] developed an exponential friction model given as:

$$F(\dot{x}) = F_c + (F_s - F_c)e^{-(\dot{x}/\dot{x}_s)^\delta} \qquad \textbf{(4-5)}$$

where, $\dot{x}$ is the slip velocity, F_c, F_s, and F_v represents the kinetic friction, the static friction, and the viscous friction respectively. Parameters $\dot{x}_s$ and δ are empirically selected. The parameter $\dot{x}_s$ is known as the Stribeck velocity and its value determines the slope of the friction-velocity characteristics between the static and dynamic coefficient of friction. The parameter δ, called the Stribeck coefficient, is selected dependent on the efficiency of a boundary lubricant, a very large value suggesting an effective boundary lubricant (as shown by Armstrong-Helouvry [94] and Fuller [98]), while a smaller value suggesting lack of boundary lubrication [117]. The Stribeck coefficient for dry friction was shown by Bo and Pavelescu to be between 0.5 and 1, dependent on the materials in contact. Comparing the above two friction models, it was observed that the exponential model of Bo and Pavelescu [117] allows modelling of a wider range of friction types within a mechanism, as shown in Figure 4-4. Curves such as (a) arise when lubricants that provide little or no boundary lubrication are employed. The data of Bell and Burdekin (119-120) and Hess and Soom (116) indicate such a curve. When boundary lubrication is more effective, the friction is relatively constant up to the velocity at which partial fluid lubrication begins to play a role. Vinogradov *et al.* (121) and Khitrik and Shmakov (122) present data supporting a flat friction-velocity curve through the region of boundary lubrication as suggested by curve (b) of Figure 4-4.

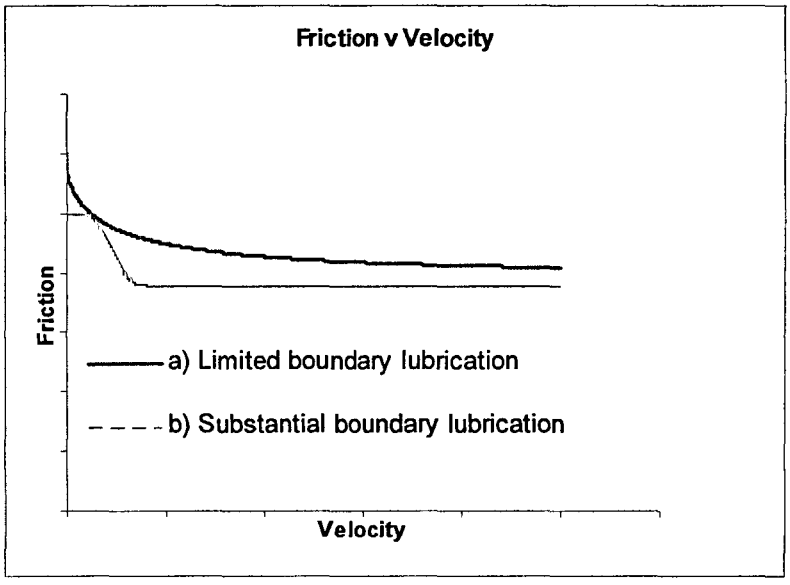

Figure 4-4. Friction as a function of steady state velocity for various lubrication levels [98]

A more complete model of friction is the integrated friction model developed by Armstrong-Helouvry [94]. This friction model has focused on lubricated friction between hard metal parts. The integrated friction model, also known as the seven parameters friction model, considers pre-sliding displacement, Coulomb friction, viscous and Stribeck friction, frictional memory (a phase lag between a change in velocity and the corresponding change in friction), and rising static friction (the length of time at which the bodies in contact have been at rest). The friction is described by:

$$F(\dot{x}) = \begin{cases} F(\dot{x},t), \ldots\ldots\ldots if \rightarrow \dot{x} \neq 0 \\ F(x), \ldots\ldots\ldots if \rightarrow \dot{x} = 0, \end{cases} \qquad \textbf{(4-6)}$$

where,

$$F(x) = -k_t x \qquad \textbf{(4-7)}$$

is the pre-sliding displacement, and k_t is the tangential stiffness of the static contact.

$$F(\dot{x},t) = -\left(F_C + F_v|\dot{x}| + F_s(\gamma,t_d)\frac{1}{1+\left(\frac{\dot{x}(t-\tau_L)}{\dot{x}_s}\right)^2} \right) \mathrm{sgn}(\dot{x}) \qquad \textbf{(4-8)}$$

describes the Coulomb+viscous+Stribeck curve with frictional memory, where τ_L is the time constant of frictional memory. The rising static friction $F_s(\gamma, t_d)$ is given by:

$$F_s(\gamma, t_d) = F_{s,a} + \left(F_{s,\infty} - F_{s,a}\right)\frac{t_d}{t_d + \gamma} \qquad \textbf{(4-9)}$$

where, $F_{s,a}$ is the Stribeck friction at the end of the previous sliding period; $F_{s,\infty}$ is the Stribeck friction after a long time at rest (with a slow application of force); t_d is the dwell time, i.e. the time since becoming stuck and γ is the temporal parameter of the rising static friction. This model represents seven different friction phenomena. However, out of the seven parameters that compose the friction model, four are empirical and thus very difficult to estimate accurately (e.g. they all depend upon the mechanism and lubricant properties).

The above-mentioned models are known as static models. However, strictly speaking neither of the models presented in equations (4-4), (4-5) and (4-6) are static models as the friction force is a function of the velocity. In the following paragraphs the dynamic friction models are called those models that are time-dependent.

Lately, there has been a significant interest in what the control literature calls dynamic friction models. However, these models also have both fundamental and practical drawbacks. For example most of these dynamic models use only Coulomb or stiction+Coulomb friction models, and thus are not predicting the Stribeck effect. The Dahl model [95] describes the friction force as being dependent only on the position. Therefore, it does not capture the Stribeck effect, which is a rate dependent phenomenon. Moreover, the Dahl model does not describe stiction. The Bristle model [123] attempts to capture the behaviour of the microscopical contact points between two surfaces. The model captures the random nature of friction but is inefficient in simulations due to its complexity. The models by Bliman and Sorine [124-126] are similar to Dahl model, but a second order model was developed to capture stiction. However, the main drawback is the dependency on only the position and not on the relative velocity between the two bodies in contact. Therefore, the stick-slip effect cannot be explained, which is the main issue in the proposed joint mechanism.

The LuGre model [127] is a dynamic friction model dependent on the relative velocity between the bodies in contact. The model is related to the bristle interpretation of

friction. When a tangential force is applied the bristles will deflect like springs. If the deflection is sufficiently large the bristles start to slip. The average bristle deflection for a steady state motion is determined by the velocity. It is lower at low velocities, which implies that the steady state deflection decreases with increasing velocity. This models the Stribeck effect. However, as shown by Ganseman *et al.* [128] the LuGre model responses differ significantly from the experimental results. Furthermore, this behaviour will not change substantially if the parameters are changed. Thus, the LuGre model can hardly be used to validate a simulation model with experimental results. More information on the dynamic friction models discussed above can be found in Olsson [129] and Olsson *et. al.* [130].

4.4 Friction Simulation

Analysis of the motion of machines with friction is performed by employing one of the four types of tools presented by Armstrong-Helouvry, B., Dupont, P. and Canudas de Wit C [94]: describing functions, algebraic analysis, phase plane analysis and simulation. For this research, a simulation analysis was preferred in order to develop and investigate different friction compensation techniques. Furthermore, by using simulations as an analysis tool for friction, a comparison of experiment and simulation was used to validate models. By carrying out extensive simulations, a measure of parameter sensitivity and experiment/analysis verification was gained.

Consider the friction model based on Coulomb friction given in equation (4-1). Due to its dependence on the sign of velocity, the friction force is discontinuous at zero velocity. A number of researchers have proposed alternate friction models with the goal of producing accurate results while minimizing algorithm complexity and simulation time. A general approach is to replace the discontinuity of the static+Coulomb model by a curve of finite slope [123, 131-133]. This type of model eliminates the need to search for the switching point (between sticking and sliding) within an integration subinterval. If the slope is large, however, small step sizes are needed and the numerical integration

remains slow. More importantly, these models do not provide a true stiction mode. The system creeps through zero velocity instead of sticking.

Several techniques have been proposed to include stiction while still avoiding the search for the switching point. In one method, best described by Karnopp [134], the model defines a zero velocity interval, D_v. Outside this interval, friction is a function of velocity. Inside the interval, velocity is considered to be zero and friction is force dependent. For velocities within this interval the velocity may change and be non-zero but the output is maintained at zero by a dead-zone. Consequently, this model does not agree with real friction. The model does not pay attention to the behaviour of friction, as the velocity is variable at very low velocities.

For simulation analysis it is important to have a mathematical model of the steady-state friction which accounts for the relative velocity between the two bodies in contact. The models presented in equations (4-4) and (4-5) prove to be the most suitable for simulation analysis and control development. In order to ensure that the system experiences stick-slip, the following equation is used:

$$\mathbf{F_f}(\dot{x}) = \begin{cases} F(\dot{x}), \ldots\ldots\ldots\ldots if \rightarrow \dot{x} \neq 0 \\ F_a, \ldots\ldots\ldots\ldots if \rightarrow \dot{x} = 0, \mid F_a \mid < F_s \\ F_s \ \mathrm{sgn}(F_a), \ldots if \rightarrow \dot{x} = 0, \mid F_a \mid \geq F_s \end{cases} \qquad \textbf{(4-10)}$$

where the function $F(\dot{x})$ can be described by equation (4-4), (4-5), or (4-6).
When the magnitude of the relative velocity is not zero, the system is said to be in *slip* mode. In the slip mode the friction is dependent only on the relative velocity, and is determined by the function $F(\dot{x})$. When the magnitude of the relative velocity $\dot{x}$ is zero, the system is in the *stick* mode. In this mode, the system is static, and the frictional force F_f cancels exactly the driving force F_a, unless F_a exceeds the maximum frictional force F_s, which is the breakaway force as well. In the later case F_f is equal to F_s and the body experiences non-zero acceleration. At this moment the transition from the stick mode to the slip mode occurs.

4.5 Friction Compensation

The successful design and analysis of friction compensators depends heavily upon the quality of the friction model used, and the suitability of the analysis technique employed. This section gives an overview of the major friction compensation techniques focusing more on the ones that are most suitable for tracking at low-velocity. Thus, the friction compensation for the proposed joint mechanism is aimed to completely cancel or to diminish the stick-slip effect. The broad classes of friction compensation strategies are problem avoidance, non-model-based compensation and model-based compensation. All of these strategies are introduced and analysed for the proposed joint mechanism.

4.5.1 Friction problem avoidance

The friction problem avoidance can be done by carefully considering the following issues: (1) mechanical design, (2) material choice, and (3) lubricant choice. 'Design for control' is usually the first approach employed to defeat friction problems. Many studies have shown that the amplitude of stick-slip can be reduced (in some cases even to zero) by decreasing the mass, increasing the damping or increasing the stiffness of a mechanical system [94, 135-137]. Damping is usually controlled through selection of the lubricant and the sliding surfaces. Inertia and stiffness are determined to a great extent by the geometry and composition of the mechanism's bulk material. The selection of actuators, bearings, and sensors can affect system damping, stiffness and inertia. The most common source of excessive machine compliance is transmission elements. The obvious solution, which has been considered by a number of researchers, is to eliminate the transmission [138], or at least to locate it at the joint [139]. However, even in the absence of transmission elements, machine compliance due to shafts and couplings was shown to be significant [140].

These considerations have been taken into account when the prototype joint mechanism was designed, as it is shown in the next chapter. However, because the proposed joint

mechanism is a brake/clutch assembly, it does need the friction between the bodies in contact in order to operate efficiently. Therefore, no lubricant can be selected, even though it was shown that a proper selection of the lubricant increases damping and thus can contribute to the reduction of stick-slip.

4.5.2 Non-Model-Based Friction Compensation

From the control literature a number of non-model-based friction compensation methods were proven effective in reducing the effect of undesired friction-related effects at low velocities. These are high-gain proportional-derivative (PD) control [94, 140], joint torque control (JTC) [141-144], sliding mode control (SMC) [145-147], dither [148-154], and impulsive control [94, 155, 156].

High gain PD control is among the most common techniques. It has been experimentally observed that sufficiently stiff and/or damped systems do not exhibit stick-slip [94]. In a control context, this is accomplished by increasing the PD gains. The PD gains can be chosen to provide a reasonably sized domain of attraction so that the equilibrium point of steady sliding remains attractive and asymptotically stable under expected perturbations as demonstrated by Dupont [140].

Joint torque control (JTC) is a sensor-based technique, which encloses the actuator-transmission subsystem in the feedback loop to make it behave more nearly as an ideal torque source [144]. Disturbances due to undesirable actuator characteristics (friction, ripple, etc) or transmission behaviours (friction, flexibility, etc) can be significantly reduced by sensing and high gain feedback.

The joint torque control has been implemented as a mean of compensating for actuator and transmission friction to achieve the desired control [141-144], but had only limited success. Luh *et. al.* [141] reported a reduction of the Coulomb friction in their Stanford robot arm of almost 3%, while Pfeffer *et. al.* [142] reports a reduction of 97% of the uncompensated level of a PUMA robot joint.

Sliding controllers based on sliding-mode theory has some features that make it a candidate as an active friction compensation technique. Sliding-mode controllers (SMC) are well known to be robust against bounded, unstructured modelling errors. However, they are also known for the fact that they tend to cause chattering. The chattering generated by SMC is not always advantageous but can be effective in removing stiction. Sliding mode control was implemented for compensating dry frictio- related effects, with good results by several authors [145-147]. Seok-Boem *et al.* [145] shows in simulations that for Coulomb friction with stick-slip in an ultra-precision machining process, a SMC will allow positioning errors of 5% with motions on the order of micrometers. Noriaki *et al.* [146] reports chattering-free sliding mode friction estimator and compensator for a mechanical instrument that assists a human operator to operate micro tasks, such as assembly or manufacturing. Zhonghua *et al.* [147] demonstrates high accuracy in a X-Y positioning table with dry friction, using a combination of SMC and adaptive control.

Dither is a high frequency signal introduced into a system to modify its behaviour. Dither can stabilize unstable systems [148], and is used to improve performance by modifying nonlinearities in adaptive control [149], communication systems [150], optics [151] and image processing [152].

In machines with friction, dither has the capability to smooth the discontinuity of friction at low velocity. The signal can be applied tangential or normal to the friction interface. The effect of tangential dither is to modify the influence of friction by averaging the nonlinearity; the effect of vibrations normal to the contact is to modify the friction by reducing the friction coefficient. Dither's main drawback is accelerating the wear of the surfaces in contact. Furthermore, the dependence on the depth of discontinuity can also restrict the application of dither. That is why dither is only occasionally applied to motor servos but is often applied and with great effect to spool valves in hydraulic servos.

A number of investigators have developed controllers that achieve precise motions in the presence of friction by applying a series of small impacts when the system is at rest (i.e. stuck condition) [94, 155, 156]. These controllers are called 'impulsive controllers'. Impulsive control is distinguished from dither in that it is the impulses themselves which are to carry out the desired motion. Impulsive control is also distinct from standard pulse width modulation (PWM) controllers, where voltage pulses are applied to a motor. In PWM controllers, the motor inductance averages the relatively high frequency (in the region of 20kHz) voltage pulses to produce a nearly constant motor current, and therefore nearly constant torque. The effect of the impulse is a small displacement or a controlled breakaway, leading the transition to another controller which regulates macroscopic movements. By making the impulses of great magnitude but short duration, the static friction is overcome and sensitivity to the details of friction is reduced.

4.5.3 Model-Based Friction Compensation

Many schemes for model based friction compensation have been proposed [94, 101-104, 130, 157-168]. The system is provided with a friction observer which tries to estimate the friction based on available measurements and a friction model. The estimated friction is then added as an input to the system. Effective friction compensation requires that good velocity measurements are available and that the input is introduced in such a way that there is little dynamics between the insertion point and the point where friction acts.

There are many schemes of this type that mainly differ in the complexity of the friction model used. Thus, there are schemes that use: (1) Coulomb friction feedforward or feedback [157-159]; (2) general friction models feedforward/feedback [160, 161]; and (3) adaptive feedforward/feedback [94, 130, 157, 158, 162-170].

The adaptive algorithms employed to compensate for friction include the recursive-least-square (RLS) and least-mean-square (LMS) algorithms of Walrath [158], Craig

[162], and Canudas de Wit [168]; the model reference adaptive control (MRAC) algorithms of Gilbart and Winston [157], Yang and Tomizuka [103], Brandenburg and Schafer [164]; or the Lyapunov's function based algorithm of Friedland and Park [165], Southward *et al.* [166], and Feemster *et al.* [167]. Another model-based friction compensation technique often used in robotic systems is computed-torque control (CTC). This method makes direct use of the complete dynamic model of a system to cancel not only the effects of gravity, but also Coriolis force, centrifugal force, friction and the manipulator inertia tensor [171].

In adaptive control methods the control law is continuously updated to adapt to changes in the parameters of the system being controlled. This characteristic of the adaptive systems allows development of controllers that are more robust so that their performance is not sensitive to modelling errors. However, adaptive control methods are based on the assumption that the parameters of the system being controlled do not change too rapidly in comparison with the system time constants. These techniques have proved quite effective when applied, for example to chemical processes where the process parameters experience gradual change. However, for robotic manipulators or machines with friction, the system parameters such as inertia, the effect of gravity and friction-related parameters tend to change rapidly as the robotic arm moves from one configuration to another. For this reason, the application of adaptive control methods to robotic manipulators and machines with friction has thus far enjoyed only limited success.

4.6 Conclusions

The aim of this chapter was to review the existing solutions regarding friction modelling and friction compensation. Furthermore, from the literature review it is required to identify the most suitable friction model that best depicts the friction characteristics. Additionally, it is required to choose several friction compensation techniques that could diminish or completely cancel the stick-slip effect in the proposed joint mechanism.

It was shown in section 4.2 that for this particular mechanism, the relationship between the friction and velocity is of utmost importance, as the control system of the proposed joint is required to regulate the position at very low position rates (i.e. velocity). Therefore, the friction model must display the Stribeck effect, which is usually associated to the friction-velocity relationship at low velocities. Hence friction models that do not display the Stribeck effect are not considered for this application.

As shown in section 4.3, there are several friction models that are capable of displaying the Stribeck effect. The exponential model of Bo and Pavelescu was chosen because of its flexibility. The model is not a strong constraint and by appropriate choice of parameters, various curves can be obtained as shown in Figure 4-4. The seven parameters model developed by Armstrong-Helouvry is more complete and potentially can approximate the friction more accurately. However, it was not selected due to the difficulty of estimating four of the seven parameters that are part of the model. These four parameters depend on the mechanism and lubricant properties, and rules regarding the selection of them are not available. This makes the validation of the friction model in a particular machine with friction very difficult and requires a lot of time and effort to make sure the empirical parameters are properly selected.

A number of friction compensation techniques were presented in section 4.5. The broad classes of friction compensation strategies are problem avoidance, non-model-based control and model-based control. The design of the prototype joint mechanism, introduced in section 3.4 and fully described in section 5.2, was done with regard to 'design for control' methodology. Thus, both the mechanical design and the material choice were carried out so that the stick-slip effect is diminished as much as possible at the very early stage. This issue is described in more details in section 5.2. Although, friction may be a desirable property for brakes and clutches, it is generally an impediment for servo control. Because of the friction high nonlinearity and difficulty to predict its dynamics, non-model-based control is preferred against model-based control. It was shown that the model-based control of friction is based on the assumption that the parameters of the system being controlled do not change too rapidly in comparison with

the system time constants. This assumption is considered by the author quite optimistic in machines with friction. Nevertheless, this method may be used in association with a non-model-based friction compensation technique in order to increase further the performance of a control strategy. This approach is recommended for further research in this area. In this study, the CTC method is investigated as a model-based friction compensation method to illustrate its advantages and disadvantages.

Within the non-model-based control techniques, dither and impulsive control were found unsuitable. This is because both techniques require an extra actuator: in case of dither is required an extra actuator that provides the high frequency signal and in case of the impulsive control is required an extra actuator that is capable of producing impulses of great amplitude but short duration. An extra actuator per joint will substantially increase the mass and geometrical dimensions of the proposed actively restrained mechatronic system, thus, making it pricier and possibly harder to manoeuvre by the human operator. Furthermore, dither has the disadvantage of accelerating the wear of the surfaces in contact. The joint torque control (JTC) method requires extra sensors, which are usually mounted on deformable surfaces such as beams and shafts. In this way, extra compliance must be allowed in the system, thus affecting the overall behaviour of the mechanism. As a result, the compensation techniques evaluated for the proposed joint mechanism are high gain PD control, computed-torque control (CTC) and sliding-mode control (SMC).

The next chapter describes the design for control of the proposed joint mechanism. Also measurements of the friction within the mechanism are taken and analysed. The development of the selected friction compensation techniques is addressed in Chapter 6. Simulation and experimental results are obtained which confirm the selection of the friction model and show the performance of the compensation techniques employed.

Chapter 5
Design of an Experimental Test-Bed

5.1 Introduction

In order to accurately evaluate a friction compensation technique and a theoretical friction model, an experimental rig needs to be built. Thus, in this chapter the design of an experimental test-bed is addressed. The 'design for control' methodology, introduced in section 4.5.1, was employed for the design of an experimental test-bed. The experimental test-bed is based on the proposed joint mechanism introduced in section 3.4. The friction within the joint mechanism is measured and analysed. This analysis intends to observe friction behaviour within the mechanism, so that the parameters of the friction model selected in section 4.3 can be suitably approximated. Furthermore, the test-bed was designed to facilitate the interchangeability of the materials in contact, whose importance was shown in Section 3.4.1. The chapter concludes with the derivation of the mathematical model, which is used later in the thesis to develop an efficient controller for position regulation.

5.2 Design of an Experimental Test-Bed

In order to overcome the difficulties of the existing joint mechanisms, presented in section 3.3, the components of the proposed joint mechanism have to fulfil several requirements. These requirements have been carefully investigated in section 3.4. As shown in section 4.5, in order to develop a system that is easy to control and has better

performance a 'design for control' methodology needs to be employed so that the stiffness of the entire mechanism is maximised. Figure 5-1 show the scheme of the experimental test-bed, which consists of a main shaft (1), a brake disc (2), a pulley (3) and a weight system (4), a cantilever (5), a DC motor N9M4T from Kollmorgen, Motion Technologies Group (6), a connexion shaft (7), a lever (8), and an incremental encoder Hengstler, type 0523246 (9). A picture of the real system is shown in Figure 5-2.

Onto the main shaft (1) are rigidly mounted the brake disc (2), pulley (3) and the encoder (9). The shaft is mounted on two angular contact ball bearings, and its motion is to be controlled. The pulley-weight system is used to produce a driving torque, T_u, apply to the main shaft. A braking mechanism is used to restrain the motion of the shaft so that different tasks can be performed (e.g. reach a position, follow a trajectory, etc). This braking mechanism consists of a DC motor (6), connexion shaft (7), lever (8), cantilever (5) and the brake disc (2). The DC motor (6) is used to produce a controllable torque T_{DC}, which is converted into a mechanical force F_N onto the braking disk (2) by the lever (8). The cantilever (5) acts as a frictional pad onto the braking disk (2), thus creating the sliding friction (i.e. frictional force, F_f / frictional torque, T_f). The braking mechanism that provides the frictional torque T_f is better illustrated in Figure 5-1b. The incremental encoder (9) mounted on the shaft (1) is used to measures the shaft's actual position, θ. This position is the one that needs to be regulated by a control system. The other parameters in the figure are presented in the 'Notation' section at the beginning of the thesis. The technical drawings of the experimental test-bed are shown in Appendix F. Moreover, the clutch parameters and the DC motor performance specifications are presented in Appendix D.

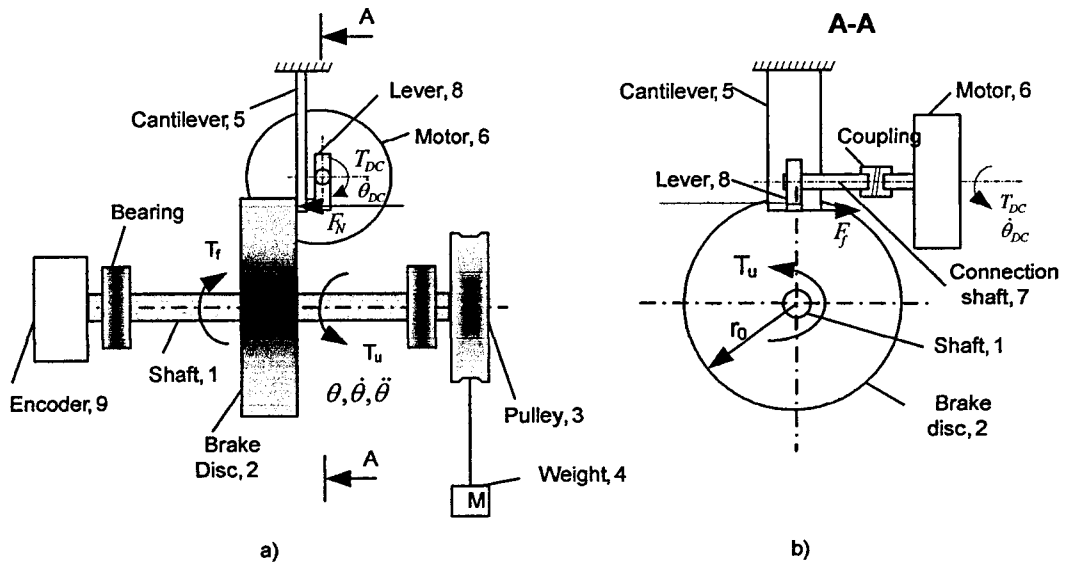

Figure 5-1 Scheme of the experimental test-bed

Front view, b) Side view

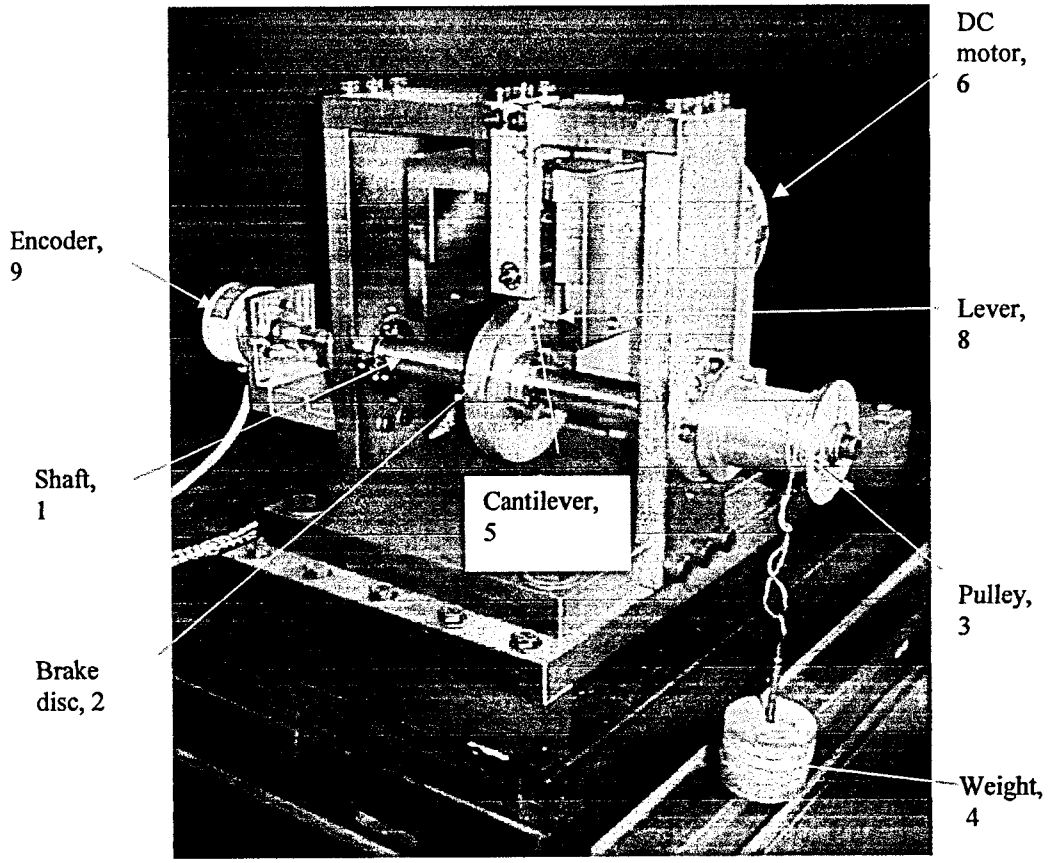

Figure 5-2. Experimental test-bed

This mechanical design of the clutch ensures stability and simplicity due to the choice of a calliper disc brake/clutch. The stiffness of the mechanism is guaranteed by the design of the brake pad as a cantilever, and by the design of the shaft and brake disc of appropriate dimensions. The material selected for both the brake disc and the cantilever is stainless steel UNS S20100, as shown in section 3.4. This material was selected due to the good physical properties and lower cost. The properties of the selected material are also presented in section 3.4.

The test–bed was designed based on the same principle as the one proposed for the actively restrained passive joint, which was introduced in section 3.4. In order to investigate different materials or different material combinations to further improve the performance of the proposed clutch (i.e. joint mechanism), several components are assembled so that they can easily be replaced. Thus, the cantilever and the braking disc, which are critical components of the braking mechanism, were designed so that the interchangeability is enhanced. Furthermore, the experimental test-bed provides a space for a second braking mechanism so that the braking torque produced can be doubled. Therefore, the joint mechanism can be made capable of resisting to a greater user-input force. This advantage is not used in this project, as the objective of this research is to prove the principle of an electromechanical friction clutch as an actively restrained passive joint and not to have a commercially ready system. However, this idea is proposed for further developments. The mechanical assembly of the braking mechanism (without the actuators) is shown in Figure 5-3a and the design of the brake disc is shown in Figure 5-3b. The technical drawings of the experimental test-bed are shown in Appendix F.

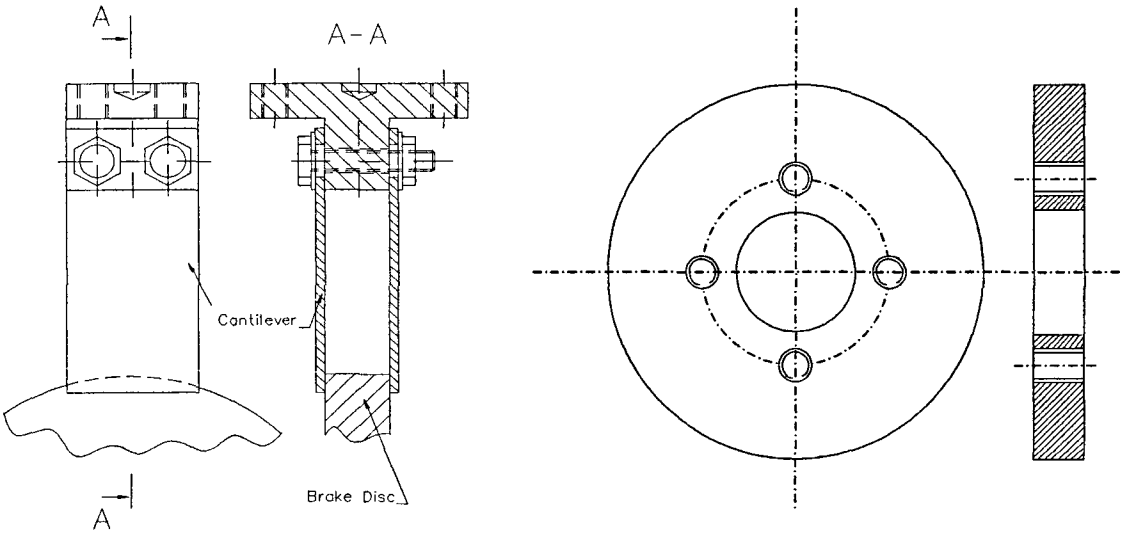

a) b)

Figure 5-3. Friction mechanism design:
a) the braking mechanisms (without the actuators), b) the brake disc

5.3 Friction Measurement

The friction measurement and the investigation of the friction within the proposed clutch mechanism are addressed in this section. The section was completed so that better understanding of the friction within the proposed clutch system is obtained. This understanding is important from two points of view: firstly, the understanding of the friction within the proposed mechanism helps to identify the limitations and drawbacks of the proposed friction clutch; and secondly, from the understanding of the real friction a reliable friction model can be develop so that future developments can be completed in simulations. The measurement of the friction was experimentally performed using the computational workstation described in Appendix G.

The friction is obtained from the clutch's equation of motion (5-2), derived in the next section, $T_f(\dot{\theta}) = T_u - I\ddot{\theta} - C_d\dot{\theta}$. Replacing the driving torque T_u as given by equation (5-3) and the frictional torque $T_f(\dot{\theta})$ as given by equation (5-4), the coefficient of friction is obtained from the following equation

$$\mu(\dot{\theta}) = \frac{Mg \cdot R_p - C_d\dot{\theta} - J\ddot{\theta}}{K_{COF} \cdot v_a} \qquad \textbf{(5-1)}$$

where, M is mass hanged onto the pulley, R_p represents the pulley radius, $J = I+MR_p^2$ represents the system total inertia, C_d indicate the damping coefficient, v_a is the applied voltage, and $K_{COF} = \frac{r_i \cdot K_t \cdot A}{A_{lever} \cdot R_a \cdot r_c}$ is considered a constant of the coefficient of friction, obtained in section 5.4.2.2 'Friction model'.

The measurement of the friction was completed on the existing rig in the following way: A mass was suspended onto the pulley while the applied voltage was manually adjusted until the mass start falling. In this way the static coefficient of friction can be accurately obtained. The dynamic coefficient of friction was obtained after the acceleration became constant. Both the mass M and the applied voltage v_a were recorded. The velocity $\dot{\theta}$ and the acceleration $\ddot{\theta}$ were estimated from the measured position using the backward difference algorithm. This method is known to be prone to errors and therefore an accurate measurement is not possible. The errors due to the differentiation techniques can clearly be seen in Figure 5-4 in a form of noise. However, for this work, the aim of the measurement is to assume the friction regimes as defined by Stribeck so that the friction properties of the proposed clutch can be evaluated.

For a mass of 0.2 kg it was detected that a voltage of v_a = 1.2544 V was the maximum value that allows the mass to start falling. The experimentally obtained friction versus velocity curve is illustrated in Figure 5-4a. Similarly, for a mass of 0.3 kg it was detected that a voltage of v_a = 1.962 V was the maximum value that allows the mass to start falling, experiment shown in Figure 5-4b. The experiments for each mass were repeated six times and Figures 5-4a and 5-4b illustrate the general observations. As a result of the friction measurement, the static coefficient of friction is equal to 0.2, and the dynamic coefficient of friction is 0.15.

Based on the measurements taken, an estimated friction characteristic of the friction in mechanism is considered, as shown in Figure 5-4. The friction regimes shown in the generalised Stribeck curve, illustrated in Chapter 4, can easily be recognised. It can be

seen that between 0 rad/s and 0.4 rad/s the friction is assumed to be in the 'boundary lubrication' regime; between 0.4 rad/s and 2rad/s the friction is considered to be in the 'partial lubrication' regime; and for velocities greater than 2rad/s the friction is considered to be in the hydrodynamic regime.

From the friction measurement it was observed that for velocities less than 0.4 rad/s (i.e. about 24 deg/s) the friction is in the boundary lubrication regime, which means stick-slip will occur, therefore the motion below 0.4 rad/s is practically impossible to be smoothly controlled. This result shows a very important limitation of this clutch as it is required to control the motion for velocities in the region of 0.1 rad/s (i.e. approx 1rpm or 6deg/s). Therefore, the task of designing a controller able to diminish the stick-slip effect, which is highly challenging, is necessary.

From Figure 5-4 the nonlinearity of the friction can be observed. This nonlinearity is particularly important for velocities between 1 rad/s and 2 rad/s (approx. 58-115deg/s) where the coefficient of friction drops significantly. The friction is relatively constant up to the velocity at which partial fluid lubrication begins to play a role. These experimental results are in accordance with Stribeck model of friction. Such a drop in the coefficient of friction means that only a relative smaller frictional torque can be produced at the contact between the cantilever and the braking disc in this speed range. These observations are, however, dependent on the materials in contact and with a different combination of materials these results are likely to change.

A final conclusion from the friction measurement is associated with the difficulty of accurately modelling friction. Many empirical models for approximating friction were presented in section 4.3. However, none of these truly represents a real system as noted from the experimental measurements. Thus, the parameters of the selected friction model are chosen so that high possibility of stick-slip is promoted. This model is explained in section 5.4.2.2, and the friction parameters are given in Appendix D1. The main challenge of the control system, however, is to regulate the position rate of the proposed clutch mechanism for values around 0.1 rad/s (approx. 6 deg/s) while avoiding

the friction-related effects such as stick-slip. The strategy to achieve this performance is described in the next chapter.

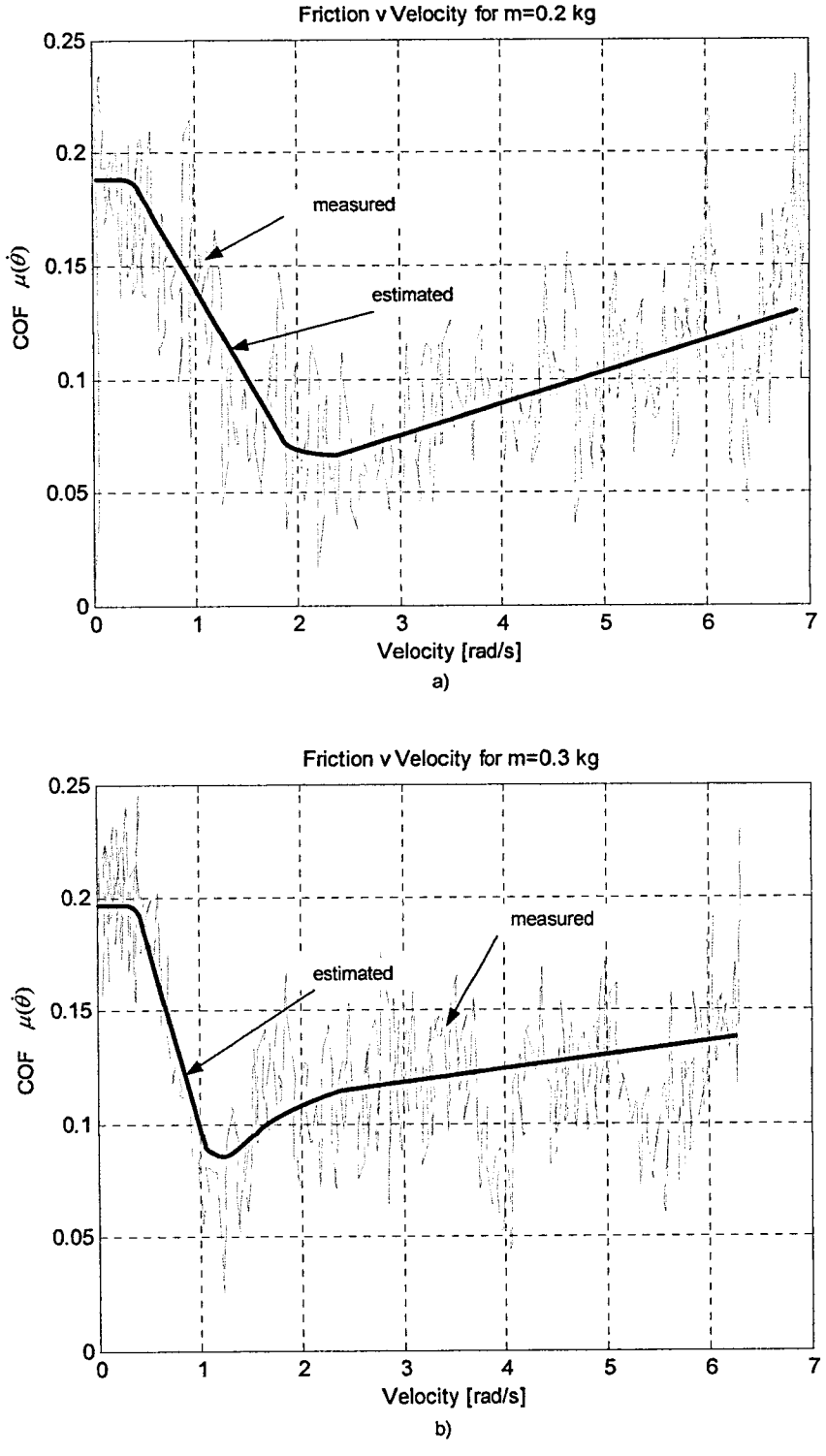

Figure 5-4. Friction experiment:

a) M = 0.2 kg, v_a = 1.2544V, b) M = 0.3 kg v_a = 1.962V

5.4 Mathematical Model

The block diagram of the control system is shown in Figure 5-5. In the next sections all the blocks from the Figure 5-5 are discussed and modelled, except for the controller block which is discussed in the next chapter.

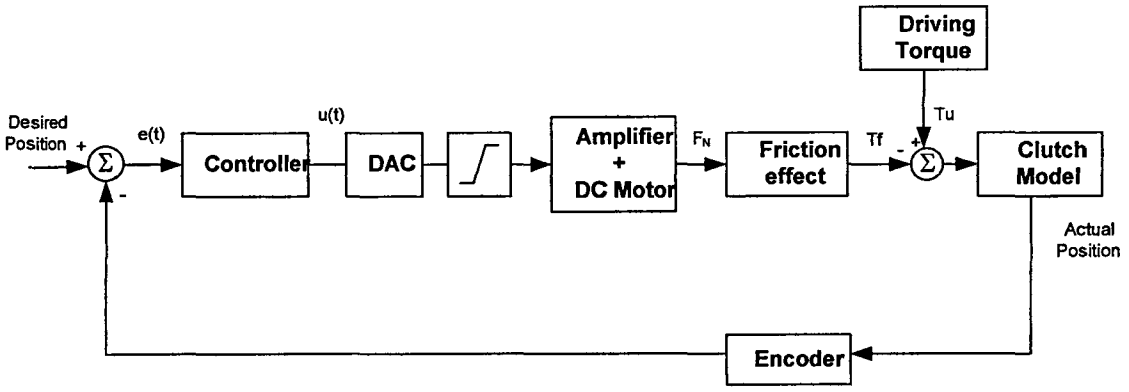

Figure 5-5. System block diagram

5.4.1 Clutch model

The free-body diagram of the experimental test-bed is shown in Figure 5-6. A driving torque T_u is produced on the main shaft, and a frictional torque T_f is regulated so that a desired position profile of the shaft can be achieved.

From the free body diagram shown in Figure 5-6, the equation of motion is obtained as:

$$I\ddot{\theta} + C_d\dot{\theta} + T_f(\dot{\theta}) = T_u \qquad \textbf{(5-2)}$$

where, $\theta,\dot{\theta},\ddot{\theta}$ denotes the shaft motion, C_d represents the viscous damping coefficient, and $I = I_{shaft} + I_{disc} + I_{pulley}$ is the total inertia of the clutch (i.e. $I = I_1 + I_2 + I_3$ in Figure 5-6). The driving torque, T_u, is obtained from the free-body diagram as:

$$T_u = F_u \cdot R_p = MgR_p - MR_p^2\ddot{\theta} \qquad \textbf{(5-3)}$$

where F_u is the tension force in the wire due to the mass M, and R_p represents the radius of the pulley. The frictional torque, T_f, is obtained as shown in section 3.4, and reproduced in equation (5-4):

$$T_f(\dot{\theta}) = \mu(\dot{\theta}) \cdot p(t) \cdot r_i \cdot A \qquad \textbf{(5-4)}$$

where μ is the coefficient of friction, p denotes the pressure applied by the lever onto the brake disc, r_i represents the inner radius of the brake disc, and A is the area of the contact between the brake pad and brake disc. Thus, the equation of motion of the clutch mechanism can be written as

$$\ddot{\theta} = J^{-1}\left[MgR_p - \mu(\dot{\theta}) \cdot p(t) \cdot r_i \cdot A - C_d\dot{\theta}\right] \qquad \textbf{(5-5)}$$

where $J = I + MR_p^2$ represents the total moment of inertia of the experimental test-bed.

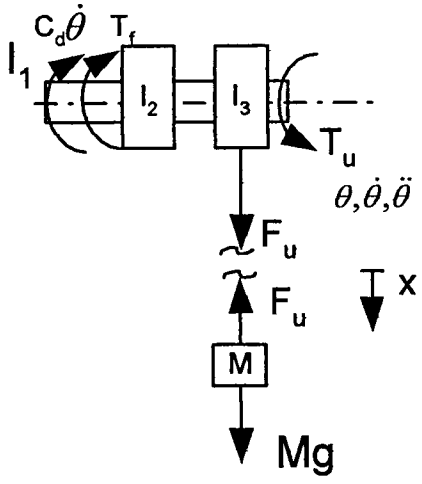

Figure 5-6. Free body diagram of the experimental test-bed

5.4.2 Braking mechanism model

5.4.2.1 Actuation model

A low inertia, low impedance DC motor is used to provide the controllable torque, T_{DC}. The motor's torque is armature controlled and a lever is used to transform the motor torque into normal force onto the brake disc as illustrated in Figure 5-7.

The flexibility between the lever and the brake disc, as well as the flexibility between the motor shaft and the connection shaft are negligible, because a torque feedback control system is used to control the applied normal force (thus the frictional force). The equation of motion of the actuation assembly shown in Figure 5-7, is given by:

$$J_T\ddot{\theta}_{DC} + b\dot{\theta}_{DC} = T_{DC} \qquad \textbf{(5-6)}$$

where $J_T = J_{DC} + J_{connection\ shaft} + J_{lever}$ represents the resulting moment of inertia considered for the actuation model, b denotes the viscous friction coefficient in the motor, $\theta_{DC}, \dot{\theta}_{DC}, \ddot{\theta}_{DC}$ represents the motor's shaft motion. Due to the fact that the position of the motor's shaft is almost motionless and the inertia of the load is small in comparison with the inertia of the motor, the velocity and the acceleration of the motor are neglected. Thus, the motor torque, T_{DC}, is given as $T_{DC} = K_t i_a$, where K_t represents the motor torque constant and i_a is the armature current obtained from the electrical circuit of the motor as:

$$i_a = \frac{1}{R_a}\left(v_a - v_b - L_a\frac{di_a}{dt}\right) \qquad \textbf{(5-7)}$$

where, R_a is the armature resistance, v_a represents the armature voltage, v_b denotes the back emf voltage, and L_a is the armature inductance of the motor. A derivation of the DC motor mathematical model is given in Appendix E2.

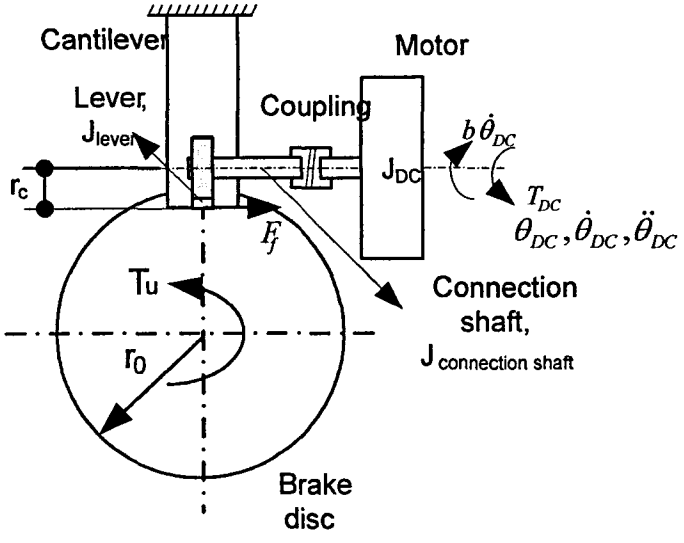

Figure 5-7. The actuation assembly

Because of the almost motionless rotation of the motor shaft, the electromotive force given by v_b, and the armature inductance, L_a, can be neglected without affecting the control of the system. Thus, the normal force F_N onto the brake disc is given by:

$$F_N = \frac{T_{DC}}{r_c} = \frac{K_t}{r_c \cdot R_a} \cdot v_a(t) \qquad \textbf{(5-8)}$$

where r_c is the distance between the centre of the motor shaft and the contact point on the braking disc.

The normal pressure, p(t) in equation (5-4), is defined as the normal force F_N produced by the motor and lever mechanism exerted on the area defined by the lever rectangular section A_{lever}. Thus, the pressure p(t) onto the braking disc, obtained from the motor, can be written as:

$$p(t) = \frac{F_N}{A_{lever}} = \frac{K_t}{A_{lever} \cdot r_c \cdot R_a} v_a(t) \qquad \textbf{(5-9)}$$

The system block diagram, shown in Figure 5-5 is presented in more details in Figure 5-8. The system and motors parameters are presented in Appendix D.

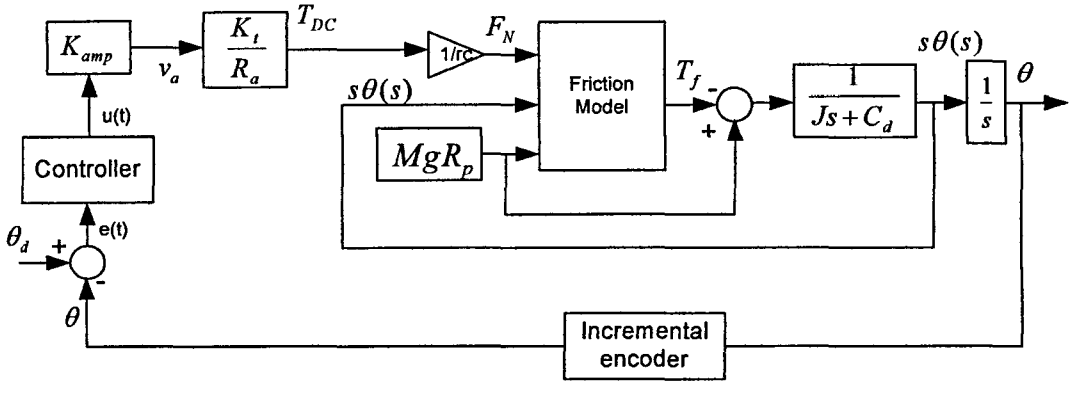

Figure 5-8. Experimental test-bed control diagram

5.4.2.2 Friction model

In order to obtain the frictional torque, T_f, defined in equation (5-4), the coefficient of friction $\mu(\dot{\theta})$, needs to be modelled. The friction modelling was discussed in Chapter 4, and the friction from the experimental test-bed was presented in section 5.3. From these two sections, was concluded that for this application the most suitable friction model must incorporate the Stribeck friction as well as high possibility of stick-slip. Regarding these two issues, Dupont [140] and Armstrong-Helouvry [94] demonstrate that the exponential friction model is the most appropriate. Thus, the coefficient of friction $\mu(\dot{\theta})$ is modelled as:

$$\mu(\dot{\theta}) = \left(\mu_d + (\mu_s - \mu_d) e^{-\left|\dot{\theta}/\dot{\theta}_s\right|^{\delta}} \right) \mathrm{sgn}(\dot{\theta}) \qquad \textbf{(5-10)}$$

where μ_d represents the dynamic coefficient of friction, μ_s denotes the static coefficient of friction, $\dot{\theta}_s$ is the Stribeck velocity, and δ is the Stribeck coefficient. The parameters μ_d, μ_s, $\dot{\theta}_s$ and δ are specified so that stick-slip is promoted, and their values are listed in Appendix D1 together with all the parameters of the experimental clutch system.

Replacing equation (5-9 and (5-10) into equation (5-4), the frictional torque becomes:

$$T_f(\dot{\theta}) = \left(\mu_d + (\mu_s - \mu_d) e^{-\left|\dot{\theta}/\dot{\theta}_s\right|^{\delta}} \right) \mathrm{sgn}(\dot{\theta}) \cdot \frac{r_i \cdot K_t \cdot A}{A_{lever} \cdot R_a \cdot r_c} v_a(t) \qquad \textbf{(5-11)}$$

where A is the area of contact between the brake disc and cantilever, obtained in section 3.4. Substitution of equation (5-3) and (5-11) into equation (5-5), the system equation of motion is obtained as:

$$\ddot{\theta} = J^{-1}\left[MgR_p - \mu(\dot{\theta}) \cdot \frac{r_i \cdot K_t \cdot A}{A_{lever} \cdot R_a \cdot r_c} v_a(t) - C_d\dot{\theta} \right] \qquad \textbf{(5-12)}$$

or

$$\ddot{\theta} = J^{-1}\left| MgR_p - \mu(\dot{\theta}) \cdot K_{COF} \cdot v_a(t) - C_d\dot{\theta} \right| \qquad \textbf{(5-13)}$$

where $K_{COF} = \dfrac{r_i \cdot K_t \cdot A}{A_{lever} \cdot R_a \cdot r_c}$ represents a constant of the frictional torque.

For simulation purposes, in order to ensure that the system experiences stick-slip, the following mathematical relationship is used to model the frictional torque T_f:

$$T_f = \begin{cases} T_f(\dot{\theta}), & \forall \dot{\theta} \neq 0 \\ T_u, & \forall \dot{\theta} = 0, |T_u| < T_{f\max} \\ T_{f\max}\,\mathrm{sgn}(T_u), & \forall \dot{\theta} = 0, |T_u| \geq T_{f\max} \end{cases} \qquad \textbf{(5-14)}$$

where, $T_f(\dot{\theta})$ is given by equation (5-11).

When the magnitude of the relative velocity between the brake disc and cantilever is not zero, the system is said to be in *slip* mode. In the slip mode the friction is dependent only on the relative velocity, and is determined by the function $\mu(\dot{\theta})$. When the magnitude of the relative velocity $\dot{\theta}$ is zero, the system is in the *stick* mode. In this mode, the system is static, and the frictional torque T_f cancels exactly the driving torque T_u, unless T_u exceeds the maximum frictional torque $T_{f\,max}$, which is the breakaway torque as well. In the later case T_f is equal to $T_{f\,max}$ and the body experiences non-zero acceleration. At this moment the transition from the stick mode to the slip mode occurs. The friction algorithm has been implemented into the simulation model, using the MathWorks Matlab/Simulink package, as illustrated in Figure 5-9.

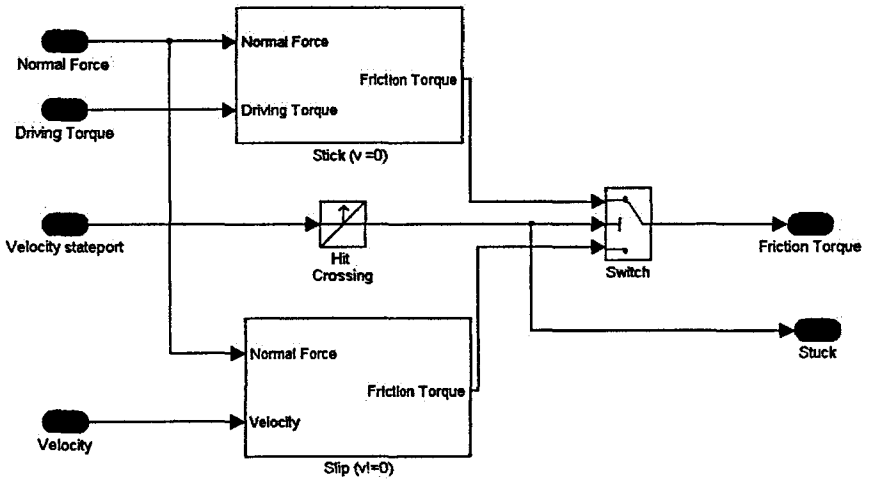

Figure 5-9. Friction algorithm implementation

5.4.3 Digital-to-analogue converter (DAC) model

The DAC is derived from the specifications of the real DAC employed in the computational workstation for real-time control, which is presented in Appendix G. Thus, the digital-to-analogue converter DAC 312 employed on the single axis motion card (SAMC) is modelled. The model used for the DAC is graphically illustrated in Figure 5-10. The input in the motor's amplifier is between +/- 5V analogue, which is equivalent to +/-1024 digital. Thus, a multiplication constant $K_{DAC} = 0.0049$ is required to convert from digital to analogue value. The resolution of the DAC is 0.005V and is represented in the model by a quantizer.

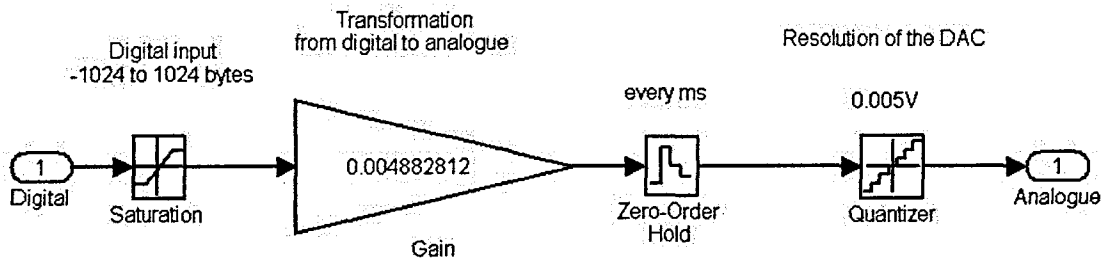

Figure 5-10. DAC model

5.4.4 Position sensor model

The revolute motion of the experimental test-bed was measured using a 5000 pulses per revolution (PPR) incremental encoder from Hengslter. Using a decoder such as HCTL-1100, the quadrature encoder signal was decoded to give 20000 counts per revolution. Thus, a resolution of 0.018 deg (3.14×10^{-4} rad) is obtained for the angular position. The model used for the incremental encoder is illustrated in Figure 5-11.

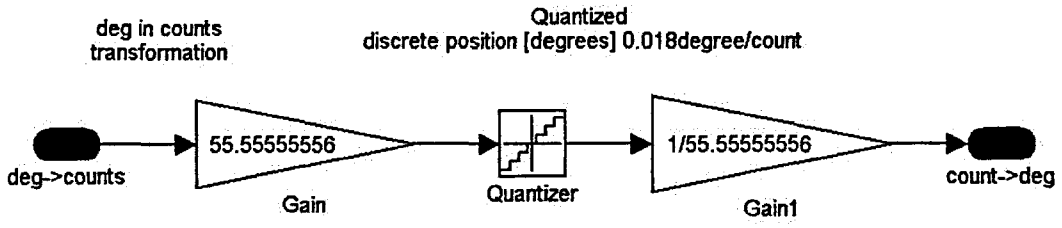

Figure 5-11. Incremental encoder model

5.5 Conclusions

A 'design for control' methodology was employed to design the experimental test-bed, which is similar to the principle applied for an actively restrained revolute joint. Increasing the stiffness of a mechanism and avoiding transmission elements such as gearboxes, chains and belt pulley, it was hoped that will increase the capability of the joint to diminishing the stick-slip phenomenon. As it was shown in literature, while 'design for control' does not guarantee the passive elimination of stick-slip, it usually produces a system that is easier to control and which possesses better performance characteristics.

The friction within the proposed electromechanical friction clutch was measured and several observations were acknowledged. The high nonlinearity and unpredictability of the friction within the proposed joint mechanism can easily be noticed from the experiments carried out. It was noticed that for a velocity less than 0.4 rad/s (approx. 24deg/s) the friction is in the boundary lubrication regime, which means stick-slip will occur, therefore the motion below 0.4 rad/s is practically impossible to be smoothly controlled. This result shows a very important limitation of this clutch as it is required to control the motion for velocities in the region of 0.1 rad/s (i.e. approx 1rpm or 6deg/s). Therefore, the task of designing a controller able to diminish the stick-slip effect, which is highly challenging, is necessary. Another important observation of the friction in the proposed clutch is the fact that the coefficient of friction drops

significantly for velocities between 1 rad/s and 2 rad/s (approx. 58-115deg/s). These experimental results are in accordance with Stribeck model of friction. Such a drop in the coefficient of friction means that only a relative smaller frictional torque can be produced at the contact between the cantilever and the braking disc in this speed range. These observations are, however, dependent on the materials in contact and with a different combination of materials these results are likely to change.

From the friction measurement it can be seen that another challenge in this research is finding a friction model that simulates the stick-slip effect, so that a mathematical model of the system can be obtained and used for developing control algorithms to compensate for stick-slip. None of the empirical models described in section 4.3 represents the friction quite like the one observed from the experimental measurements. Thus, a model that is most suitable for systems with high possibility of stick-slip was preferred. This was demonstrated by Dupont and Armstrong-Helouvry to be the exponential friction model. This model was the one selected for the modelling of friction in the proposed clutch mechanism. In the next chapter, controllers capable of diminishing or completely cancelling the stick-slip effect are developed and investigated. Simulation and experimental results of the developed control system are performed, which demonstrate the validity of the mathematical model.

Chapter 6
Development and Evaluation of Selected Friction Compensation Techniques

6.1 Introduction

In this chapter, the control of the proposed electromechanical friction clutch is addressed. This issue was first introduced in Chapter 4 and is fully described in this chapter. Firstly, the three controllers capable of diminishing or completely cancelling the stick-slip effect are developed. Secondly, simulation and experimental results are obtained to evaluate the performance of each friction compensation technique. The results demonstrate the effectiveness of the sliding-mode control and the potential of a computed-torque control for the position regulation at low velocities. Furthermore, the mathematical model derived in Chapter 5 is validated, which allows one to perform further analyses with the proposed electromechanical friction clutch, without building another prototype. In the end, several conclusions are draw, which allows for development of an efficient control system for the proposed actively restrained passive mechatronic system.

6.2 Controller Development

In order to have an efficient control system when the position rate is very low, a controller that is capable of regulating the position smoothly and accurately needs to be

developed. It was shown in Section 5.3 that for a velocity less than 0.4rad/s (approx. 24deg/s) friction is in the boundary lubrication regime, which means that stick-slip will occur, thus the motion below 0.4rad/s is practically impossible to be smoothly controlled. However, for the proposed joint mechanism it is required to control the system's motion for a velocity in the region of 0.1rad/s (approx. 6deg/s), which is highly predisposed to the stick-slip effect. Therefore, the task of designing a controller able to diminish the stick-slip effect, which is highly challenging, is necessary. The maximum position rate at which the position is regulated also needs to be limited so that the motion is effectively controlled. The maximum position rate that was chosen is 1.75rad/s (approx. 100deg/s), which ensures that in case of a sudden stop the stopping distance is less than the accuracy of the revolute joint.

Besides avoiding the stick-slip effect within the mechanism, the controller is required to track the desired position with an error less than 0.2deg. This level of error ensures that the overall error of the two-DOF prototype, introduced in section 3.3, is less than 1mm. From the existing actively restrained devices presented in section 3.2, the most accurate was proved to be PTER with a maximum error of 4mm [69]. Thus, even if an error of around 0.8deg is obtained, the proposed system is still the best in its class, because of the advantages explained in Chapter 3.

It was shown in Section 4.5 that the most suitable controllers capable of diminishing or completely cancelling the stick-slip effect are the PD controller, the computed-torque controller (CTC) and the sliding-mode controller (SMC). These three controllers are developed in the next sections. To remind the reader the functionality of the proposed electromechanical friction clutch, a diagram of the control system is illustrated in Figure 6-1. The electromechanical clutch consists of a disc mounted on a shaft, a cantilever and a DC motor. An external driving torque T_u is produced using a pulley-weight system, and the friction generated using an actuation assembly restrains the shaft so that the shaft's motion can be controlled. The system's equation of motion was derived in Section 5.5 and is shown in equation (6-1).

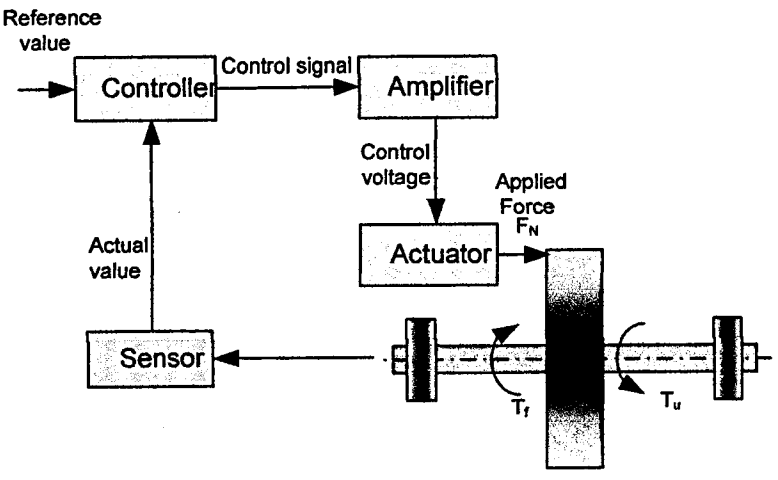

Figure 6-1. System's control diagram

$$\ddot{\theta} = J^{-1}\left[MgR_p - \mu(\dot{\theta}) \cdot K_{COF} \cdot v_a(t) - C_d\dot{\theta}\right] \quad \textbf{(6-1)}$$

6.2.1 Proportional-Derivative (PD) Control Development

In the diagram presented in Figure 6-1, the reference value and the actual value are used to compute the error e(t) of the system. Thus, the error e(t) of the system is defined as the difference between the desired position, θ_d(t), and the measured position, θ(t).

$$e(t) = \theta_d(t) - \theta(t) \quad \textbf{(6-2)}$$

This error is used to compute the PD control law u(t) as

$$u(t) = K_p e(t) + K_d \frac{d}{dt} e(t) \quad \textbf{(6-3)}$$

where, K_p and K_d are the controller gains. The derivative of the error with respect to time is approximated using the Kalman filter [176]

$$\frac{d}{dt} e(t) = \dot{e}_k = (1 - K_{Kal}) \cdot \dot{e}_{k-1} + K_{Kal} \cdot \frac{(e_k - e_{k-1})}{T} \quad \textbf{(6-4)}$$

where, K_{Kal} is between 0.2 and 1 and denotes the Kalman constant, T represents the chosen sampling time. The controller gains, K_p and K_d, are optimised through trial and

error and their values are set to K_p = 5000, and K_d = 50. The block diagram of the proposed clutch system with a PD controller is shown in Figure 6-2.

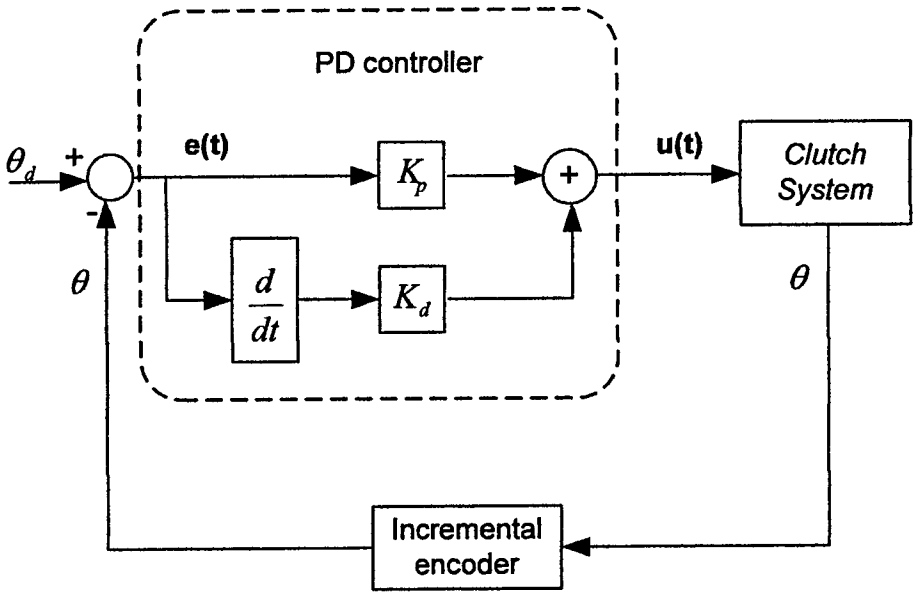

Figure 6-2. System's control diagram with PD control

6.2.2 Computed-Torque Control (CTC) Development

The CTC method assumes that the planned trajectory $\theta_d(t)$ is sufficiently smooth so that it has at least two derivatives. It is an approach that makes direct use of the complete dynamic model of a system to cancel not only the effects of gravity, but also Coriolis force, centrifugal force, friction and the manipulator inertia tensor. From equation (6-1), the system acceleration can be written as:

$$\ddot{\theta} = J^{-1}[MgR_p - T_f(\dot{\theta}) - C_d\dot{\theta}] \qquad \textbf{(6-5)}$$

Defining the control input function $\tau(t)$ as:

$$\tau(t) = \ddot{e} = \ddot{\theta}_d - J^{-1}[MgR_p - T_f(\dot{\theta}) - C_d\dot{\theta}] \qquad \textbf{(6-6)}$$

the frictional torque T_f is obtained as

$$T_f(\dot{\theta}) = MgR_p - J(\ddot{\theta}_d - \tau) - C_d\dot{\theta} \qquad \textbf{(6-7)}$$

Equation (6-7) represents the *computed-torque control* (CTC) law. Substituting equation (5-11) in (6-7), the control law u(t) is obtained as:

$$u(t) = \frac{A_{lever} \cdot R_a \cdot r_c [MgR_p - J(\ddot{\theta}_d - \tau) - C_d \dot{\theta}]}{\mu(\dot{\theta}) \cdot r_i \cdot K_t \cdot A} \qquad \textbf{(6-8)}$$

The control input function $\tau(t)$ is chosen as:

$$\tau(t) = -K\left[K_p e(t) + K_d \frac{d}{dt} e(t)\right] \qquad \textbf{(6-9)}$$

where, the error differentiate was estimated using the Kalman filter given in equation (6-4). Substituting equation (6-9) into equation (6-8), the CTC law becomes:

$$u(t) = \frac{A_{lever} \cdot R_a \cdot r_c [MgR_p - J(\ddot{\theta}_d + K \cdot K_p e + K \cdot K_d \dot{e}) - C_d \dot{\theta}]}{\mu(\dot{\theta}) \cdot r_i \cdot K_t \cdot A} \qquad \textbf{(6-10)}$$

The controller gains, K, K_p and K_d, are optimised through trial and error and their values are set to K = 90, K_p = 100 and K_d = 0.7. The block diagram of the proposed clutch system with a CTC law is illustrated in Figure 6-3.

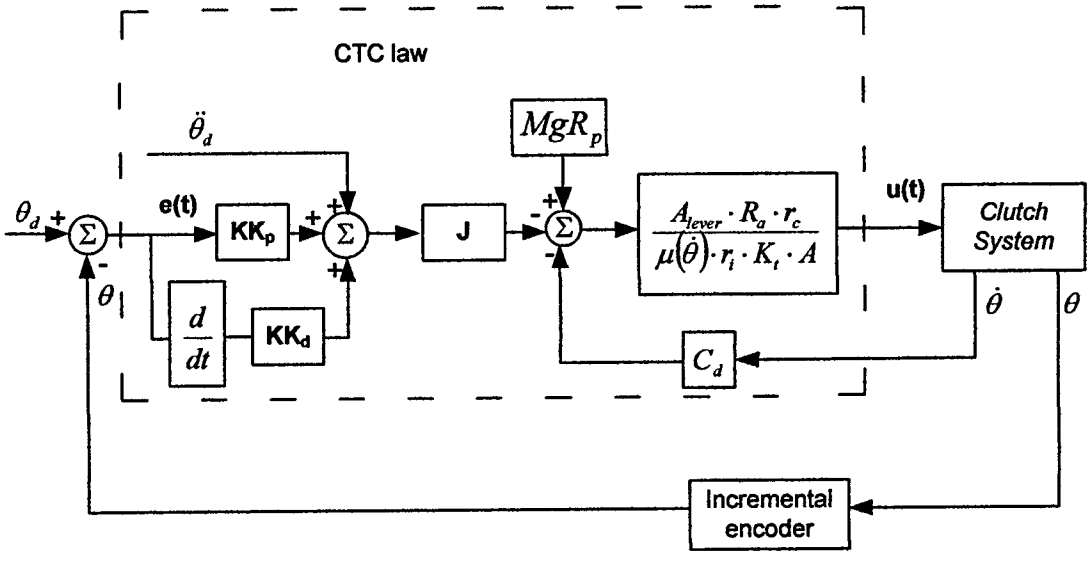

Figure 6-3. System control diagram with CTC

Please note that no sensor is used to measure the actuator-transmission behaviour so that this measurement can be used to make the system behave closer to an ideal torques source, as shown in section 4.5.2. Instead, an estimation of the parameters shown in equation (6-7) is adopted. This method is most certainly not as good as that, when a torque/force sensor would be employed. Thus, the adopted method is very sensitive to errors, in particular the errors due to modelling of friction. However, because not much information is known regarding compensation of friction of the proposed friction clutch, the adopted method was used in this research to understand more the requirements of an effective compensation technique for this particular mechanism. Even though was known that this method requires accurate estimation of the system parameters, it was not known how accurate the parameters needed to be estimated, in order to diminish the stick-slip effect. The simulation and experimental results, shown in the next section, contribute to a better understanding of the system friction and opens a new area in which this research can be taken in future.

6.2.3 Sliding-Mode Control (SMC) Development

A more robust method used for diminishing the stick-slip within a mechanism with dry friction is the sliding-mode control (SMC). To apply sliding-mode control, one does not have to know the exact system parameters, instead only bounds on these parameters. Supposing that the planned trajectory $\theta_d(t)$ is sufficiently smooth so that it has at least one derivative, a state vector is defined as $\chi=[e, w]^T$, where $e = \theta_d - \theta$ and $w = \dot{e}$. From equation (6-1), the closed-loop equation of motion of the novel clutch system in terms of e and w is

$$\begin{cases} \dot{e} = w \\ \dot{w} = \ddot{e} = \ddot{\theta}_d - J^{-1}[MgR_p - \mu(\dot{\theta}) \cdot K_{COF} v_a(t) - C_d \dot{\theta}] \\ \tau = f(e, w) \end{cases} \quad \textbf{(6-11)}$$

The objective is to find a sliding-mode control law $\tau = f(\chi)$ such that the solution of the closed-loop system satisfies $\chi(t) \to 0$ as $t \to \infty$. Sliding–mode control considers the linear constraint

$$\sigma(\chi) = f \cdot e + w = 0 \qquad \textbf{(6-12)}$$

called the *sliding surface*. The parameter f is a positive defined constant called the sliding-mode gain. The sliding-mode gain, f, determines the speed of convergence of the tracking error, e, to zero during the sliding mode regime defined by $\sigma(\chi)$. Thus, when the system is in the sliding mode, the tracking error is independent of the system parameters. The solution depends only on the sliding-mode gain. This property of the sliding-mode control make it ideal for controlling plants that operate in presence of unmodeled dynamics, parametric uncertainties, external disturbances and noise. The sliding surface design is shown in Figure 6-4.

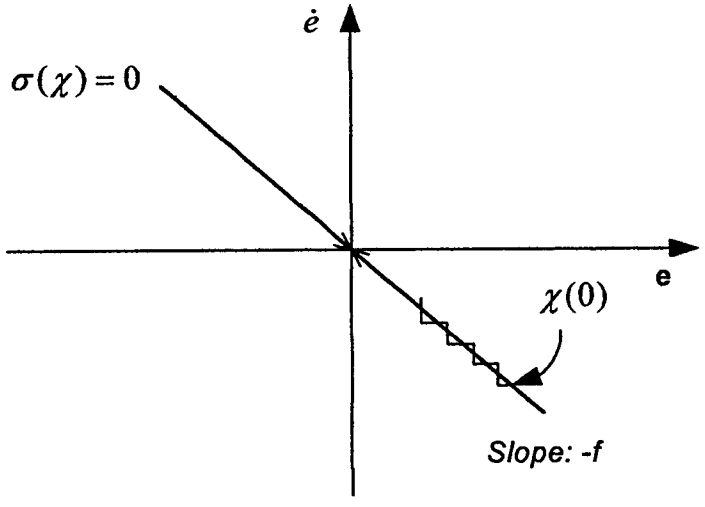

Figure 6-4. Sliding surface design

To develop a control law $\tau = f(\chi)$ which will ensure that the system operates in the sliding mode, the following Lyapunov-type function is considered [174]

$$V_L(\chi) = \frac{\sigma^T(\chi) \cdot \sigma(\chi)}{2} \qquad \textbf{(6-13)}$$

This is a Lyapunov-type function in the sense that $V_L(\chi)$ is continuously differentiable, $V_L(\chi) \geq 0$, and $V_L(\chi) = 0 \rightarrow$ *if and only if* $\rightarrow \sigma(\chi) = 0$. Robust stability and good performance is guaranteed if all trajectories are guaranteed to converge to the sliding surface given in equation (6-12): $\sigma(\chi) = f \cdot e + w = 0$. To show that the solution of the closed-loop system approaches the switching surface, it is sufficient to show that, along solutions of equation (6-11) $\dot{V}_L(\chi(t)) \leq 0$, and $\dot{V}_L(\chi(t)) \equiv 0$ implies $\sigma(\chi(t)) \equiv 0$, where $\dot{V}_L(\chi) = \sigma^T(\chi) \cdot \dot{\sigma}(\chi)$. This condition guarantees that the solution approaches the switching surface in the limit as $t \rightarrow \infty$. To ensure that the solution of the closed-loop system hits the switching surface in a finite time, a somewhat stronger condition needs to be defined. Thus, if there exist a $\gamma > 0$ such that $\sigma^T(\chi) \cdot \dot{\sigma}(\chi) \leq -\gamma \| \sigma(\chi) \|$ along with solution of equation (6-11), than $\chi(t)$ will hit the switching surface at time t_{switch}, where

$$t_{switch} \leq \frac{\| \sigma(\chi(0)) \|}{\gamma} \qquad \textbf{(6-14)}$$

The proof is demonstrated in reference [174]. Thus, if $V_L(\chi(t))$ decreases at a rate proportional to $\| \sigma(\chi(t)) \|$, the solution of equation (6-11) will strike the switching surface within a time that is bounded from above by t_{switch}. Once $\chi(t)$ reaches the switching surface, the dynamics that brought it there will also keep it there.

Deriving the sliding surface given in equation (6-12) we obtain

$$\dot{\sigma}(\chi) = f \cdot \dot{e} + \dot{w} = f \cdot \dot{e} + \ddot{\theta}_d - \theta \qquad \textbf{(6-15)}$$

Equation (6-15) can be written more explicit as

$$\dot{\sigma}(\chi) = f \cdot \dot{e} + \ddot{\theta}_d - J^{-1} \left[MgR_p - \mu(\dot{\theta}) \cdot \frac{r_i \cdot K_t \cdot A}{A_{lever} \cdot R_a \cdot r_c} v_a(t) - C_d \dot{\theta} \right] \qquad \textbf{(6-16)}$$

Isolating the control parameter, $v_a(t)$, the equation (6-16) becomes

$$\dot{\sigma}(\chi) = \left[v_a(t) + \frac{C_d \dot{\theta}}{\mu(\dot{\theta}) K_{COF}} + \frac{J \ddot{\theta}_d}{\mu(\dot{\theta}) K_{COF}} - \frac{MgR_p}{\mu(\dot{\theta}) K_{COF}} + \frac{Jf\dot{e}}{\mu(\dot{\theta}) K_{COF}} \right] \cdot \frac{\mu(\dot{\theta}) K_{COF}}{J} \qquad \textbf{(6-17)}$$

To show that $\dot{V}_L(\chi(t)) \le 0$, and $\dot{V}_L(\chi(t)) \equiv 0$ implies $\sigma(\chi(t)) \equiv 0$, the following equation is calculated

$$\sigma(\chi)\cdot\dot{\sigma}(\chi) = \sigma(\chi)\frac{\mu(\dot{\theta})K_{COF}}{J}\left[v_a(t) + \frac{C_d\dot{\theta}}{\mu(\dot{\theta})K_{COF}} + \frac{J\ddot{\theta}_d}{\mu(\dot{\theta})K_{COF}} - \frac{MgR_p}{\mu(\dot{\theta})K_{COF}} + \frac{Jf\dot{e}}{\mu(\dot{\theta})K_{COF}}\right] \quad \textbf{(6-18)}$$

$$= |\sigma(\chi)|\frac{\mu(\dot{\theta})K_{COF}}{J}v_a(t) + |\sigma(\chi)|\left[\frac{C_d\dot{\theta}}{J} - \frac{MgR_p}{J} + \ddot{\theta}_d + f\dot{e}\right] \quad \textbf{(6-19)}$$

for $\theta = \theta_d - e$ this yields

$$= |\sigma(\chi)|\frac{\mu(\dot{\theta})K_{COF}}{J}v_a(t) + |\sigma(\chi)|\left[\frac{C_d\dot{\theta}_d}{J} - \frac{MgR_p}{J} + \ddot{\theta}_d + \frac{(Jf - C_d)\dot{e}}{J}\right] \quad \textbf{(6-20)}$$

The bounds on the system given in equation (6-1), including the rate of change of the reference trajectory are

$$0 < J_0 < J < J_1 \quad \textbf{(6-21-a)}$$

$$(MgR_p)_1 < (MgR_p) < (MgR_p)_2 \quad \textbf{(6-21-b)}$$

$$C_d < C_{d1} \quad \textbf{(6-21-c)}$$

$$\mu_{\min} \le \mu_d \le \mu_{d1} \quad \textbf{(6-21-d)}$$

$$\mu_{\min} \le \mu_s \le \mu_{s1} \quad \textbf{(6-21-e)}$$

$$|\mu(\dot{\theta})| < \mu_{s1} + \mu_{d1} \quad \textbf{(6-21-f)}$$

$$|\dot{\theta}_d| < \theta_{d1},\ |\ddot{\theta}_d| < \theta_{d2} \quad \textbf{(6-21-g)}$$

$$K_{COF1} < K_{COF} < K_{COF2} \quad \textbf{(6-21-h)}$$

Thus, the equation (6-20) can be rewritten as

$$\sigma(\chi)\cdot\dot{\sigma}(\chi) \le |\sigma(\chi)|\frac{(\mu_{s1} + \mu_{d1})K_{COF2}}{J_0}v_a(t) + \\ + |\sigma(\chi)|\left[\frac{C_{d1}\theta_{d1}}{J_0} - \frac{(MgR_p)_1}{J_0} + \theta_{d2} + \frac{(J_1 f - C_{d1})\dot{e}}{J_0}\right] \quad \textbf{(6-22)}$$

Selecting the SMC law as,

$$v_a(t) = u(t) = -\{K_p sign[\sigma(\chi)] + K_d sign[\sigma(\chi)\dot{e}]\dot{e}\} \tag{6-23}$$

Equation (6-22) becomes

$$\sigma(\chi)\cdot\dot{\sigma}(\chi) \le \left[-K_p|\sigma(\chi)| - K_d[\sigma(\chi)\dot{e}]\right]\frac{(\mu_{s1}+\mu_{d1})K_{COF2}}{J_0} + \\ + |\sigma(\chi)|\left[\frac{C_{d1}\theta_{d1}}{J_0} - \frac{(MgR_p)_1}{J_0} + \theta_{d2} + \frac{(J_1 f - C_{d1})\dot{e}}{J_0}\right] \tag{6-24}$$

Hence,

$$\sigma(\chi)\cdot\dot{\sigma}(\chi) \le |\sigma(\chi)|\left[-K_p\frac{(\mu_{s1}+\mu_{d1})K_{COF2}}{J_0} + \frac{C_{d1}\theta_{d1}}{J_0} - \frac{(MgR_p)_1}{J_0} + \theta_{d2}\right] + \\ + |\sigma(\chi)\dot{e}|\left[-K_d\frac{(\mu_{s1}+\mu_{d1})K_{COF2}}{J_0} + \frac{(J_1 f - C_{d1})}{J_0}\right] \tag{6-25}$$

From equation (6-25) it can be seen that $\sigma(\chi)\cdot\dot{\sigma}(\chi)$ can be made negative if the controller gains K_p and K_d are sufficiently large, that is, if

$$K_p > \frac{J_0\theta_{d2} + C_{d1}\theta_{d1} - (MgR_p)_1}{(\mu_{s1}+\mu_{d1})\cdot K_{COF2}} \tag{6-26}$$

$$K_d > \frac{J_1 f - C_{d1}}{(\mu_{s1}+\mu_{d1})\cdot K_{COF2}} \tag{6-27}$$

The constant γ is obtained from $\sigma(\chi)\cdot\dot{\sigma}(\chi) \le -\gamma\,|\,\sigma(\chi)\,|$ as

$$\gamma = \frac{K_p(\mu_{s1}+\mu_{d1})\cdot K_{COF2} - J_0\theta_{d2} + C_{d1}\theta_{d1} - (MgR_p)_1}{J_0} \tag{6-28}$$

The resulting controller is given as follows

$$\begin{cases} \sigma(\chi) = f \cdot e + \dot{e} \\ K_p > \dfrac{J_0\theta_{d2} + C_{d1}\theta_{d1} - (MgR_p)_1}{(\mu_{s1} + \mu_{d1}) \cdot K_{COF2}} \\ K_d > \dfrac{J_1 f - C_{d1}}{(\mu_{s1} + \mu_{d1}) \cdot K_{COF2}} \\ v_a(t) = u(t) = -\{K_p sign[\sigma(\chi)] + K_d sign[\sigma(\chi)\dot{e}]\dot{e}\} \end{cases} \quad \textbf{(6-29)}$$

This controller can cause excessive high frequency oscillations due to the discontinuous characteristics of the control input. To reduce this oscillation, the function signum in equation (6-29) is replaced by the saturation function [172]

$$sat\left(\frac{\sigma}{\varepsilon}\right) = \begin{cases} sign\left(\dfrac{\sigma}{\varepsilon}\right), & if \quad |\sigma| > \varepsilon \\ \dfrac{\sigma}{\varepsilon}, & if \quad |\sigma| < \varepsilon \end{cases} \quad \textbf{(6-30)}$$

where ε is a positive term that defines the thickness of the boundary layer as shown in Figure 6-5.

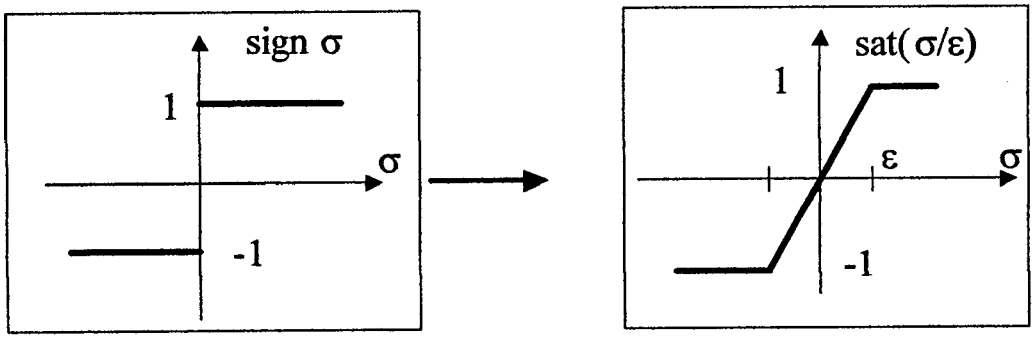

Figure 6-5. Saturation function

Thus, equation (6-29) can be written as

$$\begin{cases} \sigma(\chi) = f \cdot e + \dot{e} \\ K_p > \dfrac{J_0\theta_{d2} + C_{d1}\theta_{d1} - (MgR_p)_1}{(\mu_{s1} + \mu_{d1}) \cdot K_{COF2}} \\ K_d > \dfrac{J_1 f - C_{d1}}{(\mu_{s1} + \mu_{d1}) \cdot K_{COF2}} \\ v_a(t) = u(t) = -\left\{ K_p sat\left[\dfrac{\sigma(\chi)}{\varepsilon}\right] + K_d sat\left[\dfrac{\sigma(\chi)\dot{e}}{\varepsilon}\right]\dot{e} \right\} \end{cases} \quad \textbf{(6-31)}$$

The SMC block diagram illustration of the above equation is shown in Figure 6-6, and the controller gains chosen for all three controllers are tabulated in Table 6-1.

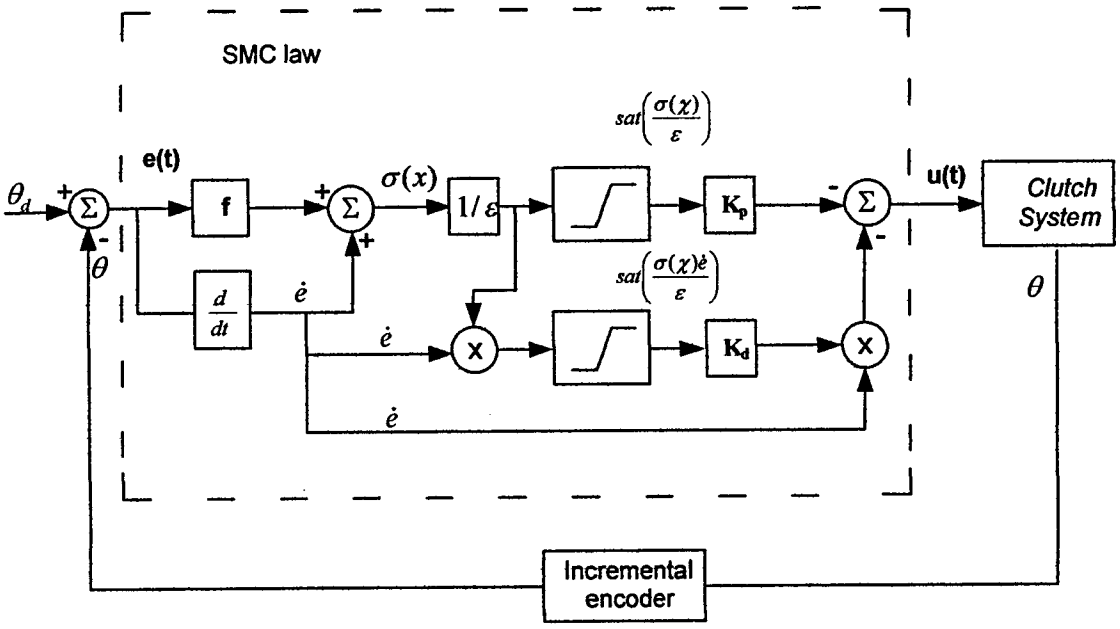

Figure 6-6. SMC Block diagram

Table 6-1. Controller design parameters

	Controller parameters				
Controller	K_p	K_d	K	f	ε
PD Controller	5000	50	-	-	-
CTC	100	0.7	90	-	-
SMC	3	400	1	70	0.1

6.3 Results and Discussions

The above developed controllers are investigated and evaluated in this section. The desired position was simulated as a first order polynomial with different position rates. The aim of the investigation is to control the motion of the clutch shaft smoothly and accurately, for a position rate between 6-100deg/s. Moreover, this investigation intends to validate the friction model chosen, as well as the mathematical model derived to assist in designing friction compensators. In addition, the study aims at finding the performance of the proposed controllers, especially with respect to compensating for stick-slip friction. Simulation and experiments were performed for both constant and variable driving torque. The experiments were performed using the computational workstation for real-time control described in Appendix G. The constant driving torque is provided by gravity acting on a mass using a pulley; and the variable driving torque is produced by changing the weight on the pulley while controlling the shaft position, so that a step change in driving torque is produced during the motion. Simulations were performed using the Matlab/Simulink package. A sampling rate of 1ms is chosen, and the solver used is based on explicit Runge-Kutta formula (4,5), the Dormand-Prince pair.

6.3.1 PD controller

6.3.1.1 Simulation results with constant driving torque

In Figure 6-7 is shown the simulation results of the experimental test-bed, where the desired path gradient (i.e. position rate) is set to 100deg/s (Figures 6-7a and 6-7b), 20deg/s (Figures 6-7c and 6-7d) and 2deg/s (Figures 6-7e and 6-7f). The desired and actual positions are displayed in Figures 6-7a, 6-7c, 6-7e, and the positional errors for each position rate are displayed in Figures 6-7b, 6-7d, and 6-7f. The driving torque is set to 0.047Nm.

From Figures 6-7a, 6-7b, 6-7c, and 6-7d it can be seen that for a position rate greater than 20deg/s the position is smoothly controlled, without any discontinuities, thus without significant stick-slip. It was also observed that independent of the position rate, the position error is very similar for velocities greater than 20deg/s, as shown in Figures 6-7b and 6-7d. A positional error of under 0.13deg is demonstrated, which is well within the requirements mentioned in section 6.2. As the position rate decreases below 20deg/s, the PD controller can no longer contribute to cancelling the stick-slip phenomenon and the effect is very noticeable. This is illustrated in Figure 6-7e for a position rate of 2deg/s.

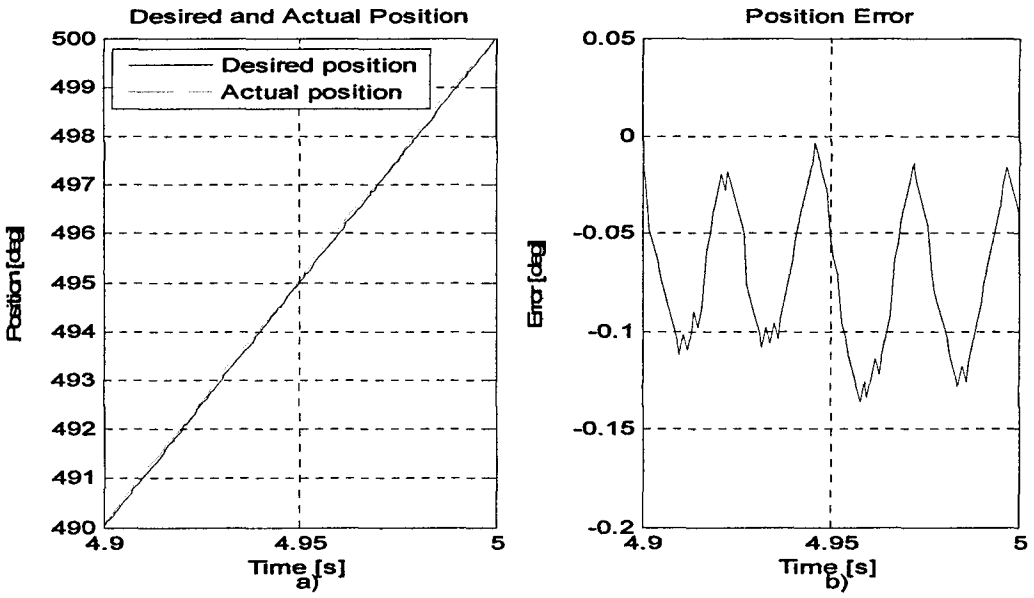

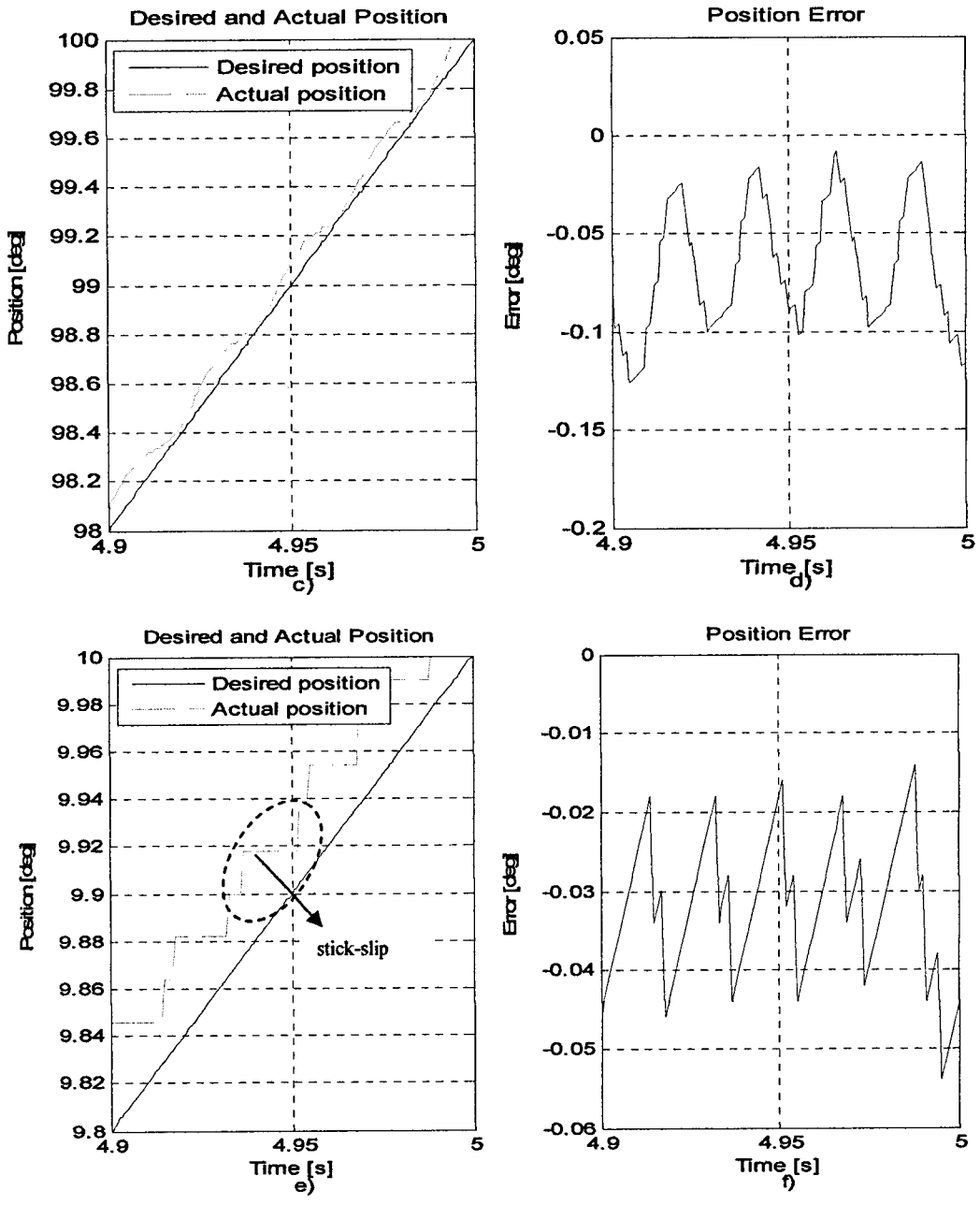

Figure 6-7. PD Simulation results: Straight line with constant driving torque [(a) and (b) for $\dot{\theta}_d = 100$ deg/s; (c) and (d) for $\dot{\theta}_d = 20$ deg/s); (e) and (f) for $\dot{\theta}_d = 2$ deg/s)]

6.3.1.2 Experimental results with constant driving torque

Figure 6-8 shows the experimental results for the same desired paths as presented for the simulation analysis. Thus, the desired and actual position and the position error for a desired path with a gradient of 100deg/s are illustrated in Figures 6-8a and 6-8b; for a gradient of 20deg/s in Figures 6-8c and 6-8d; and for a gradient of 2deg/s the desired and actual position and the position error are illustrated in Figures 6-8e and 6-8f.

It can be seen that the experimental results are very similar to the results obtained from the simulation analysis. Thus, the conclusions extracted from the simulation results also apply for the experiments. It can be seen that for a position rate greater than 20deg/s the position is smoothly controlled, without any discontinuities, thus without stick-slip. Also, it was observed that independent of the position rate, the position error is very similar for velocities greater than 20deg/s, as shown in Figures 6-8b and 6-8d. A positional error of under 0.15deg is demonstrated, which is within the requirements mentioned in section 6.2. As the position rate decrease below 20deg/s, the PD controller can no longer contribute to cancelling the stick-slip phenomenon and the effect is highly noticeable. This is illustrated in Figure 6-8e for a position rate of 2deg/s.

Comparing the simulation and experimental analysis it can be seen that both the stick-slip effect and the positional error were captured precisely in the simulations. These results demonstrate the validity of the friction model used as well as the validity of the mathematical model derived to assist in designing friction compensators. It can be observed from Figures 6-8b, 6-8d, and 6-8f that the position error is similar to the error obtained from the simulations shown in Figures 6-7b, 6-7d, and 6-7f. To illustrate better the similarities between the errors obtained from simulations and experiments, a root mean square (rms) is obtained. The rms is calculated using the equation (6-32), and the results are tabulated in Table 6-2.

$$rms(x) = \sqrt{\frac{\sum_{i=1}^{n} x_i^{\,2}}{n}} \qquad \textbf{(6-32)}$$

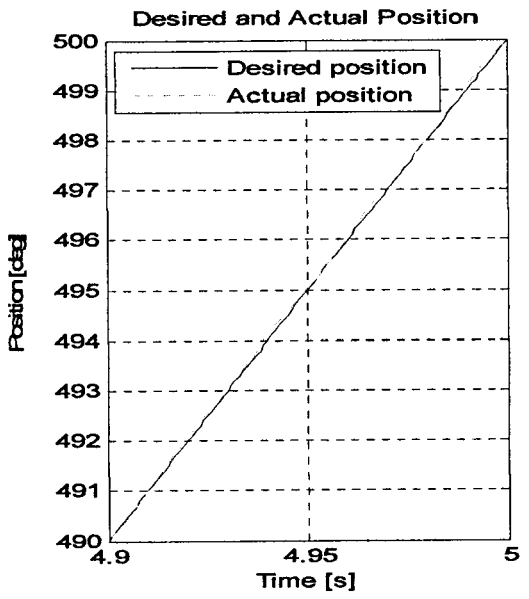
Desired and Actual Position
Desired position
Actual position
Position [deg]
Time [s]
500
499
498
497
496
495
494
493
492
491
490
4.9
4.95
5

a)

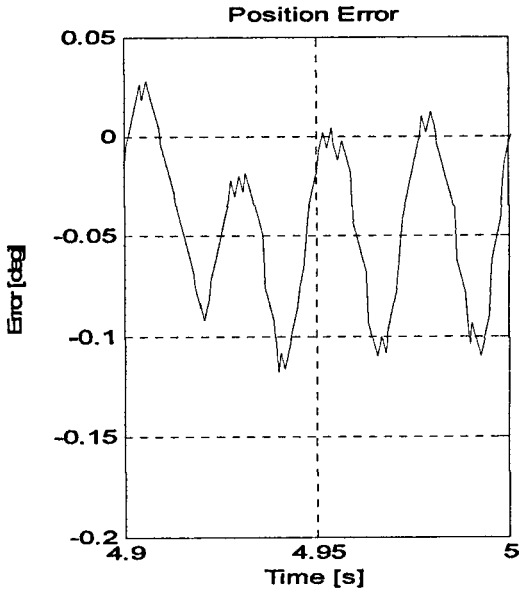
Position Error
Error [deg]
Time [s]
0.05
0
-0.05
-0.1
-0.15
-0.2
4.9
4.95
5

b)

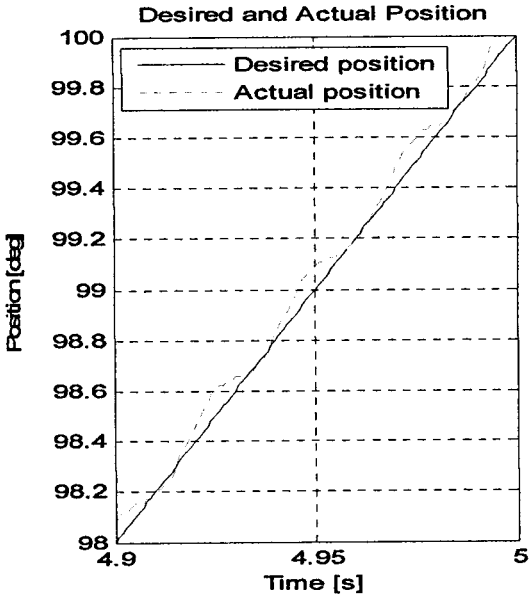
Desired and Actual Position
Desired position
Actual position
Position [deg]
Time [s]
100
99.8
99.6
99.4
99.2
99
98.8
98.6
98.4
98.2
98
4.9
4.95
5

c)

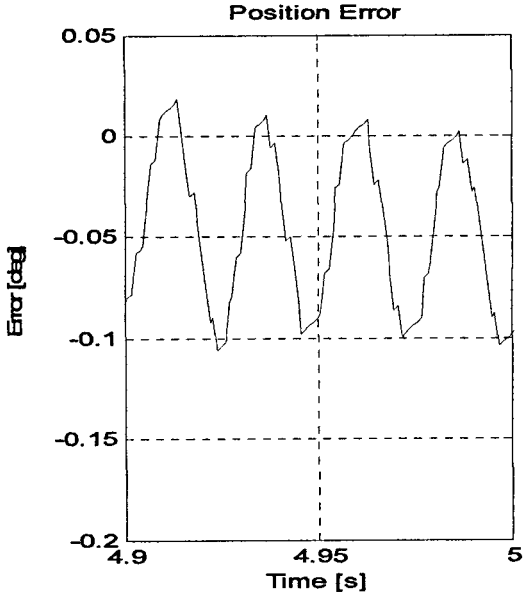
Position Error
Error [deg]
Time [s]
0.05
0
-0.05
-0.1
-0.15
-0.2
4.9
4.95
5

d)

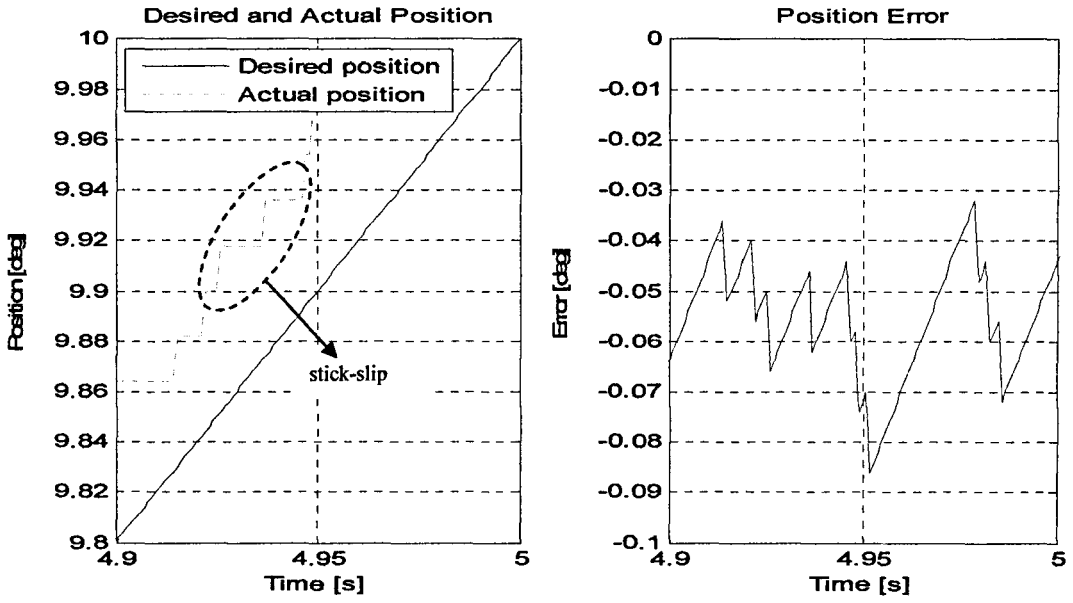

e) f)

Figure 6-8. PD Experimental results: Straight-line paths with constant driving torque [(a) and (b) for $\dot{\theta}_d = 100$ deg/s; (c) and (d) for $\dot{\theta}_d = 20$ deg/s; (e) and (f) for $\dot{\theta}_d = 2$ deg/s]

6.3.1.3 Simulation results with variable driving torque

For similar desired paths and controller gains as described for the analysis with constant torque, the next analysis is performed with a variable driving torque. The desired and actual position, and the position error for a desired path with a gradient of 100deg/s are shown in Figures 6-10a and 6-10b, and for a desired path with a gradient of 20deg/s are shown in Figures 6-10c and 6-10d. The driving torque is steeply changed from 0.047 Nm to 0.071 Nm as shown in Figure 6-9.

Note that because of the small difference between the desired and actual positions in Figures 6-10a and 6-10c, the lines can hardly be distinguished. However, from the position error, shown in Figures 6-10b and 6-10d, the influence of the step change in the driving torque can be observed. This outcome is due to the controller's ability to reject

external disturbances such as the externally produced driving torque. Nonetheless, the effect of the external disturbance is minimal, which demonstrate the relatively high robustness of the controller.

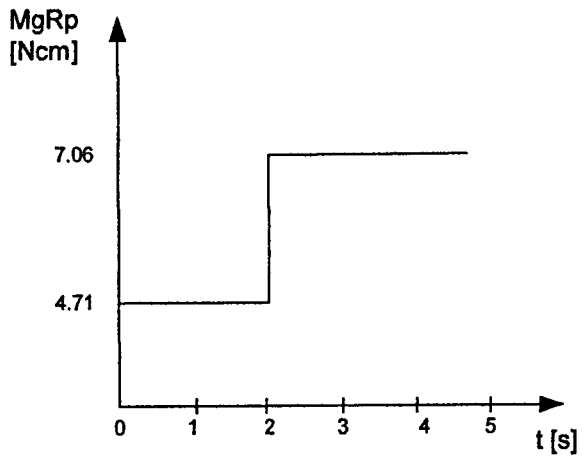

Figure 6-9. Driving torque profile

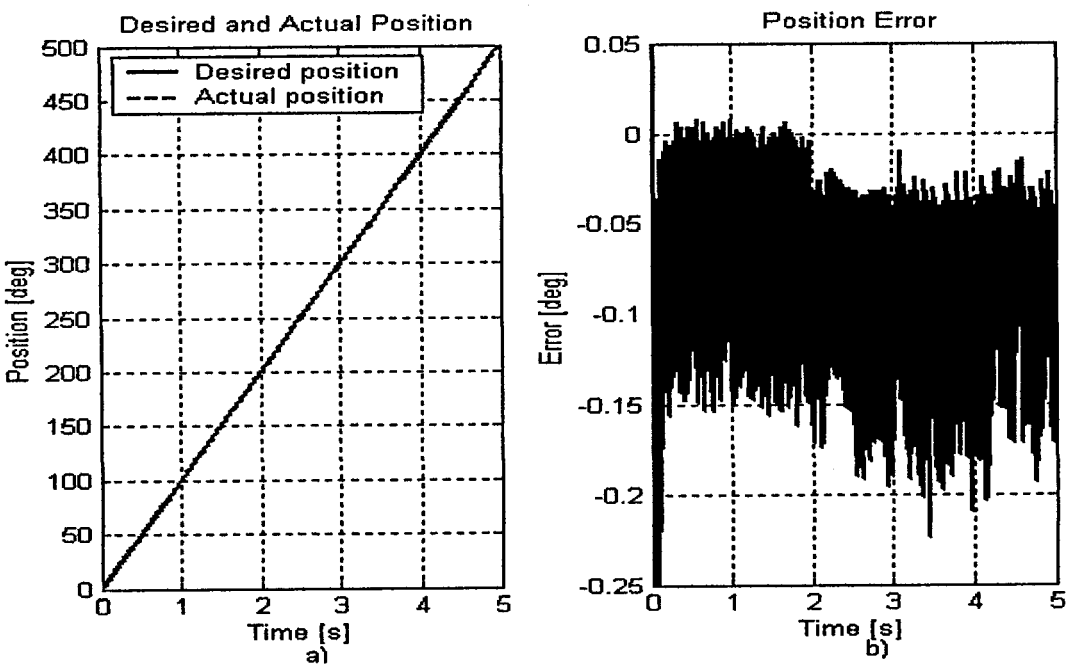

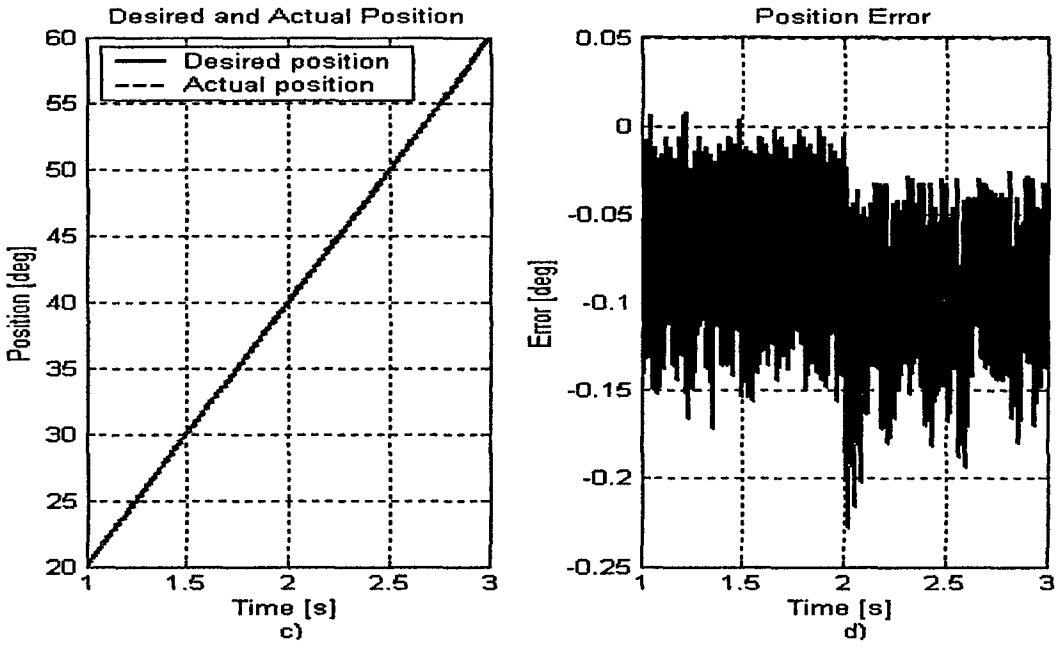

Figure 6-10. PD Simulation results: Straight line with variable driving torque [(a) and (b) for $\dot{\theta}_d$ = 100 deg/s; (c) and (d) for $\dot{\theta}_d$ = 20 deg/s]

6.3.1.4 Experimental results with variable driving torque

Figure 6-12 shows the experimental results for same trajectories, while the driving torque is sharply changed from 0.0471 Nm to 0.071 Nm as seen in Figure 6-11a for a desired path of 100deg/s slope and 6-11b for a desired path of 20deg/s slope. The desired and actual positions, and the position error for a desired path of 100deg/s slope are shown in Figures 6-12a and 6-12b, and for a desired path of 20deg/s slope are shown in Figures 6-12c and 6-12d. Note that in Figures 6-12a and 6-12c the desired and actual position can hardly be distinguished. This is due to the scale at which the positions are plotted and also because of the small errors shown in more detail in Figure 6-12b and 6-12d.

Again, the conclusions extracted from the simulation results apply for the experiments. The influence of sharply change in driving torque and the positional error were captured

precisely in the simulations. These results demonstrate yet again the validity of the friction model used as well as the validity of the mathematical model derived to assist in designing friction compensators. It can be observed that the position error is similar to the error obtained from the simulations shown in Figure 6-10. The root mean square (rms) of the error obtained from experiment and simulation are shown in Table 6-2.

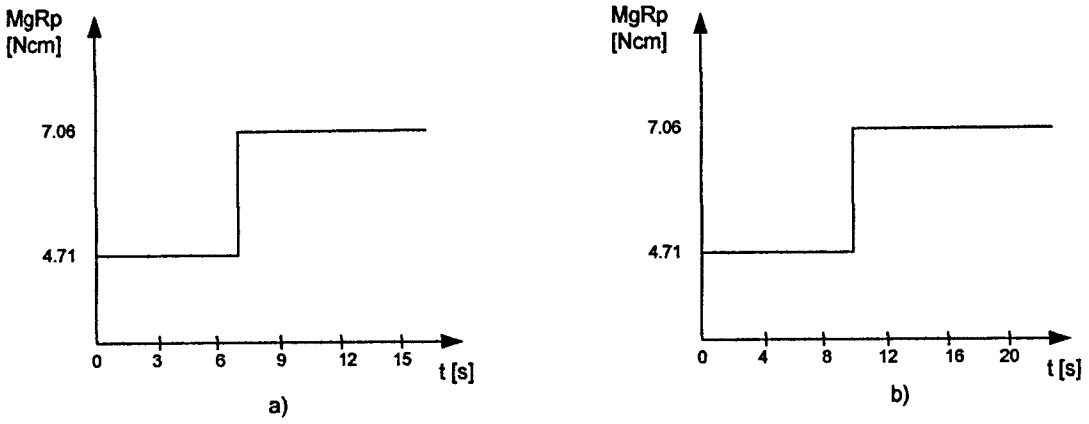

Figure 6-11. Driving torque profile:
a) for $\dot{\theta}_d$ = 100deg/s, b) for $\dot{\theta}_d$ = 20deg/s

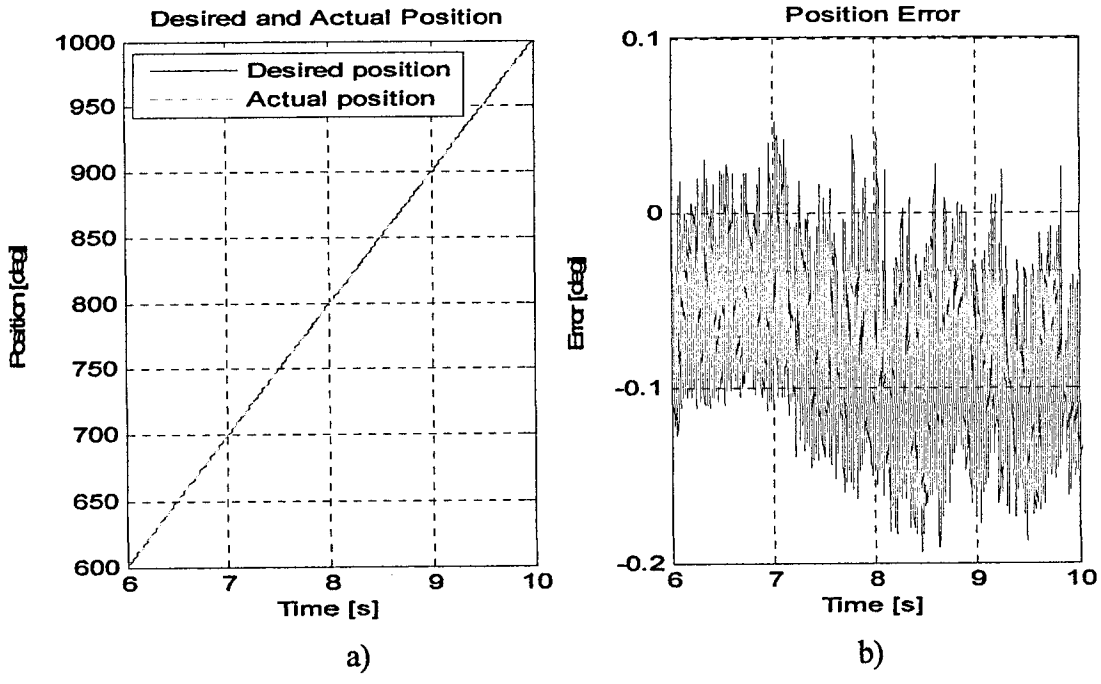

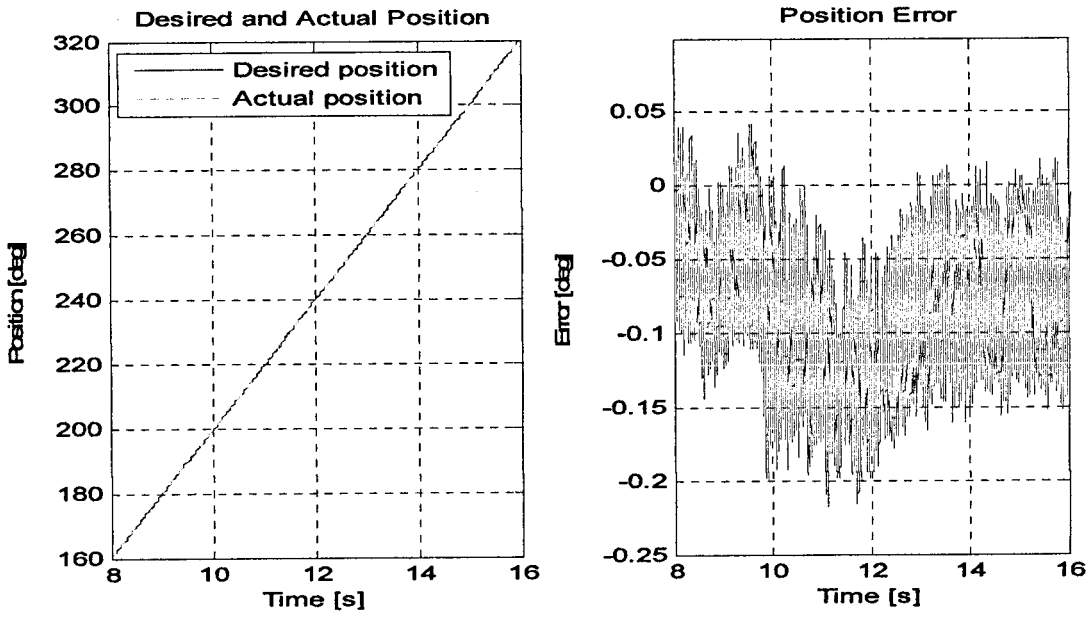

c) d)

Figure 6-12. PD Experimental results: Straight-line path with variable driving torque [(a) and (b) for $\dot{\theta}_d$ = 100 deg/s; (c) and (d) for $\dot{\theta}_d$ = 20 deg/s]

It can be seen that the simulation results are very similar to the results obtained from the experimental analysis. Thus, the conclusions extracted from the simulation results also apply for the experiments. Both the stick-slip effect and the positional error were captured precisely in the simulations for both constant and variable driving torque. These results demonstrate the validity of the friction model used as well as the validity of the mathematical model derived to assist in designing friction compensators. Furthermore, it was shown that using a high gain PD controller the stick-slip was successfully compensated for velocities higher than 20deg/s. Moreover, the PD controller proved to regulate the position accurate enough for the operating environment. The PD controller also proved quite robust against the sharply change in driving torque.

To illustrate better the similarities between the errors obtained from simulations and experiments a root mean square (rms) is obtained for a position rate of 100deg/s and 20deg/s (i.e. the velocity for which the stick-slip was successfully compensated for) and the results are tabulated in Table 6-2. From the Table 6-2 it can be seen that the simulation results show a slightly higher position error compared with the experimental

results. This is encouraging information as further developments on the proposed actively restrained passive mechatronic system can be done in simulations, without building another prototype.

Table 6-2. Error rms – PD controller

	Error rms	
$\dot{\theta}_d$ = 100 deg/s	Const. driving torque	Variable driving torque
Experiment	0.0626	0.089
Simulation	0.088	0.1096
$\dot{\theta}_d$ = 20 deg/s		
Experiment	0.0636	0.0909
Simulation	0.0912	0.1041

6.3.2 CTC controller

The CTC controller was developed in section 6.2. In the above section it was shown that a PD controller can successfully compensate for stick-slip for a velocity greater than 20deg/s. However, it is required to control the system's motion for velocities much below 20deg/s, thus a better controller is required to diminish the stick-slip for a velocity between 6deg/s and 20deg/s. The CTC law derived in equation (6-10) was implemented in both simulations and on the experimental test-bed.

6.3.2.1 Simulation results with constant driving torque

The simulation analysis for a constant torque set to 0.047Nm is shown in Figure 6-13. Figures 6-13a and 6-13b show the desired and actual positions and the position error for a desired path of 20deg/s slope. Note that in Figure 6-13 the discontinuity that can be

observed is the encoder resolution of 0.018deg, and not due to stick-slip. Thus, the CTC method is shown to be able to successfully compensate for stick-slip, keeping the error at the limit of the encoder resolution. This observation is also true for any velocity below 20deg/s. Figures 6-13c and 6-13d shows the desired and actual positions and the position error for a desired path of 2deg/s slope. It can be observed that the stick-slip effect is successfully compensated for even for a desired path of 2deg/s slope.

From Figure 6-13 it can be observed the superiority of CTC method when compared with the PD controller. Besides fully avoiding the stick-slip effect, even for a position rate of 2deg/s, the controller is capable of tracking the position at the limit of the encoder resolution. This is somehow expected as a complete knowledge of the system was considered. However, for the experimental analysis, it is anticipated to obtain different results, because of the estimations used for the system parameters such as friction-related parameters.

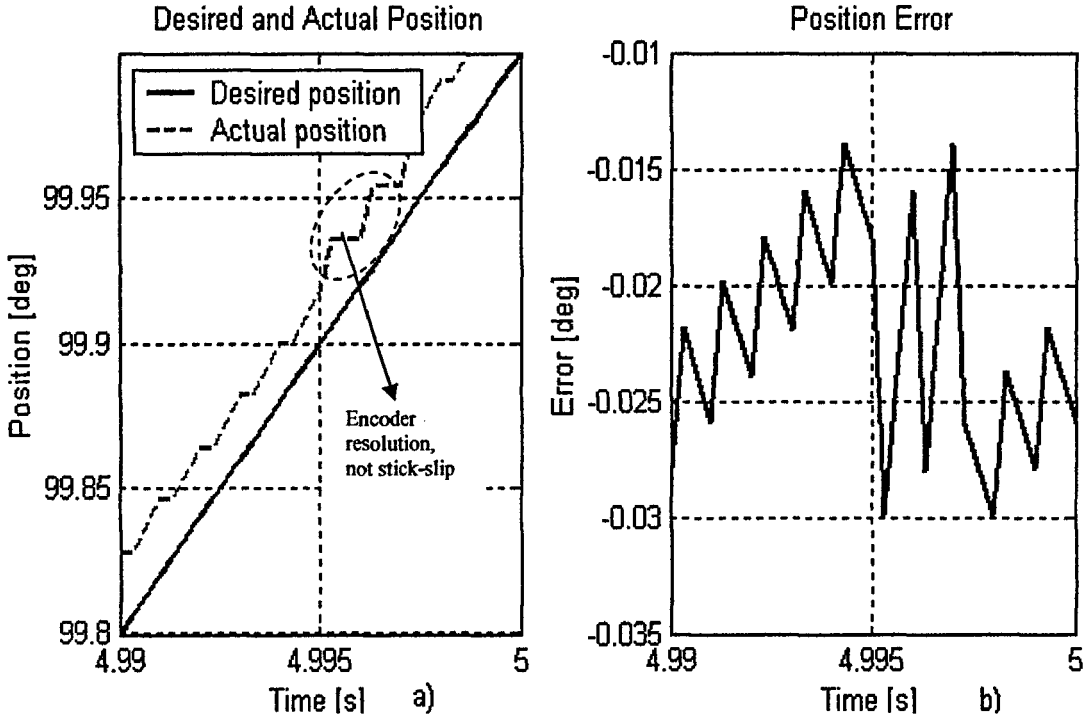

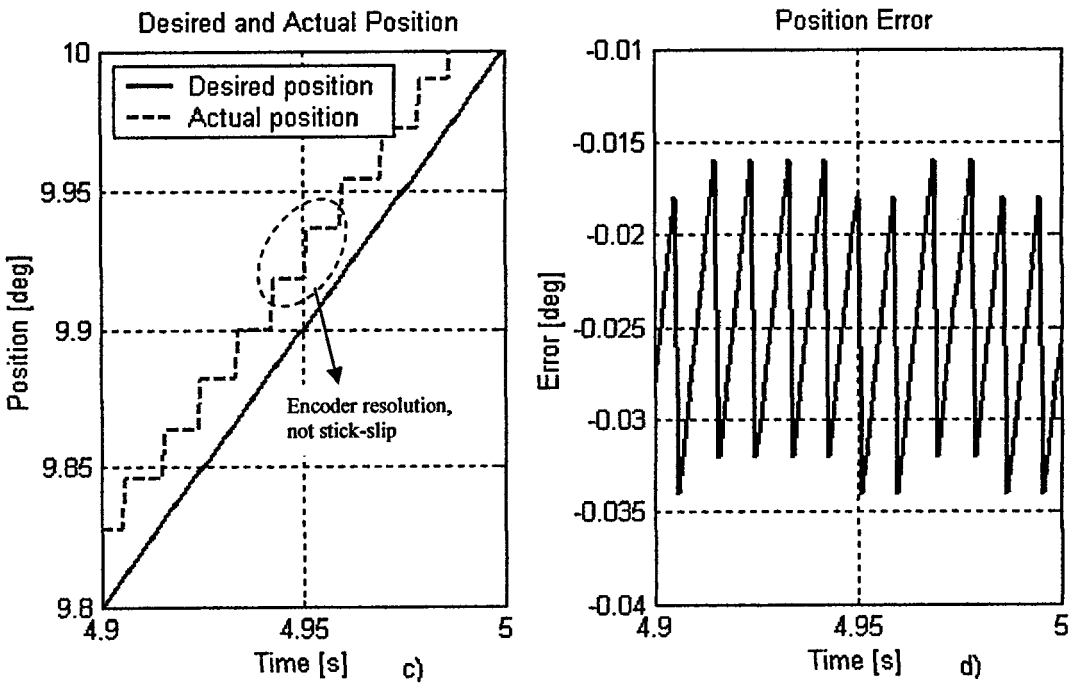

Figure 6-13. CTC Simulation results: Straight-line path with constant driving torque [(a) and (b) for $\dot{\theta}_d$=20deg/s; (c) and (d) for $\dot{\theta}_d$=2deg/s]

6.3.2.2 Experimental results with constant driving torque

The experimental results are completed for the same desired paths and controller gains as the simulations. Figures 6-14a and 6-14b show the desired and actual position, and the position error for a desired path of 20deg/s slope, and Figures 6-14c and 6-14d show the desired and actual positions and the position error for a desired path of 2deg/s slope.

It can be observed that the experiments show a completely different response compared with the simulations. The system exhibits stick-slip for any position rate less than 20deg/s and the level of accuracy is even higher than the one obtain with a PD controller. This discrepancy between the simulation and experimental analysis is because the simulations were performed assuming perfect knowledge of the system parameters (friction-related parameters in particular), whilst real friction, as it was shown in Chapter 4 and Chapter 5, is very difficult to be accurately modelled. However, if the system friction can be accurately measured or exactly estimated, as shown in the

simulation analysis, the CTC law is demonstrated to have the potential to achieve minimum error, while avoiding stick-slip for velocities as low as 2deg/s.

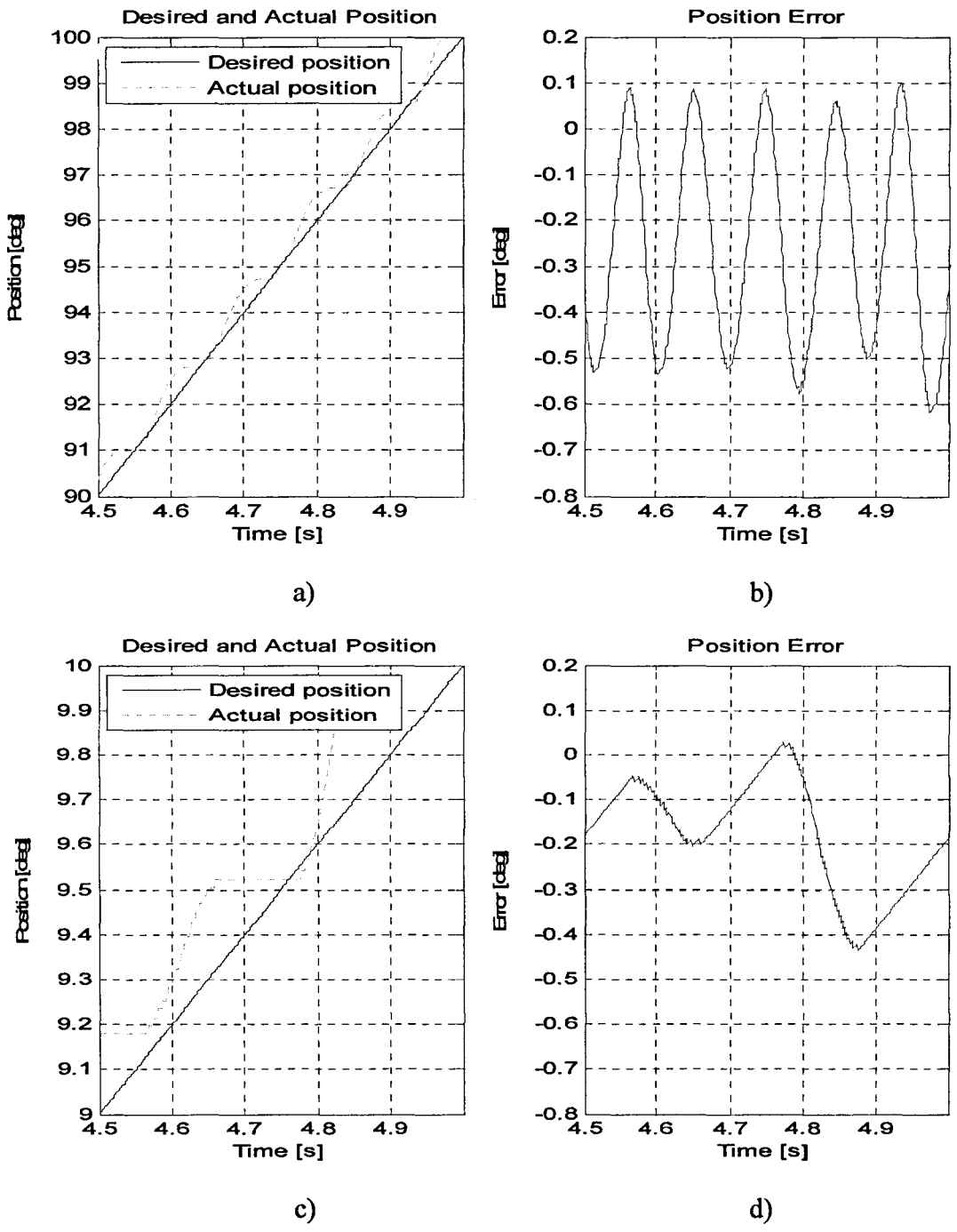

Figure 6-14. CTC Experimental results: Straight-line path with constant driving torque [(a) and (b) for $\dot{\theta}_d$=20deg/s; (c) and (d) for $\dot{\theta}_d$=2deg/s]

As the results shows a great potential for diminishing the stick-slip effect with a suitable measurement technique or an accurate estimated model, it is recommended that further research into both torque measurement and accurate estimation of highly non-linear parameters such as friction-related parameters to be undertaken.

Because friction in the proposed mechanism was demonstrated to be very difficult to model, and because of the results obtained with the CTC law for constant driving torque, the analysis of the CTC law for a variable driving torque was not performed. This means that, because the conclusions taken already from the simulation and experimental analysis with constant driving torque will most certainly not going to change, the analysis of the CTC law for a variable driving torque was considered redundant, and therefore not undertaken.

6.3.3 SMC controller

The SMC law was developed in section 6.2. The PD controller can successfully compensate for stick-slip for a velocity greater than 20deg/s. However, it is required to control the system's motion for velocities higher than 6deg/s, thus a better controller is required to diminish the stick-slip for a velocity between 6deg/s and 20deg/s. The CTC law was proved to be efficient, but only if major changes are completed. Thus, still a better controller is required to diminish the stick-slip for a velocity between 6deg/s and 20deg/s. The SMC law derived in equation (6-31) was implemented in both simulations and on the experimental test-bed with the aim of cancelling or diminishing the stick-slip effect for a velocity between 6deg/s and 20deg/s.

6.3.3.1 Simulation results with constant driving torque

Figure 6-15 shows the desired and actual position, and the position error for a straight-line path with a gradient of 20deg/s, shown in Figures 6-15a and 6-15b; a gradient of

6deg/s is shown in Figures 6-15c and 6-15d; and a gradient of 2deg/s is shown in Figures 6-15e and 6-15f. The driving torque is set to 0.047Nm.

From Figures 6-15a and 6-15c it can be seen that stick-slip is fully diminished, even though the discontinuous line that can be seen at a first glance may look like stick-slip. This discontinuity however, denotes the encoder resolution, which reads the position with an accuracy of 0.018deg. This effect is illustrated better in Figures 6-16a and 6-16b, where the desired and actual position and the position error for the 2deg/s slope, plotted in Figures 6-15e and 6-15f, are plotted on a larger figure. The difference between the stick-slip and encoder resolution can clearly be seen. From the simulation analysis with a constant driving torque, only tracking a desired position with a slope of 2deg/s shows signs of stick-slip.

It can also be observed that the position error is very similar for all the velocities shown in Figure 6-15. A positional error of just under 0.09deg is demonstrated for a desired velocity of 20deg/s and 2deg/s and a positional error of just under 0.11deg is demonstrated for a desired velocity of 6deg/s. The root mean square (rms) of the error obtained from experiments and simulations are shown in Table 6-3. Furthermore, it is observed that the amplitude of the position error is much smaller when compared with the results obtained with the PD controller. Amplitude of just 0.02deg is noticed from the results obtained with the SMC, while amplitude of about 0.1deg is obtained with the PD controller. This denotes the superior performance of the SMC due to the fact that when the system is in the sliding mode, the tracking error is independent of the system parameters, while the PD controller is dependent on the system dynamics.

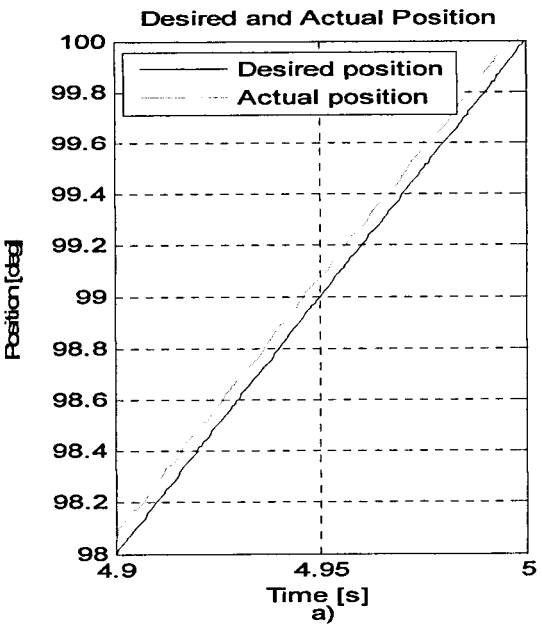
Desired and Actual Position
Desired position
Actual position
Position [deg]
100
99.8
99.6
99.4
99.2
99
98.8
98.6
98.4
98.2
98
4.9
4.95
5
Time [s]
a)

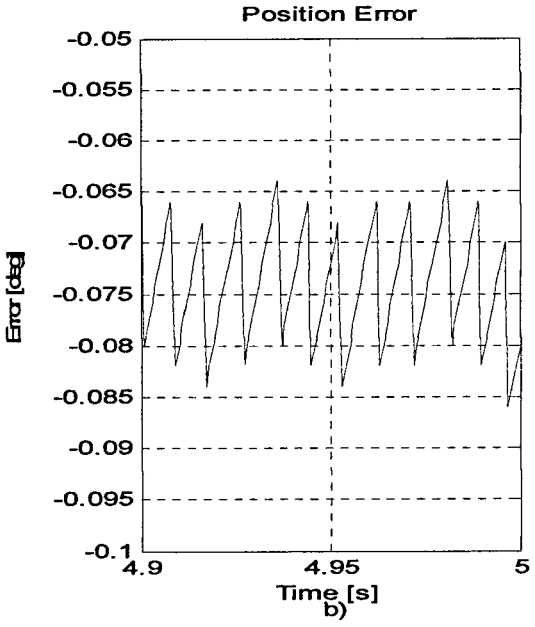
Position Error
Error [deg]
-0.05
-0.055
-0.06
-0.065
-0.07
-0.075
-0.08
-0.085
-0.09
-0.095
-0.1
4.9
4.95
5
Time [s]
b)

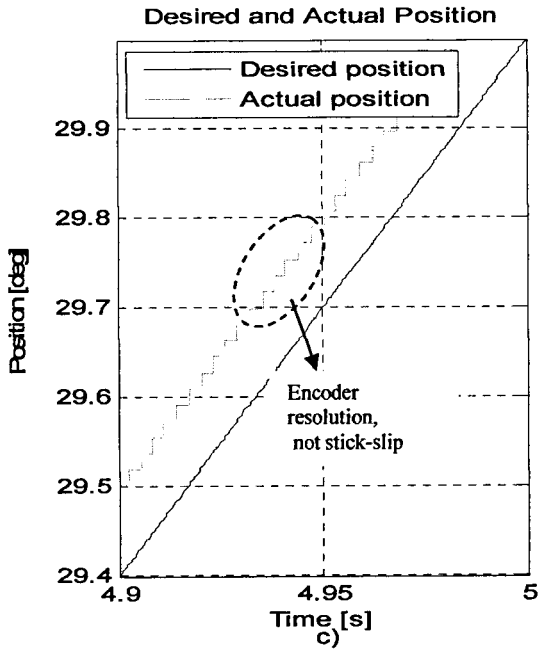
Desired and Actual Position
Desired position
Actual position
Position [deg]
29.9
29.8
29.7
29.6
29.5
29.4
Encoder
resolution,
not stick-slip
4.9
4.95
5
Time [s]
c)

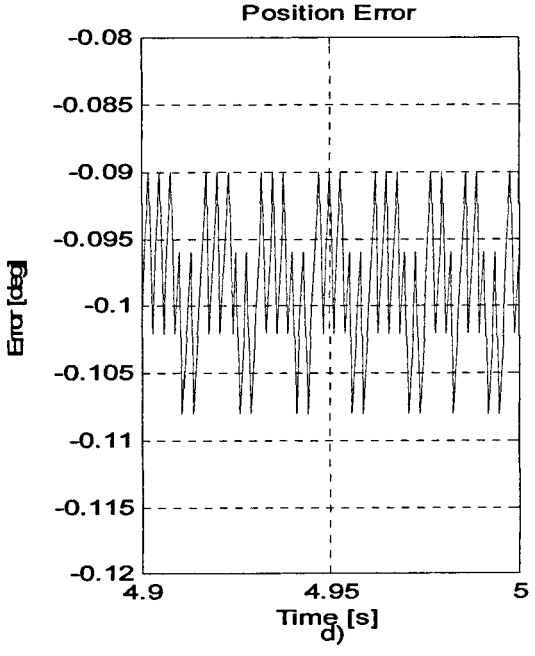
Position Error
Error [deg]
-0.08
-0.085
-0.09
-0.095
-0.1
-0.105
-0.11
-0.115
-0.12
4.9
4.95
5
Time [s]
d)

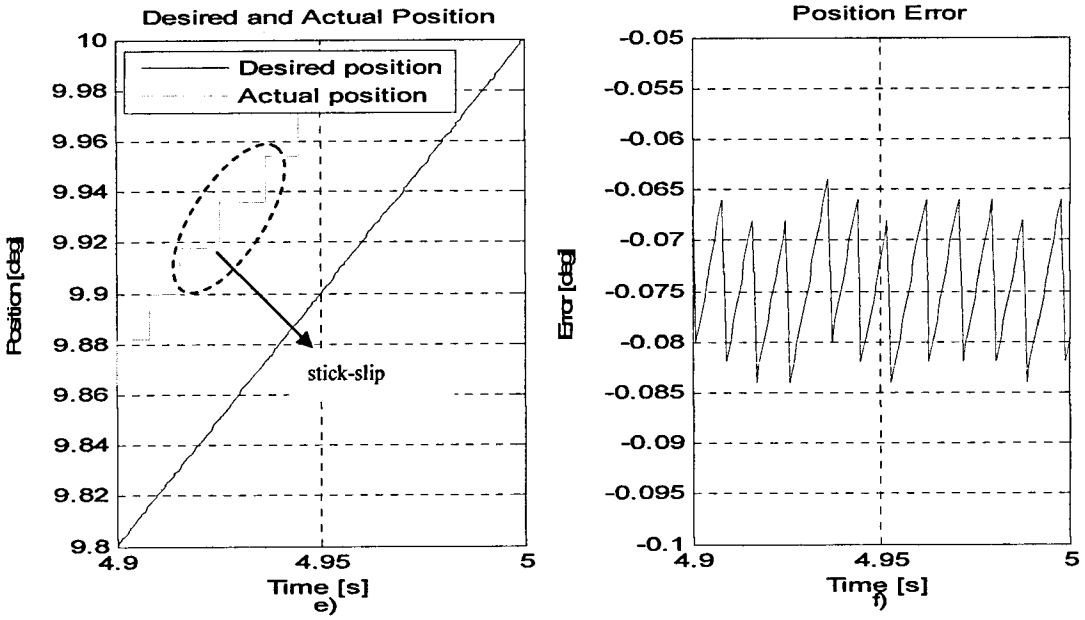

Figure 6-15. SMC Simulation results: Straight-line with constant driving torque [(a) and (b) for $\dot{\theta}_d$=20deg/s;(c) and (d) for $\dot{\theta}_d$=6deg/s; (e) and (f) for $\dot{\theta}_d$=2deg/s]

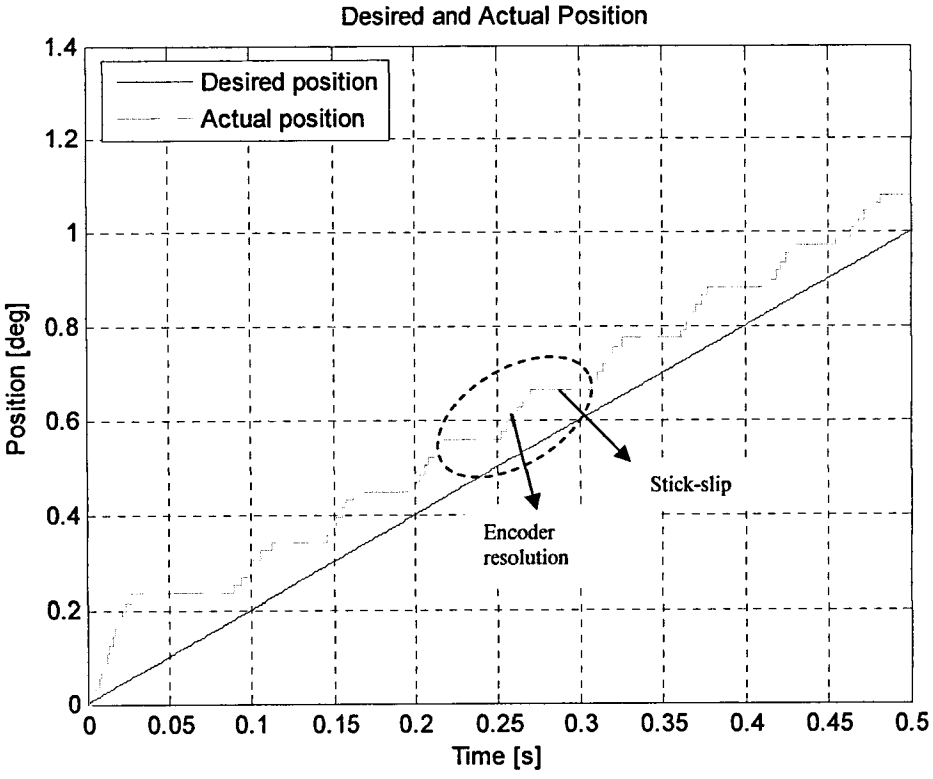

a)

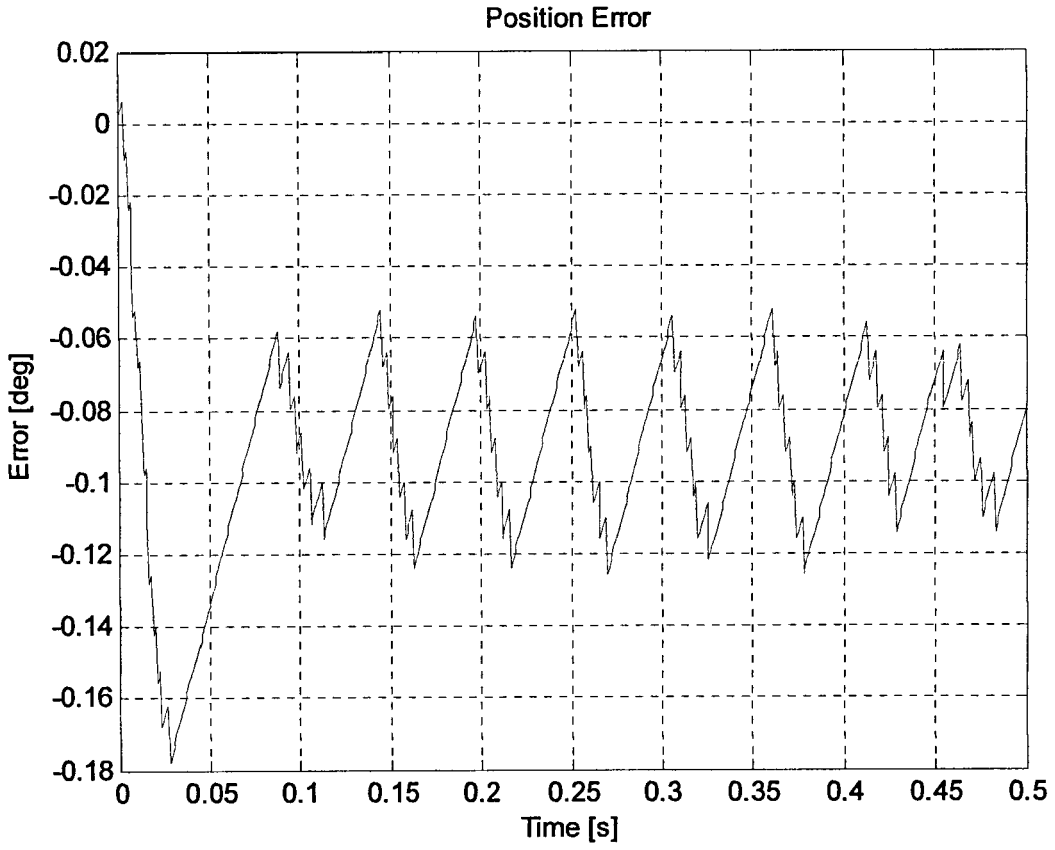

b)

Figure 6-16. Stick slip versus encoder resolution for $\dot{\theta}_d = 2$deg/s: a) desired and actual position, b) position error

Using the SMC it was observed that the stick-slip was much reduced at low velocities and a velocity around 6deg/s could be controlled with very satisfactory results, as shown in Figures 6-15c and 6-15d. However, for a velocity of 2deg/s, the stick-slip is clearly visible in Figures 6-15e and 6-16a, even though is much reduced when compared with the results obtained with the PD controller. Regarding the reduction of stick-slip, a comparison between the experimental results obtained with the PD control and SMC is presented in Table 6-4. The stick-slip reduction is presented in percentage and is calculated considering the results with the PD controller as 100% stick-slip. Thus, the stick-slip percentage obtained with the SMC versus PD is calculated as follows:

$$\text{SMC vs PD}_{\text{stick-slip}}\,[\%] = \frac{SMC_{stick-slip}}{PD_{stick-slip}} \cdot 100 \qquad \textbf{(6-33)}$$

where $SMC_{stick\text{-}slip}$, and $PD_{stick\text{-}slip}$ represent the number of stick-slip cycles during 1sec. The stick-slip percentage was averaged from ten measurements and the results are given in Table 6-4.

6.3.3.2 Experimental results with constant driving torque

The experimental results obtained using the SMC law derived in equation (6-31) are shown in Figure 6-17. The driving torque is set to 0.047Nm. In Figure 6-17a and 6-17b is shown the desired and actual position, and the position error for a straight-line path with a gradient of 20deg/s. From Figure 6-17a it can be seen that the actual position is rather discontinuous. This discontinuity denotes stick-slip and the effect occurs for any position rate greater than 20deg/s. However, for position rates less than 20deg/s, shown in Figures 6-17c and 6-17e, the stick-slip is significantly reduced. When compared with the results obtained with the PD controller, the stick-slip was reduced by as much as 89% for a desired path with a slope of 6deg/s, and 85% for a desired path with a slope of 2deg/s. A comparison between the experimental results obtained with the PD controller and SMC is presented in Table 6-4. The stick-slip reduction is presented in percentage and is calculated conform to equation (6-33). For example, if with a PD controller one hundred stick-slip limit cycles occur in t = 1s, and if with a SMC eleven stick-slip limit cycles occur in the same time, a reduction of 89% is obtained.

Just as in the simulation analysis, the experiments show that the position error is very similar for all velocities analysed, as shown in Figures 6-17b, 6-17d, and 6-17f. A positional error of approximately 0.1deg is demonstrated, which is well within the requirements. The root mean square (rms) of the error obtained from experiments and simulations are shown in Table 6-3.

From the simulation analysis it was observed that the amplitude of the position error is much smaller when compared with the results obtained with the PD controller. Amplitude of just 0.02deg was noticed from the results obtained with the SMC, while amplitude of about 0.1deg was obtained with the PD controller. However, from the

experimental results shown in Figure 6-17, it can be seen that the position error has amplitude of about 0.1deg, therefore, quite different from the simulation analysis. This discrepancy is because of the differences between the simulation model and experimental set-up. Therefore, the friction model used in simulations needs to be further improved in order to capture more efficiently the friction within the proposed joint mechanism. This is very much recommended for future development.

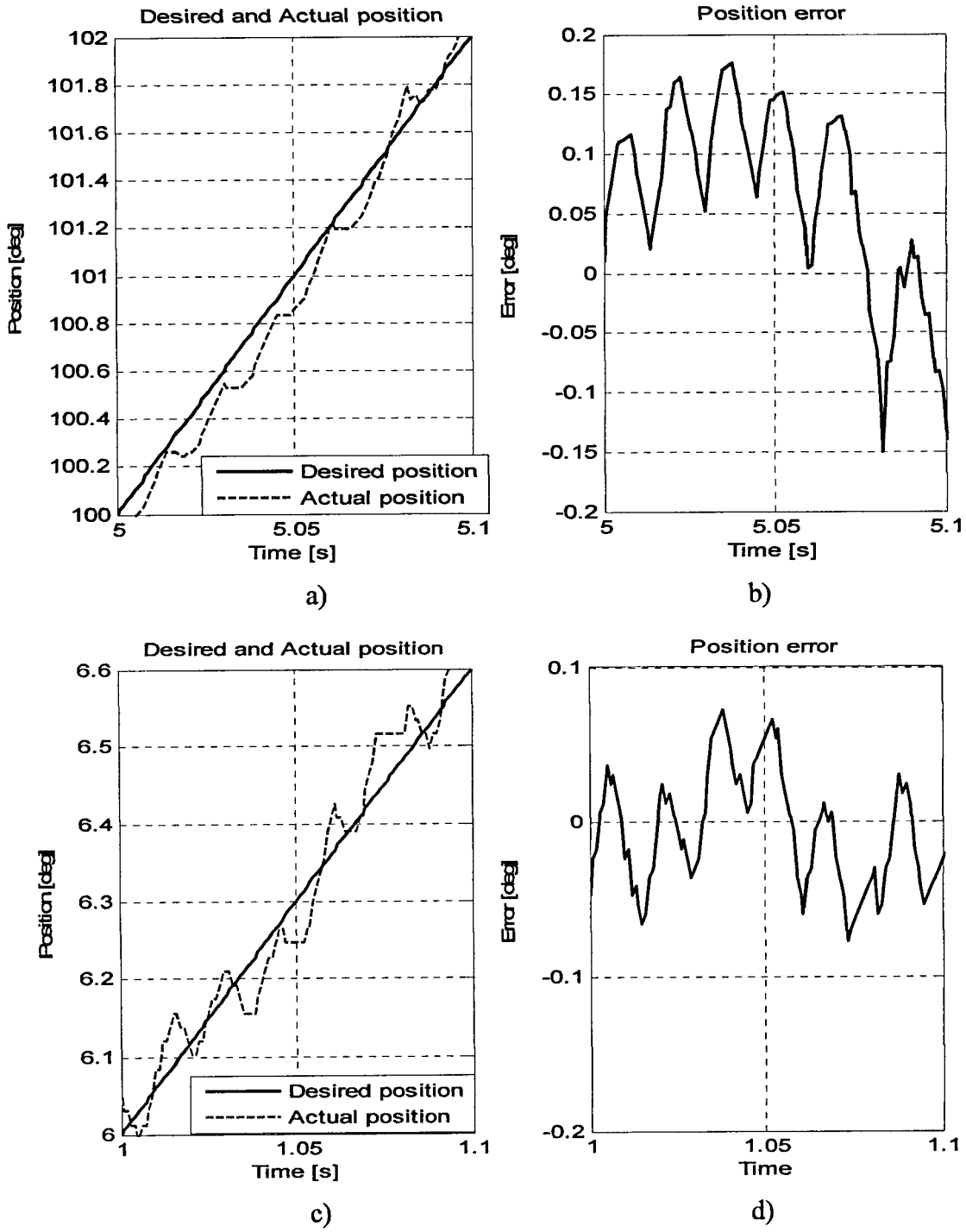

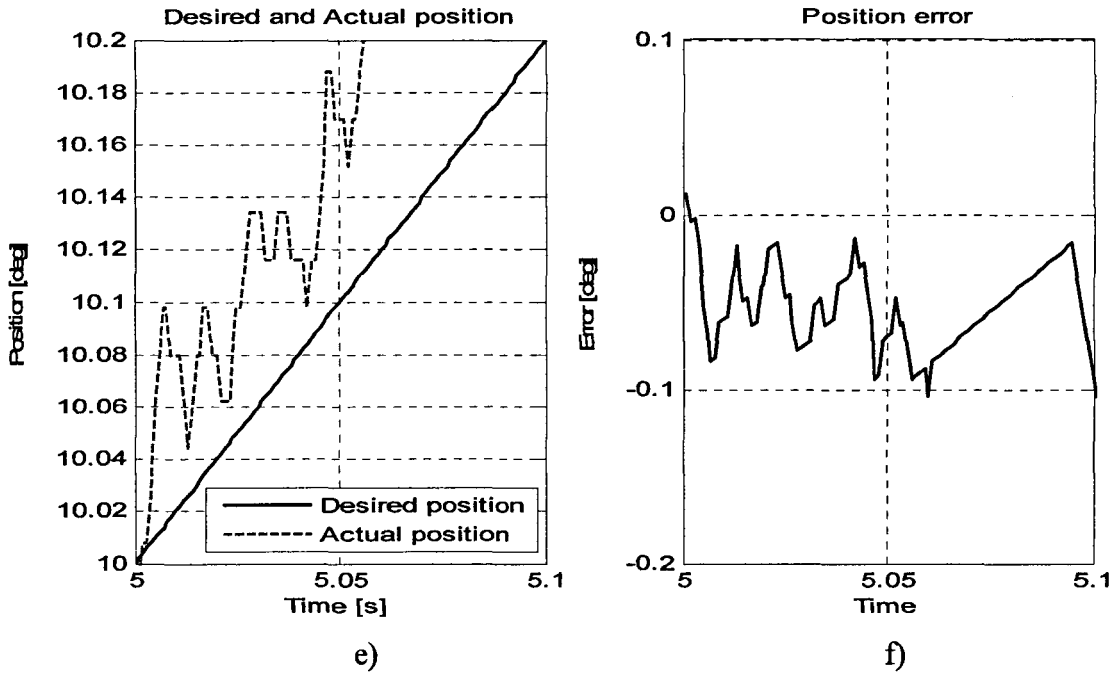

Figure 6-17. SMC Experimental results: Straight-line with constant driving torque [(a) and (b) for $\dot{\theta}_d$=20deg/s;(c) and (d) for $\dot{\theta}_d$=6deg/s; (e) and (f) for $\dot{\theta}_d$=2deg/s]

6.3.3.3 Simulation results with variable driving torque

The analysis for the same straight-line paths and control gains, but with a variable driving torque, is shown in Figure 6-19. The desired and actual position, and the position error for a desired path with a gradient of 20deg/s is shown in Figures 6-19a and 6-19b, and for a desired path with a gradient of 6deg/s is shown in Figures 6-19c and 6-19d. The driving torque is steeply changed from 0.047 Nm to 0.071 Nm as can be seen in Figure 6-18.

Note that because of the small difference between the desired and actual positions in Figures 6-19a and 6-19c, they can hardly be distinguished. However, from the position error, shown in Figures 6-19b and 6-19d, the influence of the step change in the driving torque can be clearly observed. This influence is due to high sensitivity of the controller against sudden changes. After the driving torque was changed it can be seen that the

controller is quickly finding the sliding-surface and the position error is kept within a similar amplitude. Nonetheless, the maximum position error obtained is still kept within the requirements.

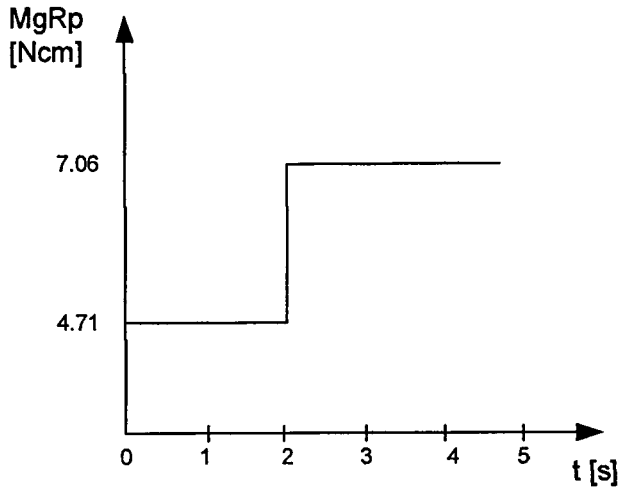

Figure 6-18. Driving torque profile

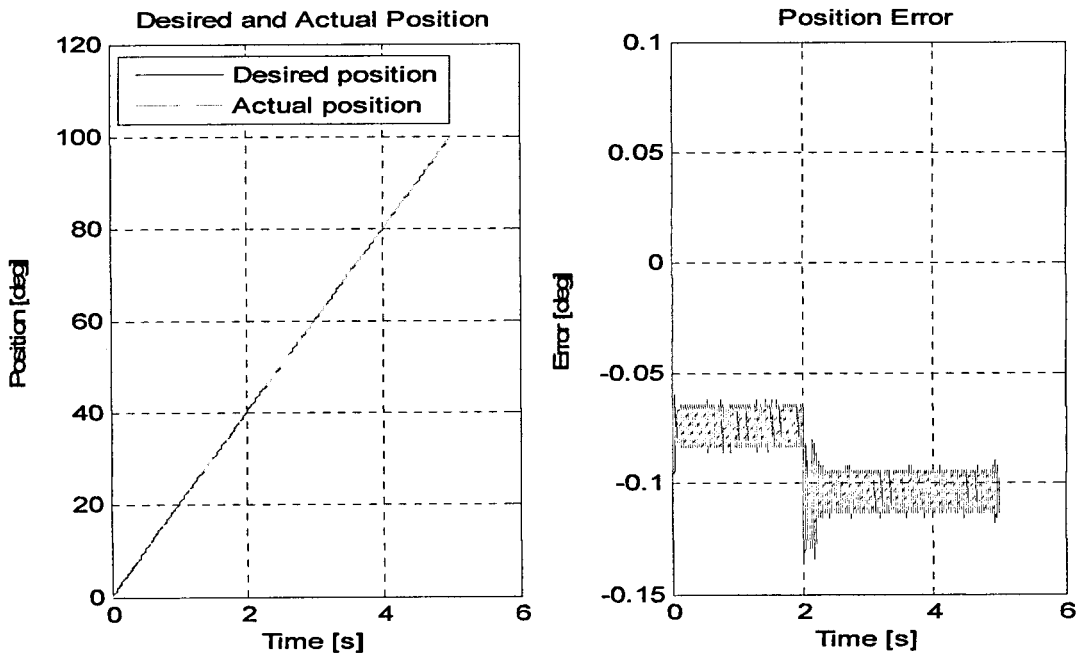

a) b)

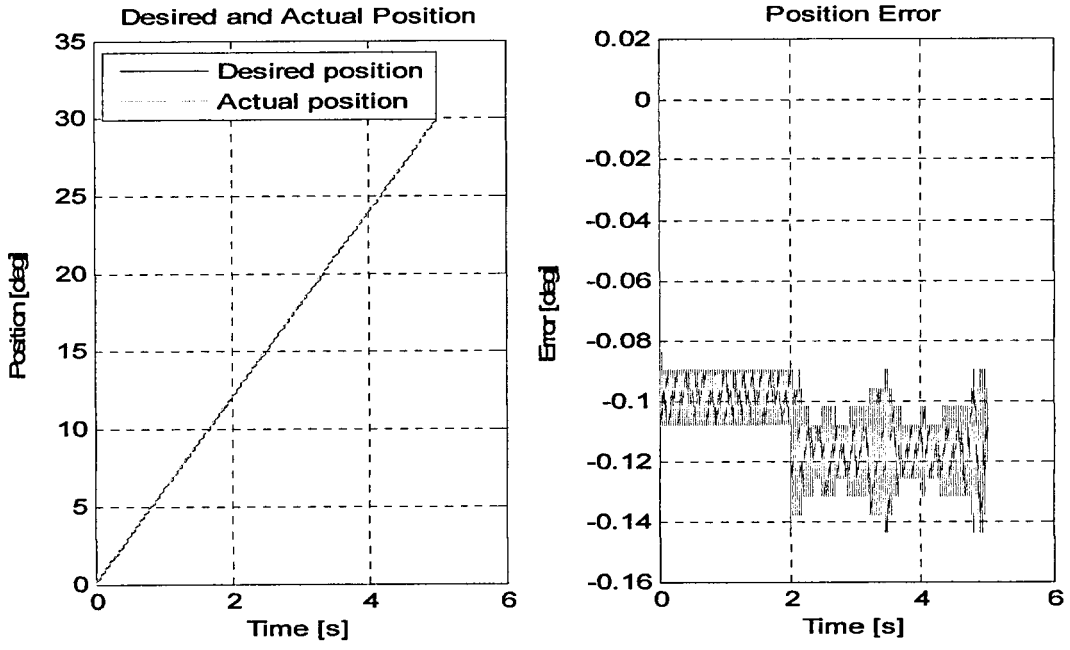

c) d)

Figure 6-19. SMC Simulation results: Straight-line with variable driving torque [(a) and (b) for $\dot{\theta}_d$=20deg/s;(c) and (d) for $\dot{\theta}_d$=6deg/s]

6.3.3.4 Experimental results with variable driving torque

The desired and actual position, and the position error for a desired path with a gradient of 20deg/s are shown in Figures 6-21a and 6-21b, and for a desired path with a gradient of 6deg/s are shown in Figures 6-21c and 6-21d. The driving torque is steeply changed from 0.047 Nm to 0.071 Nm as it can be seen in Figure 6-20a for a position rate of 20deg/s, and in Figure 6-20b for a position rate of 6deg/s.

Note that in Figures 6-21a and 6-21c the desired and actual position can hardly be distinguished. This is due to the small errors shown in Figure 6-21b and 6-21d. From the position error, shown in Figures 6-21b and 6-21d, the influence of the step change in the driving torque can be observed only in the moment when the mass is actually changed on the pulley.

This response to a drastic change in driving torque, is quite similar to the results obtained from simulations, illustrated in Figure 6-19. It can be seen from Figures 6-21b and 6-21d that the position error is more affected when the weight on the pulley is changed. After the change of weights was completed, the position error for the new driving torque is kept around the same value as for the previous driving torque. This means that the SMC is highly sensitive to sudden changes in driving torque, but very quick to compensate for it.

From the experimental results shown in Figure 6-21, it can be seen that the position error has an uneven amplitude approximated to 0.2deg, therefore, quite different from the simulation analysis. This discrepancy is because of the differences between the simulation model and experimental set-up as described for the analysis with a constant driving torque.

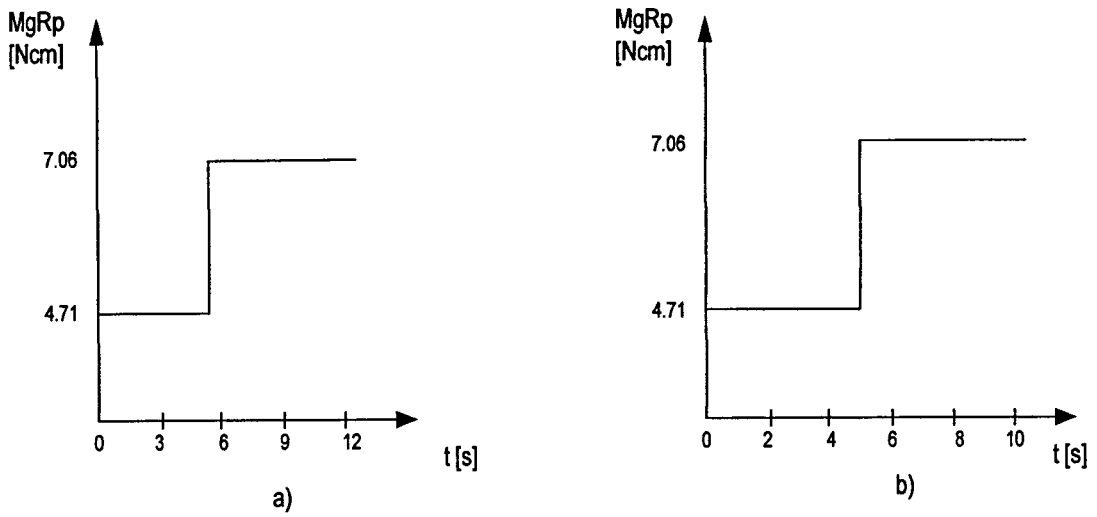

Figure 6-20. Driving torque profile:
a) for $\dot{\theta}_d$ = 20deg/s, b) for $\dot{\theta}_d$ = 6deg/s

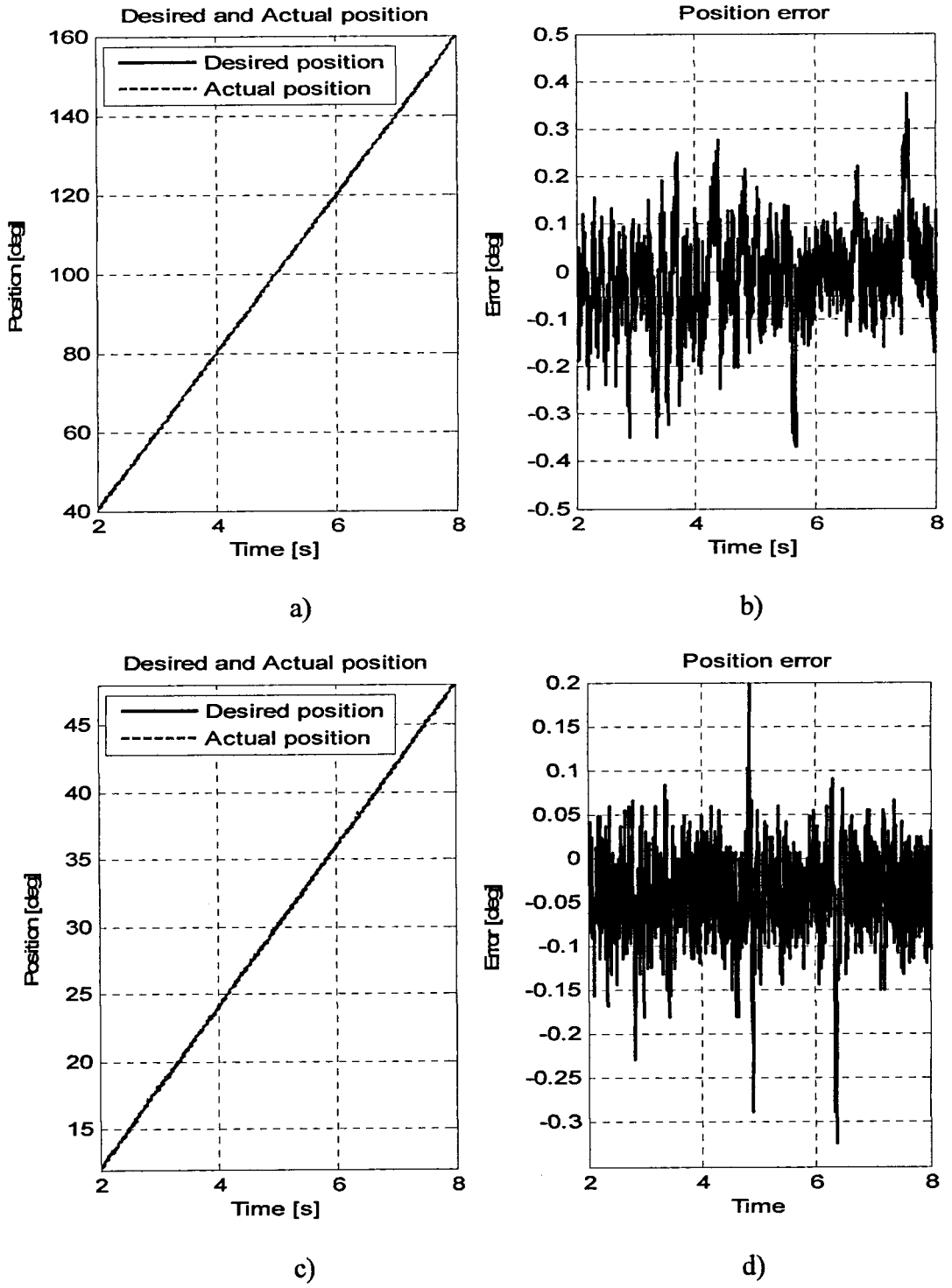

Figure 6-21. SMC Experimental results: Straight-line with variable driving torque [(a) and (b) for $\dot{\theta}_d$=20deg/s;(c) and (d) for $\dot{\theta}_d$=6deg/s]

The root mean square (rms) of the error obtained from experiment and simulation, for both constant and variable driving torque, is shown in Table 6-3. From Table 6-3 it can be seen that, except for the case in which the desired path has a 20deg/s slope, the simulation results show a slightly higher position error compared with the experimental results. This is positive information as the further developments on the proposed actively restrained passive mechatronic system can be done in simulations with reasonable accuracy. For the case in which the desired path has a 20deg/s slope, the simulations shows a much lower level of errors compared with the experiments. This rather large discrepancy is due to the fact that the developed controller is optimised for very low velocities (i.e. <20deg/s) and thus around the higher end of velocity (i.e. 20deg/s), the experimental set-up does not behave as fine as the simulation model.

A comparison between the stick-slip limit cycles obtained from the experimental results using the PD controller and SMC is presented in Table 6-4. The percentage of stick-slip is calculated using equation (6-33). Thus, if in t = 1s the results with the PD controller show 100 stick-slip limit cycles, and the results with the SMC shows just 11 limit cycles, a reduction in stick-slip of 89% is achieved.

Table 6-3. Error rms – Sliding-mode controller (SMC)

	Error rms	
$\dot{\theta}_d$ = 20 deg/s	Const. driving torque	Variable driving torque
Experiment	0.20	0.26
Simulation	0.088	0.09
$\dot{\theta}_d$ = 6 deg/s		
Experiment	0.091	0.06
Simulation	0.1344	0.11
$\dot{\theta}_d$ = 2 deg/s		
Experiment	0.059	0.057
Simulation	0.09	0.1

Table 6-4. Stick-slip comparison for experimental results with constant torque

	Stick-slip [%]	
Velocity	PD Control	SMC
$\dot{\theta}_d$ = 10deg/s	100	11.43
$\dot{\theta}_d$ = 6deg/s	100	11.11
$\dot{\theta}_d$ = 2deg/s	100	16.22

6.4 Conclusions

It was shown in Section 5.3 that for a velocity less than 0.4 rad/s (approx. 24 deg/s) the friction is in the boundary lubrication regime, which means stick-slip will occur, therefore the motion below 0.4 rad/s is practically impossible to be smoothly controlled. However, for the proposed joint mechanism it is required to control the system's motion for velocities in the region of 0.1 rad/s (i.e. approx 1 rpm or 6 deg/s). Therefore, the task of designing a controller able to diminish the stick-slip effect, which is highly challenging, is necessary.

The maximum position rate at which the position is regulated also needs to be limited so that the motion is effectively controlled. The maximum position rate was chosen 100deg/s, which ensures that in case of a sudden stop, the stopping distance is less than the accuracy of the revolute joint.

Besides avoiding the stick-slip effect within the mechanism, the controller is required to track the desired position with an error less than 0.2 deg. This level of error ensures that the overall error of the two-DOF prototype introduced in section 3.3 is less than 1 mm. From the existing actively restrained devices presented in section 3.2, the most accurate was proved to be PTER with a maximum error of 4 mm. Thus, even if an error of

around 0.8deg is obtained for the proposed revolute joint, the proposed system is still the best in its class, because of the other advantages presented in Chapter 3.

Three controllers capable of diminishing or completely cancelling the stick-slip effect were developed and investigated. A PD controller was first developed and investigated. Simulation and experiments were performed for both constant and variable driving torque. From the analysis with the PD controller it can be seen that the simulation results are very similar to the results obtained from the experimental analysis. Thus, the conclusions extracted from the simulation results also apply for the experiments. Both the stick-slip effect and the positional error were similar in the simulations for both constant and variable driving torque. These results demonstrate the validity of the friction model used as well as the validity of the mathematical model used to assist in designing friction compensators. Furthermore, it was shown that using a high gain PD controller the stick-slip was successfully compensated for velocities higher than 20deg/s. Moreover, the PD controller proved to regulate the position accurate enough for the operating environment.

Next, the computed-torque control (CTC) law was developed and investigated. The CTC method proved to be very efficient as long as exact system parameters are assumed. This is shown in the simulation analysis, where is illustrated that besides fully avoiding the stick-slip effect, even for a position rate of 2 deg/s, the controller is capable of tracking the position at the limit of the encoder resolution.. However, exact knowledge of the system parameters is impossible in practice, thus the experimental analysis suffers from the sensitivity to errors in the estimates of these parameters. This is illustrated in the experimental analysis shown in Figure 6-14. Consequently, as the results show a great potential for diminishing the stick-slip effect with an accurate estimated model, it is recommended that further research into accurate estimation of highly non-linear parameters such as friction-related parameters to be undertaken.

A more robust approach is the SMC method where is not necessary to know exactly the system parameters, instead only bounds on these parameters. The PD controller was shown to successfully compensate for stick-slip for a velocity greater than 20 deg/s.

However, the system's motion for velocities between 6 deg/s and 20 deg/s is required to control. Using the SMC it was demonstrated that the stick-slip was much reduced at low velocities and a velocity around 6 deg/s could be controlled with very satisfactory results, as shown in Figures 6-15c and 6-15d. Even for a velocity of 2 deg/s, the stick-slip was very much reduced when compared with the results obtained with the PD controller. From the stick-slip point of view, a comparison between the PD controller and the SMC was performed, which is illustrated in Table 6-4. It can be seen that the stick-slip was reduced by as much as 89% for a desired path with a slope of 6 deg/s, and 85% for a desired path with a slope of 2 deg/s.

The SMC was shown to be more sensitive to sudden changes in driving torque when compared with the PD controller. However, the SMC is quicker to compensate for this change than the PD controller. Consequently, in order to have an efficient control strategy for the proposed actively restrained passive mechatronic system, a combination of these two controllers must be used. In the next chapter a control strategy based on the combination of the PD controller and SMC is employed in order to achieve the objectives 3, 4, and 5 defined in section 2.8.

From the simulation analysis with SMC it was observed that the amplitude of the position error is much smaller when compared with the results obtained with the PD controller. Amplitude of just 0.02 deg was noticed from the results obtained with the SMC, while amplitude of about 0.1 deg was obtained with the PD controller. However, from the experimental results shown in Figure 6-17, it can be seen that the position error has amplitude of about 0.1 deg, therefore, quite different from the simulation analysis. This discrepancy is because of the differences between the simulation model and experimental set-up. Therefore, the friction model used in simulations needs to be further improved in order to capture more efficiently the friction within the proposed joint mechanism. This is very much recommended for future development.

Chapter 7
Control of an Actively Restrained Passive Revolute Joint

7.1 Introduction

In this chapter the control of an actively restrained passive revolute joint is addressed. Firstly, the observations and conclusions from the preceding chapter are used to develop an efficient control strategy to smoothly and accurately regulate the position for a desired position rate between 6deg/s and 100deg/s. Secondly, a strategy to perform the objectives 3, 4, and 5 defined in section 2.8, for a one-DOF system, is developed. Finally, simulation and experimental results are obtained to evaluate the performance of the control strategy for all three modes of operation: (1) reach a predefined position, (2) follow a predefined trajectory, and (3) stay within a predefined safety region. The results demonstrate the effectiveness and robustness of the proposed control system, even though the accuracy of the system suffers slightly because of the controllers' performance.

7.2 Control Strategy

7.2.1 Control strategy for friction compensation

As it was shown in the conclusions of the previous chapter, in order to smoothly and accurately regulate the position for a variety of position rates, a combination of PD control and SMC must be employed. The PD controller was shown to successfully compensate for stick-slip for a velocity greater than 20deg/s. Furthermore, the accuracy obtained with the PD controller for a velocity greater than 20deg/s is within the prespecified requirements. However, the system's motion for velocities between 6deg/s and 100deg/s is required to be controlled. The SMC was demonstrated to significantly compensate for the stick-slip for a velocity between 6deg/s and 20deg/s. Consequently, an integration of both of these two controllers can achieve the control requirements, which are to diminish the stick-slip effect as much as possible, and to smoothly and accurately control the position of the clutch's shaft (i.e. the revolute joint).

In order to develop a robust control strategy with respect to the frictional non-linearities and unknown behaviour, the control scheme has been divided into two modes: (1) a *fine mode*, where the desired position rate is high enough so that a controller can fully compensate for stick-slip; thus, the position can be smoothly controlled; and (2) a *gross mode*, where the desired position rate is very low and stick-slip cannot be fully compensated for; thus the stick-slip effect is likely to occur.

The *fine mode* is considered when the desired position needs to be controlled at a higher position rate than a predefined value. Thus, stick-slip is avoided partly due to the stiffness of the mechanism and partly because of the controller abilities. The predefined value, P_v, is obtained experimentally, while the desired position rate, $\dot{\theta}_d$, is given as

$$\dot{\theta}_d = \frac{\theta_k - \theta_{k-1}}{t_k - t_{k-1}} \qquad \textbf{(7-7-1)}$$

where, θ_k and θ_{k-1} represent the actual and previous desired position points; and t_k and t_{k-1} denotes the time when the positions, θ_k and θ_{k-1} are reached. As a result, as long as $\dot{\theta}_d \geq P_v$, the controller will be in the *fine mode.*

The *gross mode* is considered when the desired position rate, $\dot{\theta}_d$, drops below the predefined value, P_v. Thus, for any $\dot{\theta}_d < P_v$ the control is switched to the *gross mode*. In this mode, although the position error is kept to a minimum, a slight chattering effect is likely to occur due to the discontinuous motion introduced by the stick-slip effect uncompensated for. A flow chart of the control scheme is given in Figure 7-1.

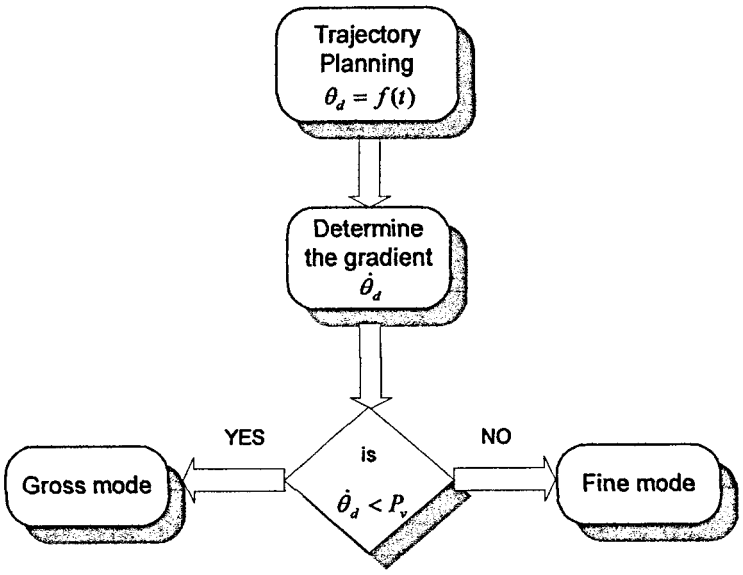

Figure 7-1. Control scheme for effective position control

The advantage of this control scheme is that for each of the modes a different controller can be developed. In this research, the PD controller was employed for the *fine mode* and the SMC was applied for the *gross mode*. Consequently, the predefined value P_v in this case is set to 20 as above this value the position can be smoothly and accurately control using the PD controller and below this value, the SMC was demonstrated to be the most efficient in compensating for the stick-slip phenomenon.

7.2.2 Strategy for definition of the three modes of operation

As defined in section 2.8, the proposed actively restrained passive mechatronic system should be able to (1) reach a pre-specified position, (2) follow a pre-defined trajectory, and (3) stay within a pre-programmed region. These three requirements are seen as three different modes in which the proposed manipulator operates. Consequently, to reach a pre-specified position, in order to insert a drill bit, a needle, or an electrode, the manipulator is controlled in the *'position'* mode; to follow a pre-defined trajectory, as it is required by more complex surgical procedures, the system is controlled in the *'trajectory'* mode; and to stay within a pre-programmed region, in order to avoid certain anatomical obstacles (i.e. blood vessels or ligaments), the manipulator is controlled in the *'region'* mode. These three modes of operations were first introduced in Chapter 3 for a two-DOF manipulator. In this section these three modes are developed for a one-DOF system (i.e. an actively restrained passive revolute joint) and will be later extended to a two-DOF system.

7.2.2.1 'Position' mode

In the *'position'* mode of a one-DOF revolute joint, the initial and final desired position points, θ_i and θ_f respectively, as well as the initial in final time in which these points are reached, t_i and t_f respectively, are predefined. Given an initial position point and a final position point, as shown in Figure 7-2, the intermediate controller desired input positions, between these two points, are obtained using a linear polynomial.

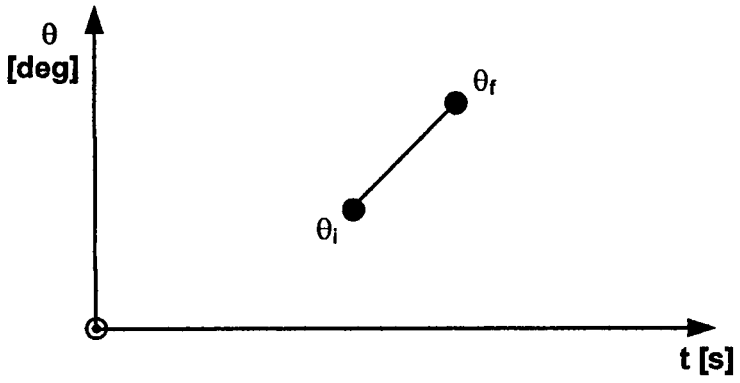

Figure 7-2. Initial and final position points

The position rate for the revolute joint is calculated as $m_\theta = \dot{\theta} = \Delta\theta/\Delta t$, where $\Delta\theta = \theta_f - \theta_i$, and $\Delta t = t_f - t_i$. Consequently, the desired angular position function of time $\theta_d(t)$ is obtained using the linear polynomial given by:

$$\theta_d(t) = \theta_i + m_\theta t \qquad (7\text{-}2)$$

where $t = nT$, $n = 0, 1, 2, \ldots$, and T is the sampling time.

The definition of this mode is similar to the definition of the desired path in the previous chapter. The difference is that in the previous chapter the desired path was controlled in either the *fine mode* or the *gross mode*. Thus, the results of this analysis were already shown in the previous chapter. However, in section 7.3 an example of the 'position' mode will be presented in which both the *fine* and the *gross mode* are joining together.

7.2.2.2 'Trajectory' mode

A desired path is defined as a set of position points, as shown in Figure 7-3. By considering a new point further along the path, the amount that the revolute joint needs to move to reach the new point can be calculated (i.e. $\Delta\theta_j = \theta_i - \theta_{i-1}$, where i represents the number of points that defined the trajectory i= 0 to 6 in Figure 7-3, and j denotes the number of segments that defines the trajectory and is therefore, equivalent to j = i-1). Just as it was shown for the *'position'* mode, from the angular displacement, $\Delta\theta_j$ and the time in which these position points are to be reached, $\Delta t_j = t_i - t_{i-1}$, the position rate for the

revolute joint is calculated as $m_{\theta j} = \dot{\theta} = \Delta\theta_j/\Delta t_j$. Consequently, the desired angular position function of time $\theta_d(t)$ is obtained using the linear polynomials given by:

$$\theta_d(t) = \theta_i + m_{\theta j} t_j \qquad \textbf{(7-3)}$$

where $0 \leq t_j \leq \Delta t_j$.

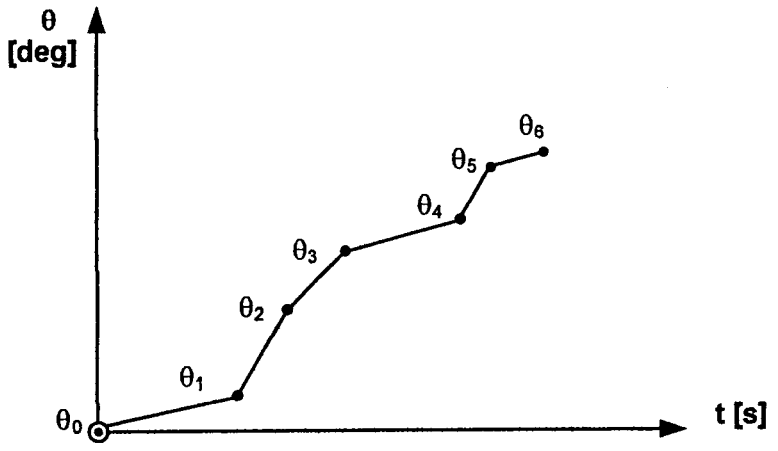

Figure 7-3. Desired position points that defines a trajectory

7.2.2.3 'Region' mode

The 'region' mode for the proposed two-DOF actively restrained passive mechatronic system was introduced in Chapter 3. The full description of this mode is given in the next chapter. For the one-DOF revolute joint, the 'region' mode is defined in the following way: An initial and a final position values, θ_i and θ_f, are predefined as boundaries of each of the three zones in which the control strategy was divided. Thus, zone I, where the motion of the joint is completely free (i.e. unrestricted by any means), is defined from zero (i.e. the rest position of the joint) to the initial position θ_i. Zone II, where the motion of the joint is restrained with the aim of warning the user that s/he is approaching the ultimate border, is defined between the initial and the final position values, θ_i and θ_f . Finally, zone III, which is a completely restricted area, is defined as the final position point θ_f. Therefore, no motion is allowed for any $\theta_a \geq \theta_f$, where θ_a is

the actual position of the joint. The definition of the 'region' mode is graphically illustrated in Figure 7-4.

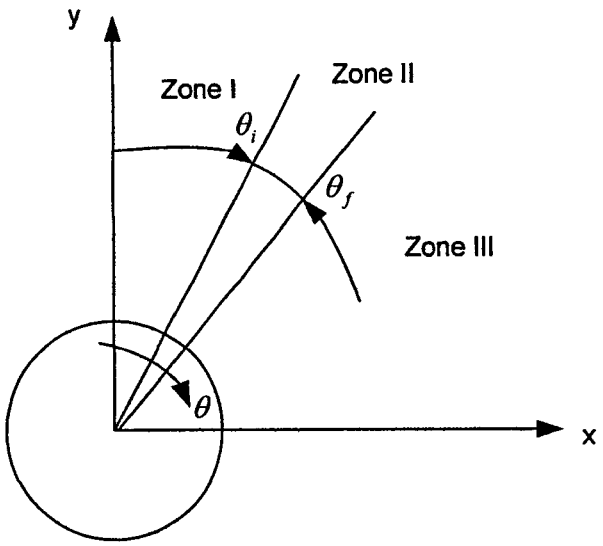

Figure 7-4. Definition of the 'region' mode for a one-DOF

The zones in which the 'region' mode was divided can be mathematically written as shown in equation (7-4):

$$\begin{aligned} \theta_a &< \theta_i \text{ for zone I} \\ \theta_i \le \theta_a &< \theta_f \text{ for zone II} \\ \theta_a &\ge \theta_f \text{ for zone III} \end{aligned} \qquad \textbf{(7-4)}$$

Knowing the actual position of the joint, θ_a, and where the safety boundary lay, a distance λ is obtained as

$$\lambda = \theta_f - \theta_a \qquad \textbf{(7-5)}$$

Thus, when $\lambda < \theta_i$ the revolute joint needs to be constrained as it is in zone II. From equation (7-5) it can be seen that if the actual position, θ_a, is approaching the safety boundary, θ_f, the value of λ is decreasing and becomes zero when the actual point reaches the boundary given by the value of θ_f. Consequently, when the actual position is in zone II, $\lambda < \theta_i$, the velocity of the revolute joint decreases according to equation (7-

5). Hence, the definition of the desired control in zone II of the 'region' mode is performed according to the following equation

$$\dot{\theta}_d = \dot{\theta}_{\min} + \lambda_{transf} \cdot K_{region} \qquad \textbf{(7-6)}$$

where $\dot{\theta}_{\min}$ represents the minimum allowed velocity, K_{region} is a positive defined constant set to enhance the feeling of the user, and λ_{transf} is given by the equation

$$\lambda_{transf} = \lambda / (\theta_f - \theta_i) \qquad \textbf{(7-7)}$$

so that the difference shown in equation (7-5) is generalised to be between 1 and 0.

Equation (7-6) represents the desired velocity to be controlled, parameter that is activated only when $\lambda < \theta_i$. The motion in zone II is controlled using a PD controller similar to the controller used for the *'fine' mode* described in section 6.2.

7.3 Results and Discussions

The aim of the study in this section is to evaluate the performance of the strategy employed for the definition of all three modes of operation: (1) reach a predefined position, (2) follow a predefined trajectory, and (3) stay within a predefined safety region. Simulation and experiments were performed for both constant and variable driving torque. The experiments were performed using the computational workstation presented in Appendix G. The constant driving torque is provided by gravity acting on a mass using a pulley; and the variable driving torque is produced by changing the weight on the pulley while controlling the shaft position, so that a step change in driving torque is produced during the motion. Simulations were performed using the Matlab/Simulink environment. A sampling rate of 1ms is chosen, and the solver used is based on explicit Runge-Kutta formula (4,5), the Dormand-Prince pair.

7.3.1 Position mode

The 'position' mode is illustrated for an angular displacement, $\Delta\theta = \theta_f - \theta_i$, of 138deg. This displacement can be performed in a time which is between $t_1 = \Delta\theta/V_{max} = 138/100 = 1.38$s and $t_2 = \Delta\theta/V_{min} = 138/6 = 23$s. Thus, for any time, t, between t_1 and t_2 (i.e. $t_1 \leq t \leq t_2$) the position θ_d can be controlled linearly as shown in the previous chapter. Consequently, the 'position' mode in *fine mode* and *gross mode* were shown separately, but not joint together, as it may be the case for a two-DOF manipulator when is required to adjust the position rate at some intermediate points so that the position of the revolute joint and the position of the prismatic joint meet at a certain time, in order to achieve a desired point in Cartesian or polar coordinates. This issue is addressed in the next chapter, however, the integration of the *fine mode* and *gross mode* for a one-DOF are shown in this section.

In the next subsections, an angular displacement of 138deg is to be reached in t = 6s using two different position rates. If only one position rate was to be used, than a slope $m_\theta = \dot{\theta} = \Delta\theta/\Delta t = 138/6 = 23$deg/s would have been necessary to utilize. However, the angular displacement of 138deg is achieved by employing a 6deg/s slope for t = 3s, which is controlled in the *gross mode* by the SMC, and another slope of 40deg/s for the other t = 3s (i.e. 6deg/s x 3 + 20deg/s x 3 = 138deg), which is controlled in the *fine mode* by the PD controller. The desired position is illustrated in Figure 7-5.

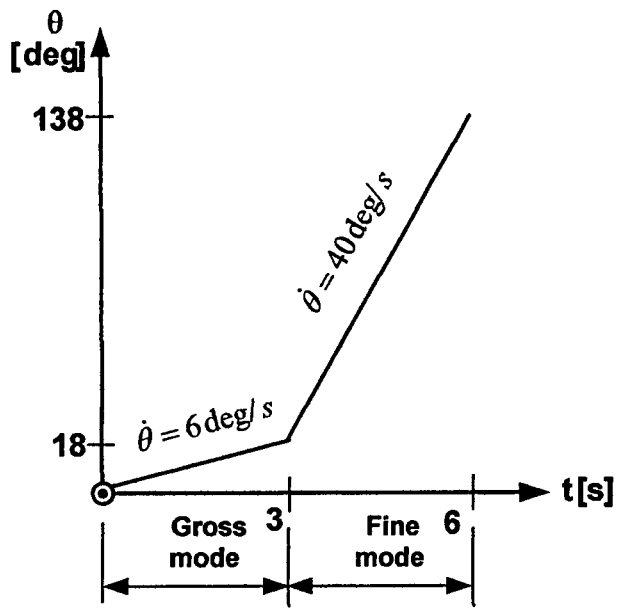

Figure 7-5. Example of a desired position in 'position' mode

7.3.1.1 Simulation results with constant driving torque

In Figures 7-6 and 7-8 is shown the simulation results with a constant driving torque. Figure 7-6 shows the desired and actual position, and the position error for a constant driving torque set to 0.047Nm. Note that because of the small difference between the desired and actual positions, the positions can hardly be distinguished. However, from the position error, shown in Figures 7-6b and 7-8b, the influence of the step change in velocity can easily be observed.

In Figure 7-6b it can be seen that at time t = 3s, when the desired velocity changes from 6deg/s to 40deg/s a large fluctuation occurs. This fluctuation, illustrated at a larger scale in Figure 7-7, happen because of the step change in velocity (i.e. from 6deg/s to 40deg/s). The rather large fluctuation, however, does not affect the smoothness of the controlled motion, but only the overall accuracy, as shown in Figure 7-7.

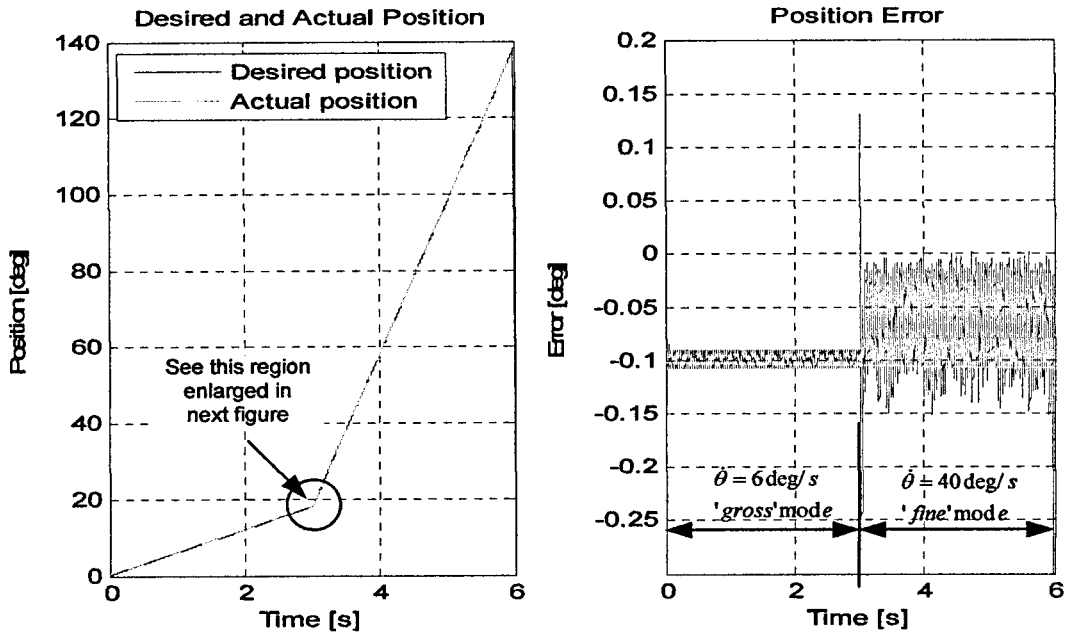

a) b)

Figure 7-6. Position mode: Simulations with constant driving torque of 0.047Nm

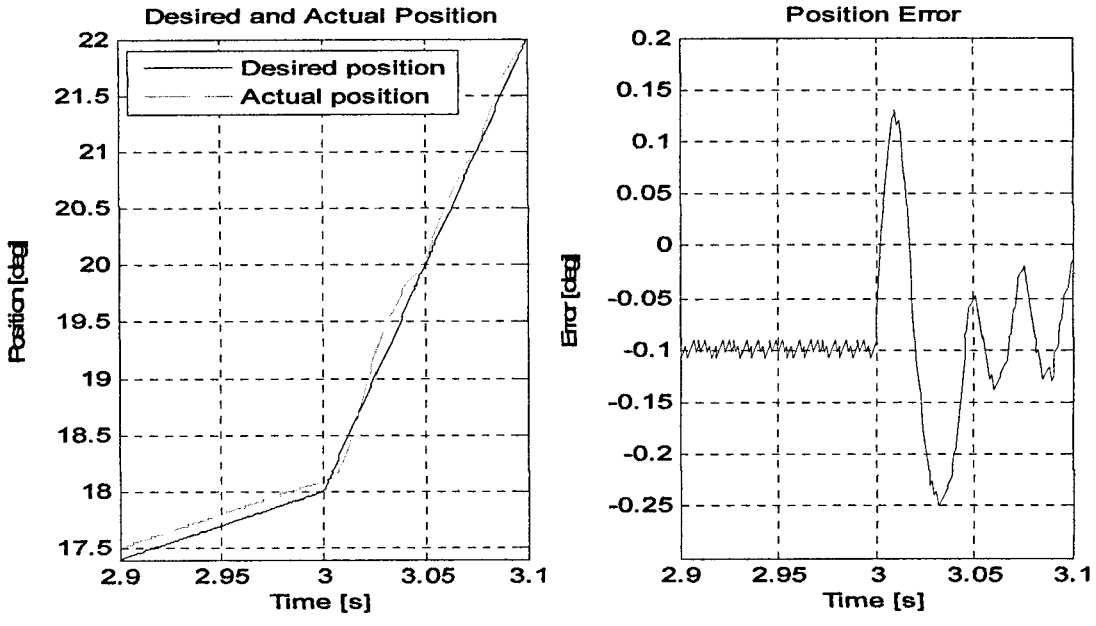

a) b)

Figure 7-7. Position mode: Simulations with constant driving torque of 0.047Nm (enlarged)

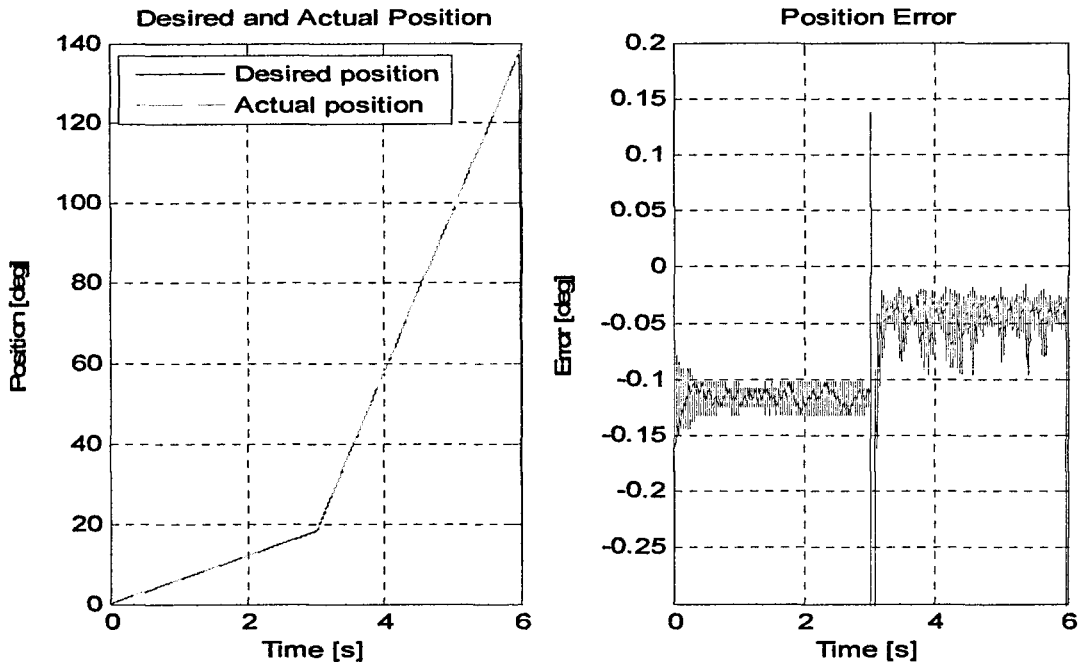

a) b)

Figure 7-8. Position mode: Simulations with constant driving torque of 0.071Nm

At time t = 3s, when the control switches from the *gross mode* to the *fine mode*, the position error shows a larger error for the PD control compared with the SMC. This denotes the superior performance of the SMC due to the fact that when the system is in the sliding mode, the tracking error is independent of the system parameters, while the PD controller is dependent on the system dynamics. The same conclusions can be draw from Figure 7-8, where the desired and actual position, and the position error for a constant driving torque of 0.071Nm are illustrated.

7.3.1.2 Experimental results with constant driving torque

Figures 7-9 and 7-11 show the experimental results with a constant driving torque. Figure 7-9 shows the desired and actual position, and the position error for a constant driving torque set to 0.047Nm, and Figure 7-11 illustrates the desired and actual positions, and the position error for a constant driving torque of 0.071Nm.

From Figures 7-9b and 7-11b it can clearly be seen the effect that each controller employed for the *fine* and *gross mode* has on the position error. This denotes the superior performance of the SMC due to the fact that when the system is in the sliding mode, the tracking error is independent of the system parameters, while the PD controller is dependent on the system dynamics.

For a constant driving torque of 0.047Nm, the moment when the change in velocity (i.e. from 6deg/s to 40deg/s) occurs is illustrated at a larger scale in Figure 7-10. It can be seen that the step change in velocity does not affect the smoothness of the controlled motion, just as shown in simulations.

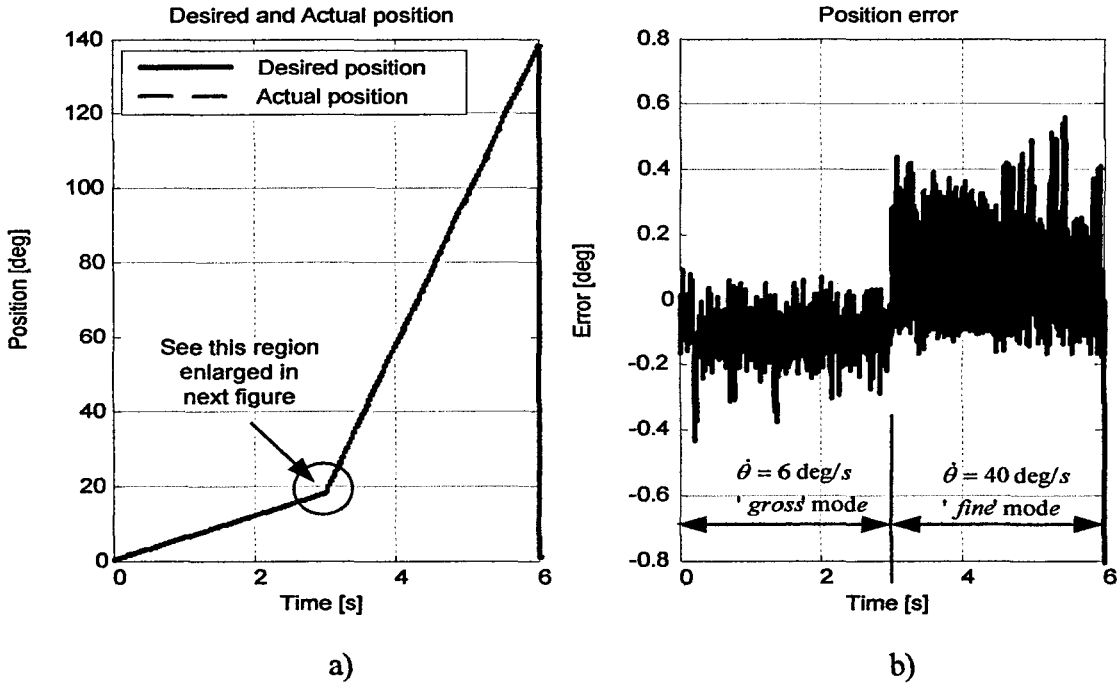

a) b)

Figure 7-9. Position mode: Experiments with constant driving torque of 0.047Nm

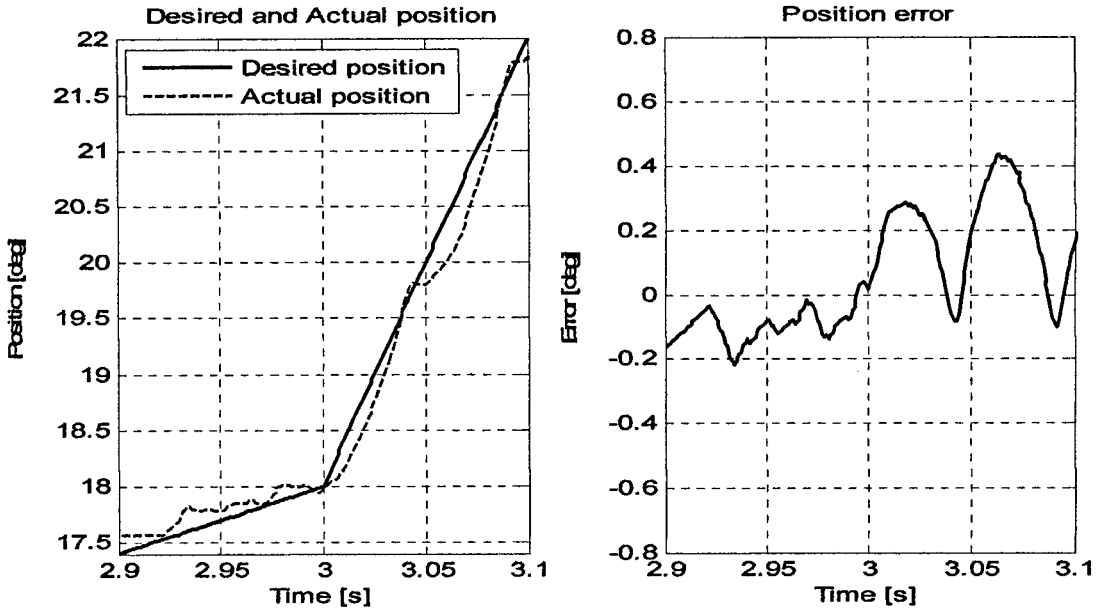

a) b)

Figure 7-10. Position mode: Experiments with constant driving torque of 0.047Nm (enlarged)

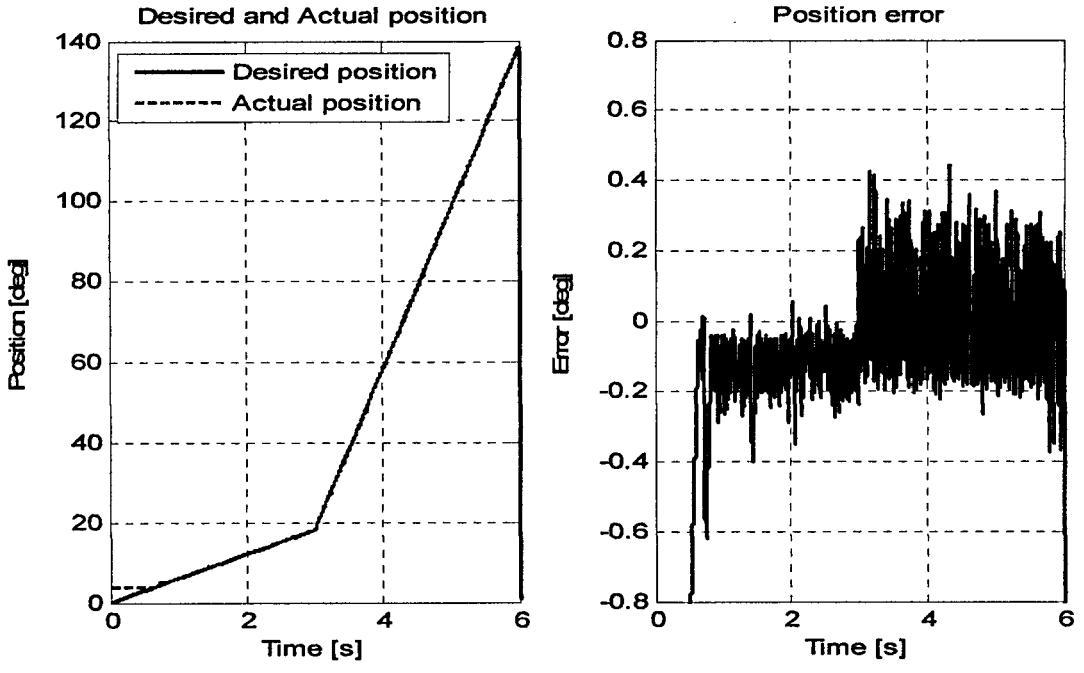

a) b)

Figure 7-11. Position mode: Experiments with constant driving torque of 0.071Nm

7.3.1.3 Simulation results with variable driving torque

As for the analysis with constant torque, the same desired position is analysed for a variable driving torque. The driving torque is steeply changed from 0.047 Nm to 0.071 Nm and back, as shown in Figure 7-12.

Similar with the simulation analysis with a constant driving torque, in Figure 7-13b it can clearly be seen that at time t = 3s, when the desired velocity changes from 6deg/s to 40deg/s a large fluctuation occurs. The rather large fluctuation, however, does not affect the smoothness of the controlled motion, but only the overall accuracy, as shown in Figure 7-13b. The effect that each controller employed for the *fine* and *gross mode* has on the position error can also be seen from Figure 7-13b. This is due to the controller's performance, which was discussed in the previous chapter.

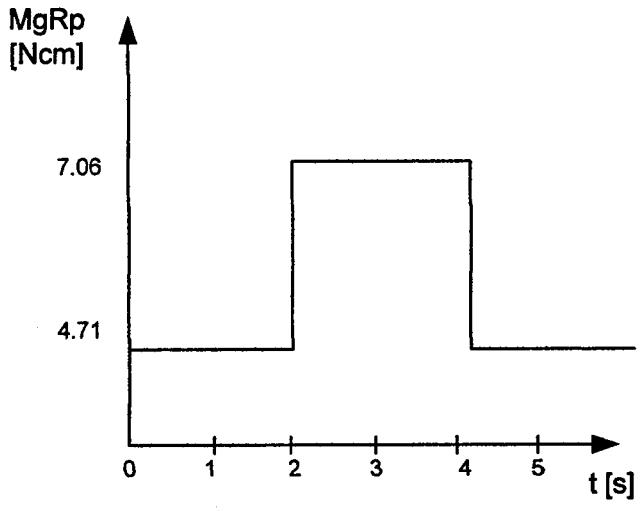

Figure 7-12. Driving torque profile

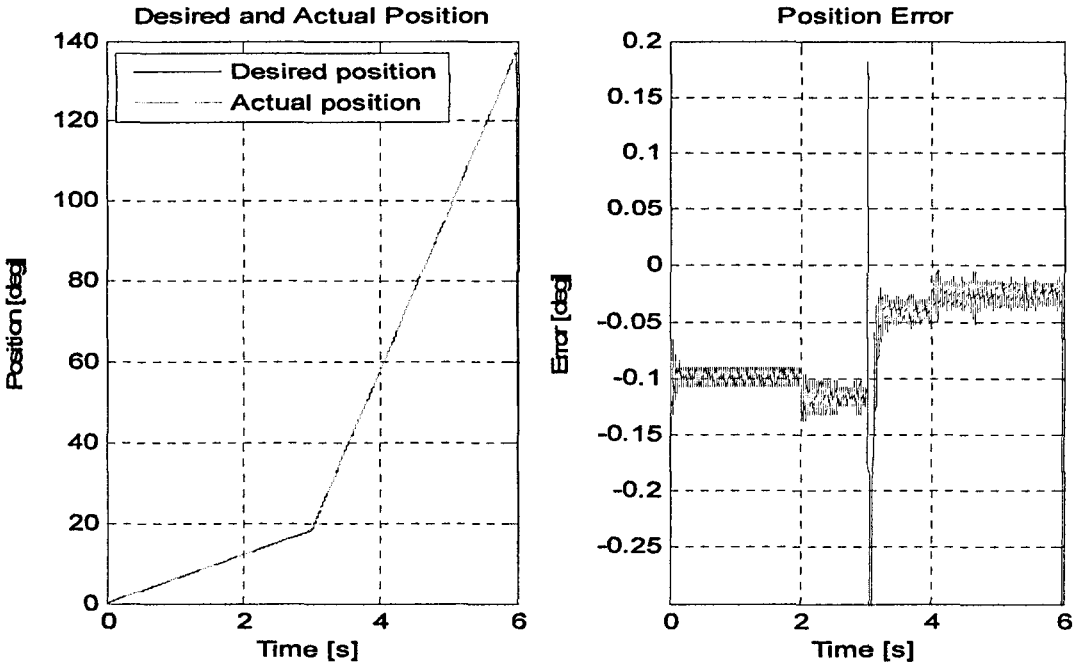

a) b)

Figure 7-13. Position mode: Simulations with variable driving torque

From the position error, shown in Figures 7-13b, the influence of the step change in the driving torque can be observed, just as it was noticed for the analysis completed in the previous chapter. This issue is related to the sensitivity of the controller, and it can be seen that both controllers have rather similar drawbacks regarding the sensitivity against external disturbances such as the driving torque. Nonetheless, the maximum position error obtained is still kept within the requirements.

7.3.1.4 Experimental results with variable driving torque

Figure 7-15 shows the experimental results for the desired position shown in Figure 7-5 while the driving torque is sharply changed from 0.0471Nm to 0.071Nm and back, as illustrated in Figure 7-14. From Figure 7-15b it can be seen that the effect of sharp change in driving torque does not significantly change the profile of the actual position. This observation is better illustrated in Figure 7-16, where the position error for both the

experimental results obtained with constant and variable driving torque are shown again, side-by-side. This outcome obtained means that the controllers are more robust in reality compared with the virtual environment. Thus, the main drawback of the controllers is the accuracy of the position error, which is still better than the error obtained by the existing systems.

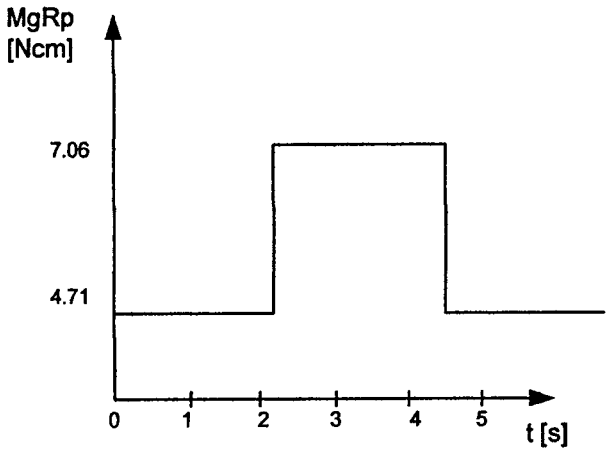

Figure 7-14. Driving torque profile

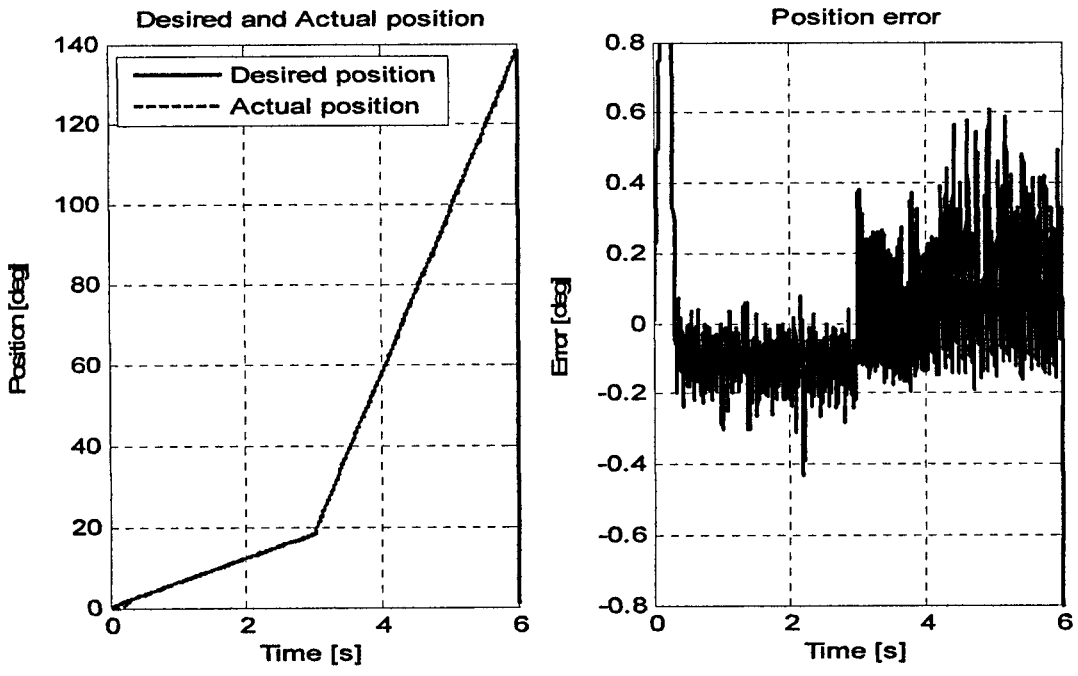

a) b)

Figure 7-15. Position mode: Experiments with variable driving torque

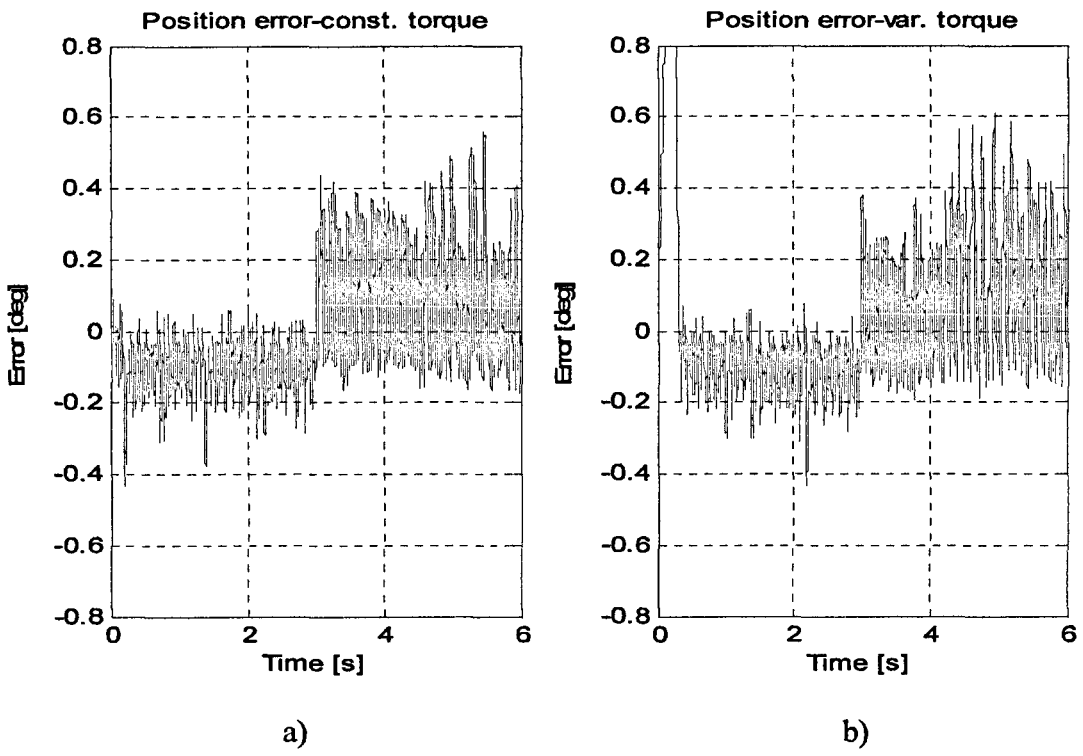

Figure 7-16. Experimental results: a) constant torque, b) variable torque

7.3.2 Trajectory mode

The 'trajectory' mode is illustrated for six predefined position points θ_i , where i = 0 to 5, as shown in Figure 7-17. Thus, five different segments $\Delta\theta_j = \theta_i - \theta_{i-1}$ are obtained, which can all have a different slope $m_{\theta j} = \dot{\theta} = \Delta\theta_j/\Delta t_j$. Therefore, by predefining the times, t_i, five different slopes were selected to illustrate the 'trajectory' mode. The desired slopes are $m_\theta = \dot{\theta} = [6, 20, 80, 30, 10]$, and are illustrated in Figure 7-17.

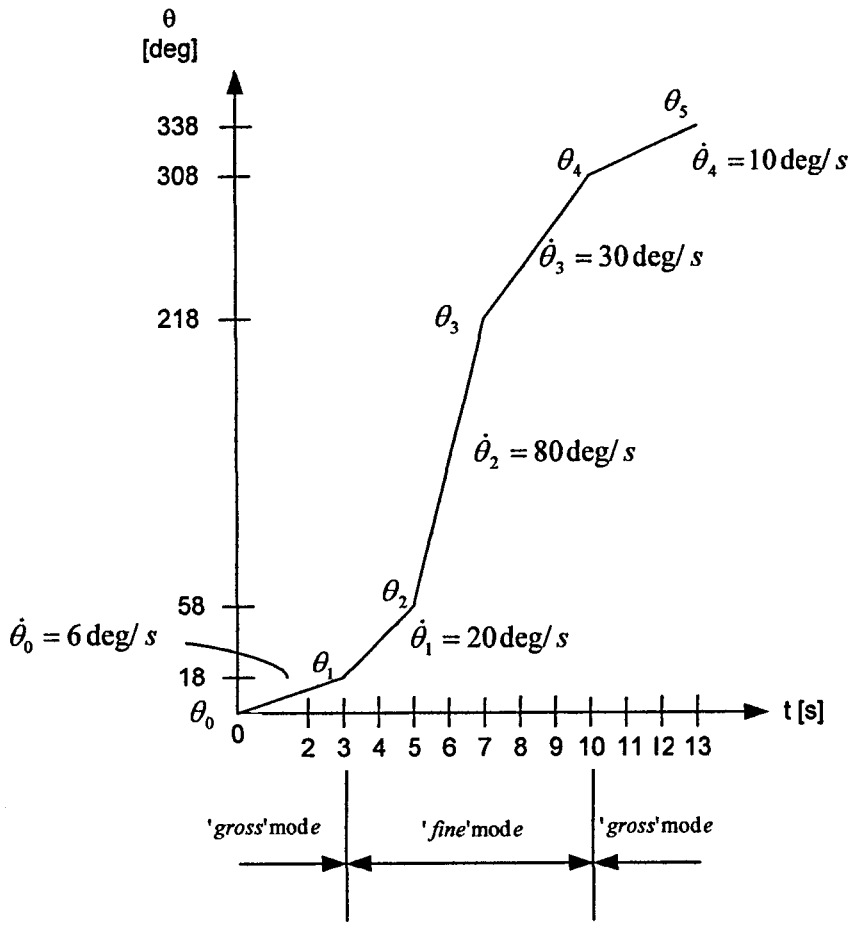

Figure 7-17. Example of a desired path in 'trajectory' mode

Consequently, the 'trajectory' mode represents a series of 'position' modes, which are controlled following the strategy explained in section 7.2.1. For any desired position rate greater than a predefined value, P_v the control is performed in the *'fine' mode*; for any desired position rate less than a predefined value, P_v the control is performed in the *'gross' mode.*

7.3.2.1 Simulation results with constant driving torque

In Figures 7-18 and 7-19 is shown the simulation results with a constant driving torque. Figure 7-18 shows the desired and actual position, and the position error for a constant driving torque set to 0.047Nm. From Figure 7-18b it can be seen that when the desired

velocity changes from 20deg/s to 80deg/s, and from 80deg/s to 30deg/s, a large fluctuation occurs. These fluctuations are similar with the fluctuation shown for the analysis of the 'position' mode, presented in the section 7.3.1. These fluctuations happen because of the large step change in velocity. This conclusions is confirmed by the fact that for small changes in velocity (e.g. from 6deg/s to 20deg/s, and from 30deg/s and 10deg/s) the large fluctuations disappear, as it can be seen from Figure 7-18. The rather large fluctuation, however, does not affect the smoothness of the controlled motion, but only the overall accuracy, as shown in section 7.3.1.

Similar to the observations draw from the analysis of the 'position' mode shown in section 7.3.1, when the control switches between the *gross mode* and the *fine mode*, the position error shows a larger error for the PD control compared with the SMC. This denotes the superior performance of the SMC due to the fact that when the system is in the sliding mode, the tracking error is independent of the system parameters, while the PD controller is dependent on the system's dynamics. The same conclusions can be draw from Figure 7-19, where the desired and actual position, and the position error for a constant driving torque of 0.071Nm are illustrated.

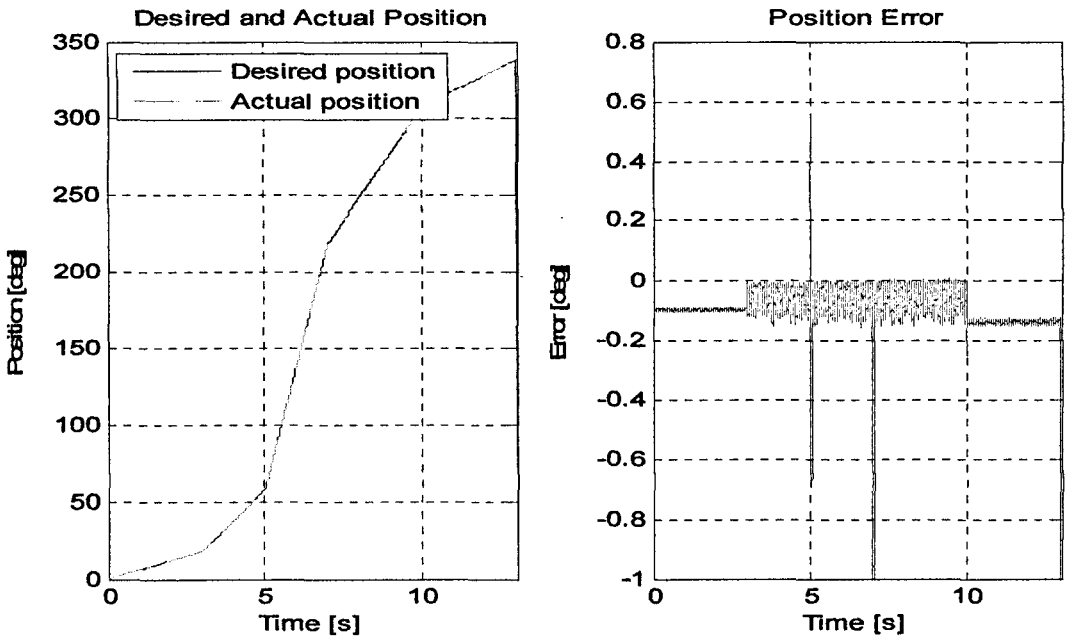

Figure 7-18. Trajectory mode: Simulations with constant driving torque of 0.047Nm

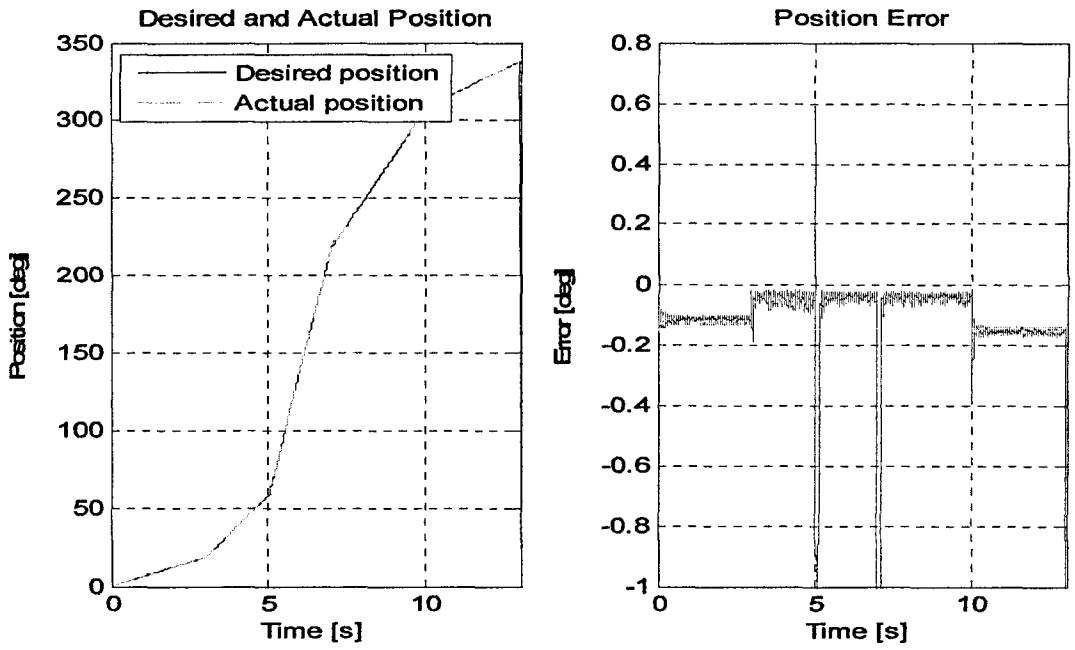

a) b)

Figure 7-19. Trajectory mode: Simulations with constant driving torque of 0.071Nm

7.3.2.2 Experimental results with constant driving torque

Figure 7-20 and 7-21 shows the experimental results with a constant driving torque. Figure 7-20 shows the desired and actual position, and the position error for a constant driving torque set to 0.047Nm, and Figure 7-21 illustrates the desired and actual positions, and the position error for a constant driving torque of 0.071Nm.

Just as in simulations, from Figures 7-20b and 7-21b it can be seen that when the desired velocity changes from 20deg/s to 80deg/s, and from 80deg/s to 30deg/s, relatively large fluctuation occurs. These fluctuations happen because of the large step change in velocity. This conclusions is confirmed by the fact that for small changes in velocity (e.g. from 6deg/s to 20deg/s, and from 30deg/s and 10deg/s) the large fluctuations disappear, as it can be seen from Figures 7-20b and 7-21b. The rather large

fluctuation, however, does not affect the smoothness of the controlled motion, but only the overall accuracy, as shown in section 7.3.1.

Similar to the observations draw from the analysis of the 'position' mode shown in section 7.3.1, when the control switches between the *gross mode* and the *fine mode*, the position error shows a slightly larger error for the PD control compared with the SMC. This denotes the superior performance of the SMC as discussed in the above sections.

For the same desired trajectory as shown in the simulations, it can be seen from both Figures 7-20b and 7-21b that the experimental results show a larger position error compared with the simulation analysis. This difference is because of the differences between the simulation model and experimental set-up, just as noticed in the previous chapter.

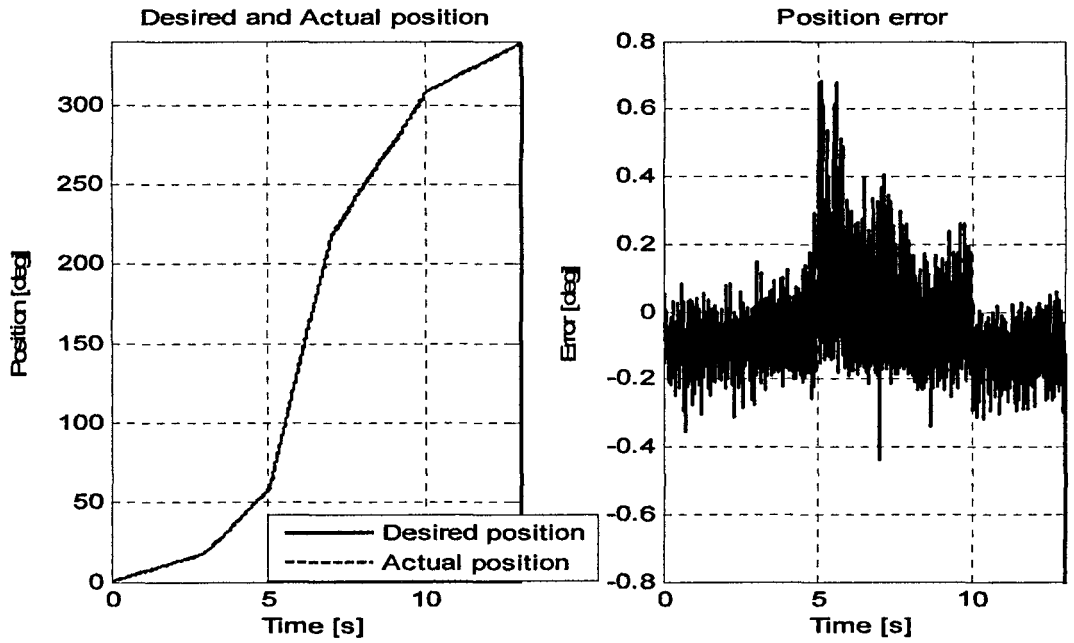

a) b)

Figure 7-20. Trajectory mode: Experiments with constant driving torque of 0.047Nm

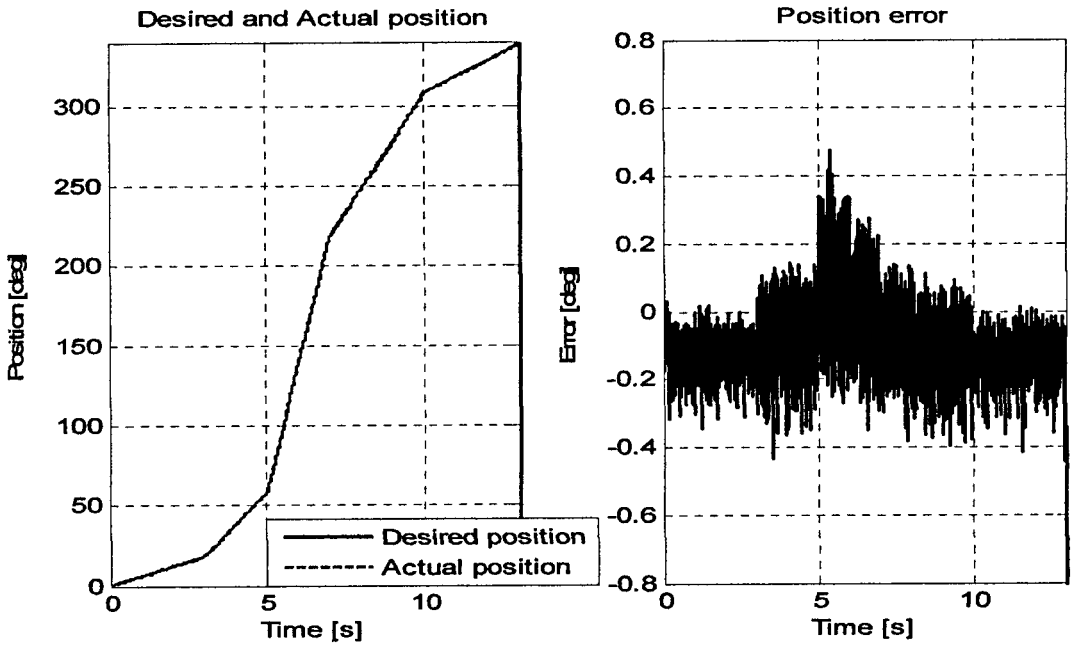

a) b)

Figure 7-21. Trajectory mode: Experiments with constant driving torque of 0.071Nm

7.3.2.3 Simulation results with variable driving torque

As for the analysis with constant torque, the same desired trajectory is analysed for a variable driving torque. The driving torque is steeply changed from 0.047 Nm to 0.071 Nm and back, as shown in Figure 7-22.

From the position error, shown in Figures 7-23b, the influence of the step change in the driving torque can be observed, just as it was noticed for the analysis completed in the previous chapter. This issue is related to the sensitivity of the controller, and it can be seen that both controllers have rather similar drawbacks regarding the sensitivity against external disturbances such as the driving torque. Nonetheless, the maximum position error obtained is still kept within the requirements.

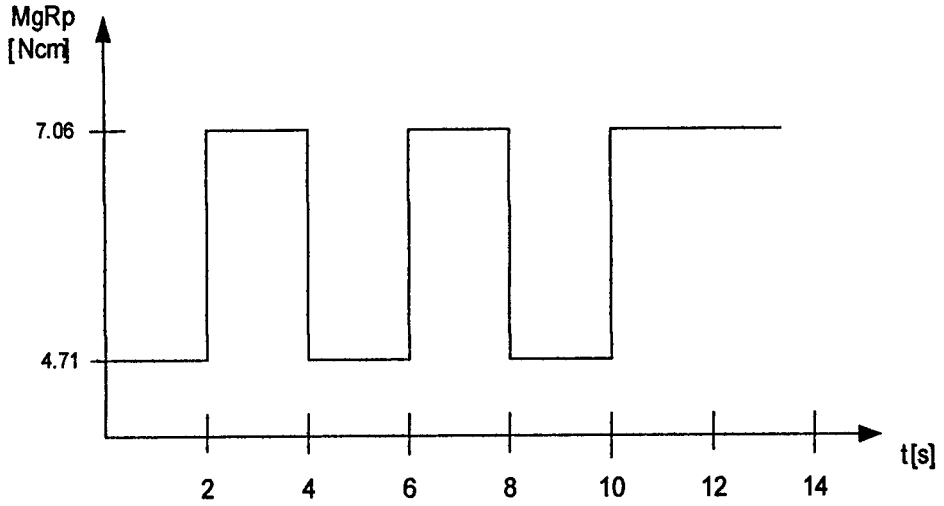

Figure 7-22. Driving torque profile

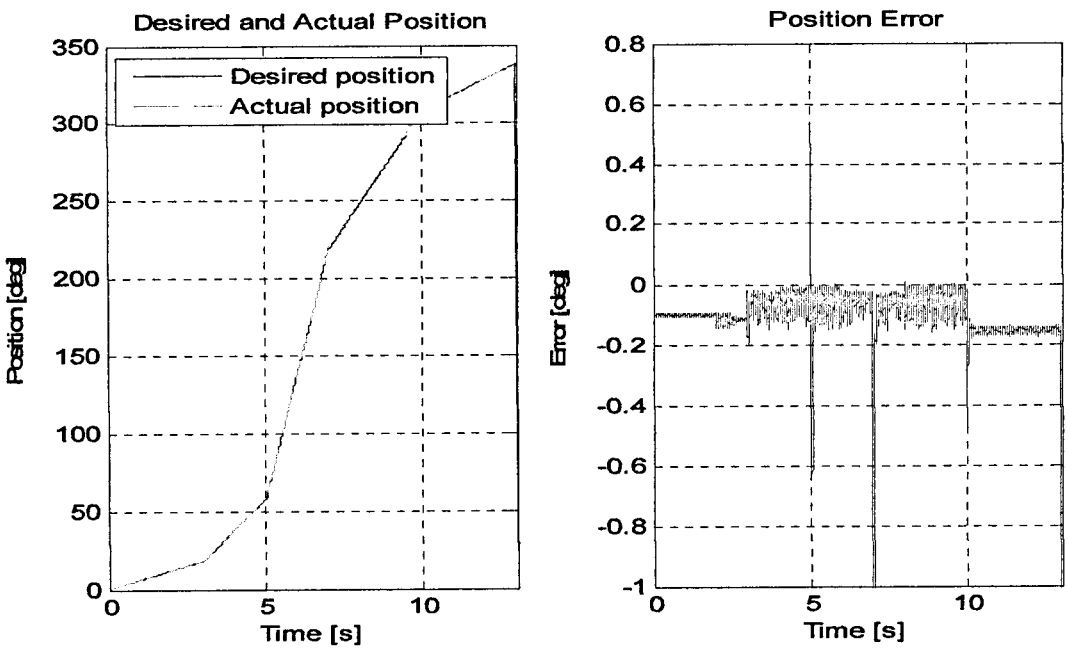

a) b)

Figure 7-23. Trajectory mode: Simulations with variable driving torque

7.3.2.4 Experimental results with variable driving torque

Figure 7-25 shows the experimental results for same desired trajectory while the driving torque is sharply changed from 0.0471Nm to 0.071Nm and back, as illustrated in Figure 7-24. From Figure 7-25b it can be seen that the effect of sharp change in driving torque does not significantly change the profile of the actual position. This observation is better illustrated in Figure 7-26, where the position error for both experimental results obtained with constant and variable driving torque are shown again, side-by-side. This outcome obtained means that the sensitivity of the controller, discussed in the simulation analysis with variable driving torque and also in the previous chapter, is higher in experiments. Thus, the main drawback of the controllers is the accuracy of the position error, and the lack of robustness with respect to sharply change in velocity.

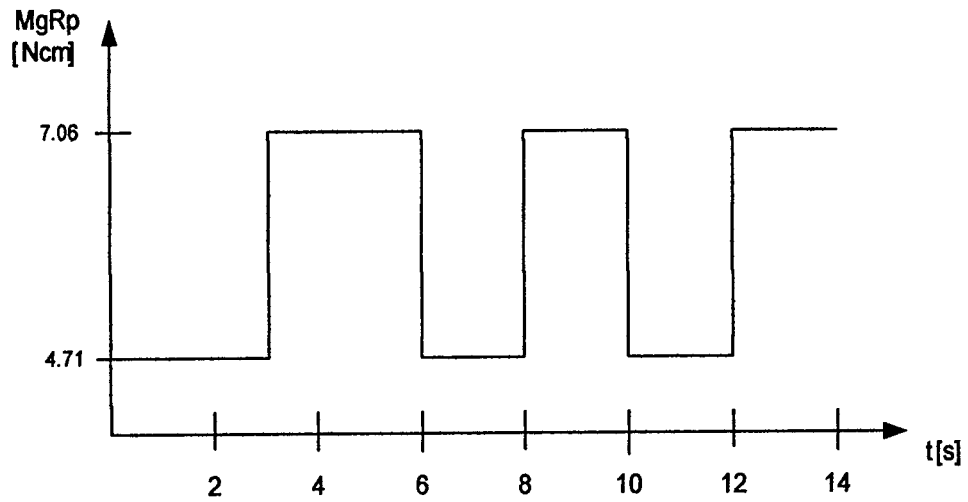

Figure 7-24. Driving torque profile

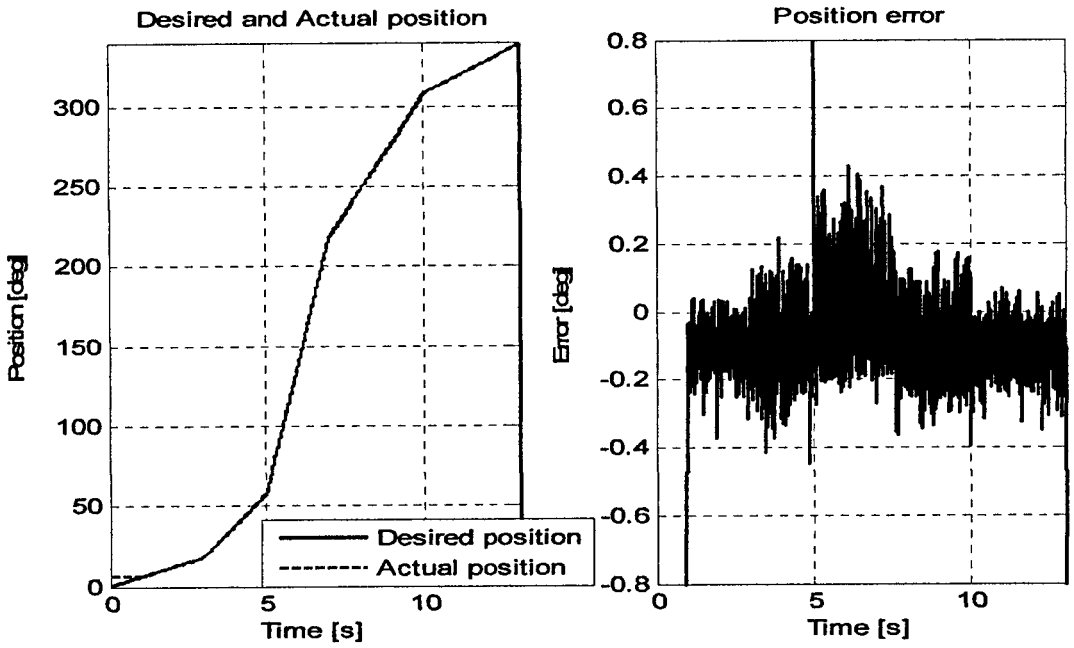

a) b)

Figure 7-25. Trajectory mode: Experiments with variable driving torque

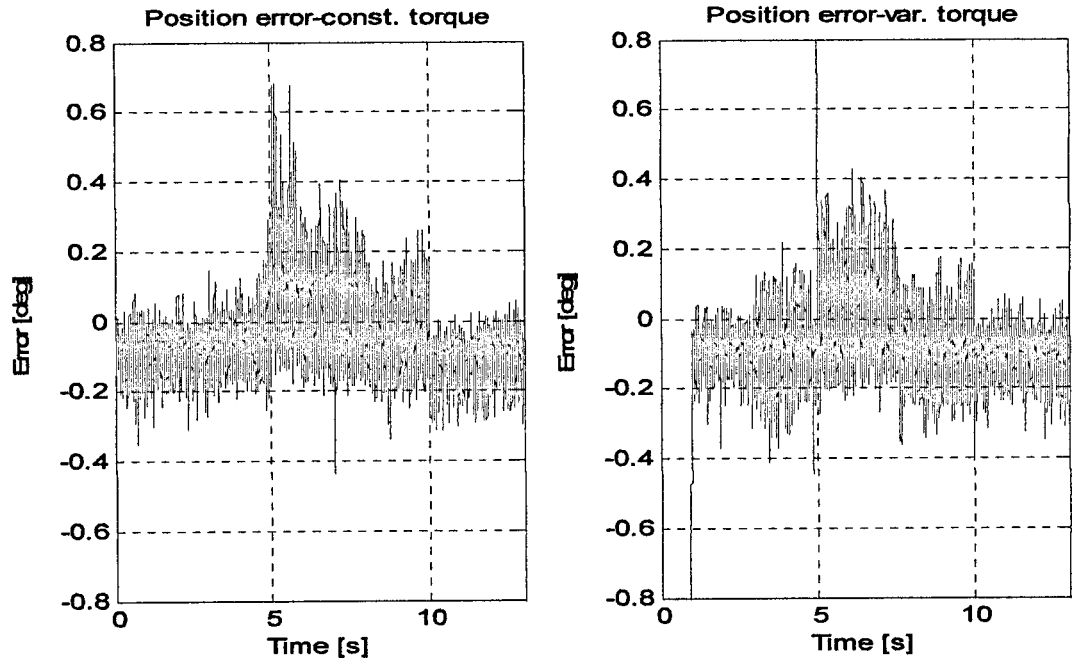

a) b)

Figure 7-26. Trajectory mode experiments: a) constant torque, b) variable torque

7.3.3 Region mode

The 'region' mode is illustrated for an initial position θ_i = 50deg and a final position θ_f = 80deg. Thus, zone I is defined from zero to 50deg; Zone II is between 50deg and 80deg; and zone III is defined for any position greater or equal to 80deg. An example of a control scenario in the 'region' mode is graphically illustrated in Figure 7-27. For the control of the motion in zone II, given by equation (7-6), the minimum allowed velocity $\dot{\theta}_{min}$ is set to 20deg/s, and K_{region} is set to 500. In the following subsections, a simulation and an experimental analysis is completed to illustrate the effectiveness of the proposed control strategy for the 'region' mode described in section 7.2.2.3.

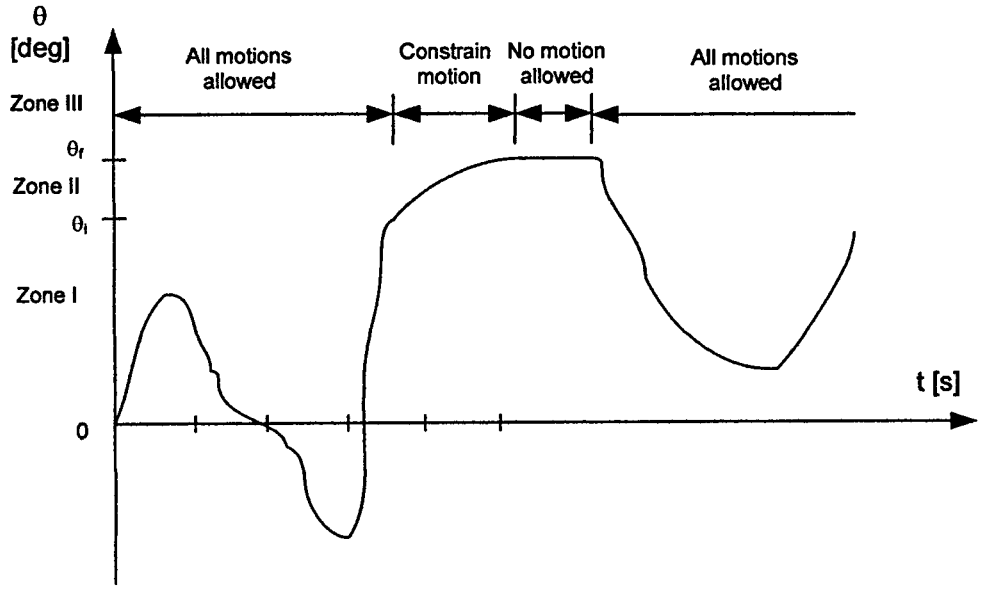

Figure 7-27. Example of a control scenario in 'region' mode for a revolute joint

7.3.3.1 Simulation results

Figures 7-28 and 7-30 show the simulation results for a constant driving torque set to 0.047Nm and 0.071Nm respectively. Figures 7-28a and 7-30a presents the actual

position, and Figures 7-28b and 7-30b illustrate the desired and actual velocity. By releasing a mass on the pulley the control system is letting the mass fall until the controlled shaft reaches the initial position θ_i = 50deg. This is the unrestricted motion, or zone I. Between the initial position θ_i = 50deg and the final position θ_f = 80deg the motion of the joint is restricted according to equation (7-6). This restrained motion, or zone II, is illustrated in Figures 7-29 and 7-31 for a driving torque of 0.047Nm and 0.071Nm respectively. From Figures 7-29 and 7-31 it can be seen that as soon as the actual position θ_a reaches the initial position θ_i = 50deg, the velocity of the revolute joint is starting to be controlled. As the revolute joint continues its motion towards the final safety boundary (i.e. final position θ_f = 80deg) the velocity is reduced until it reaches zero, which is equivalent to the restricted area, or zone III.

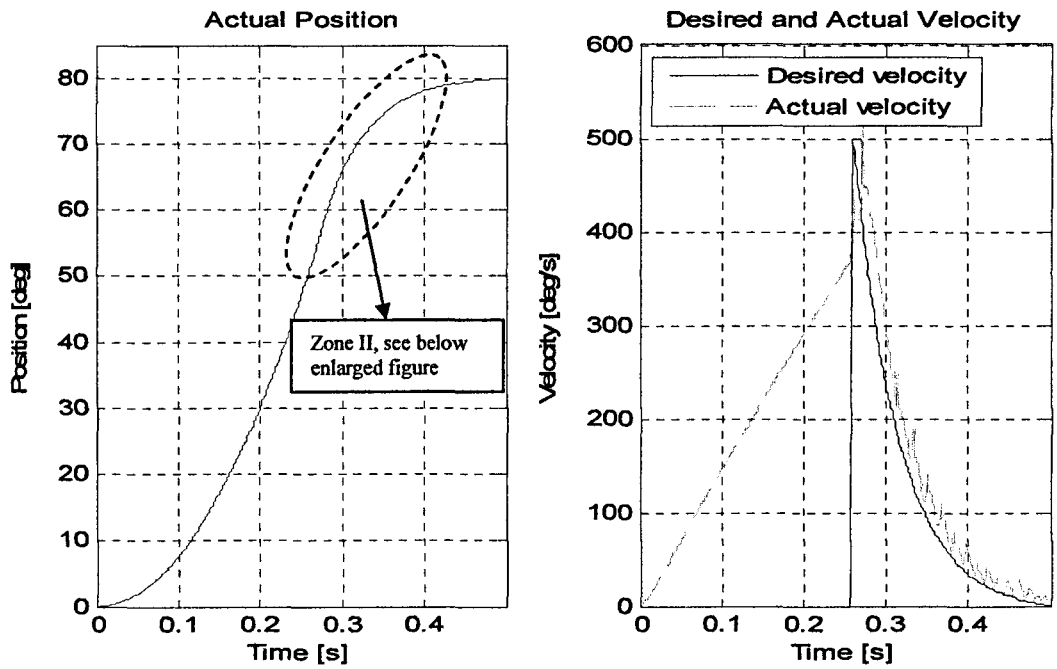

Figure 7-28. Region mode: Simulations with a constant driving torque of 0.047Nm

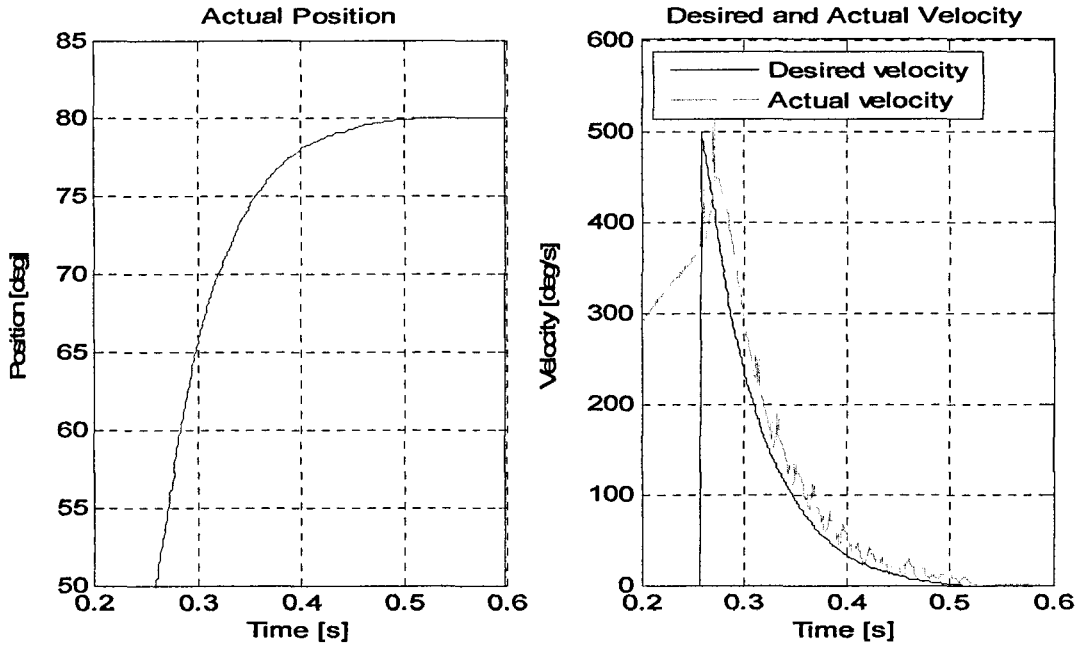

a) b)

Figure 7-29. Region mode: Simulations with a constant driving torque of 0.047Nm in zone II

From both Figures 7-29 and 7-31 it can be seen that the strategy employed is very efficient. As soon as the shaft's position reaches the initial position, the controller is activated and the velocity is decreased until the shaft is finally stopped. However, it can be seen that the actual velocity of the joint is not very smoothly controlled. The smoothness of the motion, however, is not of much concern in this case as the aim of the restrained motion for zone II is to give feedback to the user regarding how close s/he is to the safety boundary. Nevertheless, the quality of the controlled motion can be furthered improved as at the moment a simple PD controller is employed for this task.

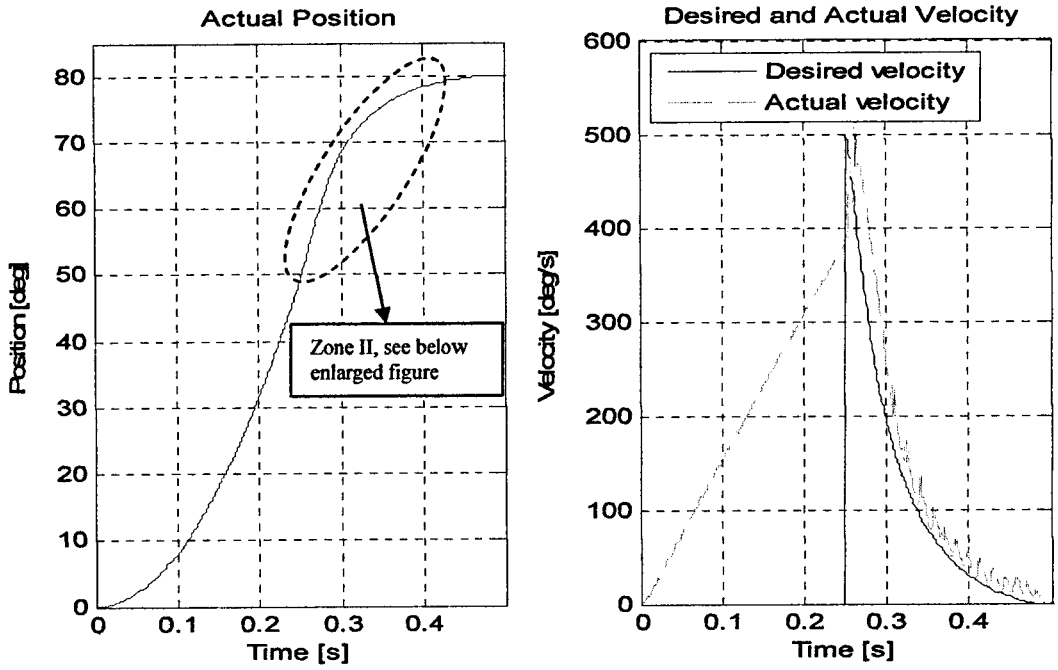

a) b)

Figure 7-30. Region mode: Simulation with a constant driving torque of 0.071Nm

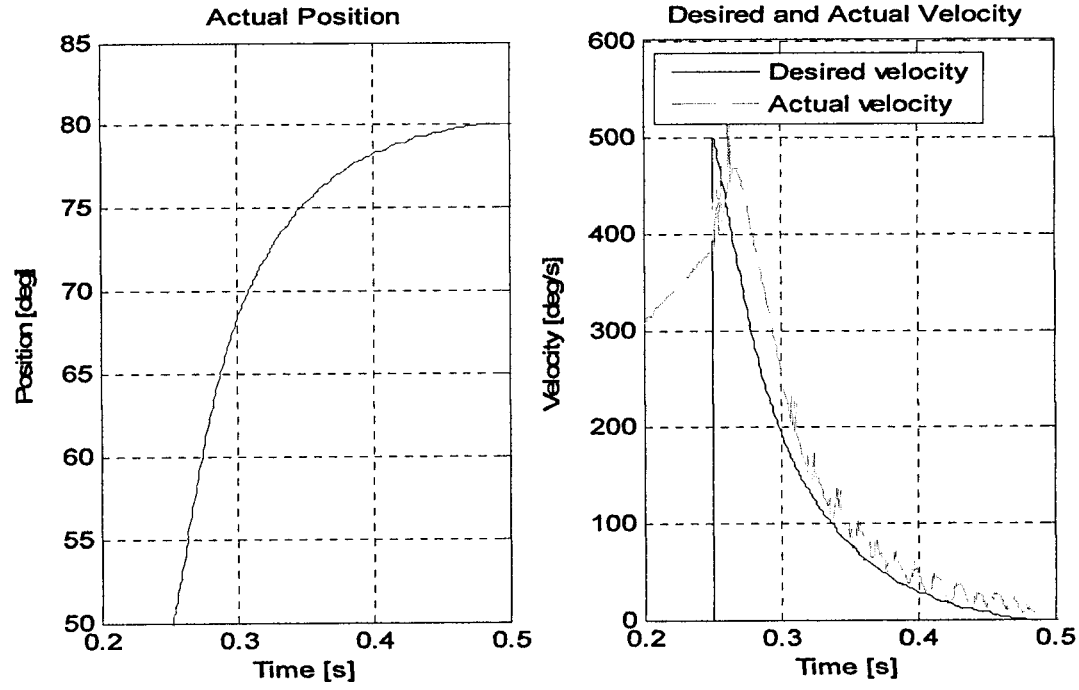

a) b)

Figure 7-31. Region mode: Simulation with a constant driving torque of 0.071Nm in zone II

7.3.3.2 Experimental results

Figures 7-32 and 7-34 show the experimental results for a constant driving torque set to 0.047Nm and 0.071Nm respectively. Figures 7-32a and 7-34a presents the actual position, and Figures 7-32b and 7-34b illustrate the desired and actual velocity. By releasing a mass on the pulley the control system allows the mass to fall until the controlled shaft reaches the initial position θ_i = 50deg. This is the unrestricted motion, or zone I. Between the initial position θ_i = 50deg and the final position θ_f = 80deg the motion of the joint is restricted according to equation (7-6). This restrained motion in zone II, is illustrated in Figures 7-33 and 7-35 for a driving torque of 0.047Nm and 0.071Nm respectively. From Figures 7-33 and 7-35, it can be seen that as soon as the actual position θ_a reaches the initial position θ_i = 50deg, the velocity of the revolute joint is controlled. As the revolute joint continues its motion towards the final safety boundary (i.e. final position θ_f = 80deg) the velocity is reduced until the shaft is stopped, which is equivalent to the restricted area, or zone III.

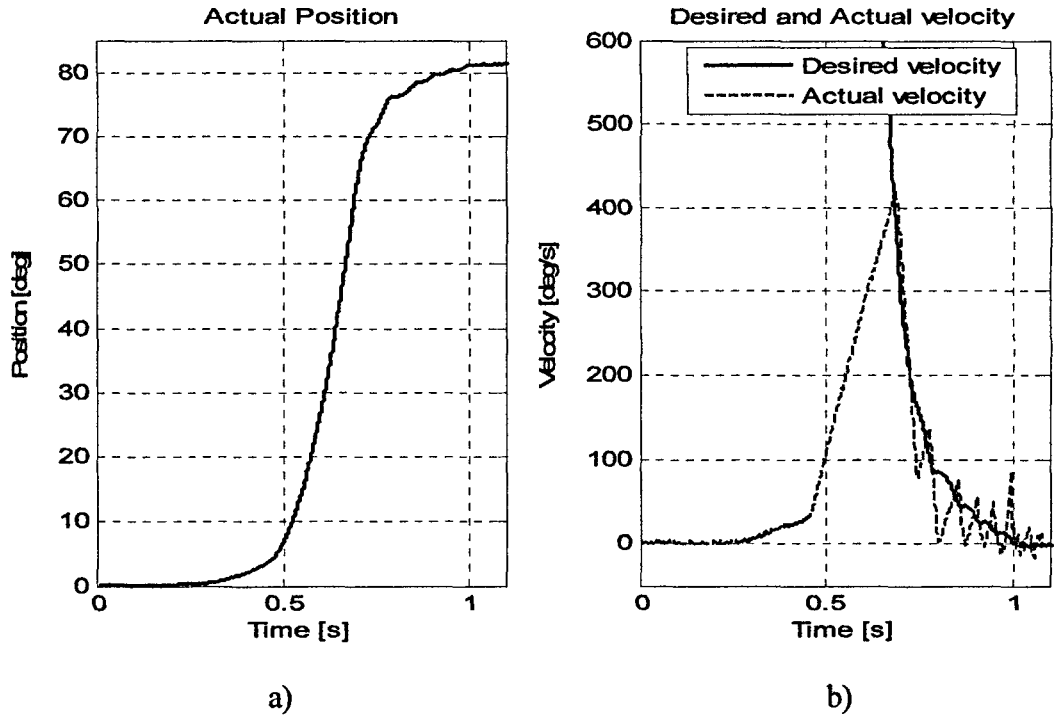

a) b)

Figure 7-32. Region mode: Experiments with a constant driving torque of 0.047Nm

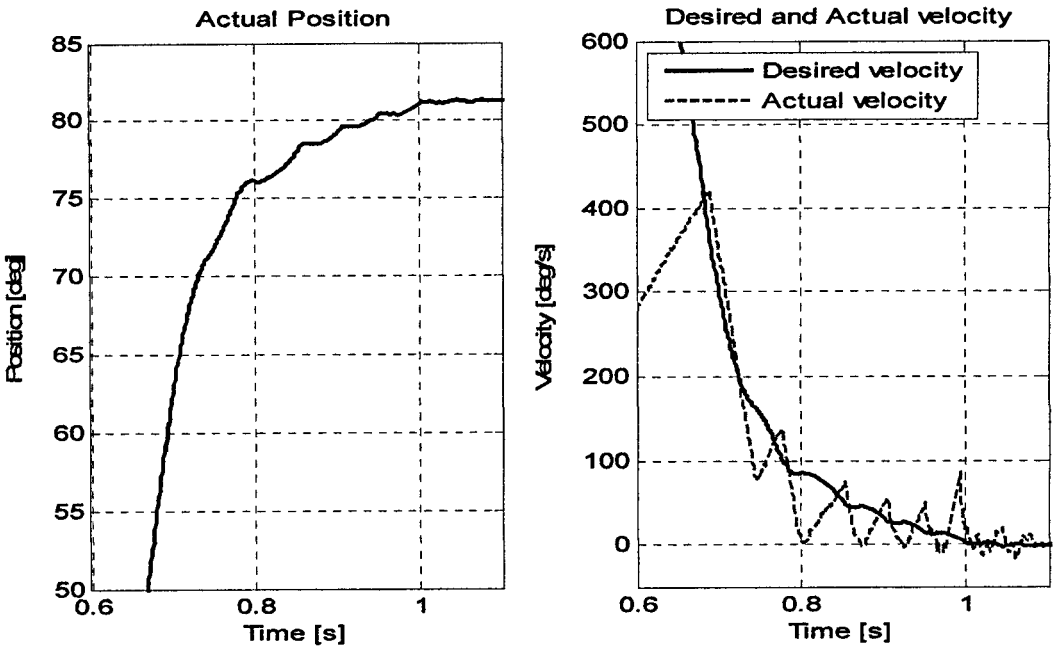

a) b)

Figure 7-33. Region mode: Experiments with a constant driving torque of 0.047Nm in zone II

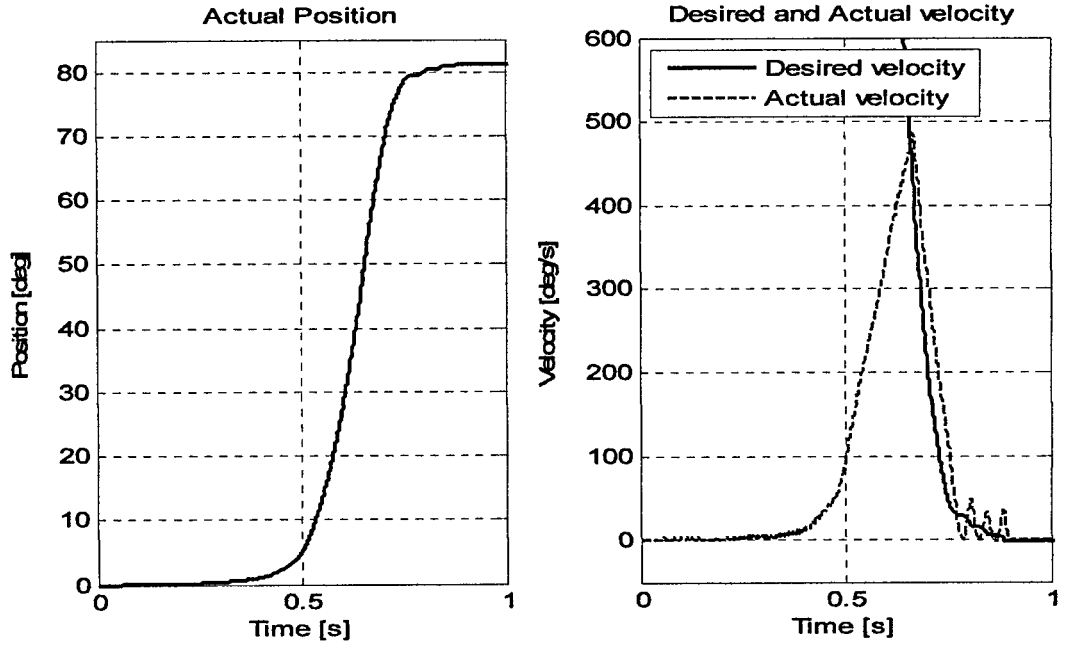

a) b)

Figure 7-34. Region mode: Experiments with a constant driving torque of 0.071Nm

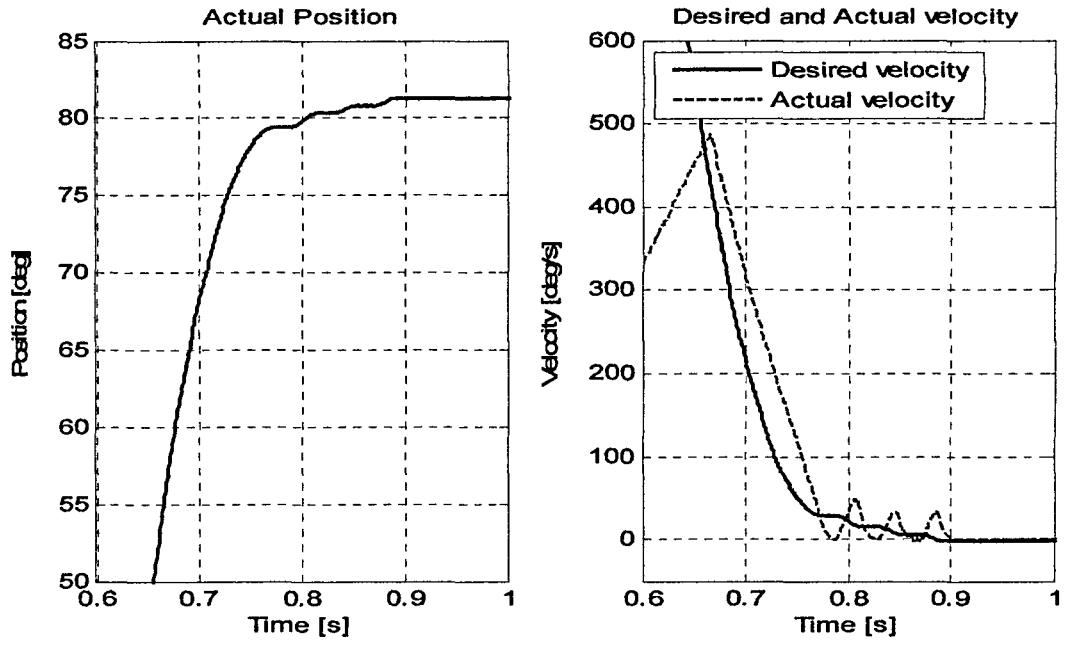

a) b)

Figure 7-35. Region mode: Experiments with a constant driving torque of 0.071Nm in zone II

From both Figures 7-33 and 7-35 it can be seen that the strategy employed is very efficient, just as shown in the simulation analysis. As soon as the shaft's position reaches the initial position, the controller is activated and the velocity is decreased until the shaft is finally stopped. However, it can be seen that the actual velocity of the joint is not very smoothly controlled, also shown in the simulation study. The smoothness of the motion, however, is not of concern in this case as the aim of the restrained motion for zone II is to give feedback to the user regarding how close s/he is to the safety boundary. Nevertheless, the quality of the controlled motion can be further improved as at the moment a simple PD controller is employed for this task.

Experimental result with a user-input force is shown in Figures 7-36 and 7-37. The actual position of the one-DOF joint under user-input force is shown in Figure 7-36, and the velocity controlled in zone II is shown in Figure 7-37b. From Figure 7-37 it can be seen that as soon as the joint position reaches the initial position, and the user continues to push towards zone III, the control of the joint starts restraining the action of the user until it finally stops. However, if the user pushes the end-effector slower than the

restrained velocity $\dot{\theta}_{lim}$, as discussed in section 7.2, it can be seen from Figure 7-37b (for 5.1s<t<5.7s) that the actual velocity is restrained only for joint velocities greater or equal to the derived restrained velocity, as given by equation (7-8).

From Figures 7-32 to 7-37, it can be seen that the strategy employed to restrain an external driving torque (i.e. due to gravity or due to human input force) is efficient. However, when the motion is approaching the final boundary the motion becomes discontinuous. This is due to the fact that a velocity control strategy is used, while the velocity is obtained by approximating the measured position. This needs to be improved in future by either employing an accelerometer to obtain the velocity by integrating the measured value, or by adapting the control strategy so that a position control is used rather than a velocity control.

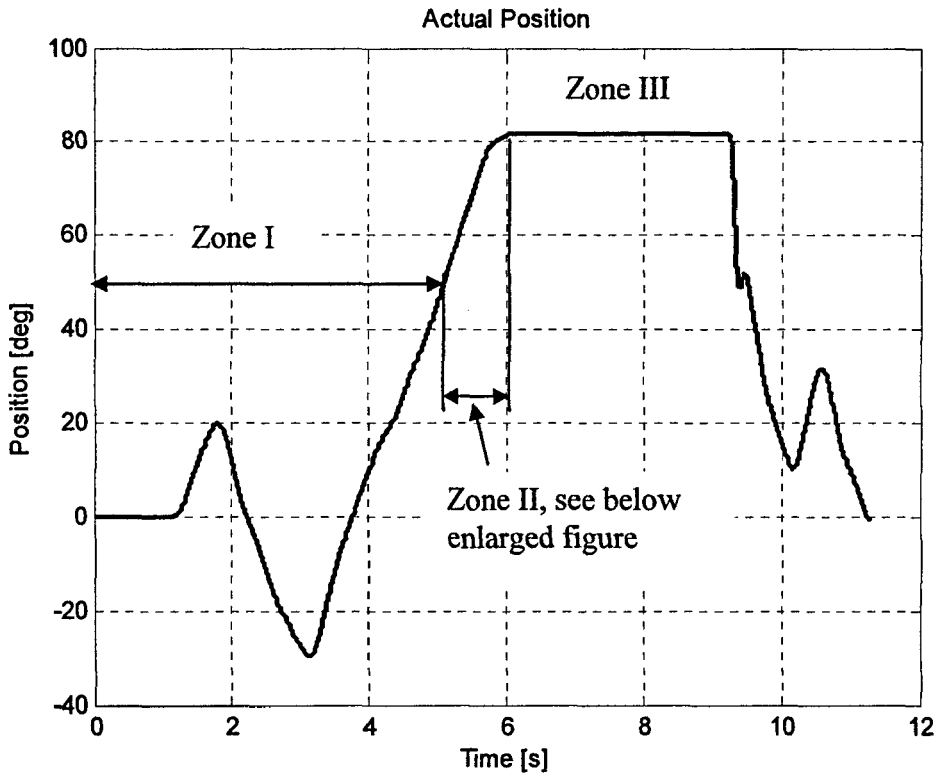

Figure 7-36. Region mode: Experiments with a user-input driving torque

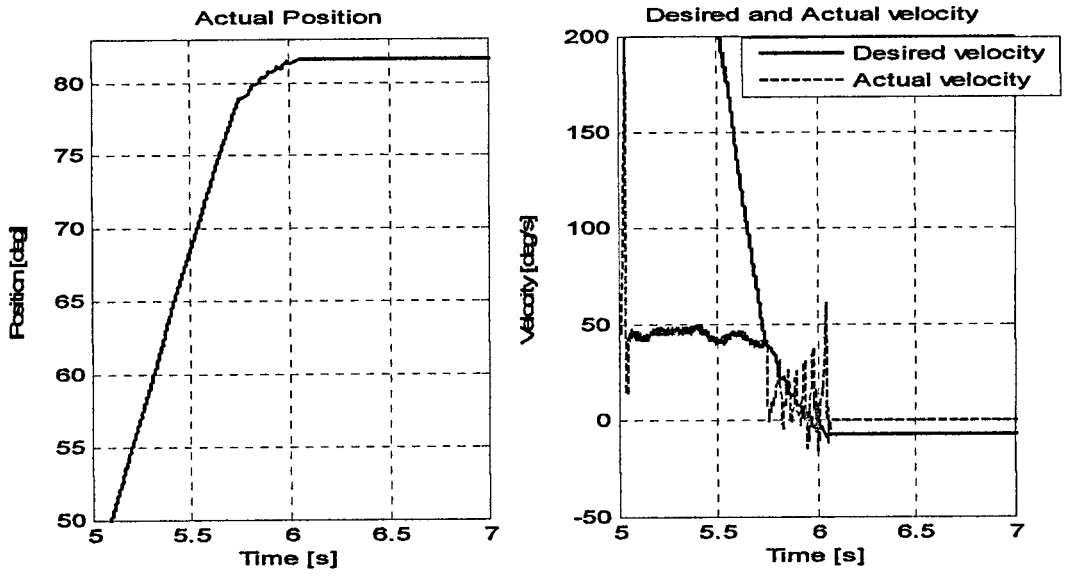

a) b)

Figure 7-37. Region mode: Experiments with a user-input driving torque in zone II

7.4 Conclusions

In this chapter was presented the control of an actively restrained passive revolute joint. An efficient control strategy based on a combination of PD control and SMC was developed. It was shown that the control strategy is capable of regulating the position of the shaft rather smoothly and accurately for a wide range of velocities.

A strategy to reach a predefined position, to follow a predefined path, and to stay within a predermined region was also developed in this chapter. The strategy to achieve a task was shown to be efficient, however, because of the steeply change in velocity required to reach a predefined position and to follow a predefined path, the accuracy of the system was significantly affected. Every time a large velocity change occurs a fluctuation can be seen in the positional error. This indicates that accelerated motion takes place from one mode to another and this is ignored in modelling, but accounts for the sudden spikes observed in the results. This is less noticeable in the experimental work, because real world includes the effect of acceleration as it can be seen from the Figures 7-9 and 7-11.

This fluctuation, however, does not affect the smoothness of the motion. Furthermore, for the 'position' and 'trajectory' modes, when the control switches between the *gross mode* and the *fine mode*, the position error shows a larger error for the PD control compared with the SMC. This denotes the superior performance of the SMC due to the fact that when the system is in the sliding mode, the tracking error is independent of the system dynamics, while the PD controller is dependent of the system dynamics. Thus, the main drawback of the controllers is the positional accuracy when the velocity is sharply altered.

For the 'region' mode, it can be seen that the strategy employed to restrain an external driving torque (i.e. due to gravity or due to human input force) is efficient. However, when the motion is approaching the final boundary the motion becomes discontinuous. This is due to the fact that a velocity control strategy is used, while the velocity is obtained by approximating the measured position. This needs to be improved in future by either employing an accelerometer to obtain the velocity by integrating the measured value, or by adapting the control strategy so that a position control is used rather than a velocity control.

Chapter 8
Control of a Two-DOF Actively Restrained Passive Mechatronic System

8.1 Introduction

This chapter describes the control of a two-DOF actively restrained passive mechatronic system. The control strategy shown in the previous chapter for a one-DOF system is extended in this chapter for a two-DOF manipulator. This issue was first addressed in Chapter 3 and is fully described in this chapter. By measuring joint positions and the user-input force, a 'task interpreter algorithm' is developed for task definition so that efficient control is guaranteed. The control strategy employed for the revolute joint in the previous chapter is retained and is further applied for a prismatic joint. Simulation results are carried out to demonstrate the effectiveness of the proposed control system for all three modes of operation: (1) reach a predefined position, (2) follow a predefined trajectory, and (3) stay within a predefined safety region.

8.2 Task Interpreter Algorithm

The interaction between the surgeon and the proposed actively restrained passive mechatronic system conforms to the scheme shown in Figure 8-1. The surgeon selects one of the three modes of operation (i.e. *'position'*, *'trajectory'* or *'region'* mode) that

are part of the 'Task Interpreter Algorithm' and the direction and magnitude of the user-input force are used by the respective control strategy to restrict the motion accordingly.

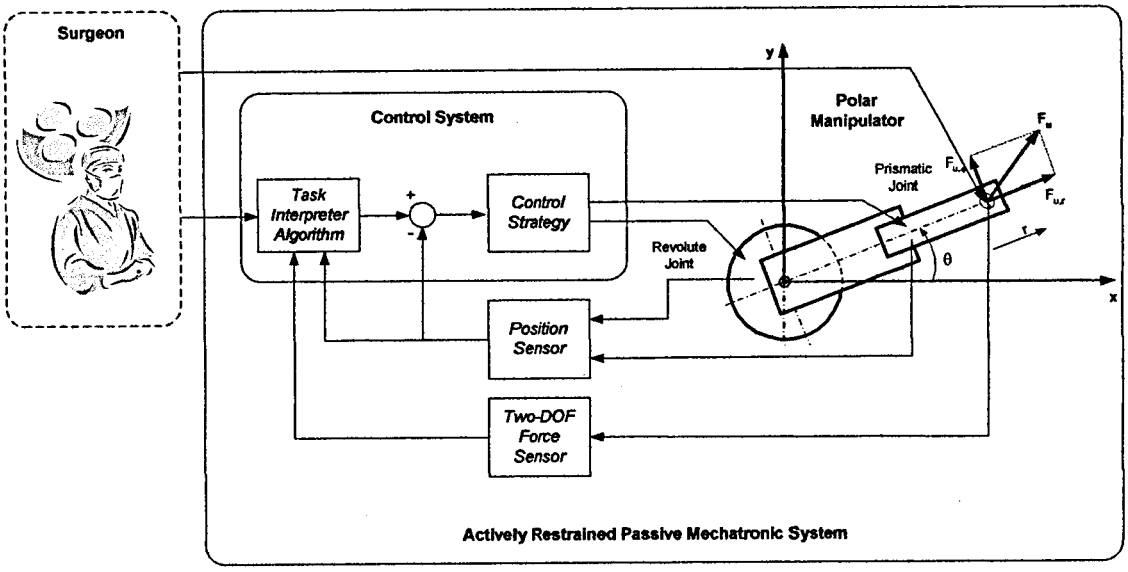

Figure 8-1. Scheme of the interaction between the surgeon and the proposed actively restrained passive mechatronic system

Consider the two-DOF polar manipulator (RP) shown in Figure 8-2. The end-effector is required to track a path $P_d(x_d, y_d)$ while the user applies a force $\mathbf{F}_u = (F_{u,r}\ F_{u,\varphi})^T$, where $F_{u,\varphi}$ and $F_{u,r}$ are the tangential and radial components of the user-input force as shown in Figure 8-2.

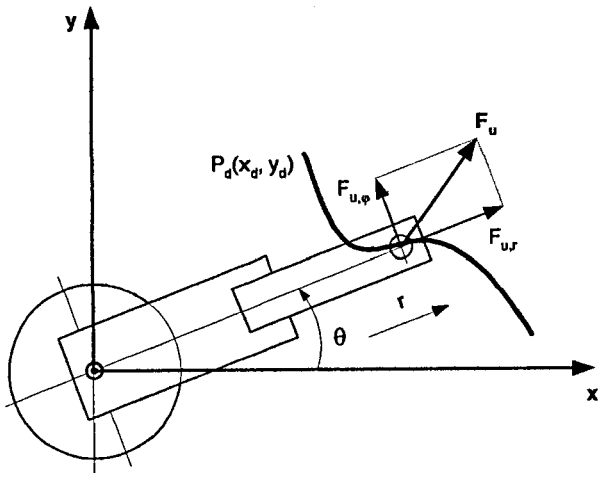

Figure 8-2. Trajectory following using a passive polar manipulator

Due to the joint actuators limited output torque, (i.e. limited frictional torque/force), a maximum magnitude of the user-input force needs to be continuously specified/computed, as above such a force the motion of the end-effector cannot be controlled. It should be noted that the maximum magnitude of the user-input force allowable is a function of the direction of the user-input force and the joint variables r and θ. Furthermore, a minimum driving force needs to be specified in order to avoid undesired movements caused by the user when s/he does not desire to move the end-effector while holding the control handle. Thus, in order to effectively control the manipulator in all three modes of operation certain conditions apply as shown in Figure 8-3. It can be seen that dependently on the user-input force three cases are distinguished:

1. If the components $F_{u,\varphi}$ and $F_{u,r}$ of the user-input force, $\mathbf{F}_u = (F_{u,r}\ F_{u,\varphi})^T$, are less than the predefined values $F_{u,\varphi\,min}$ and $F_{u,r\,min}$ respectively, then the system will not allow motion;

2. If only one component of the user-input force is greater than a minimum defined magnitude than the motion will depend on the desired path and the kinematic configuration of the arm as defined below:

2.1. if $|F_{u,\varphi}| > |F_{u,\varphi\,min}|$ and $|F_{u,r}| \leq |F_{u,r\,min}|$ the control system will not allow motion in the r direction, but will allow motion in the θ direction so long as the orientation of the desired path coincides with the θ direction;

2.2. if $|F_{u,r}| > |F_{u,r\,min}|$ and $|F_{u,\varphi}| \leq |F_{u,\varphi\,min}|$ the control system will not allow motion in the θ direction, but will allow motion in the r direction so long as the orientation of the desired path coincides with the r direction;

3. If the components $F_{u,\varphi}$ and $F_{u,r}$ of the user-input force are greater than the predefined values $F_{u,\varphi\,min}$ and $F_{u,r\,min}$ respectively, then the motion is allowed on both axes;

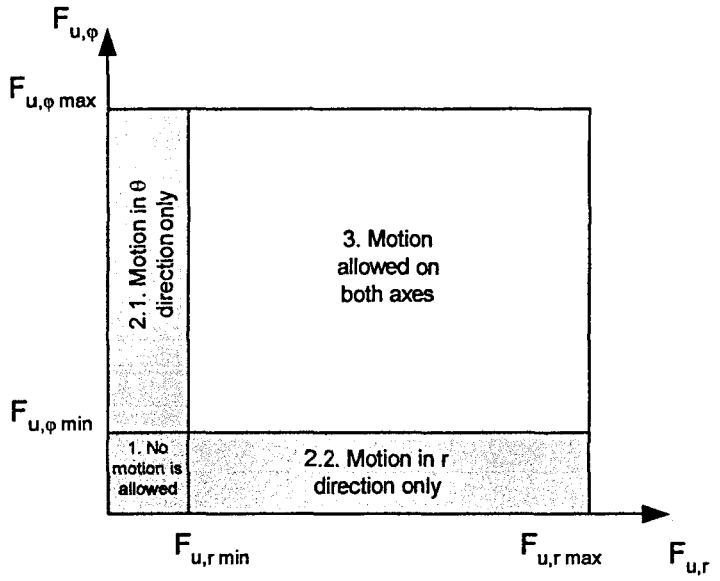

Figure 8-3. Diagram of the user-input force strategy employed for task control

In addition, due to the existing dry friction in the proposed joint mechanism, which is based on an electromechanical friction clutch, a minimum velocity at which each joint can effectively be controlled has to be defined. It was shown in Chapter 5, section 5.4 that for efficient control (i.e. smooth and accurate motion) the velocity of the joint has to be above a certain value, $\mathbf{V_{min}}$, to avoid the unpredictability and jerkiness introduced by the stick-slip effect. A maximum velocity $\mathbf{V_{max}}$ of each joint is also specified so that the motion due to the surgeon's input-force is effectively controlled (i.e. due to the braking performance of the proposed brake/clutch).

The above-mentioned specifications are part of the 'task interpreter algorithm' and based on them three modes of operations have been developed. Assuming the motion of the manipulator is allowed on both axes (i.e. the components of the user-input force are greater than the minimum defined magnitude as shown in Figure 8-3), the development of the three modes of operation: *'position'*, *'trajectory'* and *'region'* mode, is described in the following sections.

8.2.1 'Position' mode

In the *'position'* mode, the initial and final desired points can be defined in both Cartesian or polar coordinates. Given an initial position point $Q_i(r_i, \theta_i)$ and a final position point $Q_f(r_f, \theta_f)$ in polar coordinates, as shown in Figure 8-4, the intermediate controller desired input positions, between these two points, are obtained using a linear polynomial.

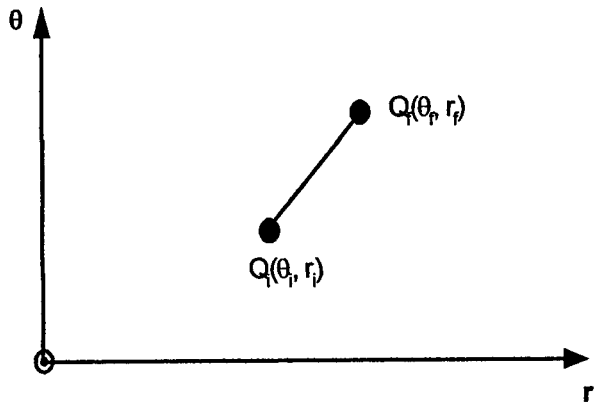

Figure 8-4. Initial and final points in polar coordinates

Bearing in mind that a minimum and a maximum velocity are initially specified, the desired control in the *'position'* mode is performed following the flow chart illustrated in Figure 8-5. Using the angular and linear displacements (i.e. $\Delta\theta = \theta_f - \theta_i$, and $\Delta r = r_f - r_i$), and the minimum and maximum predefined velocities for each joint, $V_{\theta,\,min}$ and $V_{\theta,\,max}$ for the revolute joint, and $V_{r,min}$ and $V_{r,max}$ for the prismatic joint, a maximum and a minimum time required to move from the initial to the final positions on both axes can be calculated as given by the equations below:

$$t_{\theta,\max} = \frac{\Delta\theta}{V_{\theta,\min}} \quad and \quad t_{\theta,\min} = \frac{\Delta\theta}{V_{\theta,\max}} \qquad \textbf{(8-1)}$$

$$t_{r,\max} = \frac{\Delta r}{V_{r,\min}} \quad and \quad t_{r,\min} = \frac{\Delta r}{V_{r,\max}} \qquad \textbf{(8-2)}$$

It can be seen from Figure 8-5 that the minimum and maximum times obtained for the revolute joint and for the prismatic joint are used to split the *'position'* mode in two different cases. For clarity, these two cases are illustrated in Figure 8-6.

In 'Case I', shown in Figure 8-6, the range $t_\theta \in [t_{\theta,min}, t_{\theta,max}]$ and the range $t_r \in [t_{r,min}, t_{r,max}]$ overlap (i.e. $t_\theta \cap t_r \neq 0$). This means that both joints can be controlled to reach the desired position simultaneously. The maximum value of the overlap, t_f, is selected as the time in which both joints will reach the desired points, θ_f and r_f. The position rates for the revolute and prismatic joints are calculated as $m_\theta = \Delta\theta/t_f$ and $m_d = \Delta r/t_f$, respectively. Consequently, the desired angular and linear positions $\theta_d(t)$ and $r_d(t)$ are obtained using the linear polynomials given by:

$$\theta_d(t) = \theta_i + m_\theta t \qquad \textbf{(8-3)}$$

$$r_d(t) = r_i + m_d t \qquad \textbf{(8-4)}$$

with $0 \leq t \leq t_f$ and $t = nT$, where $n = 0, 1, 2, \ldots$, and T is the sampling time.

In 'Case II' the range $[t_{\theta,\,min}, t_{\theta,\,max}]$ and $[t_{r,\,min}, t_{r,\,max}]$ do not have any common point (i.e. $t_\theta \cap t_r = 0$). This means that it is not possible for the joints to reach the respective desired position at the same time. The position rate for the revolute and prismatic joints, m_θ and m_d respectively, are selected so that the stick-slip is fully compensated for (i.e. in the 'fine' mode of the control strategy). The desired angular and linear positions, θ_d and r_d, are obtained using the linear polynomials given below:

$$\theta_d(t) = \theta_i + m_\theta t \text{ , where } 0 \leq t \leq t_{\theta,fine} \qquad \textbf{(8-5)}$$

$$r_d(t) = r_i + m_d t \text{ , where } 0 \leq t \leq t_{r,fine} \qquad \textbf{(8-6)}$$

where, $t_{\theta,fine}$ is the time obtained for the revolute joint for a position rate of 20deg/s, $t_{\theta,fine} = \Delta\theta/20$, and $t_{r,fine}$ is the time obtained for the prismatic joint for a position rate of 20mm/s, $t_{r,fine} = \Delta r/20$.

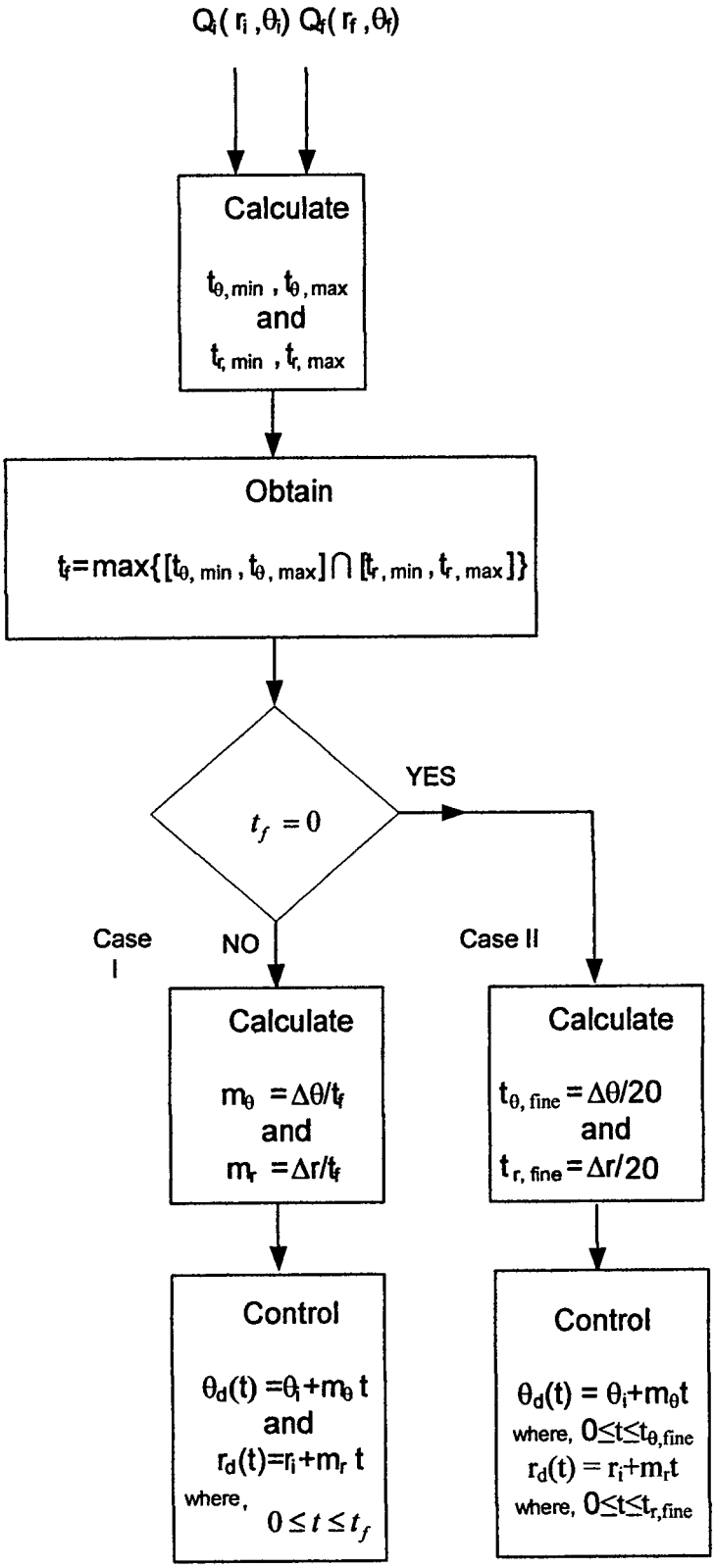

Figure 8-5. Flow chart illustrating the method used for implementing the *'position'* mode

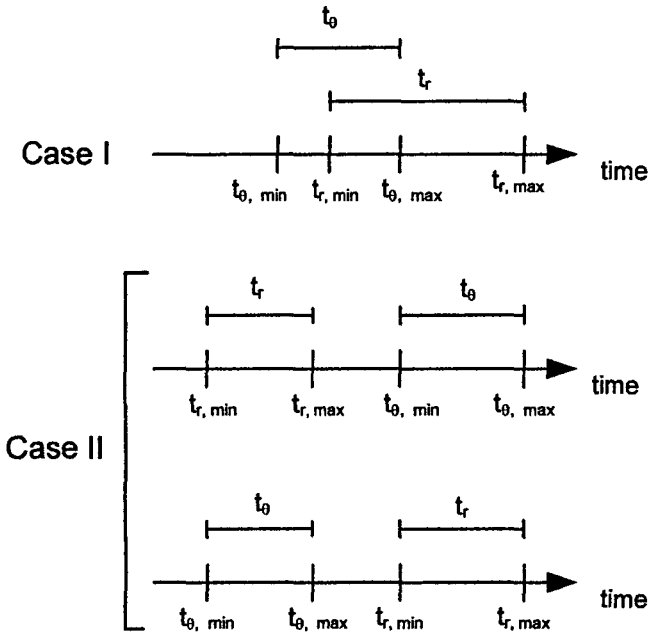

Figure 8-6. Graphic representation of the *'position'* mode conditions

Because of the fact that the velocity can only be regulated between the predefined velocities, $\mathbf{V_{min}}$ and $\mathbf{V_{max}}$, as discussed at the beginning of the section 8.2, the motion between the desired position points cannot be blended at the beginning and end of the motion, as it is usually performed by active robots. Thus, at the beginning and end of the motion, the system has to start and stop from an initial velocity. This discontinuity in the velocity command contributes to a decrease in the overall accuracy of the manipulator.

An example of the task definition in the *'position'* mode, is given in Figure 8-7. An initial and a final position points are selected in Cartesian space as shown in the top left graph of Figure 8-7a. The desired positions are then converted into polar coordinates, and the corresponding points are shown in the top right graph of Figure 8-7a. Consequently, the angular and linear displacements (i.e. $\Delta\theta = \theta_f - \theta_i$, and $\Delta r = r_f - r_i$) can be obtained. With the displacement obtained in this way, the motion on each axis can be defined as given by equations (8-3) and (8-4). The controlled motion $\theta_d(t)$ and $r_d(t)$, are

shown by the bottom two graphs of Figure 8-7a. The complete motion in Cartesian coordinates is illustrated in Figure 8-7b.

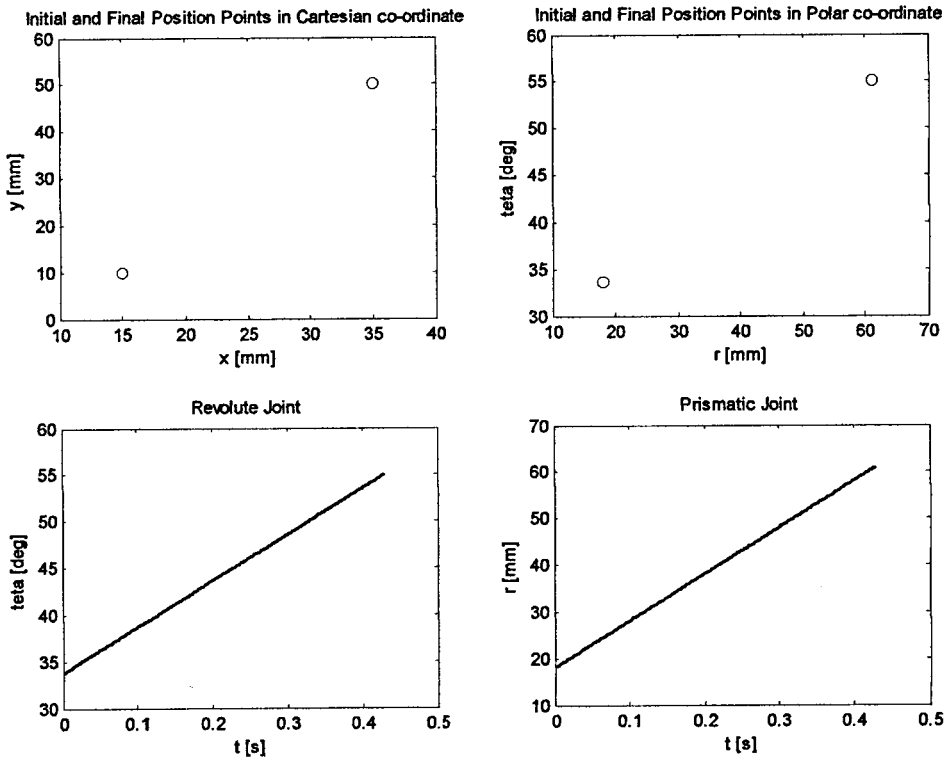

a)

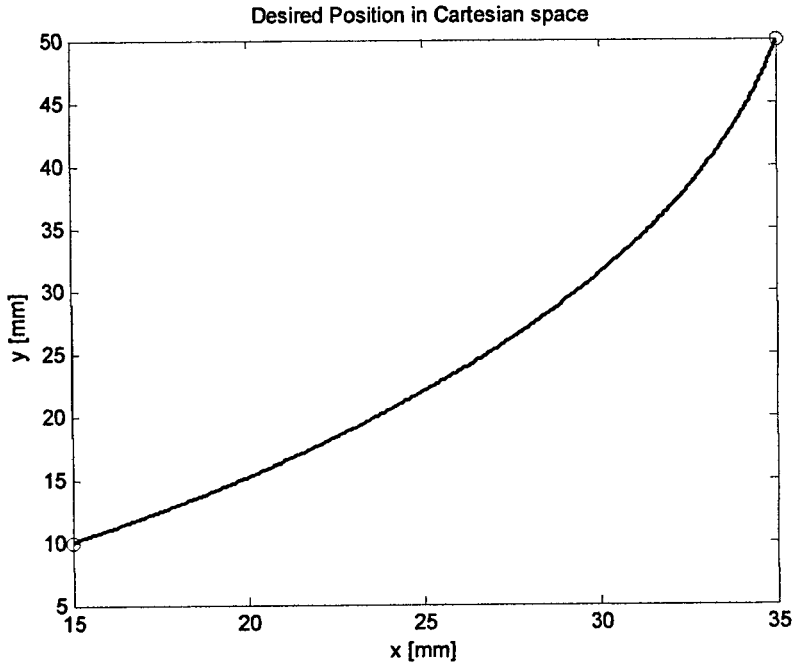

b)

Figure 8-7. Example of task definition for *'position'* mode

8.2.2 'Trajectory' mode

In general, polynomial functions describe the position of each Cartesian variable with respect to time. This allows for the velocity and acceleration of the motion along the path to be specified. For this application only the path itself is predefined, because the velocity on the path needs to be limited in order to effectively control the motion of the proposed clutch mechanism, as discussed in section 6.2. A desired path is defined as a set of points in either Cartesian or polar coordinates.

The method employed to define the desired trajectory of the proposed actively restrained passive mechatronic system involves approximating the joint-space path with a set of straight lines. The implementation of the *'trajectory'* mode is shown in the flow chart displayed in Figure 8-8. A Cartesian path is converted into polar coordinates, and a number of points are selected on the polar coordinates path so that the path can be approximated using straight lines. By considering a new point, a joint-space distance $\Delta Q_j = Q_i - Q_{i-1}$ further along the path, the amount that each joint needs to be moved to reach the new point can be calculated (i.e. $\Delta\theta_j = \theta_i - \theta_{i-1}$, and $\Delta r_j = r_i - r_{i-1}$). Just as it was shown for the *'position'* mode, from the angular and linear displacements $\Delta\theta_j$ and Δr_j, and from the minimum and maximum predefined velocities for each joint, $V_{\theta,\,min}$ and $V_{\theta,max}$ for the revolute joint, and $V_{r,min}$ and $V_{r,max}$ for the prismatic joint respectively, a maximum and a minimum time required to move from the initial point to the final one on both axes can be calculated as given by equations (8-1) and (8-2). Depending on the minimum and maximum time obtained for both the revolute and the prismatic joints, the *'trajectory'* mode is divided into two cases, similar to the *'position'* mode situations shown in Figure 8-6. Thus, the *'trajectory'* mode is defined as a set of displacements, where each displacement is controlled as shown for the *'position'* mode.

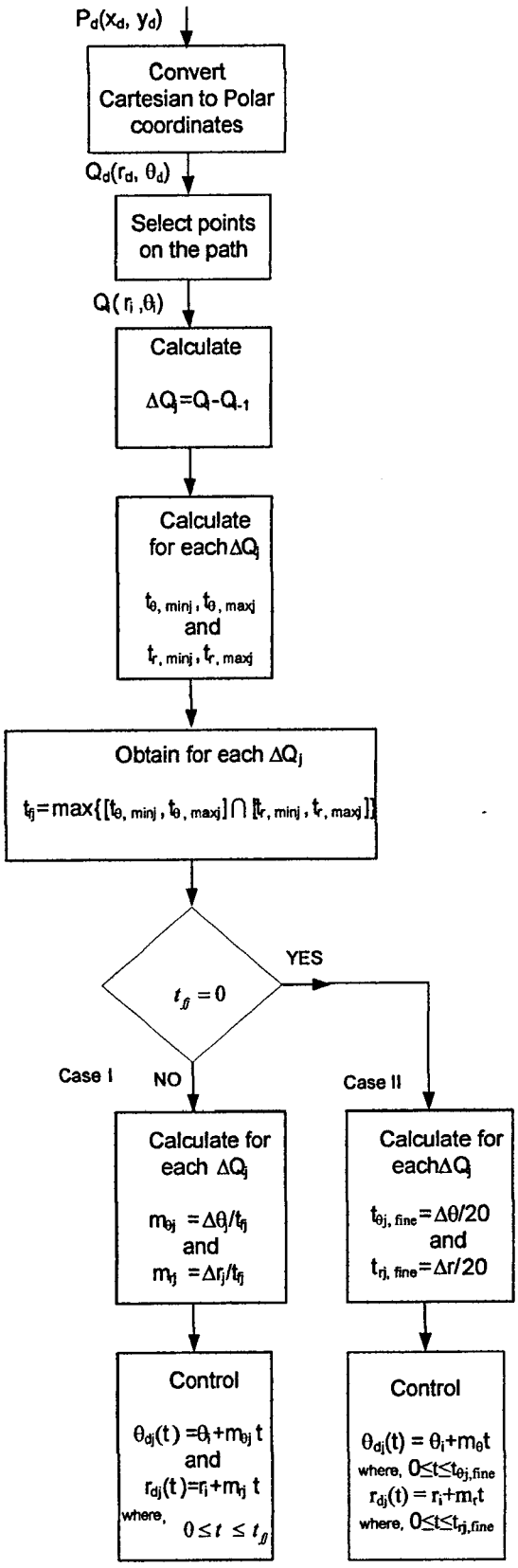

Figure 8-8. Flow chart illustrating the method used for implementing the *'trajectory'* mode

An example of task definition in *'trajectory'* mode is given in Figure 8-9. A Cartesian path is defined and a polar space path is obtained, illustrated in Figure 8-9a and Figure 8-9b respectively. Next, several position points are selected on the polar path so that the path can be approximated using straight lines. Thus, in order to accurately represent a path, a reasonable number of points need to be specified. For the example illustrated in Figure 8-9, five position points are defined as shown in the top left graph of Figure 8-10. Following the flow chart illustrated in Figure 8-8, the motion on each axes can be obtained. The motions of the revolute and prismatic joints are illustrated by the bottom graphs of Figure 8-10.

The approximated paths obtained in this way are presented in Figure 8-11. Figure 8-11a shows the approximated path in polar coordinates, and Figure 8-11b shows the approximated path in Cartesian coordinates. The desired and approximated paths in polar and Cartesian coordinates are shown in Figure 8-12. It can be seen that there are very small errors between the desired and approximated paths.

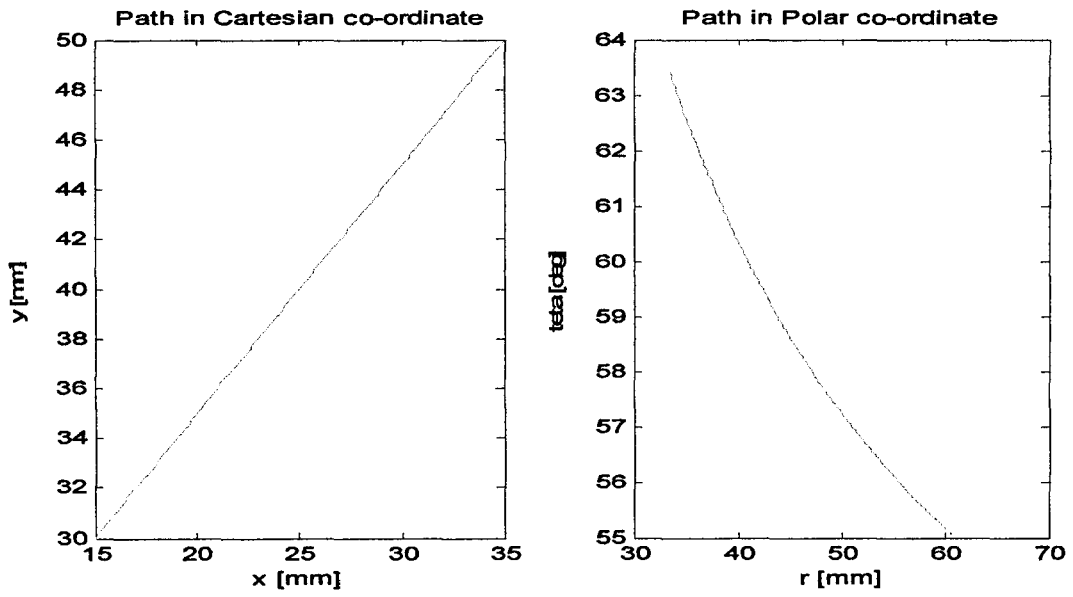

a) b)

Figure 8-9. Desired path in
a) Cartesian coordinates and b) Polar coordinates

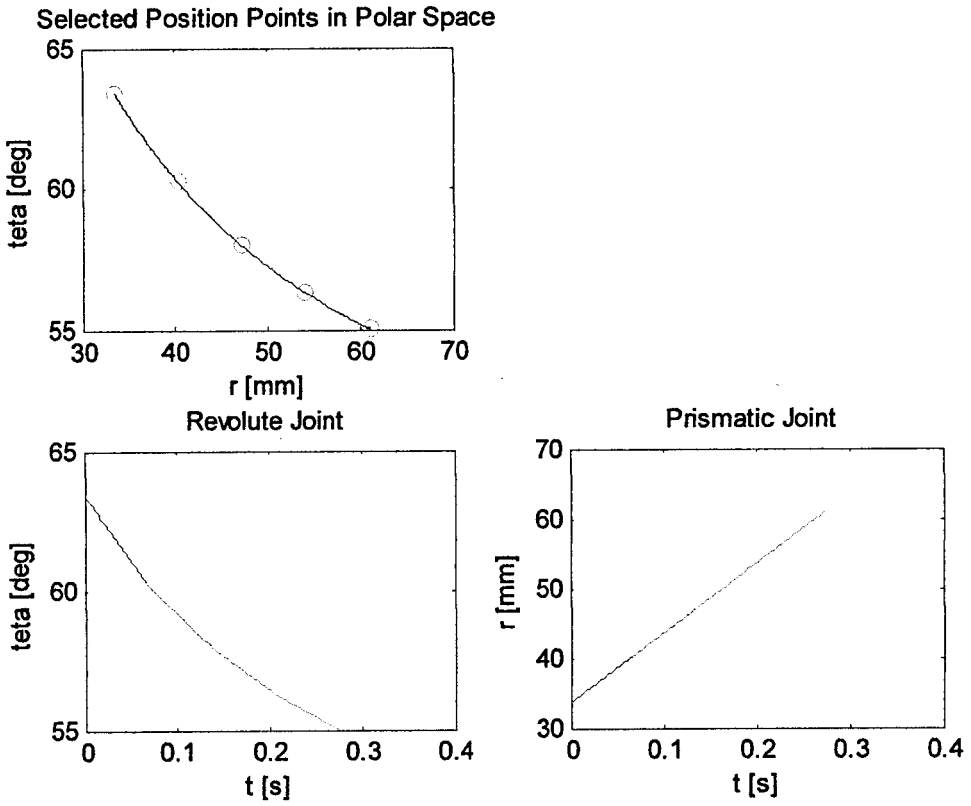

Figure 8-10. Position points selection and path control

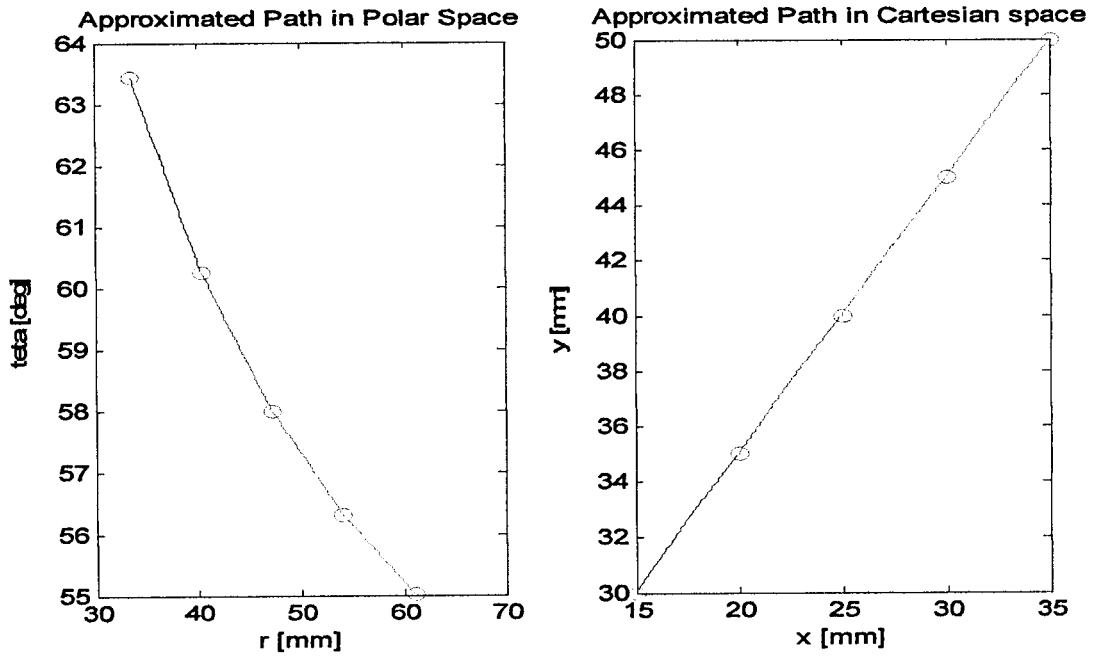

a) b)

Figure 8-11. Approximated path in
a) Polar coordinates and b) Cartesian coordinates

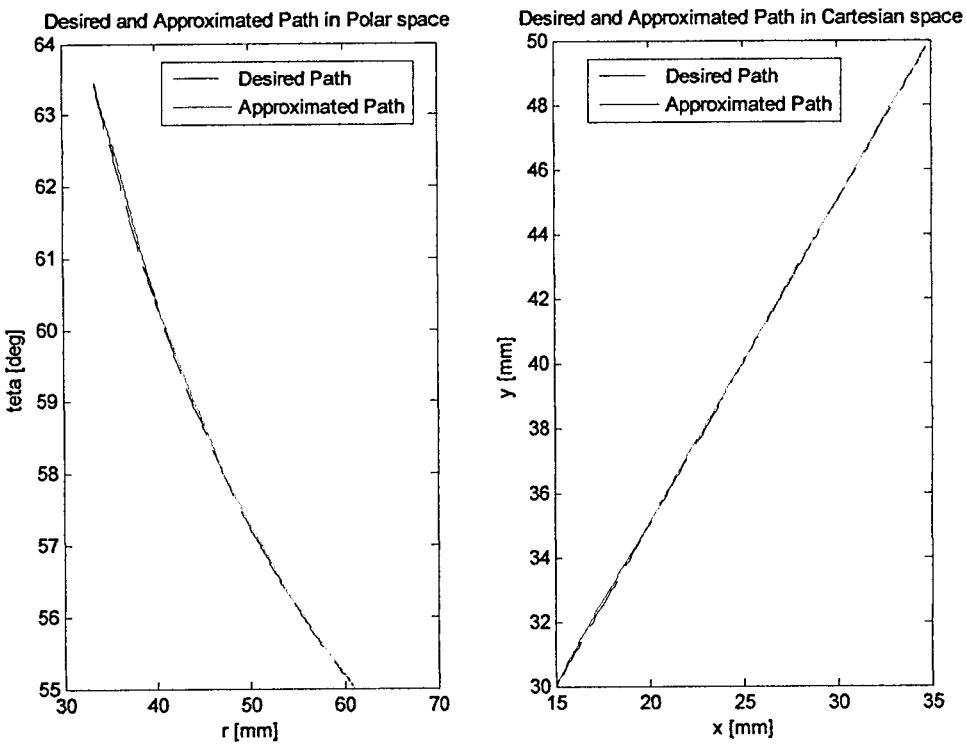

Figure 8-12. Desired and Approximated Path in
a) Polar space, and b) Cartesian space

8.2.3 'Region' mode

The strategy employed to keep the tip of the manipulator inside a 'safety' region is based on creating another region, inside the 'safety' region, called an 'intermediate' region. Between the border of the 'intermediate' region and the 'safety' region, different levels of resistance of the surgeon efforts are applied, as shown in Figure 8-13b. Inside the 'intermediate' region (i.e. zone I in Figure 8-13) the user can move freely as there is no control action to restrain the motion (or the user-input force). As soon as the user approaches the boundary of the 'intermediate' region, for example point A in Figure 8-13, the control system starts restraining the user-input force warning the surgeon about the fact that the boundary of the 'intermediate' region was reached and that s/he is

going towards the border of the 'safety' region. If the surgeon continues pushing towards the 'safety' region the control system allows the surgeon to move the end-effector along, but not beyond, the boundary, (i.e. safety border). If the user pushes the tip of the manipulator into zone III, maximum resistance will be applied. However, if the user pushes the tip of the manipulator back towards zone I, no restriction is applied as shown in Figure 8-13b.

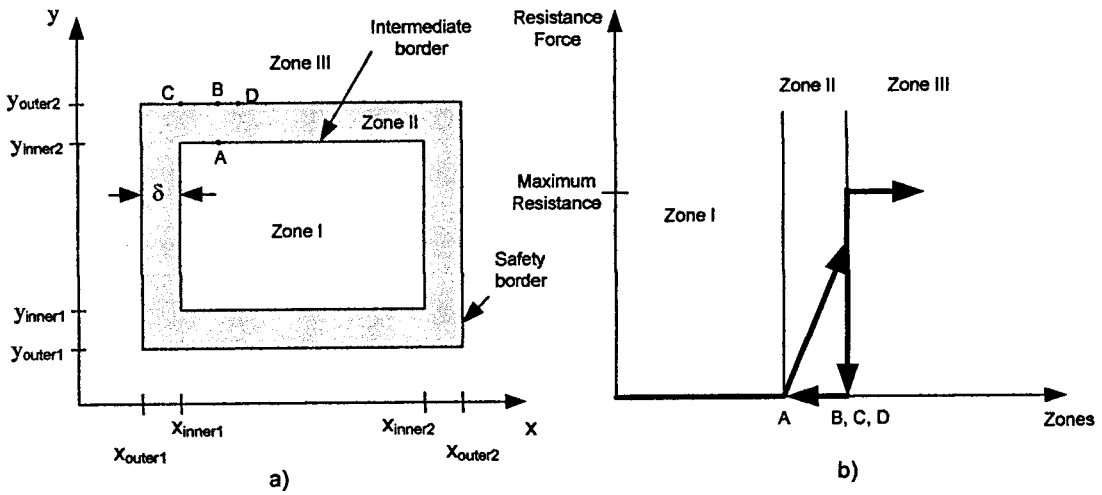

Figure 8-13. Control strategy in the *'region'* mode

As an example, the safety region could be defined as a rectangle in Cartesian coordinates. The intermediate border, shown in Figure 8-13, is defined by another rectangle at a desired distance δ with respect to the initial region, as shown in Figure 8-13a. The control in region mode is performed according to the flow chart illustrated in Figure 8-14.

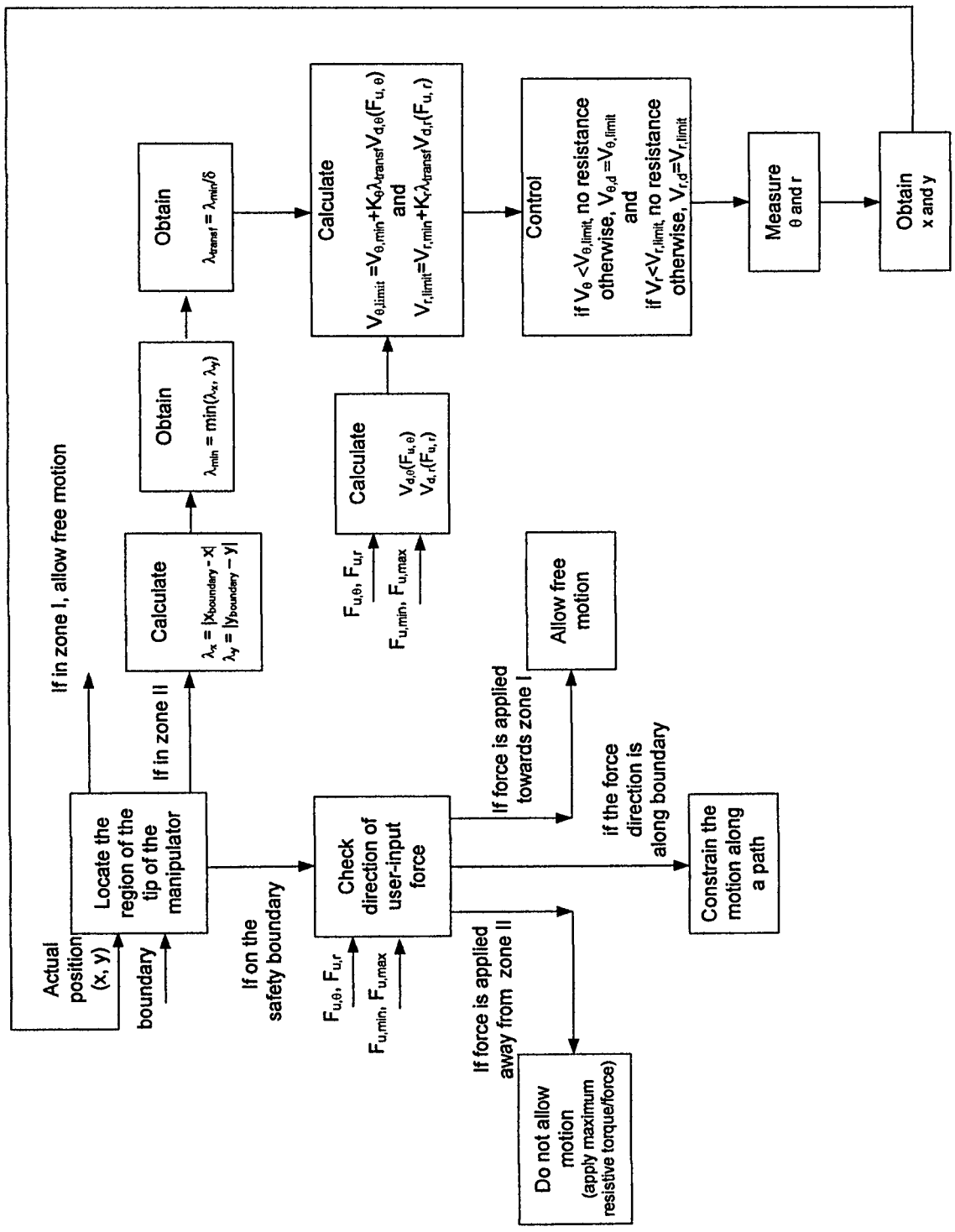

Figure 8-14. Diagram of the method used for implementing the 'region' mode

The position of the tip of the manipulator is continually monitored. To locate the region in which the tip of the manipulator is at a certain time, the equations (8-7), (8-8) and (8-9) are used. Thus, for the tip of the manipulator to be in zone I, the inequalities in equation (8-7) have to be satisfied. Therefore, if the inequalities in equation (8-7) are true, the tip of the manipulator is in zone I. For the tip of the manipulator to be in zone II, the inequalities in equation (8-8) have to be satisfied. Hence, if any of the inequalities shown in equation (8-8) is true, the tip of the manipulator is in zone II. Finally, for the tip of the manipulator to lay on the boundary of zone III any one of the equalities shown in equation (8-9) has to be true. The parameters y_{inner1}, y_{inner2}, y_{outer1}, y_{outer2} and x_{inner1}, x_{inner2}, x_{outer1}, x_{outer2} are illustrated in Figure 8-13a.

$$x_{inner1} \le x \le x_{inner2} \quad and \quad y_{inner1} \le y \le y_{inner2} \tag{8-7}$$

$$\begin{aligned} & x_{outer1} < x < x_{inner1}, \ and \ y_{outer1} \le y \le y_{outer2} \\ & or \ x_{inner2} < x < x_{outer2}, \ and \ y_{outer1} \le y \le y_{outer2} \\ & or \ y_{inner2} < y < y_{outer2}, \ and \ x_{outer1} \le x \le x_{outer2} \\ & or \ y_{outer1} < y < y_{inner1}, \ and \ x_{outer1} \le x \le x_{outer2} \end{aligned} \tag{8-8}$$

$$\begin{aligned} & x = x_{outer1}, or \\ & x = x_{outer2}, or \\ & y = y_{outer1}, or \\ & y = y_{outer2} \end{aligned} \tag{8-9}$$

If the above equations (8-7), (8-8), and (8-9) are not satisfied then the tip of the manipulator is in zone III.

If the end-effector of the manipulator is in zone I, there is no control input to the manipulator joint clutches. Thus, the operator is free to move the end-effector until the intermediate border, shown in Figure 8-13, is reached.

If the end-effector of the manipulator is in zone II, the motion is restrained according to the diagram shown in Figure 8-14, and illustrated again for clarity in Figure 8-15.

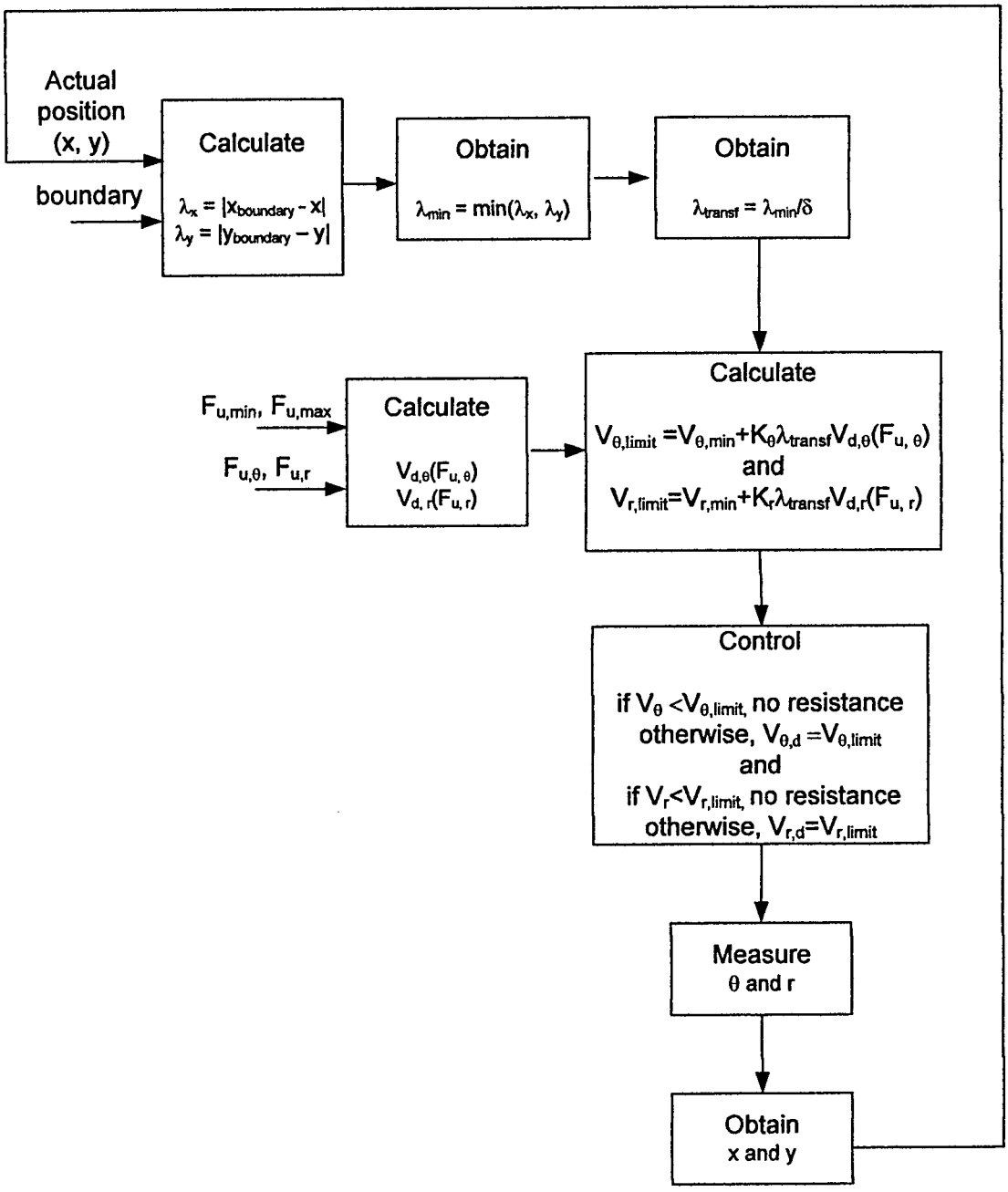

Figure 8-15. Diagram of the modified damping control employed for the *'region'* mode in zone II

In order to restrain the user-input force in the 'intermediate' region, a force control strategy based on the damping control is developed. In general, force control is applied to robotic system to keep a desired contact force between the end-effector and its

environment [174]. However, for actively restrained passive mechatronic systems the force control is used to generate a resistance force that the surgeon feels when s/he moves the end-effector of a passive manipulator. The principle is called 'active constraints', which has also been applied by the authors of Acrobot, described in section 2.5.4. With respect to the control strategy in the 'region' mode, both systems consider the user-input force magnitude, the current position and the direction of motion. The authors of Acrobot [68] use the above information to regulate the velocity of the motorised robot joints (i.e. desired variable stiffness for the robot). However, in this work the user-input force magnitude, the current position and the direction of motion are used to define the velocity of the joint via a clutch system. The amount of restraint needed is obtained from a friction clutch, and not directly from an electrical motor at each joint. The proposed method is described below.

Knowing the actual positions of each joint, x and y, and where the safety boundary lay, a distance $\lambda = [\lambda_x \ \lambda_y]^T$ is obtained, as given by equations (8-10) and (8-11). A graphical description is shown in Figure 8-16 for a point E.

$$\lambda_x = |x_{boundary} - x| \qquad \textbf{(8-10)}$$

$$\lambda_y = |y_{boundary} - y| \qquad \textbf{(8-11)}$$

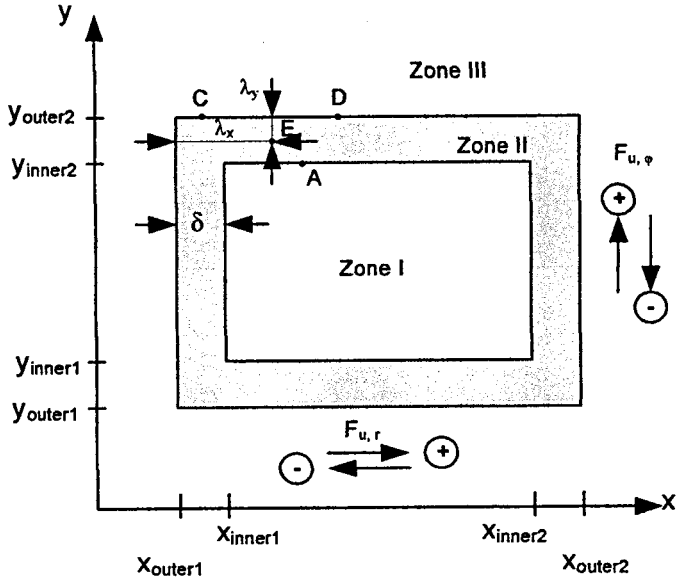

Figure 8-16. Graphical description of is obtained the distance used for the strategy employed for *'region'* mode

The shortest distance between λ_x and λ_y, $\lambda_{min} = \min(\lambda_x, \lambda_y)$, is selected as part of the strategy employed for the *'region'* mode as shown in the diagram presented in Figure 8-15. Next, the distance λ_{min} is generalised to be between 0 and 1 as follows:

$$\lambda_{transf} = \lambda_{min} / \delta \qquad \textbf{(8-12)}$$

where, the parameter δ represents the distance between the outer and inner region, as shown in Figure 8-16.

From the magnitude of the user-input force on each axis, $F_{u,\varphi}$ and $F_{u,r}$, a corresponding velocities $V_{d,\theta}$ and $V_{d,r}$ are calculated so that the velocity and acceleration demands for the end-effector are continuous. The velocities $V_{d,\theta}$ and $V_{d,r}$ are obtained using the equations (8-13) and (8-14) [18]. A graphical representation of one of these equations is illustrated in Figure 8-17. The parameters $\mathbf{V_{d,\,max}}$, $\mathbf{F_{u,\,min}}$, and $\mathbf{F_{u,max}}$ in equations (8-13) and (8-14) are all positive constants.

$$|V_{d,\theta}| = \begin{cases} 0, \forall |F_{u,\varphi}| < F_{u,\varphi\min} \\ V_{d,\theta\max}\left(-\dfrac{2(|F_{u,\varphi}| - F_{u,\varphi\min})^3}{(F_{u,\varphi\max} - F_{u,\varphi\min})^3} + \dfrac{3(|F_{u,\varphi}| - F_{u,\varphi\min})^2}{(F_{u,\varphi\max} - F_{u,\varphi\min})^2} \right), \forall F_{u,\varphi\min} \le |F_{u,\varphi}| \le F_{u,\varphi\max} \\ V_{d,\theta\max}, \forall |F_{u,\varphi}| > F_{u,\varphi\max} \end{cases} \qquad \textbf{(8-13)}$$

$$|V_{d,r}| = \begin{cases} 0, \forall |F_{u,r}| < F_{u,r\min} \\ V_{d,r\max}\left(-\dfrac{2(|F_{u,r}| - F_{u,r\min})^3}{(F_{u,r\max} - F_{u,r\min})^3} + \dfrac{3(|F_{u,r}| - F_{u,r\min})^2}{(F_{u,r\max} - F_{u,r\min})^2} \right), \forall F_{u,r\min} \le |F_{u,r}| \le F_{u,r\max} \\ V_{d,r\max}, \forall |F_{u,r}| > F_{u,r\max} \end{cases} \qquad \textbf{(8-14)}$$

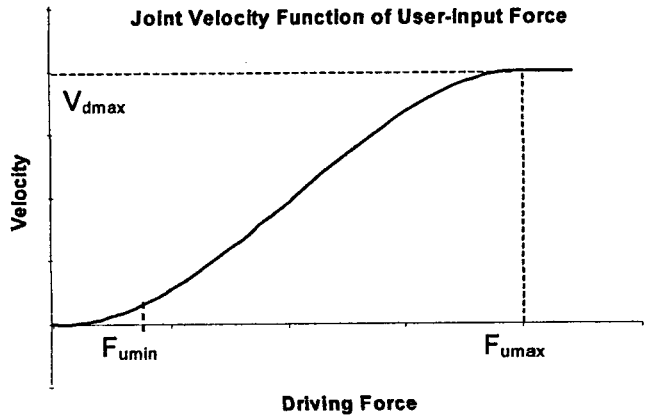

Figure 8-17. Joint velocity as a function of the user-input force

A restrained velocity is calculated for each joint, $V_{\theta,lim}$ and $V_{r,lim}$, as given by:

$$V_{\theta,lim} = V_{\theta,\,min} + K_\theta\, \lambda_{transf} |V_{d,\,\theta}| \qquad \textbf{(8-15)}$$

$$V_{r,lim} = V_{r,\,min} + K_r\, \lambda_{transf} |V_{d,\,r}| \qquad \textbf{(8-16)}$$

where $V_{\theta,\,min}$ and $V_{r,\,min}$ represents the minimum allowed velocity on the revolute and prismatic joint respectively, and K_θ and K_r are positive defined constants set for the revolute and prismatic joint respectively to enhance the feeling of the user.

The equations (8-15) and (8-16) are used to restrain the motion only if the actual velocity on each joint, V_θ and V_r, becomes greater or equal to the restrained velocities $V_{\theta,lim}$ and $V_{r,lim}$ respectively. Thus, the desired velocities, $V_{\theta,d}$ and $V_{r,d}$, on each axis are given by equation (8-17) for the revolute joint, and by equation (8-18) for the prismatic joint:

$$V_{\theta,d} = \begin{cases} V_{\theta,lim}, \forall V_\theta \geq V_{\theta,lim} \\ V_\theta, \quad \forall V_\theta < V_{\theta,lim} \end{cases} \qquad \textbf{(8-17)}$$

$$V_{r,d} = \begin{cases} V_{r,lim}, \forall V_r \geq V_{r,lim} \\ V_r, \quad \forall V_r < V_{r,lim} \end{cases} \qquad \textbf{(8-18)}$$

From equations (8-10) and (8-11) it can be seen that as the actual positions, x or y approach the safety boundary, the values of either λ_x or λ_y decrease and become zero when the actual point reaches the boundary. Thus, the joint velocities to be controlled, $V_{\theta,d}$ and $V_{r,d}$, decrease according to the equations (8-15) and (8-16). As soon as the actual point reaches the safety boundary (i.e. either $\lambda_x = 0$ or $\lambda_y = 0$), the joint velocities become equal to the minimum predefined values. At this point, depending on the user-input force direction, shown in Figure 8-16, the motion could be performed in either of the following three ways:

(1) if the user-input force is oriented towards zone III, and the force has no components towards zone II or zone I, the motion is stopped (i.e. maximum frictional torque is applied);

(2) if the user-input force is oriented towards zone I, the motion is unrestricted (i.e. free motion).

(3) if the user-input force has no component towards zone I, but has at least one component towards zone II, the motion is controlled so that the tip of the manipulator follows the safety boundary. In this situation, the boundary definition and control are given by the following equations:

- For the horizontal boundary, shown in Figure 8-16, the motion is controlled by:

$$\begin{cases} r_d = \sqrt{x^2 + y_{outer1}^{\ 2}} \\ \theta_d = \arctan\left(\dfrac{y_{outer1}}{x}\right) \end{cases}, \text{ if the end-effector is on the boundary } y_{outer1} \quad \textbf{(8-19)}$$

$$\begin{cases} r_d = \sqrt{x^2 + y_{outer2}^{\ 2}} \\ \theta_d = \arctan\left(\dfrac{y_{outer2}}{x}\right) \end{cases}, \text{ if the end-effector is on the boundary } y_{outer2} \quad \textbf{(8-20)}$$

- For the vertical boundary

$$\begin{cases} r_d = \sqrt{x_{outer1}^{\ 2} + y^2} \\ \theta_d = \arctan\left(\dfrac{y}{x_{outer1}}\right) \end{cases}, \text{ if the end-effector is on the boundary } x_{outer1} \quad \textbf{(8-21)}$$

$$\begin{cases} r_d = \sqrt{x_{outer2}{}^2 + y^2} \\ \theta_d = \arctan\left(\dfrac{y}{x_{outer2}}\right) \end{cases} \text{if the end-effector is on the boundary } x_{outer2} \textbf{ (8-22)}$$

8.3 Mathematical Model of a Two-DOF Polar Manipulator

After the capability of the proposed joint mechanism was demonstrated in the previous chapter, the concept mechanism was implemented in simulations on a two-DOF polar manipulator. The polar manipulator employed for the simulation analysis is based on an existenting custom-built two-DOF polar manipulator designed at Loughborough University by Fraucher [174]. The manipulator with a control handle is shown in Figure 8-18. The manipulator is similar in principle with the Acrobot system described in section 2.5.4. Therefore, the motion of the manipulator is directly restrained using electrical motors. For this reason, the joint mechanism used by Fraucher was adapted in simulations to include the proposed joint mechanism. A similar design to the experimental test-bed setup is proposed for the adaptation of the revolute joint and a different scheme is proposed for the adaptation of the prismatic joint from actively motorised to passively constrain. The passive system is based on the use of piezoelectric actuators and corresponding drivers. The technical drawings of the proposed designs are given in Appendix F2 and F3. Thus, the mathematical model of the two-DOF is performed for this particular manipulator with the joint–related parameters obtained from the proposed clutch mechanisms.

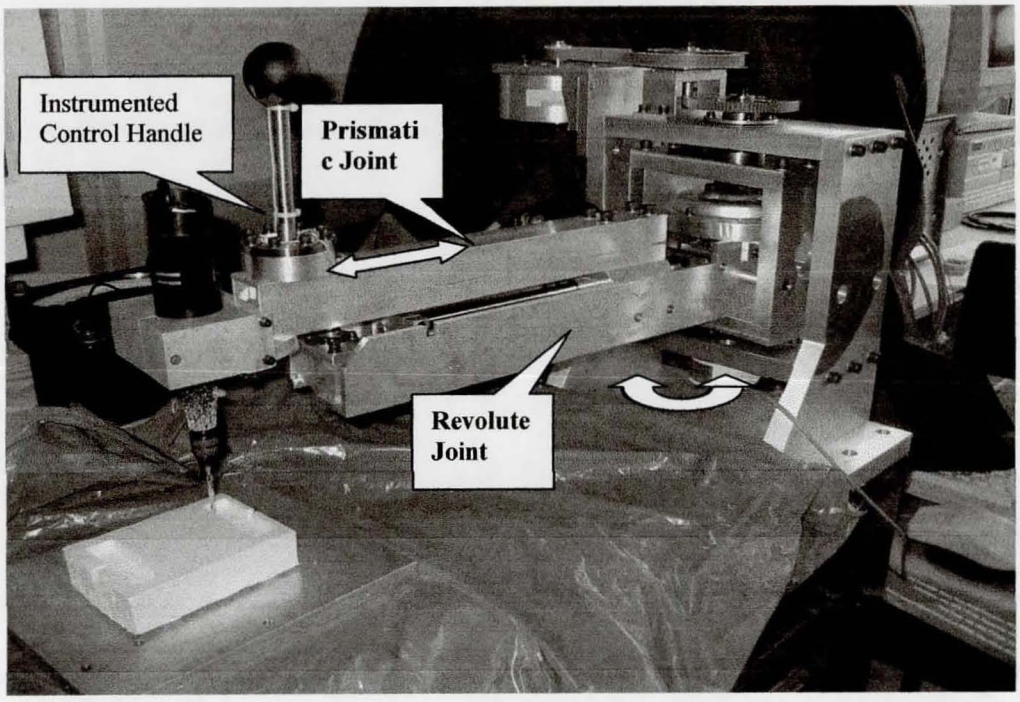

Figure 8-18. Fraucher's two-DOF polar manipulator [174]

The equations of motion of the two-DOF manipulator are derived in Appendix H2 and given as

$$M(q)\ddot{\vec{q}} + \vec{h}(q,\dot{q}) = \vec{Q} \qquad \textbf{(8-23)}$$

where: $M(q) = \begin{bmatrix} m_3 & 0 \\ 0 & m_3 r_3^{\,2} + I_{sum} \end{bmatrix}$ represents the inertial matrix of the manipulator,

$\vec{h}(q,\dot{q}) = \begin{bmatrix} m_3 r_3 \dot{\theta}^2 \\ 2m_3 r_3 \dot{r}_3 \dot{\theta} \end{bmatrix}$ represents the non-linear coriolis and centrifugal force vector, and

$\vec{Q} = \begin{bmatrix} F_{u,r} - F_{f,r} - D_r \dot{r}_3 \\ F_{u,\varphi}(r_3 + r_{Fu}) - T_{f,z} - D_z \dot{\theta} \end{bmatrix}$ denotes the generalised force vector.

where $F_{u,r}$ and $F_{u,\varphi}$ are the user-input force components acting along the r-axis and φ-axis respectively; $F_{f,r}$ denotes the frictional force produced by the proposed joint mechanism, which is acting opposite to the user's input force; $T_{f,z}$ is the frictional torque

produced by the clutch; the radius r_3 denotes the distance between the base frame and the centre of gravity of the moveable part of the prismatic joint, and r_{Fu} represents the distance between the centre of gravity of moveable part of the prismatic joint and the handle. The manipulator parameters are shown in Figure A13. Furthermore, D_r and D_z are the damping constants for the prismatic and revolute joints respectively.

Thus, the equation (8-23) can be written as

$$\begin{bmatrix} m_3 & 0 \\ 0 & m_3 r_3^{\,2} + I_{sum} \end{bmatrix} \ddot{\vec{q}} + \begin{bmatrix} m_3 r_3 \dot{\theta}^2 \\ 2m_3 r_3 \dot{r}_3 \dot{\theta} \end{bmatrix} = \begin{bmatrix} F_{u,r} - F_{f,r} - D_r \dot{r}_3 \\ F_{u,\varphi}(r_3 + r_{Fu}) - T_{f,z} - D_z \dot{\theta} \end{bmatrix} \quad \textbf{(8-24)}$$

The masses, mass moment of inertias and geometrical dimensions of the manipulator were obtained by Fraucher [177] and are given in Appendix H3. Furthermore, the travel of each joint and the encoder resolutions are considered the same as Fraucher, and are given in Appendix H3. The user-input force $\mathbf{F_u} = (F_{u,r}\ F_{u,\varphi})^T$ is measured using the instrumented control handle described in Appendix H1. A strain gauge amplifier is used to match an input force range of ±30N to an analogue-to-digital converter (ADC) input range of ±10 volt. The frictional force $F_{f,r}$ and frictional torque $T_{f,z}$ are obtained similar to the derivation completed in section 5.4. The difference in this case is the fact that the DC motor is replaced with a piezoelectric actuator. The piezoactuator was selected in section 3.4, and its properties are also given in that section. The mathematical model of a piezoactuator was derived in Appendix E1 and the force obtained from the actuator is given as

$$F_{piezo} = \frac{k_{system} \cdot k_{piezo}}{k_{system} + k_{piezo}} \cdot K_v \cdot V_{piezo} \quad \textbf{(8-25)}$$

where k_{piezo} and k_{system} denotes the stiffness of both the piezoactuator and the system; V_{piezo} represents the input voltage into the actuator, and K_v is obtained at maximum displacement, $x_{p,\,max}$ and maximum applied voltage $V_{piezo,\,max}$

$$K_v = x_{p,\,max}/V_{piezo,max} \quad \textbf{(8-26)}$$

Therefore, the frictional force F_f along r-axis and the frictional torque T_f about the z-axis are obtained using the model derived in section 5.4. Consequently,

$$F_f = \begin{cases} F_f(\dot{\theta}), & \forall \dot{\theta} \neq 0 \\ F_{u,r}, & \forall \dot{\theta} = 0, \mid F_{u,r} \mid < F_{f\max} \\ F_{f\max}\,\mathrm{sgn}(F_{u,r}), & \forall \dot{\theta} = 0, \mid F_{u,r} \mid \geq F_{f\max} \end{cases} \quad \textbf{(8-27)}$$

where, $F_f(\dot{\theta})$ is given by

$$F_f(\dot{\theta}) = \mu(\dot{\theta}) \cdot F_{piezo} \quad \textbf{(8-28)}$$

and

$$T_f = \begin{cases} T_f(\dot{\theta}), & \forall \dot{\theta} \neq 0 \\ T_u, & \forall \dot{\theta} = 0, \mid T_u \mid < T_{f\max} \\ T_{f\max}\,\mathrm{sgn}(T_u), & \forall \dot{\theta} = 0, \mid T_u \mid \geq T_{f\max} \end{cases} \quad \textbf{(8-29)}$$

where, $T_f(\dot{\theta})$ is given by

$$T_f(\dot{\theta}) = \mu(\dot{\theta}) \cdot r_o \cdot F_{piezo} \quad \textbf{(8-30)}$$

with the coefficient of friction, $\mu(\dot{\theta})$, defined as shown in section 5.4.2.2.

$$\mu(\dot{\theta}) = \left(\mu_d + (\mu_s - \mu_d) e^{-\left|\dot{\theta}/\dot{\theta}_s\right|^{\delta}} \right) \mathrm{sgn}(\dot{\theta}) \quad \textbf{(8-31)}$$

The system parameters are given in Appendix H3.

8.4 Control System

The interaction between the surgeon and the proposed actively restrained passive device was shown in Figure 8-1. A block diagram of the control system is illustrated in Figure 8-19. The task interpreter algorithm was described in the previous section. Considering known the output of the task interpreter algorithm, the control diagrams for the

'position', 'trajectory', and 'region' modes are presented in Figure 8-20. The joint controller is described in Chapter 7, and the friction model of each joint and the mathematical model of the manipulator are obtained in section 8.3.

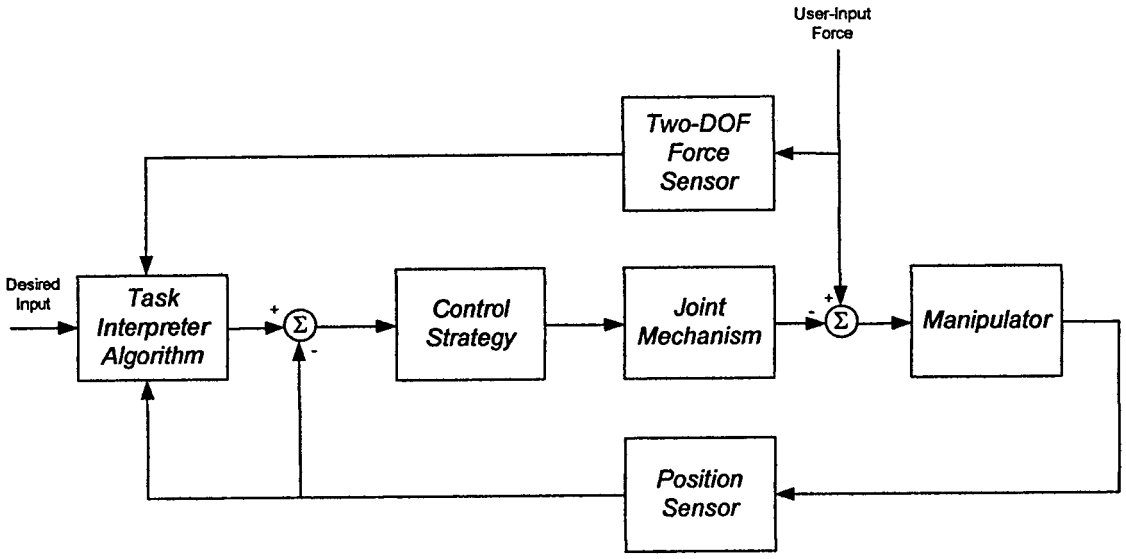

Figure 8-19. Control diagram of the actively restrained passive mechatronic system

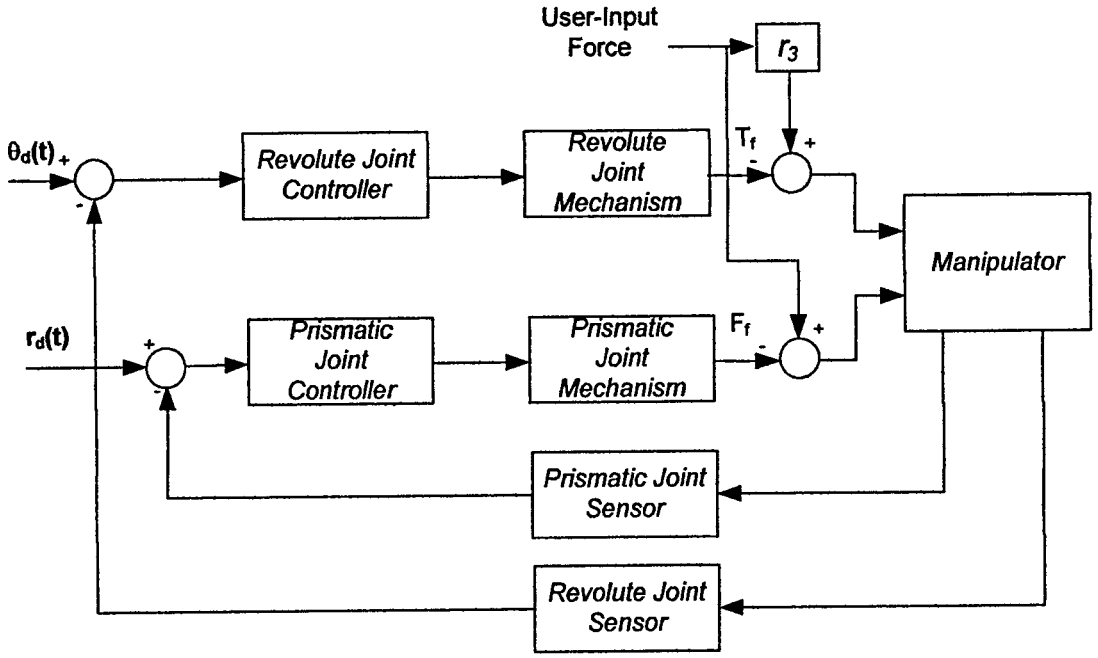

a)

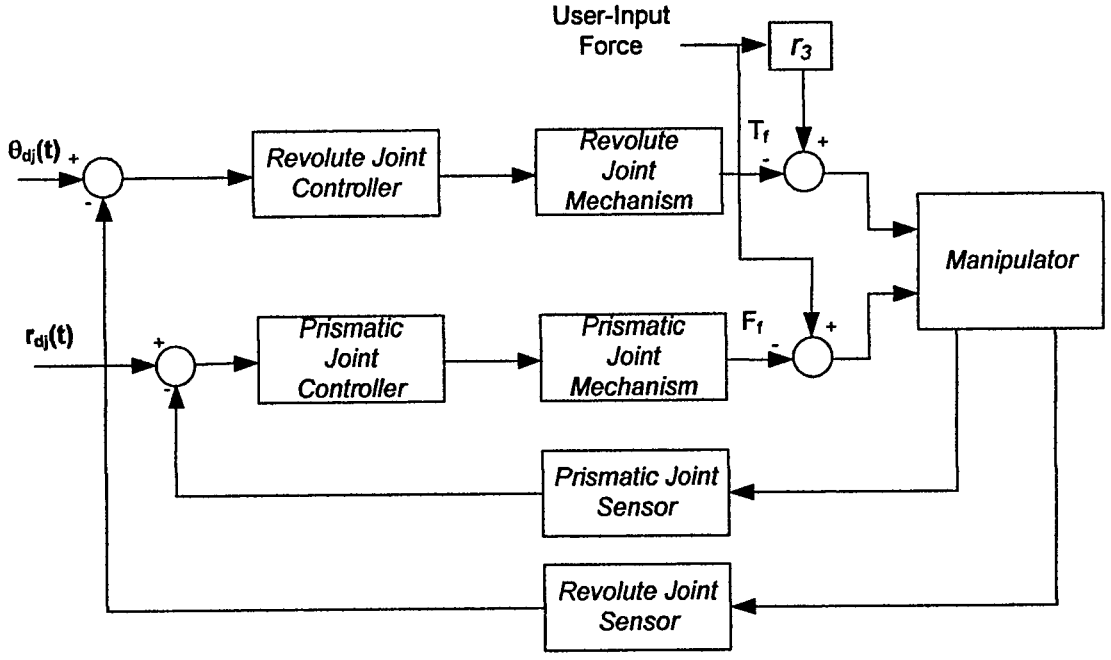

b)

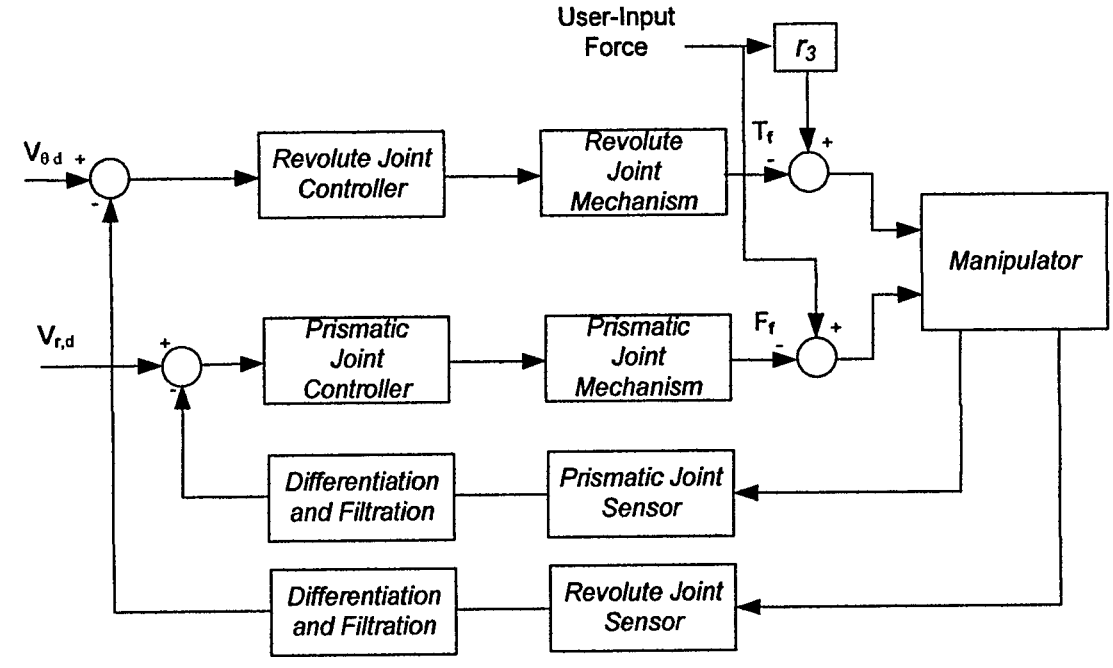

c)

Figure 8-20. Control diagram of the two-DOF manipulator
a) for *'position'* mode, b) for *'trajectory'* mode, and c) for the *'region'* mode

A PD controller is employed at each joint for the simulation analysis of the two-DOF manipulator with a friction clutch activated by piezoelectric actuators. The controller

parameters are given in Table 8-1, and the predefined parameters used in the simulations are shown in Table 8-2.

Table 8-1. Controller gains for a Two-DOF manipulator

Controller parameters	K_p	K_d
Revolute Joint	100	3
Prismatic Joint	10	1

Table 8-2. Predefined parameters of the two-DOF manipulator

Notation	Value	Description
$F_{u,\varphi\ min}$	3N	predefined minimum user-input force for θ-axis
$F_{u,r\ min}$	3N	predefined minimum user-input force for r-axis
$F_{u,\varphi\ max}$	30N	predefined maximum user-input force for θ-axis
$F_{u,r\ max}$	30N	predefined maximum user-input force for r-axis
$V_{\theta,min}$	6deg/s	predefined minimum velocity for θ-axis
$V_{r,min}$	6mm/s	predefined minimum velocity for r-axis
$V_{\theta,max}$	100deg/s	predefined maximum velocity for θ-axis
$V_{r,max}$	100mm/s	predefined maximum velocity for r-axis
$V_{d,\theta,\ max}$	94deg/s	predefined maximum velocity for the user-input force component on θ-axis
$V_{d,r\ max}$	94mm/s	predefined maximum velocity for the user-input force component on r-axis
D_r	0.001	damping constant for the prismatic joint
D_z	0.001	damping constants for the revolute joint

8.5 Results and Discussions

The aim of the study in this section is to evaluate the performance of the control strategy employed on a two-DOF manipulator in order to control the motion in all three modes of operation: 'position', 'trajectory' and 'region' modes. Simulations were performed using the Matlab/Simulink environment. A sampling frequency of 400Hz is

chosen, as it is the maximum operating frequency for the selected piezoactuator, and the solver used is based on explicit Runge-Kutta formula (4,5), the Dormand-Prince pair.

8.5.1 Position mode

An example of both case I and case II of the 'position' mode, described in section 8.2.1, is illustrated in this section. Following the flow chart used to implement the 'position' mode, shown in Figure 8-5, the calculations are given in the following sections.

8.5.1.1 Example of Case I

Consider the following predefined position points:

$\theta_i = 0$ $\quad$ $r_i = 0$

$\theta_f = 27\text{deg}$ $\quad$ $r_f = 59\text{mm}$

Obtain:

$$\Delta\theta = \theta_f - \theta_i = 27 \text{ deg} \quad \textbf{(8-32)}$$

$$\Delta r = r_f - r_i = 59 \text{ mm} \quad \textbf{(8-33)}$$

$$t_{\theta,\max} = \frac{\Delta\theta}{V_{\theta,\min}} = \frac{27}{6} = 4.5s \quad \textit{and} \quad t_{\theta,\min} = \frac{\Delta\theta}{V_{\theta,\max}} = \frac{27}{100} = 0.27s \quad \textbf{(8-34)}$$

$$t_{r,\max} = \frac{\Delta r}{V_{r,\min}} = \frac{59}{6} = 9.83s \quad \textit{and} \quad t_{r,\min} = \frac{\Delta r}{V_{r,\max}} = \frac{59}{100} = 0.59s \quad \textbf{(8-35)}$$

$$t_f = \max\left([t_{\theta,\min}, t_{\theta,\max}] \cap [t_{r,\min}, t_{r,\max}]\right) \quad \textbf{(8-36)}$$

If $t_f \neq 0$, the motion takes place in case I, as illustrated in Figure 8-21. Thus,

$$t_f = \max\left([t_{\theta,\min}, t_{\theta,\max}] \cap [t_{r,\min}, t_{r,\max}]\right) = \max(0.59, 4.5) = 4.5\text{s} \quad \textbf{(8-37)}$$

The position rate for the revolute joint is calculated as $m_\theta = \Delta\theta/t_f = 27/4.5 = 6$deg/s, and the position rate for the prismatic joint is given as $m_d = \Delta r/t_f = 59/4.5 = 13.11$deg/s.

Consequently, the desired angular and linear positions function of time $\theta_d(t)$ and $r_d(t)$ are obtained using the linear polynomials given by:

$$\theta_d(t) = \theta_i + m_\theta t \qquad \textbf{(8-38)}$$

$$r_d(t) = r_i + m_d t \qquad \textbf{(8-39)}$$

with $0 \leq t \leq t_f$ and $t = nT$, where $n = 0, 1, 2, \ldots$, and T is the sampling time.

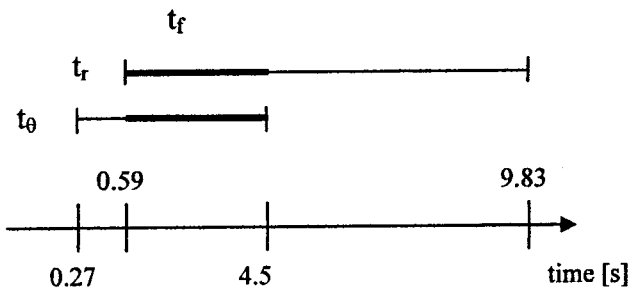

$$t_f = \max([t_{\theta,\min}, t_{\theta,\max}] \cap [t_{r,\min}, t_{r,maz}]) = \max(0.59, 4.5) = 4.5\text{s}$$

Figure 8-21. Example of position mode definition, case I, (i.e. $t_f \neq 0$)

Assuming that $\mathbf{F_u} = [3, 20]^T$, the simulation results for the motion on the revolute and prismatic joint is illustrated in Figures 8-22 and 8-24. From Figures 8-22b and 8-24b it can be seen that for both revolute and prismatic joints, the positional error is minimal. This is due to robust and efficient control strategy, as well as good actuator performance. However, from Figure 8-22b it can be seen that the positional accuracy on the revolute joint is affected by the variable driving torque, given in this case by the variable prismatic joint. Nonetheless, the position error is kept to a minimum, as it can

be seen from Figure 8-22b where an error of 0.025deg is obtained for a linear displacement of 59mm.

Enlarged figures of the desired and actual position, and the positional error for the revolute and prismatic joints are illustrated in Figures 8-23 and 8-25. It can be observed that for the revolute joint the accuracy of the system with piezoactuator is much higher than the accuracy obtained with a DC motor, shown in the previous chapter. A difference of approximately 10 times is noticed, which demonstrates a great potential of the piezoactuator for an efficient clutch mechanism.

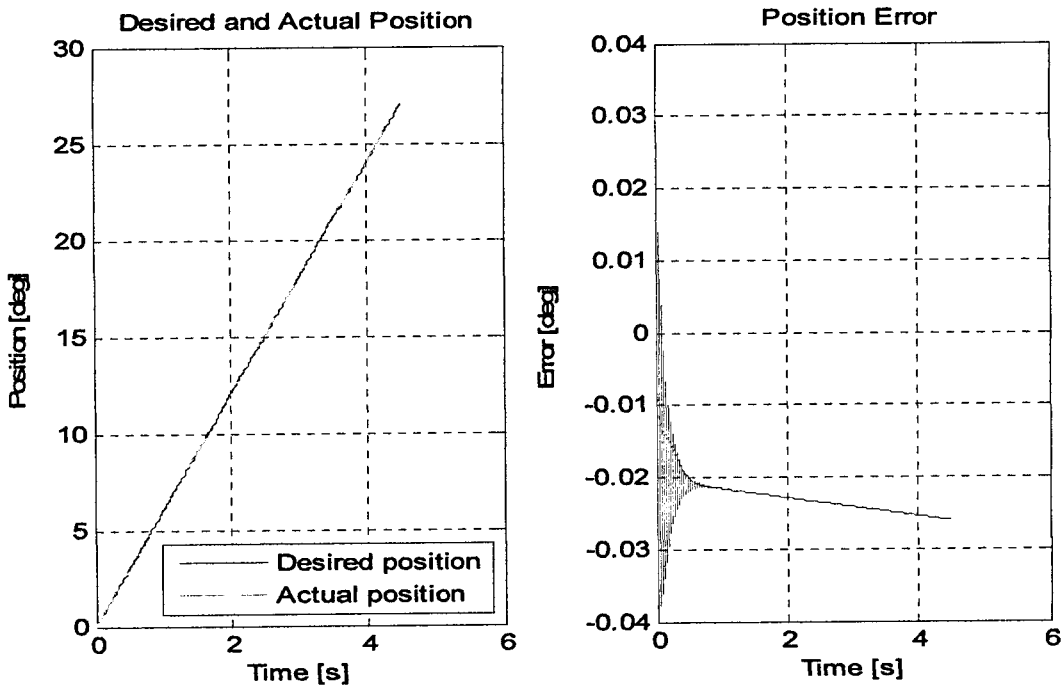

Figure 8-22. Position mode, case I: Revolute joint

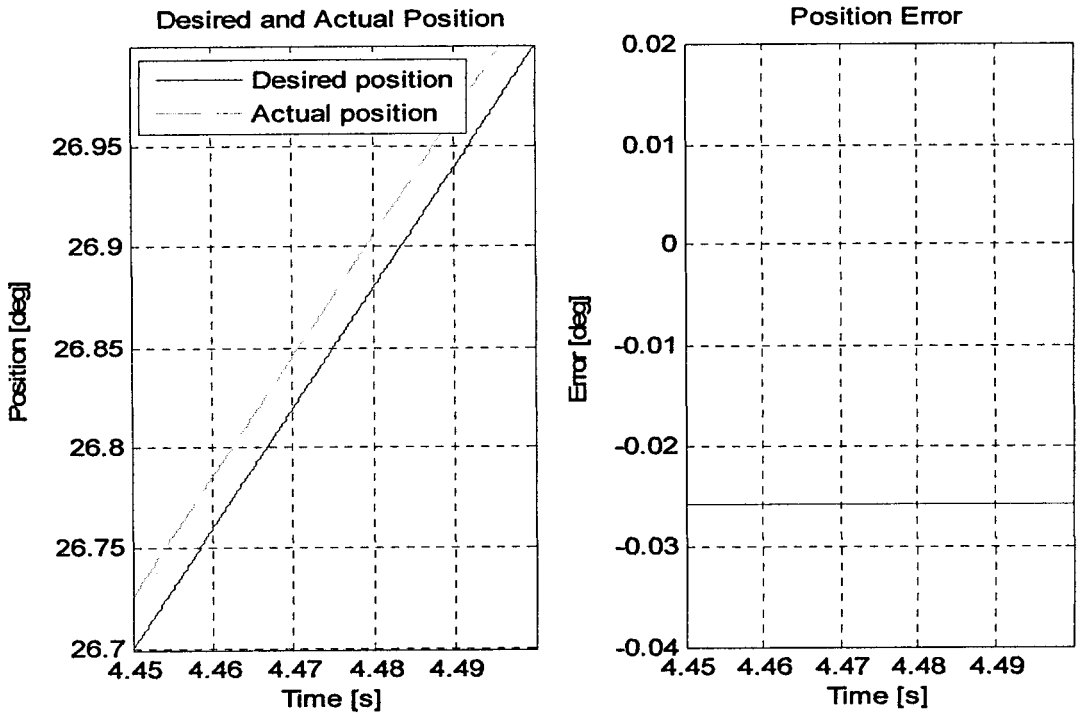

a) b)

Figure 8-23. Position mode, case I: Revolute joint, enlarged

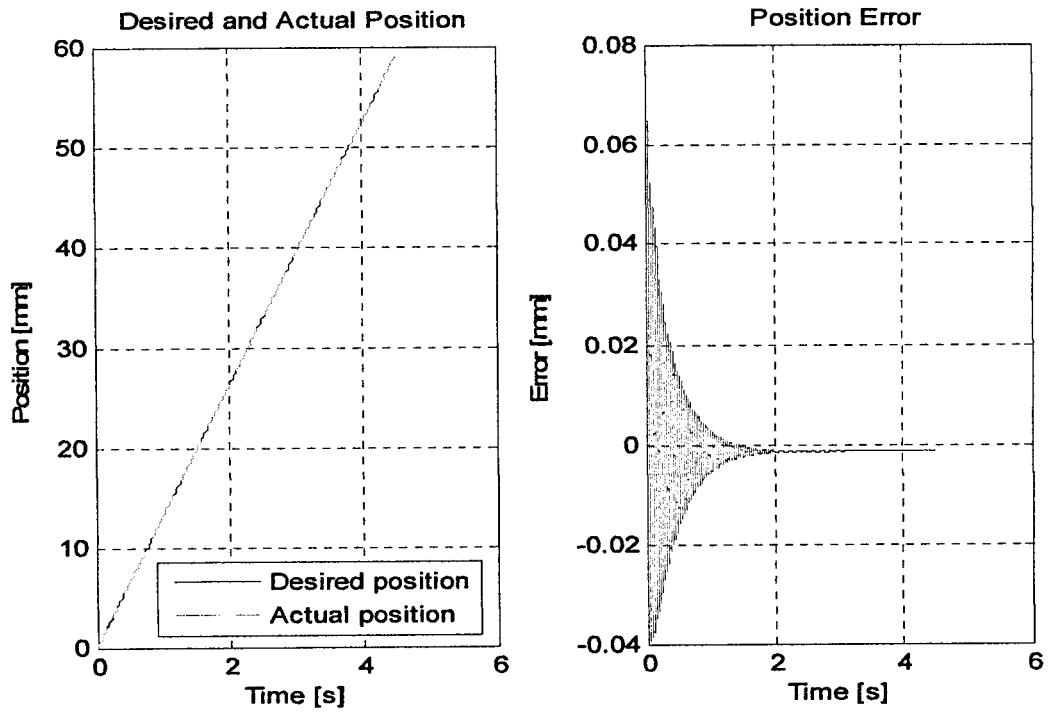

a) b)

Figure 8-24. Position mode, case I: Prismatic joint

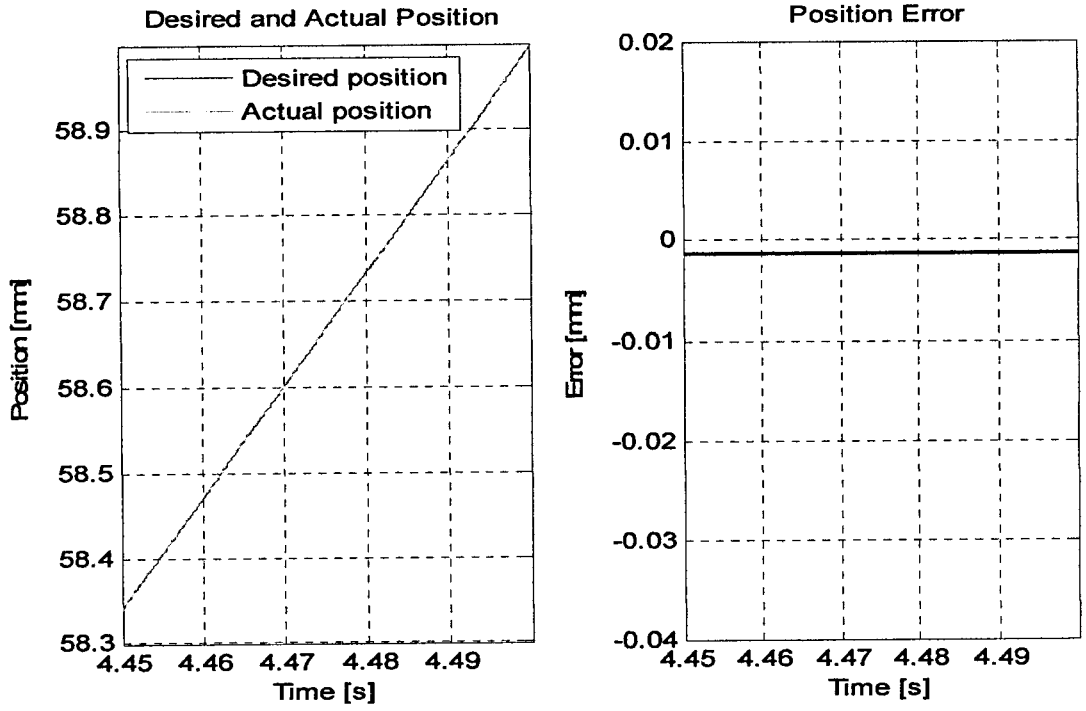

a) b)

Figure 8-25. Position mode, case I: Prismatic joint, enlarged

8.5.1.2 Example of Case II

Consider the predefined position points

$\theta_i = 0$ $r_i = 0$

$\theta_f = 27\text{deg}$ $r_f = 1\text{mm}$

Obtain

$$\Delta\theta = \theta_f - \theta_i = 27 \text{ deg} \quad \textbf{(8-40)}$$

$$\Delta r = r_f - r_i = 1 \text{ mm} \quad \textbf{(8-41)}$$

$$t_{\theta,\max} = \frac{\Delta\theta}{V_{\theta,\min}} = \frac{27}{6} = 4.5s \quad and \quad t_{\theta,\min} = \frac{\Delta\theta}{V_{\theta,\max}} = \frac{27}{100} = 0.27s \quad \textbf{(8-42)}$$

$$t_{r,\max} = \frac{\Delta r}{V_{r,\min}} = \frac{1}{6} = 0.1667s \quad and \quad t_{r,\min} = \frac{\Delta r}{V_{r,\max}} = \frac{1}{100} = 0.01s \quad \textbf{(8-43)}$$

or consider the following predefined position points

$\theta_i = 0$ $r_i = 0$

$\theta_f = 2\text{deg}$ $r_f = 59\text{mm}$

Obtain

$$\Delta\theta = \theta_f - \theta_i = 2 \text{ deg} \quad \textbf{(8-44)}$$

$$\Delta r = r_f - r_i = 59 \text{ mm} \quad \textbf{(8-45)}$$

$$t_{\theta,\max} = \frac{\Delta\theta}{V_{\theta,\min}} = \frac{2}{6} = 0.33s \quad and \quad t_{\theta,\min} = \frac{\Delta\theta}{V_{\theta,\max}} = \frac{2}{100} = 0.02s \quad \textbf{(8-46)}$$

$$t_{r,\max} = \frac{\Delta r}{V_{r,\min}} = \frac{59}{6} = 9.83s \quad and \quad t_{r,\min} = \frac{\Delta r}{V_{r,\max}} = \frac{59}{100} = 0.59s \quad \textbf{(8-47)}$$

Both examples are in case II as $t_f = \max([t_{\theta,\min}, t_{\theta,\max}] \cap [t_{r,\min}, t_{r,\max}]) = 0$.

The position rate for the revolute joint and the position rate for the prismatic joint are selected so that the stick-slip is fully avoided: $m_\theta = m_d = 20$. Consequently, the desired angular and linear positions function of time $\theta_d(t)$ and $r_d(t)$ are obtained using the linear polynomials given by:

$$\theta_d(t) = \theta_i + m_\theta t \text{ , where } 0 \le t \le t_{\theta,fine} \quad \textbf{(8-48)}$$

$$r_d(t) = r_i + m_d t \text{ , where } 0 \le t \le t_{r,fine} \quad \textbf{(8-49)}$$

where, $t_{\theta,fine}$ is the time obtained for the revolute joint for a position rate of 20deg/s, $t_{\theta,fine} = \Delta\theta/20 = 2/20 = 0.1$s, and $t_{r,fine}$ is the time obtained for the prismatic joint for a position rate of 20mm/s, $t_{r,fine} = 59/20 = 2.95$s.

Assuming that $\mathbf{F_u} = [3, 20]^T$, the simulation results for the control of the revolute and prismatic joints are illustrated in Figures 8-26 and 8-28. Figure 8-26 illustrates the desired and actual position, and the positional error for the revolute joint, and Figures 8-28 shows the desired and actual position, and the positional error for a prismatic joint.

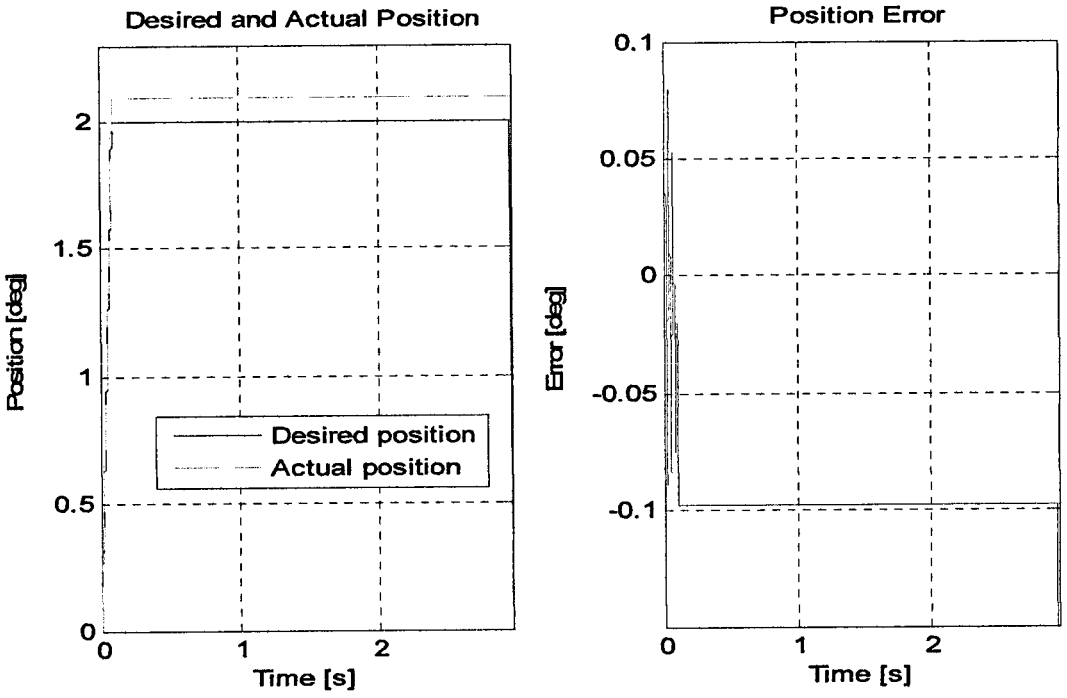

a) b)

Figure 8-26. Position mode, case II: Revolute joint

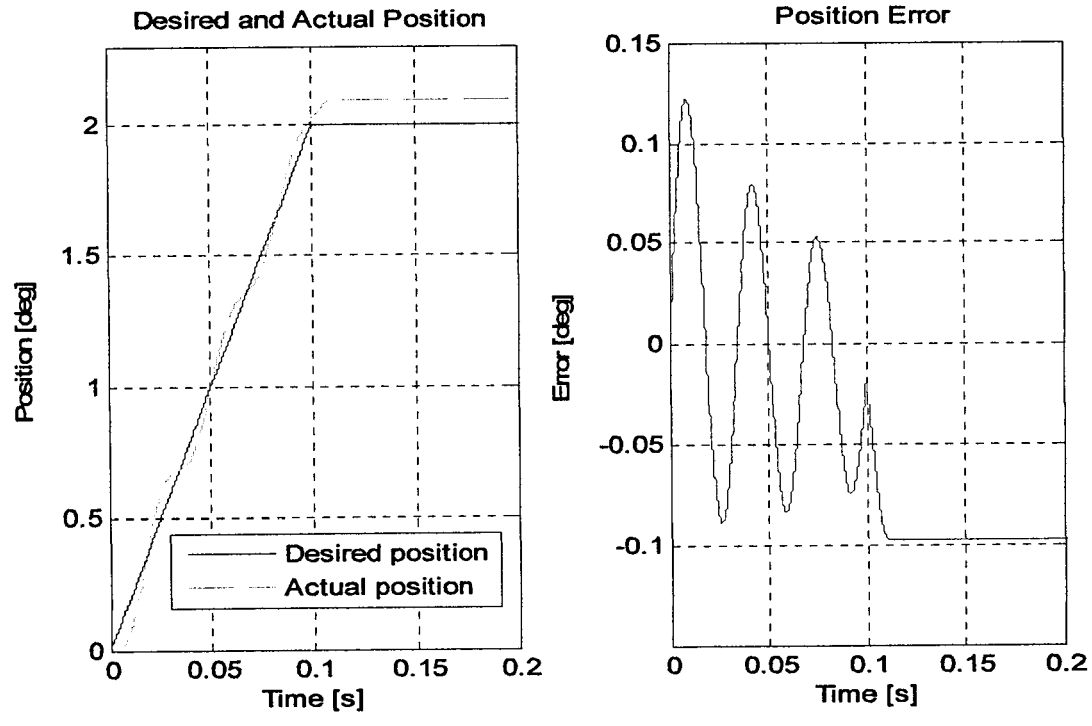

a) b)

Figure 8-27. Position mode, case II: Revolute joint, enlarged

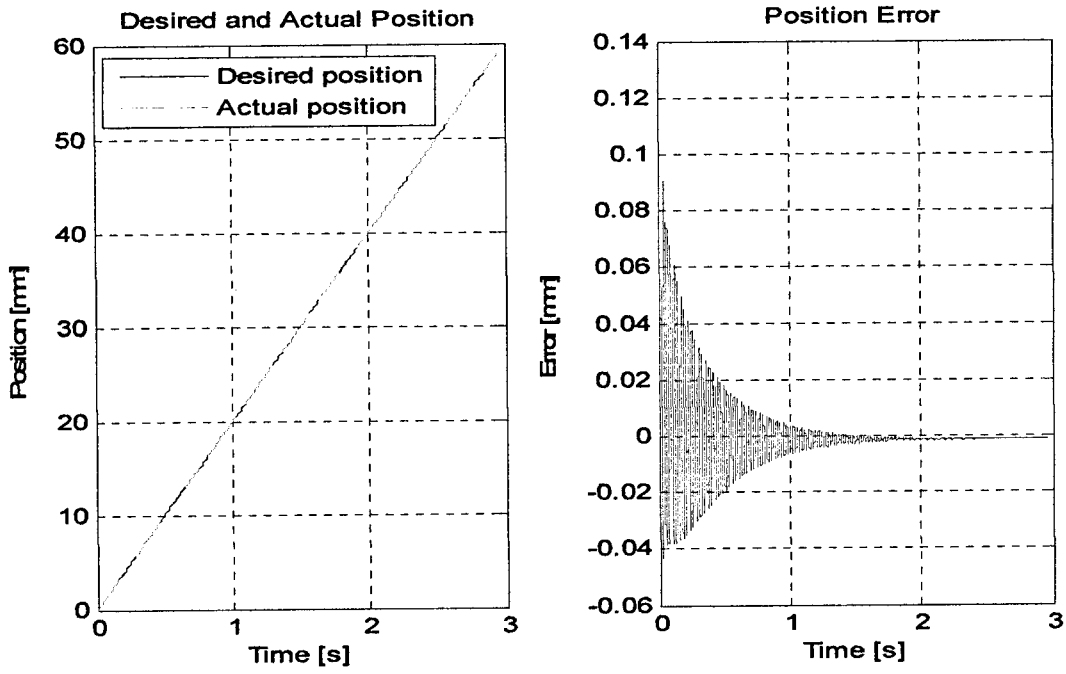

a) b)

Figure 8-28. Position mode, case II: Prismatic joint

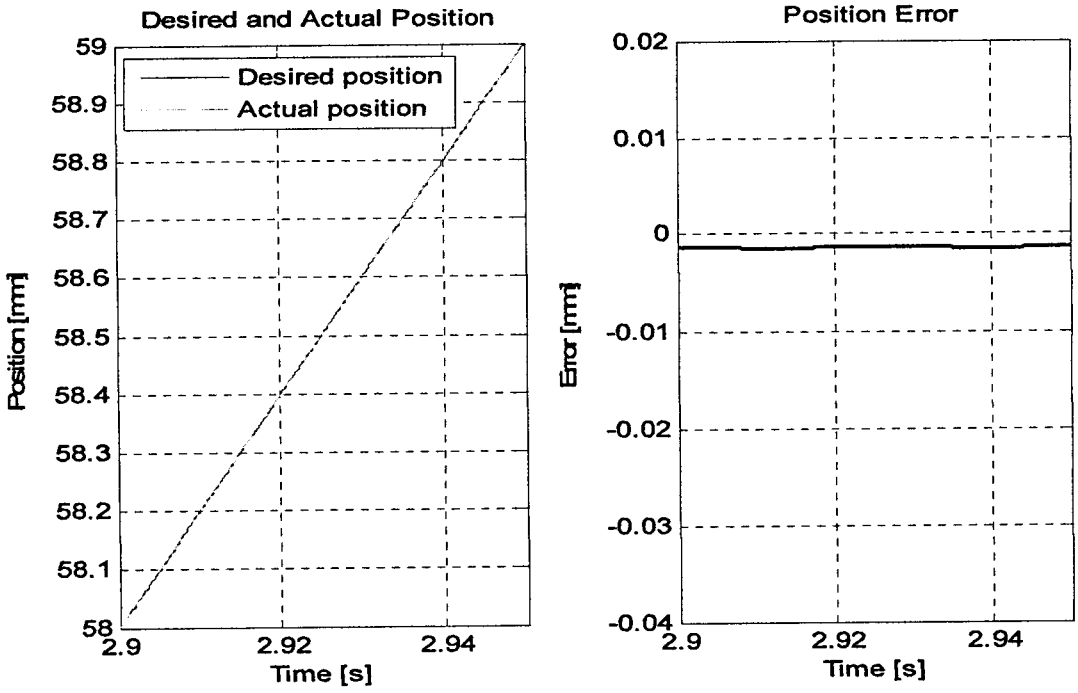

a) b)

Figure 8-29. Position mode, case II: Prismatic joint, enlarged

From Figures 8-26b and 8-28b it can be seen that for both joints, the positional error is kept similar to the error obtained from case I illustrated above in section 8.5.1.1. For the revolute joint, a maximum error of 0.12deg is obtained, while for the prismatic joint a maximum error of 0.09 mm is achieved, as it can be seen from Figures 8-27a and 8-29a.

8.5.2 Trajectory mode

Following the description of the task-interpreter algorithm for the *'trajectory'* mode, discussed in section 8.2.2, a path on Cartesian space is given and a path in polar coordinates is obtained. The predefined Cartesian path and the associated path in polar space are shown in Figure 8-30a and 8-30b. A set of position points are selected on the path defined in polar coordinates, as shown in the top left graph of Figure 8-31. The motion on each axis is obtained according to the flow chart given in Figure 8-8, and for this particular case the motion on the revolute and prismatic joints are illustrated by the bottom graphs of Figure 8-31. The simulation results of the path following for the revolute and prismatic joint are shown in Figures 8-32 and 8-33 respectively. From Figures 8-32b and 8-33b, which show the positional error for the revolute and prismatic joint respectively, it can be seen that the error is significantly affected when the velocity of the joints is severely changed. This outcome, for a manipulator that uses clutches to dissipate the user-input energy, is very difficult to be improved, as no blending can be applied due to the limited range of velocities that are possible to regulate smoothly.

The approximated path in polar and Cartesian coordinates is shown in Figures 8-33a and 8-33b respectively. It can be seen that the path obtained goes right through the predefined points, hence in order to approximate the predefined path accurately enough a reasonable amount of desired points need to be selected. The desired and approximated paths in polar and Cartesian coordinates are superimposed in Figures 8-34a and 8-34b.

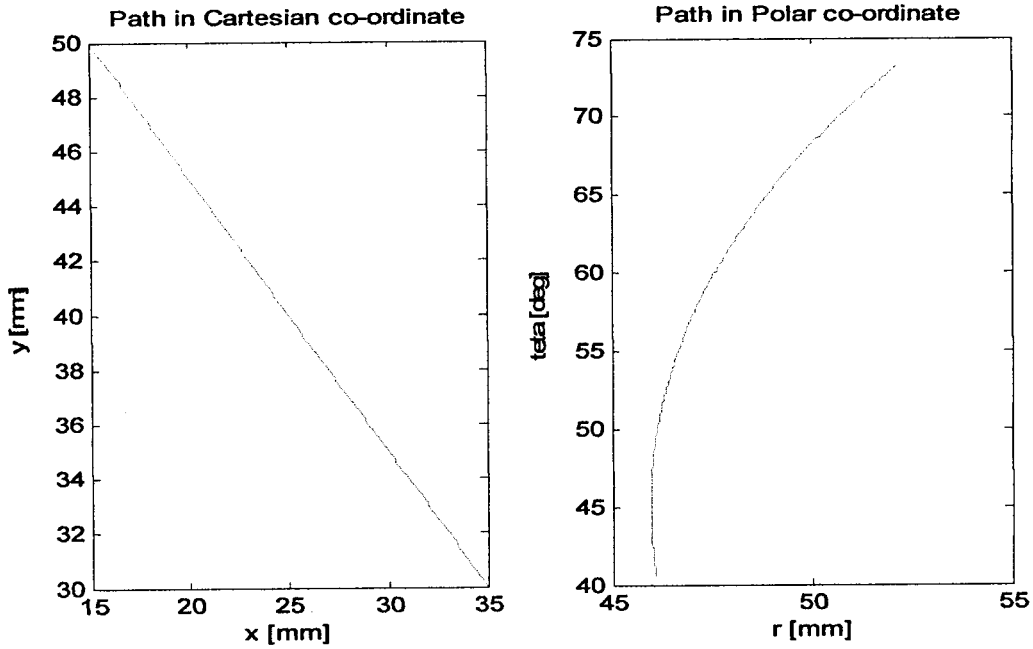

Figure 8-30. Predefined path

a) in Cartesian space and b) in polar coordinates

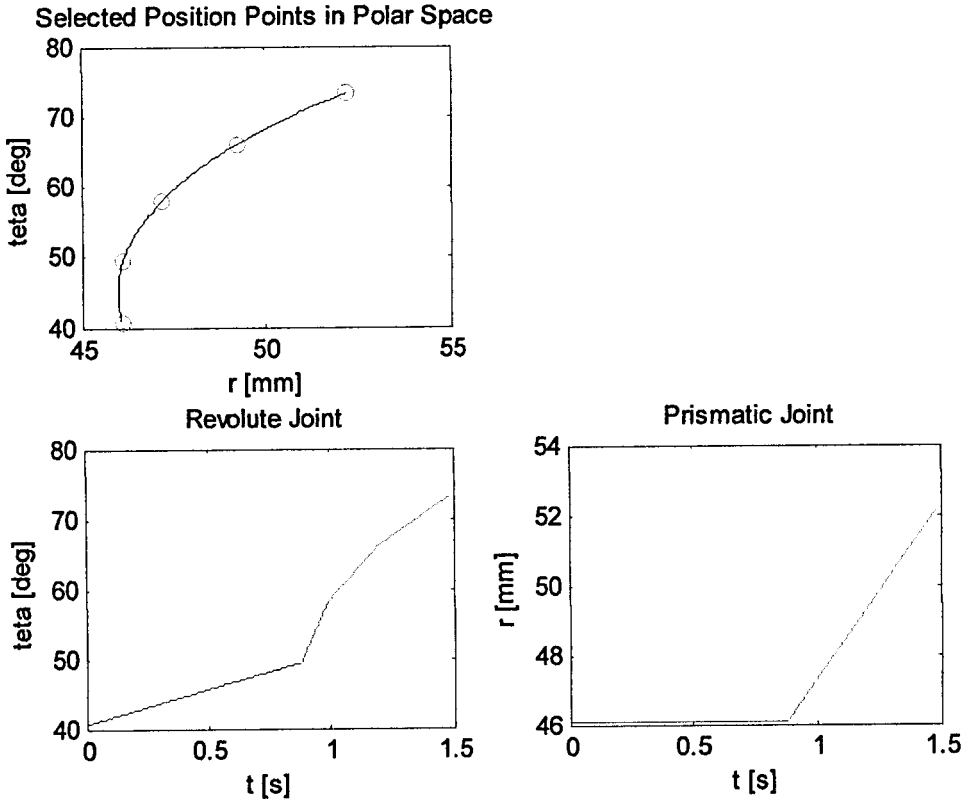

Figure 8-31. Select desired points on the polar path and perform path control

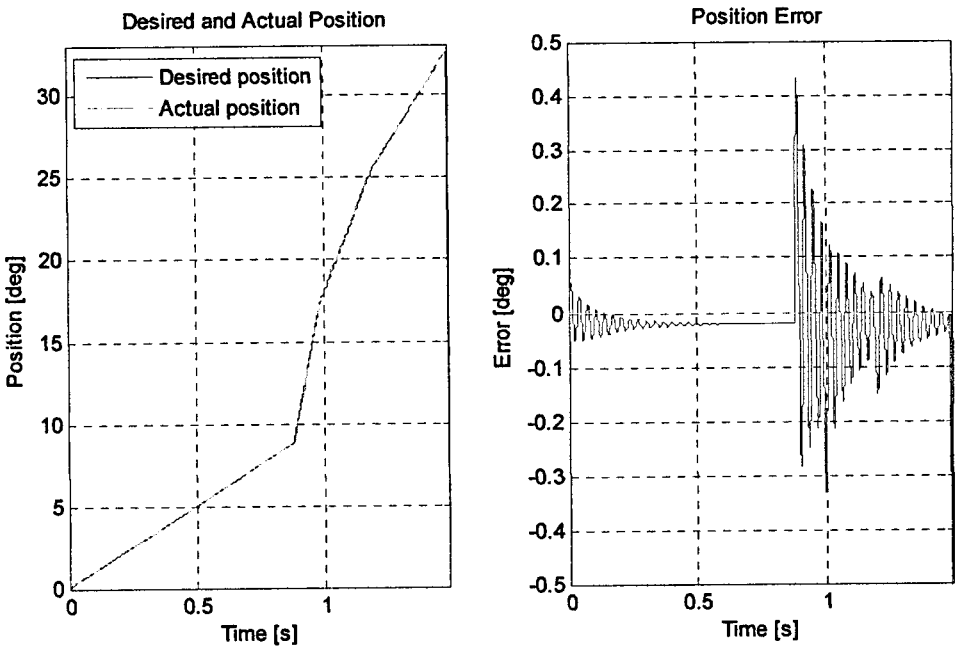

Figure 8-32. Simulation of the trajectory mode: Revolute joint

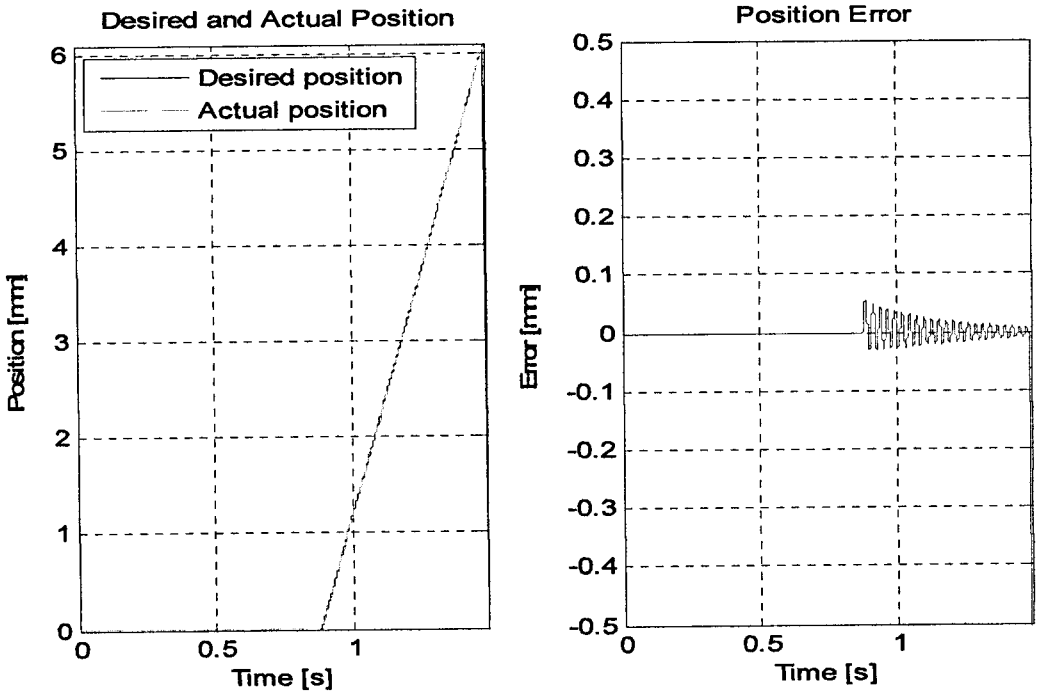

Figure 8-33. Simulation of the trajectory mode: Prismatic Joint

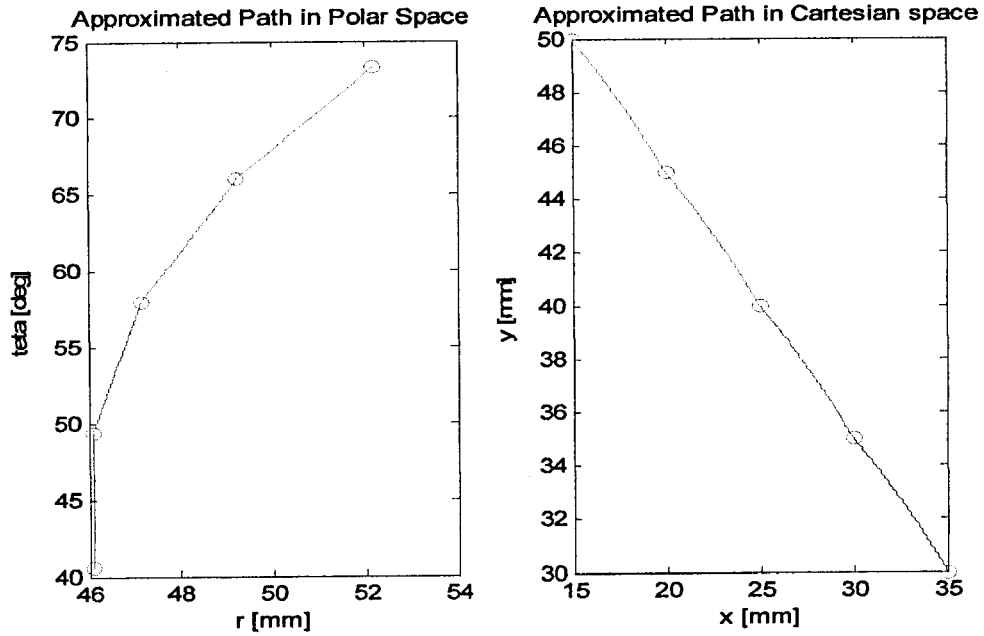

a) b)

Figure 8-34. Approximated path

a) in Polar space, and b) in Cartesian space

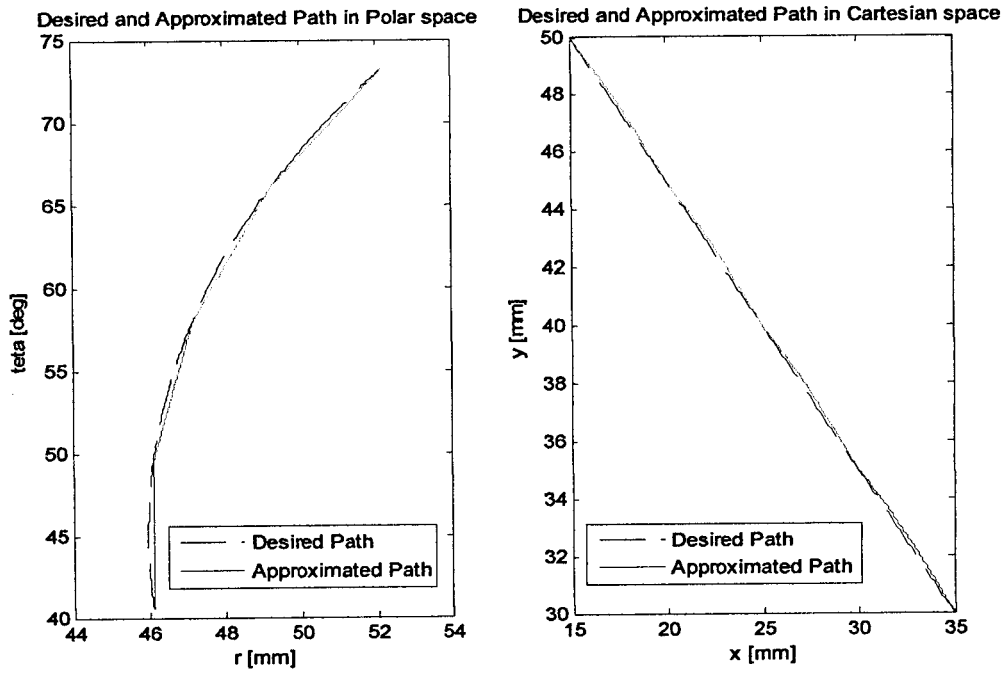

a) b)

Figure 8-35. The desired and approx path in polar and Cartesian coordinates

8.5.3 Region mode

The description of the task-interpreter algorithm for the *'region'* mode was discussed in section 8.2.3. In this section, simulation results are presented only for the situation when the tip of the manipulator is between the intermediate and safety border (i.e zone II or the restrained zone). This is because in zones I and III the control is minimum (i.e. the resistance is either zero or maximum), and because the restrain of the motion on the boundary is similar to trajectory following, which was presented in the previous section, 8.5.2.

The control of the manipulator joints when the tip of the manipulator is in zone II is performed according to the diagram shown in Figure 8-15. Depending on the actual position of the end-effector and on the user-input force magnitude and direction, the restrained motion in zone II is given by the equations (8-17) and (8-18) for the revolute and prismatic joint respectively. In this section, only one example is chosen to illustrate the efficiency of the proposed strategy, however, mare scenarios were simulated and analysed.

Consider the scenario shown in Figure 8-36. The tip of the manipulator is assumed to be in zone I at a random point R of coordinates (40, 10). It is also assumed that the user applies a force, F_u, so that the manipulator moves only on the x-axis, as shown in Figure 8-36a (i.e. $F_u = [10, 0]^T$). From Figure 8-36b it can be seen that the strategy employed for the 'region' mode allows the user to move freely in zone I (i.e. without any constraints) until the end-effector reaches the intermediate boundary, given in this case by the point A of coordinates (55, 10). As soon as the end-effector reaches the intermediate boundary, the resistive force is increased proportional to the distance from the safety border, which in this case is given by point B of coordinates (60, 10). As the user-input force pushes the end-effector towards zone III, according to the strategic definition of the *'region'* mode given in the diagram shown in Figure 8-14, a maximum resistance is applied until the end-effector is stopped.

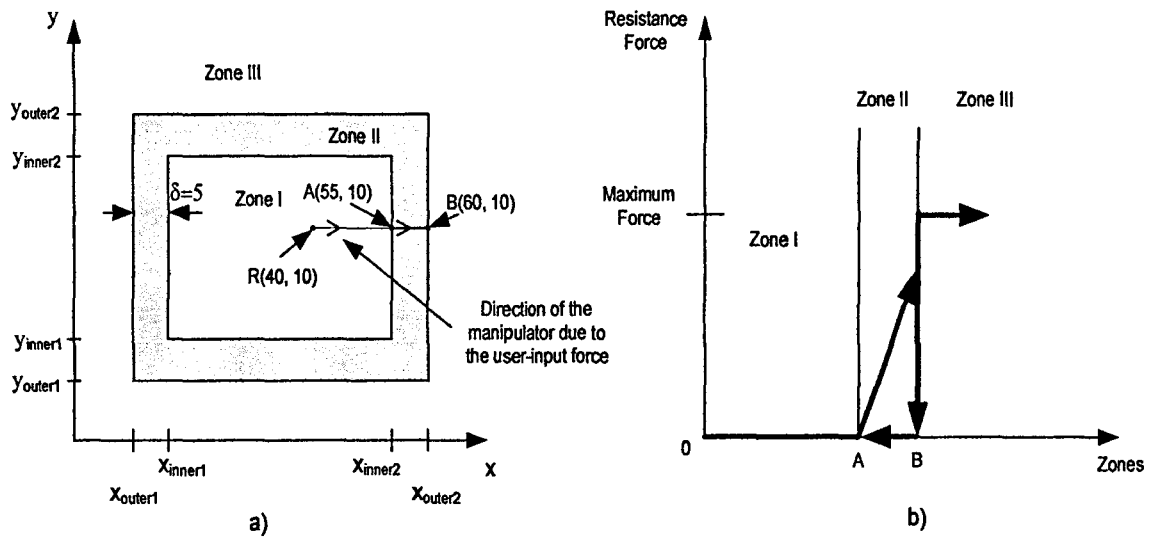

Figure 8-36. Example of the strategy employed for the 'region' mode

The unrestrained motions of the revolute and prismatic joints for this particular case are illustrated in Figures 8-37 and 8-38 in Cartesian space, and in polar space, respectively. From Figure 8-37 it can be seen that the end-effector, under the user-input force $F_{u,\varphi}$ = 10N, is reaching a position of more than 100mm on the x-axis in t = 5s. Furthermore, only 0.05 seconds are necessary to complete the motion in zone II (i.e. for 55mm $\leq x \leq$ 60mm). In the unrestrained simulation no input control has been used.

The restrained motion in zone II, (i.e. for 55mm $\leq x \leq$ 60mm) is presented in Figures 8-39 and 8-40 for polar and Cartesian coordinates. It can clearly be seen that the motion of the prismatic joint has been restrained in zone II and was finally stopped at the safety border. In zone II the user is constrained to move the end-effector with a much slower velocity, thus requiring a much longer time to pass through zone II. From Figure 8-40, it can be seen that a time of approximately 0.35 seconds has to pass until the end effector is finally brought to the safety border.

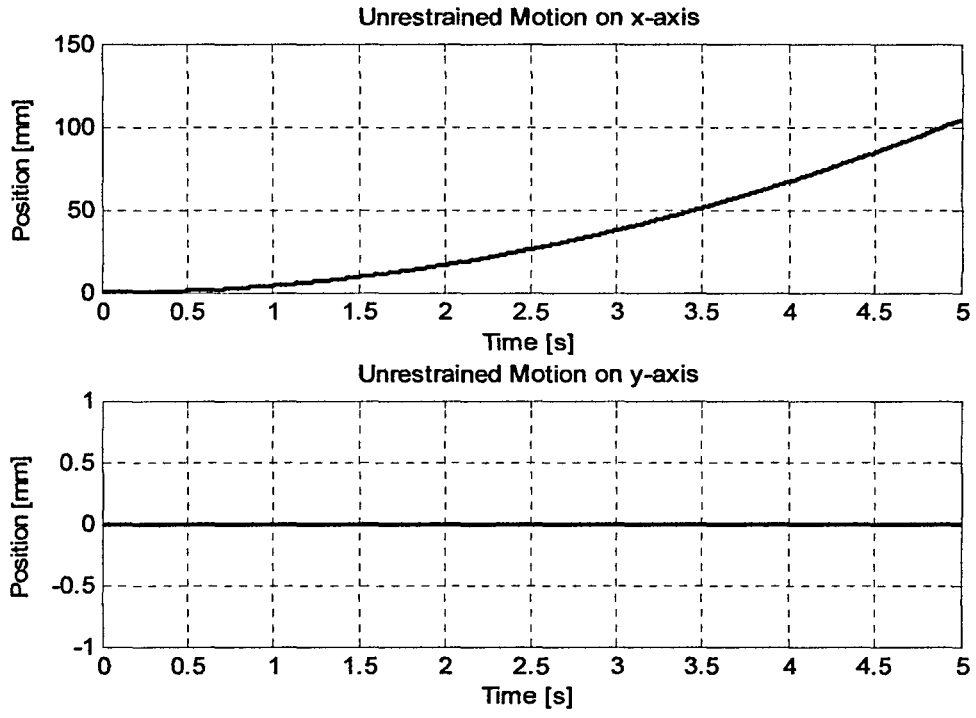

Figure 8-37. Unrestrained motion in Cartesian space

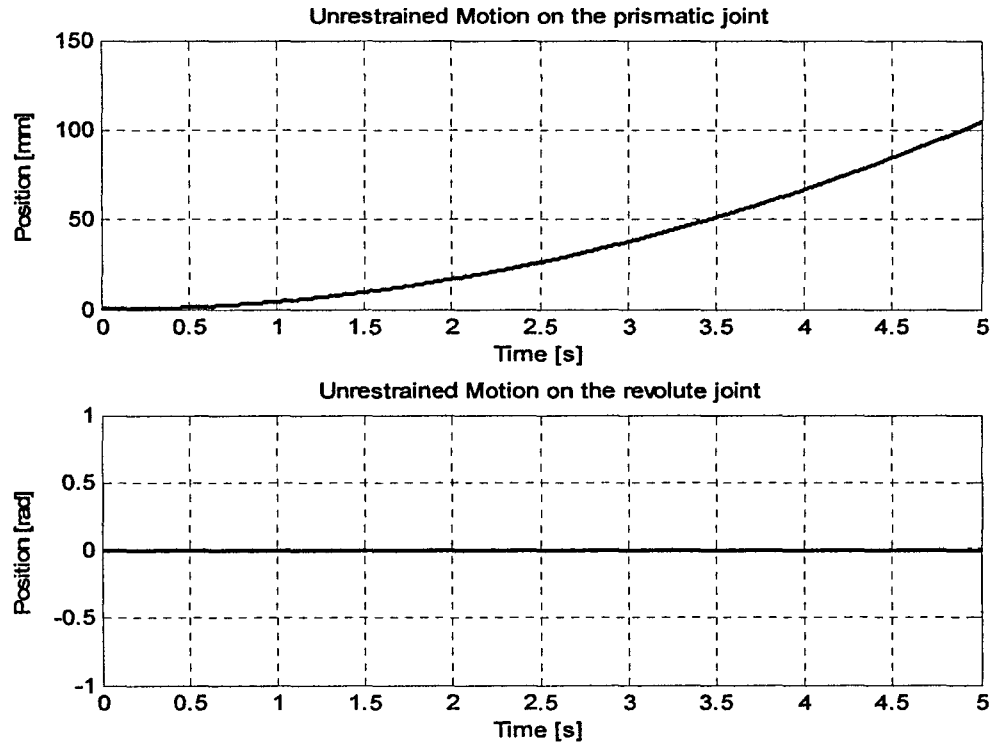

Figure 8-38. Unrestrained motion in polar space

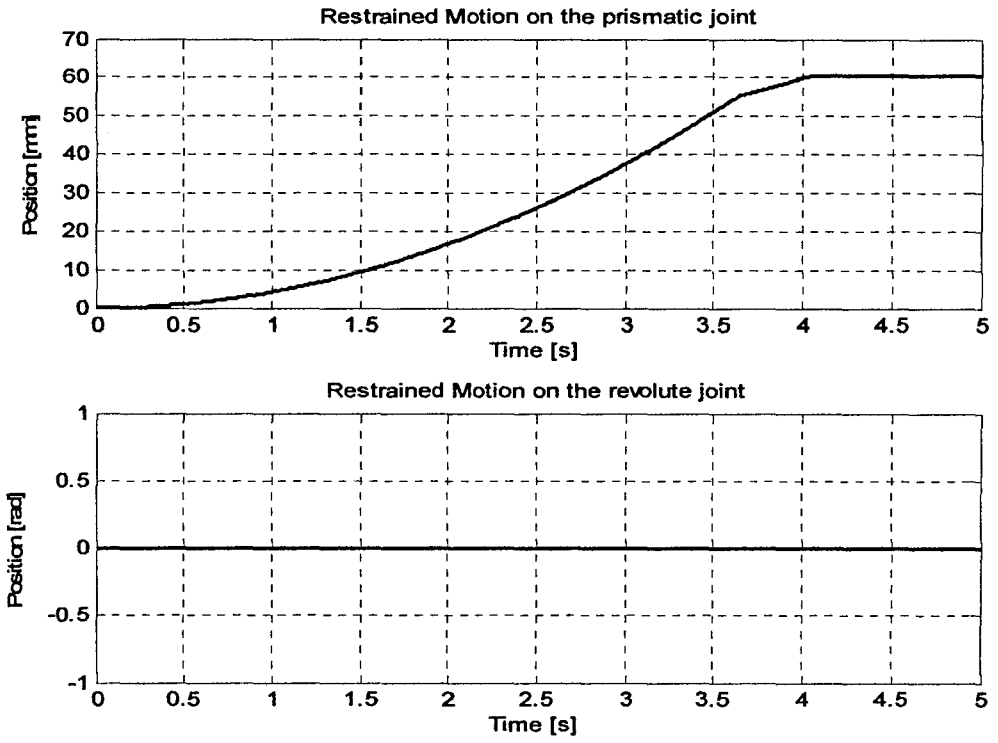

Figure 8-39. Restrained motion in polar space

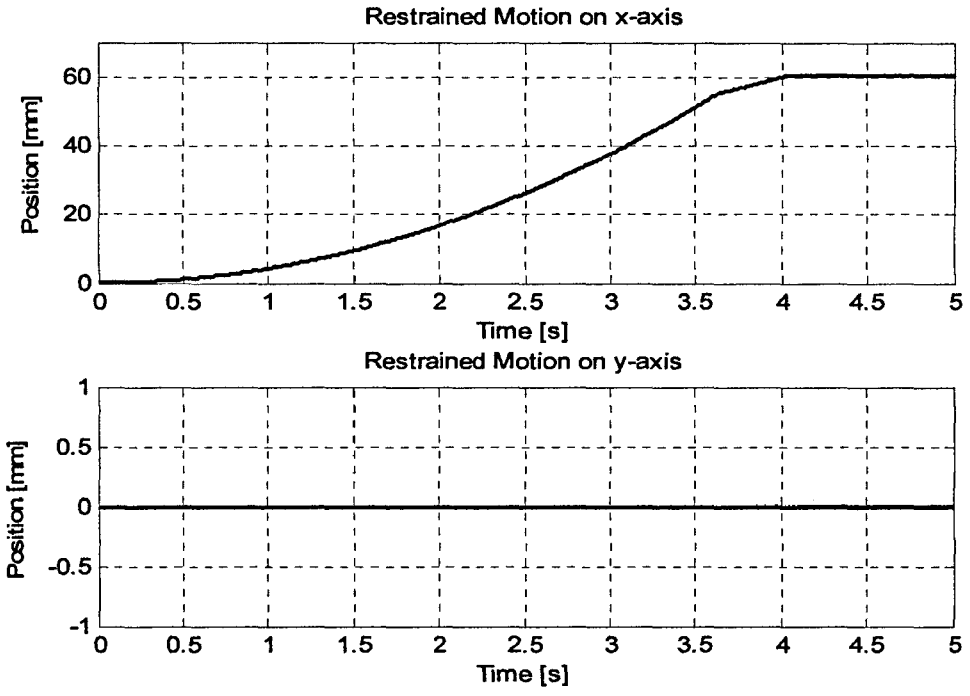

Figure 8-40. Restrained motion in Cartesian

The desired and actual velocities of the prismatic joint are shown in Figure 8-41. It can be seen that if the velocity of the joint is greater then or equal to the restrained value, then the motion is restrained according to equation (8-16). Please note that in Figure 8-41, zone II starts at the time t = 3.65s, and therefore, for t<3.65s the end-effector is in zone I where no control input was provided.

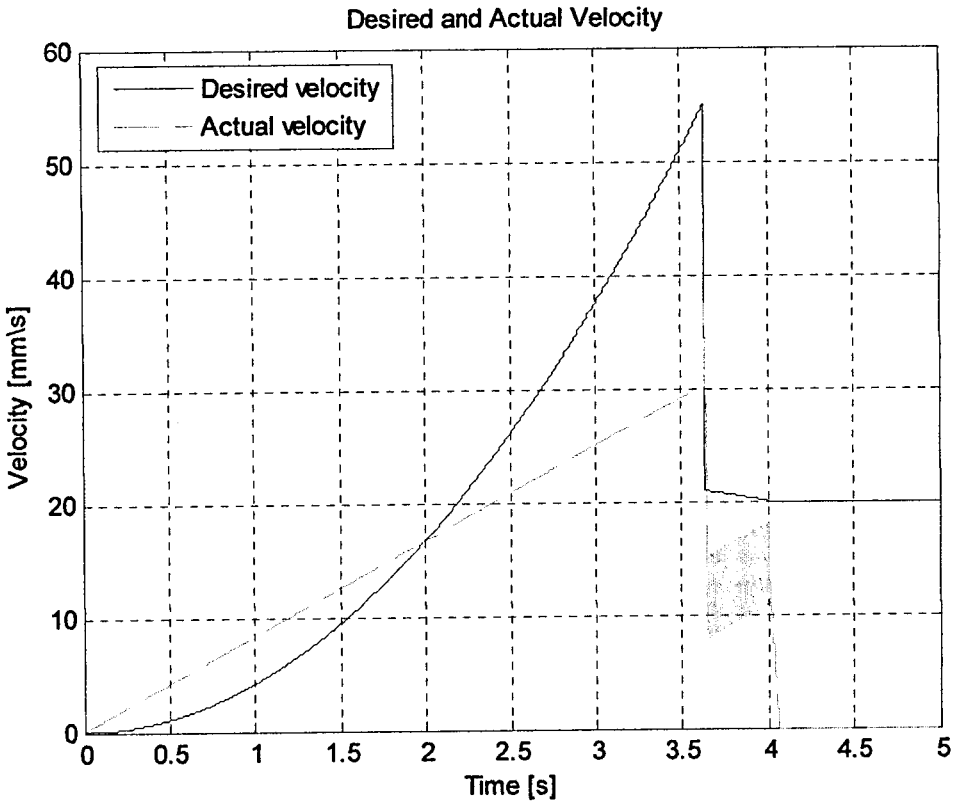

Figure 8-41. Desired and actual velocities of the prismatic joint

8.6 Conclusions

This chapter describes the control of a two-DOF actively restrained passive mechatronic system. The control strategy shown in the previous chapter for a one-DOF system was extended in this chapter for a two-DOF manipulator. By measuring joint positions and the user-input force, a 'task interpreter algorithm' was developed for task definition so that efficient control is guaranteed. The control strategy employed for the revolute joint

in the previous chapter is retained and is further applied for a prismatic joint. Simulation results were carried out, which demonstrates the effectiveness of the proposed control system for all three modes of operation: (1) reach a predefined position, (2) follow a predefined trajectory, and (3) stay within a predefined safety region.

From the analysis of the *'position'* mode it can be seen that for both revolute and prismatic joints, the positional error is minimal. This was shown to be due to robust and efficient control strategy, as well as good actuator performance. Moreover, it was observed that for the revolute joint the accuracy of the system with piezoactuator is much higher than the accuracy obtained with a DC motor, shown in the previous chapter. A difference of approximately 10 times was noticed, which demonstrates a great potential of the piezoactuator for an efficient clutch mechanism.

The simulation results of the path following for the revolute and prismatic joint show a significant change in positional error. This change is due to the fact that the velocity of the joints is severely changed. This outcome, for a manipulator that uses clutches to dissipate the user-input energy, is very difficult to be improved, as no blending can be applied due to the limited range of velocities that are possible to regulate smoothly. It was shown that because of the fact that the velocity of the proposed clutch mechanism can only be regulated between the predefined velocities, $\mathbf{V_{min}}$ and $\mathbf{V_{max}}$, the motion between the desired position points cannot be blended at the beginning and end of the motion, as it is usually performed by active robots. Thus, at the beginning and end of the motion, the system has to start and stop from an initial velocity. This discontinuity in the velocity command contributes to a decrease in the overall accuracy of the manipulator and it can easily be observed from the analysis of the *'trajectory'* mode.

The discontinuity in the velocity command cannot be avoided in a system with dry friction. Therefore, a compromise between the motion smoothness and accuracy needs to be considered before employing a clutch mechanism in an application. For safety critical applications the use of passive manipulators to ensure safety of those interacting with the operating environment was shown to be of utmost importance. However, the passive systems are limited regarding smooth and accurate motion control.

Chapter 9
Conclusions and Recommendations for Further Work

9.1 Introduction

In this research, three major limitations of existing passive devices actively restrained were addressed. It was shown that on all three areas of research significant improvements have been made, which contributes considerable to the knowledge in areas of passive robotic devices, actuators technology and control. Firstly, the kinematic configuration was significantly improved so that the path following definition is more accurate and much easier to implement in practice. Secondly, the actuator and transmission technology were improved by proposing a piezoactuator and a compact clutching method to produce the frictional torque. Finally, a control strategy able to compensate for stick-slip friction at very low velocities was developed, which allows smooth and accurate motion control.

In this chapter the conclusions that can be drawn from this study are summarised. The chapter aims to show how the objectives given in Chapter 2 have been met. The chapter concludes with recommendations for further work. A list of proposed publications that are to be made as part of this study is also included.

9.2 Conclusions from this research

This section aims to show how the objectives given in Chapter 2 have been met. The seven objectives are repeated here for clarity and are defined as:

Objective 1: The mechatronic system should not be able to move on its own, but only under the direct control of a human operator.

Objective 2: The mechatronic system must be able to be moved completely free.

Objective 3: The mechatronic system must be able to physically guide the operator so that a predefined position can be reached.

Objective 4: The mechatronic system must be able to guide the operator so that a predefined trajectory can be followed.

Objective 5: The manipulator's end-effector must stay within a pre-specified envelope or safety region.

Objective 6: The control algorithms and strategies employed should be robust against external disturbances such as the user-input force or from the mechanical properties of the device itself.

Objective 7: The manipulator must be easy to use with little or no training.

The thesis highlights the importance of safety associated with the introduction of active robot systems such as Robodoc, Acrobot, and Aesop in the operating environment. As a result, an actively restrained passive mechatronic system has been proposed as a solution for assisting surgeons in orthopaedic surgical procedure. This is because an actively restrained passive mechatronic system combines the advantages of both passive and active systems: the complexity of tasks potentially achieved by an active system with the limited risk of a passive one. By employing a friction clutch mechanism as a mechatronic joint to restrain the user-input force, the manipulator would not be able to move on its own, but only under direct control of a human operator, thus accomplishing objective 1. The proposed electromechanical friction clutch is not able to introduce motion in the system, but only to restrain the motion by dissipating the user-supplied

energy. Therefore, if no control is provided to the joints, the manipulator can be moved freely, thus satisfying the objective 2 of this research.

This thesis has identified the limitations of existing actively restrained passive devices such as PADyC, PTER and COBOT. The limitations of the manipulator kinematics for trajectory following tasks, as well as the limitations of the control strategy of such passive systems are discussed. As a solution to these limitations, a two-DOF polar manipulator has been proposed. It has been demonstrated that for the latter kinematic architecture, the path planning and path tracking issues are simpler, and complex tasks can be achieved more effectively. Furthermore, the operators do not have to 'feel' their way along a narrow corridor, bouncing from wall to wall, as is the case for PTER and PADyC. This kinematic configuration also reduces the need for training, thus satisfying objective 7.

As a result of this preliminary work an alternative joint mechanism has been designed. Besides the fact that the proposed electromechanical friction clutch satisfies objective 1, it has been shown that it can also smoothly and effectively control the joint's motion so that objectives 3, 4, and 5 are satisfied.

The proposed electromechanical friction clutch comprises an actuator, which provides a force onto a brake disc, and uses a rigid and compact friction mechanism to provide the frictional torque. As friction plays an important role in designing efficient and controllable clutches, the control of a machine with friction is generally very challenging. It has been shown that friction effects such as stick-slip can never be fully compensated for in a system with boundary lubrication. The effect often results in undesirable dynamic behaviour, and is often responsible for performance limitations. This has also been shown in the case of this friction clutch. For this particular clutch it was noticed that for a velocity less than 0.4rad/s (approx. 24deg/s) the friction is in the boundary lubrication regime, which means stick-slip will occur, therefore the motion below 0.4 rad/s is practically impossible to be smoothly controlled. This result shows a very important limitation of this clutch as it is required to control the motion for velocities in the region of 0.1 rad/s (i.e. approx 1rpm or 6deg/s). Therefore, the task of

designing a controller able to diminish the stick-slip effect, which is highly challenging, is necessary. Another important observation of the friction in the proposed clutch is the fact that the coefficient of friction drops significantly for velocities between 1 and 2rad/s (approx. 58-115deg/s). The experimental results obtained are in accordance with Stribeck model of friction. Such a drop in the coefficient of friction means that only a relative smaller frictional torque can be produced at the contact between the cantilever and the braking disc in this speed range. These observations are, however, dependent on the materials in contact and with a different combination of materials these results are likely to change.

A control strategy to effectively compensate for the nonlinearity of the friction at velocities between 6 and 100deg/s (approx. 0.1rad/s and 1.75rad/s) has been developed in this study. Three controllers capable of diminishing or completely cancelling the stick-slip effect have been developed and investigated. A PD controller was first developed and analysed, but such a controller was shown to be effective only for velocities above 0.35rad/s (approx. 20deg/s). Simulation and experimental tests were performed for both a constant and variable driving torque. Similar results were obtained from both the experimental and simulation tests. These results demonstrate the validity of the friction model used, as well as the validity of the system's mathematical model used to design friction compensators. Moreover, the position accuracy obtained with the PD controller proved to be acceptable for the operating environment.

In an attempt to compensate for stick-slip for a velocity between 6deg/s and 20deg/s, a computed-torque control (CTC) law has been considered. The CTC method proved to be very efficient as long as exact system parameters are obtained. This was shown in the simulation analysis, where it was shown that besides fully avoiding the stick-slip effect, even for a position rate of 2deg/s, the controller is capable of tracking the position with a very small error. However, exact knowledge of the system parameters is impossible in practice, and the experimental analysis was shown to suffer from the sensitivity to errors in the estimates of the system parameters such as friction-related parameters. One solution to this problem is to measure directly the frictional torque produced by the mechanism, and then try to compensate for friction nonlinearities such as stick-slip.

This solution can be successful so long as accurate torque/force measurement is achieved. The solution is linked with a suitable method of torque/force measurement as well as an appropriate mechanical design to ensure high system stiffness and effective noise isolation. Furthermore, as the results with CTC show great potential for diminishing the stick-slip effect with an accurate estimated model, it is recommended that further research into accurate estimation techniques of highly non-linear parameters such as friction-related parameters to be undertaken. This can either be performed using evolutionary algorithms such as genetic algorithms for learning different behaviours of a machine with friction, or combining a measuring technique with some intelligent control based on adaptive/predictive theory.

A more robust approach developed in this study is the sliding-mode control (SMC) method where it is not necessary to know exactly the system parameters, but only bounds on these parameters. The PD controller was shown to be effective for only velocities greater than 20deg/s. Using SMC it has been demonstrated that the stick-slip was much reduced at low velocities and a velocity down to 6deg/s could be controlled with very satisfactory results. Stick-slip reduction by almost 90% has been achieved with SMC when compared with the PD controller. This achievement is considered very important as the issue of smooth and accurate position control in a system with dry friction proved to be the most sensitive and problematic in literature.

Comparing the simulation and experimental analyses of the system with SMC the results show some differences in the amplitude of the positional error. While the simulation results show a very narrow amplitude band of 0.02deg for position error, the experimental results show an amplitude band of 0.1deg. This is because it is very difficult (almost impossible) to model friction accuratelly. Moreover, the SMC was shown to be more sensitive to sudden changes in driving torque when compared with the PD controller. However, the SMC is quicker to compensate for sudden changes than the PD controller. The superior performance of the SMC is due to the fact that when the system is in the sliding mode, the tracking error is independent of the system parameters, while the PD controller is dependent on the system dynamics, which is affected by the friction in the mechanism. Nevertheless, both controllers proved

efficient against external disturbances such as external driving torque and quite efficient against sudden changes in velocity.

As a result of this investigation a combination of PD control and SMC has been proposed in order to obtain an efficient control strategy for the motion control of the proposed actively restrained passive mechatronic system. For desired velocities higher than 20deg/s the PD controller is employed as it can control the motion smoothly and accurately (i.e. without stick-slip). For velocities between 6 and 20deg/s a SMC is used as this method shows good robustness and efficiency at low velocities. Thus, the objective 6 has been fulfilled.

Besides avoiding the stick-slip effect within the mechanism, the controller is required to track the desired position with an error less than 0.2deg. This level of error ensures that the overall error of the two-DOF prototype, introduced in section 3.3, is less than 1mm. However, position errors less than 0.6 deg were achieved on the actively restrained passive joint. This is comparable with the accuracy of PTER which reported the minimum error out of all existing actively restrained devices. However, because of the kinematic solution proposed in this research, it is believed that the system error can be minimised further by improving the performance of the proposed clutch mechanism.

A task-interpreter algorithm has been developed, which allows a two-DOF manipulator to successfully achieve objectives 3, 4, and 5 (i.e. to reach a predefined position, to track a predefined trajectory, and to stay within a prespecified region). The simplicity, yet efficiency of the proposed algorithm are demonstrated. Because the strategy used is based on rapidly switching between different velocities, it was shown to have a significant effect on the positional error. This is very difficult to improve upon, as at low velocities the stick-slip within a machine with dry friction can never be fully compensated for. Therefore, the use of friction clutches for actively restrained passive systems is compromised by the performance requirements such as smooth and accurate motion needed for a specific application. Furthermore, the motion in the 'region' mode becomes discontinued when the end-effector approaches the final boundary. This is due

to the fact that a velocity control strategy is used, with the velocity obtained by approximating the measured position. This needs to be improved in future by either employing an accelerometer to obtain the velocity by integrating the measured value, or by adapting the control strategy so that a position control is used rather than a velocity control.

Significant steps have been made towards developing a safe mechatronic device for direct human interaction. It has been shown that an electromechanical clutch can be used to restrain the motion so that a user can achieve certain tasks. A revolute joint was shown to work well, even though the accuracy was shown slightly higher. Nevertheless, the motion was smoothly controlled. The strategy employed to achieve objectives 3, 4, and 5 for both the one-DOF and two-DOF systems was shown to be simple, and easy to implement. However, the fact that the velocity has to be steeply changed in order to achieve a task was shown to increase the positional error. This condition cannot be avoided in a system with dry friction at low velocities and therefore, a compromise between the motion smoothness and accuracy needs to be considered.

9.3 Recommendations for Further Work

There are certain enhancements that are required to help improve the performance of the proposed joint mechanism and further this research. The next step is to investigate other materials for the cantilever and the brake disc (i.e. materials in contact which produce the sliding friction) so that stick-slip is diminished to a minimum at the outset. Also, with a different selection of materials in contact, the frictional torque produced can be increased, and thus more user-provided energy can be dissipated without the need for a new actuator.

In order to improve the performance of the CTC and SMC controllers developed, a more accurate mathematical model of the friction is required. This can be achieved by carrying out extensive experiments and maybe developing a particular friction model for this specific clutch.

Another natural progression of this work is to replace the DC motor with a more powerful and fast actuator such as a piezoelectric actuator. It has been shown in simulations that a piezoelectric actuator has the potential of controlling the system's motion with much greater accuracy than it is possible with the DC motor. The piezoactuator was shown to have the advantages required to design an efficient clutch however, the costs involved in acquiring the actuators and the required drivers are relatively expensive. Nevertheless, with the results from this study funding organisations or commercial companies could be approached for extra support and, therefore this option is suggested to commence in the near future.

Besides improving the mathematical model of the friction in the mechanism as discussed above, it is proposed that further research into both torque measurement and accurate estimation of highly non-linear parameters such as friction-related parameters to be undertaken. Nevertheless, a non-model-based friction compensation technique using CTC and SMC can be implemented in association with an adaptive method in order to increase further the performance of the control strategy.

The task-interpreter algorithm for a two-DOF manipulator has been shown to be simple to implement and efficient. However, the model used does not consider the human dynamics in the control loop. This issue should be taken into consideration in future research as an accurate model of the whole system and its interacting environment can be of much help in designing suitable control systems for more complicated mechanical structures.

9.4 Publications

As part of this research two journal papers have been written with plans for the submission of two other journal papers in the near future.

9.4.1 Written

Lacraru, L.M., and Bouazza-Marouf, K., Design and Control of a Clutch Mechanism Externally Driven, Proceedings of the Institution of Mechanical Engineers, Part K: Journal of Multi-body Dynamics. To be Submitted March/April 2005.

Lacraru, L.M., and Bouazza-Marouf, K., Friction Compensation of an Actively Restrained Friction Clutch, Proceedings of the Institution of Mechanical Engineers, Part I: Journal of Control and Systems Engineering. To be Submitted March/April 2005.

9.4.2 Planned

Lacraru, L.M., and Bouazza-Marouf, K., Control of an Actively Restrained Passive Revolute Joint for Safety Critical Applications. Proceedings of the Institution of Mechanical Engineers, Part I: Journal of Control and Systems Engineering, or IEEE Transaction on Robotics and Automation. To be submitted in May/June 2005.

Lacraru, L.M., and Bouazza-Marouf, K., Task Definition for an Actively Restrained Passive Mechatronic System for Safety Critical Applications, Elsevier, Journal of Computational and Applied Mathematics. To be submitted in May/June 2005.

References

[1] **National Horizon Scanning Centre,** Surgical Robots, *The University of Birmingham*, January 2000.

[2] **Insall JN, Windsor RE, Scott WN, Kelly MA, Aglietti P,** Surgery of the Knee, *Ed. Churchill Livingstone*, 1993, ISBN: 0-443-087-2.

[3] **Ian Browbank,** Interim Report, *Loughborough University*, 1997.

[4] **Kienzle T. C., Stulberg S. D., Peshkin M, Quaid A, Lea J, Goswami A, Wu Chi-Haur,** A Computer-Assisted Total Knee Replacement Surgical System Using a Calibrated Robot. *Computer-Integrated Surgery*, 1996, 409-416.

[5] **Aglietti P, Buzzi R, Gaudenzi A,** Patellofemoral functional results and complications with the posterior stabilized total condylar knee prosthesis, 1988.

[6] **Garg A, Walker P S.** Prediction of total knee motion using a three-dimensional computer graphics model. *J. Biomech.* 1990, **23**, 45-58.

[7] **Stulberg S D, Kienzle III T C,** Computer- and Robot- Assisted Orthopaedic Surgery, *Orthopaedics*, 1996, 373-378.

[8] **Leitner, F., Picard, F., Minfelde, R., Schultz, H-J, Cinquin, P., and Saragaglia, D.** Computer-Assisted Knee Surgical total Knee Replacement. *Lecture Notes in Computer Science*, 1997.

[9] **Matsen III FA, at al.,** Robotic Assistance in Orthopaedic Surgery: A proof of principle using distal femoral arthroplasty, *Clin. Orthop.* 1993, **296**, 178-186.

[10] **Fadda M, Bertelli D, Martelli S, et al.** Computer-Assisted Planning for Total Knee Arthroplasty. *Proc. of the 1st Joint Conf. on Computer Vision, Virtual Reality and robotics in Medicine and Medical Robotics and Computer Assisted Surgery*, Grenoble, 1997.

[11] **Marcacci M, Dario P., Fadda M, Marcenaro G, and Martelli S** Computer-Assisted Knee Arthroplasty. *Orthopaedics*, 1998, 417-423.

[12] www.robodoc.com/eng/robodoc.html (accessed 01.02.05).

[13] www.roboticsonline.com/public/articles/articlesdetails.cfm?id=113 (accessed 01.02.05)

[14] **Lynne Peterson,** Trends in Medicine, American Academy of Ortopaedic Surgeons, New Orleans, Feb 2003.

[15] **Davies BL, Fan KL, Hibberd RD, Jakopec M, Harris SJ,** A Mechatronic based robotic system for knee surgery. . 1997, 48-52.

[16] **Davies B.L., Harris, SJ, Lin, WJ., Hibberd RD., Middleton R, and Cobb, J. C.,** Active compliance in robotic surgery-the use of force control as a dynamic constraints, *Proc Instn IEEE Mech Engrs*, Part H, vol 211, 1997, 285-292.

[17] **Geert Van Ham, Denis K, Sloten JV, Audekercke RV, Van de Perre G, De Schutter J, Aertbelien E, Demey S,** Machining and Accuracy Studies for a Tibial Knee Implant Using a Force-Controlled Robot, *International Society for Computer Aided Surgery*, vol 3, 1998, 123-133.

[18] **Reedman, AVC** *The design and control of a manipulator for safety critical deployment applications*, PhD Thesis, Loughborough University, 2002.

[19] **Sackier JM, Wang Y,** Robotically Assisted Laparoscopic Surgery: from concept to development, *Computer-Integrated Surgery*, 1995, 577-580.

[20] **Das H, Zak H, Johnson J, Crouch J, Frambach D** Evaluation of a Telerobotic System to Assist Surgeons in Microsurgery, *Computer Aided Surgery*, vol 4, 1999, 15-25.

[21] http://www.intuitivesurgical.com/ (accessed 29.04.01).

[22] www.computermotion.com/zeus.html (accessed 29.04.01).

[23] http://www.armstrong-healthcare.com/ (accessed 05.05.01).

[24] www.robodoc.com/eng/neuromate.html/ (accessed 01.02.05).

[25] **Burckhardt CW, Flury P, Glauser D** Integrated Minerva system meets demanding robotic requirements, *IEEE Engineering in Medicine and Biology* vol 14, no. 3, 1995, 314-317.

[26] Taylor R. H., Paul, H. A., Mittelstadt B.D., Hanson W., Kazanzides P, An image-based robotic system for hip replacement surgery. 1990.

[27] Brian L. Davies, A discussion of safety issues for medical robots. *In Proceedings of 2nd International Workshop on Computer Assisted Robotic Medical Interventions*, Bristol, 1996.

[28] RH Taylor, et al. Taming the Bull: Safety in a Precise Surgical Robot, *Proceedings of the 1991 International Conference on Advanced Robotics*, 1991.

[29] Cinquin P., et al. Computer Assisted Medical Interventions, *IEEE, Eng in Medicine and Biology*, vol 14, no 3, 1995.

[30] DiGioia, A.M., Jaramaz B., and Colgan, B.D. Computer Assisted Orthopaedic Surgery, *Clinical Orthopaedic and Related Research*, 354, 1998, 8-16.

[31] Brian L. Davies, A review of robotics in surgery. *Proc. Instn. Mech. Eng.* Vol 214, Part H, 2000.

[32] DiGioia AM, Simon DA, Jaramaz B, Blackwell M, Morgan F, O'toole RV, Colgan B, Kischell E HipNav: pre-operative planning and intra-operative navigational guidance for acetabular implant placement in total hip replacement surgery, *Proceedings CAOS*, 1995.

[33] Simon DA, Jaramaz B, Blackwell M, Morgan F, DiGioia MD, Kischell E, Colgan B, Kanade T Development and validation of a navigational guidance system for acetabular implant placement. *Lecture Notes in Computer Science*, 1997, 583-592.

[34] Julliard R, Lavallee S, Dessenne V, Computer Assisted Reconstruction of the Anterior Cruciate Ligament. *Clinical Orthopaedics and Related Research*, vol. 354, 1998, 57-64.

[35] Merloz P., Tonetti J., et.al, Pedicle screw placement using image guided techniques, *Clinical Orthopaedics and Related Research* 1998, 39-48.

[36] Philips R, Viant WJ, Mohsen MMA, Griffiths JG, Bell MA, Bell TJ, Cain TJ, Sherman KP, Karpinski MR Image guided orthopaedic surgery design and analysis, *Transactions of the Institute of Measurement and Control*, vol. 17, no. 5, pp 251-264, 1995.

[37] Viant WJ, Phillips R, Griffiths JG, Ozanian TO, AMMA Mohsen, Cain TJ, Karpinski MRK, Sherman KP A Computer Assisted Orthopaedic Surgical System for Distal Locking of Intramedullary nails. *Proceedings of Mechanical Engineers: Journal of Engineering in Medicine*, vol. 211, pp 293-300, 1997.

[38] Joskowicz L, Milgrom C, Simkin A, Tockus L, Yaniv Z, FRACAS: a system for computer-aided image-guided long bone fracture surgery, *Computer Aided Surgery*, vol. 3, pp 271-288, 1998.

[39] Tonetti J, Lionel C, Lavallee S, Pittet L, Merloz P, Chirossel J-P, Percutaneous iliosacral screw placement using image guided techniques. *Clinical Orthopaedics and Related Research*, pp 103-110, 1998.

[40] Langlotz F, Bachler R, Berlemann U, Nolte l-P, Ganz R, Computer assistence for pelvic osteotomies. *Clinical Orthopaedics and Related Research*, pp 92-102, 1998.

[41] Blackwell M, Morgan F, DiGioia AM, Augmented reality and its future in orthopaedics, *Clinical Orthopaedics and Related Research*, pp 111-122, 1998.

[42] Troccaz J, Delnondedieu Y Synergistic robots for surgery: an algorithmic view of the approach, *Proceedings of the Workshop on the Algorithmic foundations of Robotics*, 1998.

[43] Troccaz J, Lavallee S, Hellion E, PADyC: a passive arm with dynamic constraints, *Proceedings of the 5th International Conference on Advance Robotics*, pp 361-366, 1993.

[44] Troccaz J, Delnondedieu Y, Semi-active guiding systems in surgery. A two-DOF prototype of the passive arm with dynamic constraints (PADyC). *Mechatronics*, vol. 6, no 4, pp 399-421, 1996.

[45] Lavallee, S and Troccaz, J., Robot de guidage ge gestes et procede de commande, *European Patent, Pat. #: EP0057433OA1*, 15 December 1993.

[46] Lavallee, S and Troccaz, J., Robot for guiding movements and control method thereof, *United States Patent, Pat. #: US005399951A*, 21 March 1995.

[47] Schneider O, Troccaz J, PADyC: A Synergistic Robot for Cardiac Puncturing, *Proceedings of the IEEE International Conference on Robotics and Automation*, vol. 3, pp 2883-2888, 2000.

[48] Kwoh YS, A new computerised tomographic-aided stereotaxis system, *Robotica* 1985.

[49] Kwoh YS, Hou J, Jonckheere EA and Hayall, S, A robot with improved absolute positioning accuracy for CT guided stereotactic brain surgery. *IEEE Trans. Biomed. Engineering*, Feb. 1998, 35(2), 153-161.

[50] Cleary K, Stoianovici D, Glossop N, Gary K, Onda S, Cody R, Lindisch D, Stanimir A, Mazilu D, Patriciu A, Watson V, Levy E, CT-Directed Robotic Biopsy Testbed: Motivation and Concept, 2000.

[51] Cook A, Ravenna O, Cook A, Yanof J, Cavnah P, Hines J, Chaturvedi A, Interactive computer user interface for planning robotic-assisted interventions, *Radiology* 213, pp 577, 1999.

[52] Bouazza-Marouf, K., Browbank I., and Hewit, J., Robotic-assisted internal fixation of femoral fractures. *Proc. of the Instn. Of Mech. Eng.* Part H, vol. 209, 51-58, 1995.

[53] http://www.qnx.com/ (accessed in 05.03.2002)

[54] Sackier JM, Wang Y, Robotically Assisted Laparoscopic Surgery: from concept to development. *Computer-Integrated Surgery*, pp 577-580, 1995.

[55] Das H, Zak H, Johnson J, Crouch J, Frambach D Evaluation of a Telerobotic System to Assist Surgeons in Microsurgery. *Computer Aided Surgery*, vol 4, pp 15-25, 1999.

[56] http://robotics.jpl.nasa.gov/tasks/rams/homepage.html (29.04.01).

[57] Kobayashi E, Masamune K, Sakuma I, Dohi T, Hashimoto D, A New Safe Laparoscopic Manipulator System with a Five-Bar Linkage Mechanism and an Optical Zoom, *Computer Aided Surgery*, vol. 4, pp 182-192, 1999.

[58] Taylor R. H., Paul, H. A., Mittelstadt B.D., Hanson W., Kazanzides P, An image-based robotic system for hip replacement surgery. 1990.

[59] Mittelstadt B, Paul HA, Kazanzides P, Zuhars, J, Williamson, B., Petit R, Cain, P., Kloth, D., Rose L, Musits BL Development of a surgical robot for cementless total hip replacement. *Robotica*. vol. 11. pp 553-560. 1993.

[60] Taylor R. H., Mittelstadt B.D., Paul H. A, Hanson W., Kazanzides HP, Zuhars J, Glassman E, Musits BL, Williamson B, Bargar WL, An Image-Directed robotic System for Precise Orthopaedic Surgery. *IEEE Transaction on Robotics and Automation*. pp 261-274. 1994.

[61] Cain, P., Kazanzides P, Zuhars, J, Mittelstadt B, Paul HA, Safety considerations in a surgical robot. *Biomedical Sciences Instrumentation*, vol. 29, 1993, pp. 291-294.

[62] Grueneis, C.O.R., Ritcher, R.H. and Hening, F.F, Clinical introduction of the CASPAR system. *In Proceedings of 4th International Symposium on Computer Assisted Orthopaedic Surgery*. Davos. Switzerland. March 1999.

[63] Brandt G, Radermacher K, Lavallee S, Staudt W, Rau G, A compact robot for image guided orthopaedic surgery: concept and preliminary results, *Lecture notes in Computer Science*, pp 767-776. 1997.

[64] Glauser D, Flury P, Villotte N, Burckardt CW, Mechanical concept of the neurosurgical robot Minerva. *Robotica* vol. 11. pp 567-575. 1993.

[65] Glauser D, Frankhauser H, Epitaux M, Hefti JL, Jaccottet A, Neurosurgical Robot Minerva. First results and current developments. *Proceedings of the Second Annual International Symposium on Medical Robotica and Computer Assisted Surgery*, pp 24-30, 1995.

[66] Flury P, Minerva. a robot dedicated to neurosurgery operations, *Proceedings of the 23rd ISIR* pp 729-733. 1992.

[67] Davies B, Harris S, Jakopec M, Cobb J, A Novel Hands-on Robot for Knee Replacement. *Proceedings of European Robotic Systems Workshop on Medical Robotics*, pp98-102 . Pisa. Italy. Sept 1999.

[68] Ho S. C., Davies B. L., Hibberd R.D, A force control strategy with active motion constraint for robot assisted knee surgery. *IEEE Engineering in Medicine and Biology*, pp 292-300. 1995.

[69] Book, W., Charles, R., Davis, R., and Gomes, M., The Concept and Implementation of a Passive Trajectory Enhancing Robot. Proceedings of the ASME Dynamic Systems and Control Division. vol. 58. 1996. pp. 633-638.

[70] Love, L.J., and Book, W., Design and Control of a Multi-Degree-of-Freedom Haptic Interface. *Proceedings of the 1994 Int. Mech. Engng. Congress and Exposition*, 2. 6-11 November. Chicago. IL. pp. 851-856.

[71] MA Peshkin, JE Colgate, C Moore Passive robots and haptic displays based on nonholonomic elements. *Proceeding of the IEEE International Conference on Robotics and Automation*, 1996.

[72] JE Colgate, W Wannasuphoprasit, MA Peshkin Cobots: Robots for Collaboration with Human operators. *ASME*. 1996.

[73] Book, WJ., Charles, RA.. Trajectory Guidance Apparatus and Method, *United States Patent, Pat. #: US005704253A*. 6 Jan 1998.

[74] Swanson DK and Book WJ., Torque Feedback Control of Dry Friction Clutches for a Dissipative Passive Haptic Interface. *IEEE Conference on Control Applications*, Anchorage, AK. 2000.

[75] Swanson DK and Book WJ., Path-Following Control for Dissipative Passive Haptic Displays. *11th Intern. Symp on Haptic Interfaces for Virtual Environment and Teleoperated Systems*. Los Angeles. CA. 2003

[76] Swanson DK and Book WJ., Obstacle Avoidance Methods for a Passive Haptic Dysplay. *IEEE/ASME International Conference on Advanced Intelligent Mechatronics*, Como, Italy, 2001.

[77] S Munir, L Tognetti, WJ Book, Experimental evaluation of a new braking system for use in passive haptic displays. *American Controls Conference*, 1999.

[78] LJ Tognetti, *Actuator design for a passive haptic display*. Master thesis, Georgia Institute of Technology. 1999.

[79] JE Colgate, MA Peshkin, W Wannasuphoprasit, Nonholonomic Haptic Display, *Proceeding of the IEEE International Conference on Robotics and Automation*, vol.1, pp 539-544, 1996.

[80] Moore CA., *Continuously Variable Transmission for Serial Link Cobot Architectures*, M.S. Thesis Northwestern University, 1997.

[81] Wannasuphoprasit W, Akella P, Peshkin M, Colgate JE, Cobots: A Novel Material Handling Technology, *Proceedings of IMECE*, 1998.

[82] Akella P, Peshkin M, Colgate JE, Wannasuphoprasit W, et. al, Cobots for the automobile assembly line, *Int. Conf. On Robotics and Automation*, 1999.

[83] B Gillespie, Peshkin M, Colgate JE, A general framework for cobot control, *IEEE Transaction on Robotics and Automation*, vol. 17, no. 4, august 2001, pp391-401.

[84] AVC Reedman and K Bouazza-Marouf, Composite adaptive control of a robotic joint for passive deployment applications, *Proc Instn Mech Engrs* vol 216 Part I: J of Systems and Control Engineering, 2002, pp 275-289.

[85]. Childs, R.N, Mechanical Design, Ed. Arnold, 1998.

[86] Orthwein, W.C, Clutches and Brakes design and selection, Marcel Dekker, Inc., 1986.

[87] Pugh, B Friction and Wear, Butterworth & Co Ltd, 1973.

[88] http://www.physlink.com/Education/AskExperts/ae139.cfm (accessed 25.05.2001)

[89] Lansdown, AR, Price AL, Materials to resist wear, Pergamon Press 1984.

[90] http://www.matweb.com/search.htm (accessed 13.07.2001).

[91] Buerbaumer HW, *The Systematic Mechatronic Approach: Passive Arm Manipulator for Surgical Applications*, Master thesis, Loughborough University, 1997.

[92] Piezomechanik Dr. Lutz Pickelmann GmbH, Piezomechanical Stackactuators-data sheet, 2001.

[93] Philips components, Piezoelectric Ceramics, properties and applications, 1991.

[94] Armstrong-Helouvry, B., Dupont, P. and Canudas de Wit C., A Survey of Models, Analysis Tools and Compensation Methods for the Control of Machines with Friction, *Automatica*, vol. 30, pp. 1083-1138, 1994.

[95] Dahl, P. R, A solid friction model TOR-158(3107-18) The Aerospace Corporation, El Segundo, CA, 1968.

[96] Dahl, P. R, Solid friction damping of mechanical vibrations, AIAA J., 14(12) 1675-1682, 1976.

[97] Dahl, P. R, Measurement of solid friction parameters of ball bearings. *Proc. of 6th Annual Symposium on Incremental Motion, Control System and Devices*, Univ of Illinois, ILO, 1977.

[98] Fuller DD, Theory and Practice of Lubrication for Engineers, John Wiley and Sons, 1984.

[99]. Armstrong-Hélouvry, B., Control of Machines with Friction, Kluwer Academic Publishers, Norwell, MA, 1991.

[100]. Gogoussis, A., and Donath, M., Coulomb Friction Joint and Drive effects in Robot Mechanisms, *IEEE*, 1987, pp. 828-836.

[101]. Kubo, T., and Tomizuka, M., Application of Nonlinear Friction Compensation to Robot Arm Control. *IEEE International Conference on Robotics and Automation*, Vol. 2, 1986, pp.722-727.

[102]. Leonard, N. E., and Krishnaprasad, P. S., Adaptive Friction Compensation for Bi-Directional Low-Velocity Position Tracking, *Proceeding of the 31st Conference on Decision and Control*, 1992, pp. 267-273.

[103]. Yang, S., and Tomizuka, M., Adaptive Pulse Width Control for Precise Positioning Under Influence of Stiction and Coulomb Friction, *IEEE*, 1987, pp. 188-193.

[104]. Canudas de Wit, C., Noel, P., Aubin, A., and Brogliato B, Adaptive Friction Compensation in Robot Manipulators: low velocities, *The International Journal of Robotics Research*, 1991, vol. 10, pp. 189-199.

[105]. Kubo, T., Anwar, G., and Tomizuka, M., Application of nonlinear friction compensation to robot arm control, *Proc. Inter. Conf. of Robotics and Automation*, 1986, San Francisco, Ca. pp 722-727.

[106]. Morel, G., and Dubowsky, S., "The Precise Control of Manipulators with Joint Friction: A Base Force/Torque Sensor Method", Proceedings of the IEEE Conference on Robotics and Automation, (1996)

[107]. Bell, R. and Burdekin M., A study of the stick-slip motion of machine tools feed drives, *Proc. of the Instn. of Mechanical Engineers*, 1969, vol. 184, no. 29, pp. 543-560.

[108]. Kato, S., Yamaguchi , K., and Matsubayashi, Stick-slip motion of machine tools sideways, *ASME Journal of Engineering for Industry*, 1974, vol. 96, pp. 557-566.

[109]. Gitis, N. V., Study of anti-stick-slip properties of machine tool guideway materials, *Soviet Journal of Friction and Wear*, 1996, vol. 7, pp. 72-76.

[110]. Tung, E. D., Urushisaki, Y., Tomizuka, M., Low velocity friction compensation for machine tool feed drives, *Proc. Americal Control Conference*, San Francisco, CA, 1993, pp. 1932-1936.

[111]. Younkin, G. W., Modelling machine tool feed servo drives using simulation techniques to predict performance, *IEEE Trans. on Industry Applications*, 1991, vol. 27, pp. 268-274.

[112] Leonardo Da Vinci. The Notebooks, Dover, NY, 1519.

[113]. Amontons, G, On the resistance originating in machines, *Proc. of the French Royal Academy of Sciences*, pp.206-222, 1699.

[114]. Coulomb , CA. Théorie des machines simples, en ayant égard au frottement de leurs parties, et e la roideur dews cordages. *Mém. Math Phus.* pp. 161-342, 1785.

[115]. Stribeck, R. Die Wesentlichen Eigenschaften der Gleit- und Rollenlager-The key qualities of sliding and roller bearings, *Zeitschrift des Vereines Seutscher Ingenieure*, 46(38), pp.1342-1348, 1902.

[116]. Hess DP, Soom A, Friction at a lubricated line contact operating at oscillating sliding velocities, *J. of Tribology* 112(1), pp. 147-152, 1990.

[117]. Bo, L.C. and Pavelescu, D., The Friction-Speed Relation and its Influence on the Critical Velocity of Stick-Slip Motion. *Wear*. Vol. 82(3). pp. 277-289, 1982.

[118]. Armstrong-Hélouvry, B., Stick-slip arising from Stribeck friction, *Proc. 1990 Intern Conf on Robotics and Automation*. Cincinnati. pp. 1377-82.

[119] Bell and Burdekin, Dynamic behaviour of plain sideways, *Proc of the Instn of Mech Engn* vol 181 no 8 169-83. 1966.

[120] Bell and Burdekin, A study of the stick-slip motion of machine tools feed drivers *Proc of the Instn of Mech Engn* vol 184 no 29 540-60. 1969.

[121] Vinogradov et al., Steel-to-steel friction over a very wide range of sliding speeds, *Wear* 10(5) 338-352. 1967

[122] Khitric and Shmakov, Static and dynamic characteristics of friction pairs Soviet *J. of Friction and Wear* 8(5) 112-115. 1987.

[123]. Haessig DA. and Friedland B, On the modelling and simulation of friction, *J. of Dyn. Syst. Measurement and Control Transaction ASME*, 113(3):354-362, 1991

[124]. Bliman and Sorine, Friction modelling by hysteresis operators. Application to Dahl, sticktion and Stribeck effects, *In Proc of the Conf "Models of Hysteresis"*, Trento, Italy, 1991.

[125]. Bliman and Sorine, A system-theoretic approach of systems with hysteresis. Application to friction modelling and compensation. *In Proc of the 2nd European Control Conference*, Groningen, The Netherlands. pp. 1844-49. 1993

[126]. Bliman and Sorine, Easy to use realistic dry friction models for automatic control, *Proceedings of 3rd European Control Conference*. Rome. Italy, pp. 3788-3794, 1991.

[127]. C. Canudas de Wit, H. Olsson, KJ Astrom, and P. Lischinsky, A new model for control of systems with friction. 40(3). 1995.

[128]. Ganseman C., Swevers J, and Al-Bender F., An integrated friction model with improved presliding behabiour. *In 5th IFAC Symp on Robot Control*, Nantes, France, 1997.

[129]. Henrik Olsson. Control Systems with Friction, PhD thesis, Lund Institute of Technology, University of Lund 1996.

[130]. Olsson, H., Astrőm, K.J., Cannudas de Wit, C., Gäfvert, M. and Lischinsky, P., "Friction Models and Friction Compensation", European Journal of Control, vol.4, no.3, pp.176-95, 1998.

[131]. Threlfall DC., The inclusion of Coulomb friction in mechanisms programs with particular reference to DRAM, *Mechanisms and Machine Theory*, 13(4), 475-483, 1978.

[132]. Bernard JE., The simulation of Coulomb friction in mechanical systems, *Simulation* 34(1), 11-16, 1981.

[133]. Rooney GT and Deravi P., Coulomb friction in mechanism sliding joints. *Mechanisms and Machine Theory*, 17(3), 207-211, 1982.

[134]. Karnopp D., Computer simulation of stick-slip friction in mechanical dynamic systems, *ASME J of Dynamic Systems, Measurement and Control* 107(1) 100-103, 1985.

[135] Rabinowicz, E., The intrinsic variables affecting the stick-slip process, *Proc. Pfysical Society of London*, 71(4), pp. 668-675, 1958.

[136]. Kato, S., Yamaguchi , K., and Matsubayashi, Stick-slip motion of machine tools sideways, *ASME Journal of Engineering for Industry*, 1974, vol. 96, pp. 557-566.

[137]. Martins J., Oden J., and Simoes F, A study of static and kinetic friction, *International Journal of Engineering Science*, 1990, vol. 28, no.1, pp.29-92.

[138]. Asada H. and Youcef-Toumi K., Analysis and design of a direct drive arm with a five-bar-link parallel drive mechanism, *J of Dynamic Systems, Measurement and Control* , 1984, 106(2) 225-30.

[139]. Townsend, WT, Salisbury JK. The effect of Coulomb friction and stiction on force control, *Proc 1987 Inter. Conf. On Robotics And Automation, IEEE*, Raleigh 883-89, 1987.

[140]. Dupont, P. E., Avoiding Stick-Slip Through PD Control, *IEEE Trans. On Automatic Control*, 1994, vol. 39, pp. 1094-1097.

[141]. Luh, J. Y. S., Fischer W. D., and Paul R. P. C., Joint torque control by a direct feedback for industrial robots. *IEEE Trans. on Automatic Control*, 1983, vol. 28, pp. 153-161.

[142]. Pfeffer, L., Khatib O. and Hake J., Joint torque sensory feedback in the control of a PUMA manipulator. *IEEE Trans. on Robotics and Automation* 1989, vol. 5, pp. 418-425.

[143]. Hashimoto, M., Robot motion control based on joint torque sensing, *Proc. Inter. Conf. On Robotics and Automation*, 1989, pp. 256-261.

[144]. Wu, C.H., and Paul, R. P., Manipulator compliance based on joint torque control, *19th Conference on Decision and Control, IEEE,* Albuquerque, NM, 1980, pp. 89-94.

[145]. Lee, Seok-Beom. Misawa, Eduardo A.. Lucca, Don A., Sliding mode compensation of dry friction, *IEEE Conference on Control Applications - Proceedings*, (1996), p 809-813.

[146]. Ando, Noriaki. Korondi, Peter. Hashimoto, Hideki. Szemes, T., Friction compensation for 6-DOF cartesian coordinate haptic interface, *IEEE International Conference on Intelligent Robots and Systems*, v3, 2002, p 2893-2898.

[147]. Wang, Zhonghua. Wang, Xingsong. Xu, Weiliang, Robust adaptive friction compensation for X-Y positioning table, Dongnan Daxue Xuebao (Ziran Kexue Ban)/Journal of Southeast University (Natural Science Edition), v 32, n 1, 2002, p 69-72

[148]. Bogoliubov, NN. And Mitropolski, YA, Asymptotyc Methods in the Theory of Non-linear Oscillations, Gordon and Beach, NY, 1961.

[149]. Anderson BDO, et. al., Stability of Adaptive Systems, Passivity and Averaging Analysis, Cambridge MIT Press, 1986.

[150]. Chou W, Dithering and its effects on sigma delta and multi-stage sigma delta modulation, *IEEE Intern. Symp. On Circuits of System*, Part 1, New Orleans, 268-71, 1990.

[151]. Hirel P, Adaptive optics, dither optimisation method in an adaptive optic model, *Proc. SPIE Inter. Soc. of Opt. Eng.* Hague, 22-32, 1990.

[152]. Chau WK, A critical analysis of dithering algorithms for image processing, *IEEE Region 10 Conf. On Computers and Communication systems*, Hong Kong 309-13, 1990.

[153]. Godfriey, D., Vibration reduces metal to metal contact and causes an apparent reduction in friction. *ASLE Transactions*, 1967, vol. 10 pp. 183-192.

[154]. Zames, G., and Shneydor, N. A., Dither in nonlinear systems, *IEEE Trans. on Automatic Control*, 1976, vol. 21, pp. 660-667.

[155]. Hojjat, Y. and Higuchi T., Application of electromagnetic impulsive force to precise positioning, *Int. Journal of Japan Soc. Precision Engineering*, 1991, vol. 25, pp. 39-44.

[156]. Suzuki A and Tomizuka M, Design and implementation of digital servo controller for high speed machine tools. *Proc. American Control Conf. AACC*, Boston WA, 1246-1251, 1991.

[157]. Gilbert JW and Winston GC, Adaptive Compensation for an optical tracking telescope, *Automatica* 10(2). 125-31, 1974.

[158]. Walrath CD., Adaptive bearing friction compensation based on recent knowledge of dynamic friction. *Automatics* 20(6) 717-27, 1984.

[159]. Canuds de Wit C., Astrom KJ., and K Braun Adaptive Friction Compensation in DC motor drives, *IEEE J of Robotics and Automation*, RA-3(6), 1987.

[160]. Brandenburg, G., and Schäfer, U., Influence and compensation of Coulomb friction in industrial pointing and tracking systems, *Proc of the Indus App Soc Annual Meeting IEEE* Dearborn, MI 1407-13, 1991.

[161]. Johnson CT., Lorentz RD, Experimental Identification of Friction and its Compensation in precise position controlled mechanisms. *Proc of the Indus App Soc Annual Meeting IEEE* Dearborn, MI 1400-1406, 1991.

[162]. Craig, J. J., Adaptive Control of Mechanical Manipulators, Addison-Wesley, 1987.

[163]. Slotine J. J. E. and Li W, On the Adaptive Control of Robot Manipulators, *Int. Journal of Robotic Research*, 1987, vo. 6, pp. 49-59.

[164] Brandenburg, G., and Schäfer, U., Influence and Adaptive Compensation of Simultaneously Acting Backlash and Coulomb Friction in Elastic Two-Mass System of Robots and Machine Tools. 1989.

[165]. Friedland B. and Park WJ, On adaptive friction compensation, *IEEE Trans on Automatic Control,* 37(10). 1992. 1609-1612

[166]. Southward, S.C., Radcliffe, C.J., and MacCluer, C.R., Robust Nonlinear Stick-Slip Friction Compensation. *Journal of Dynamic Systems, Measurement, and Control*, Vol. 113, 1991 pp. 639-645.

[167]. Feemster, M., Vedagarbha, P., Dawson, D.M., and Haste, D., "Adaptive Control Techniques for Friction Compensation". Mechatronics, Vol. 9, No. 2, 1999, pp. 125-145.

[168]. Canudas de Wit, C., Adaptive Control for Partially Known Systems –Theory and Applications. Elsevier. Amsterdam. 1988.

[169]. Wang, Zhonghua. Wang, Xingsong. Xu, Weiliang, Robust adaptive friction compensation for X-Y positioning table. Dongnan Daxue Xuebao (Ziran Kexue Ban)/Journal of Southeast University (Natural Science Edition). v 32, n 1, 2002, p 69-72

[170]. Parra-Vega, V., Adaptive compensation of dynamic friction in finite time of 1 DOF mechanical system. *Proceedings of the American Control Conference*, v 3, 2001, p 2462-2467

[171]. Schilling, R. J., Fundamental of Robotics: Analysis and Control, Prentice Hall, 1990.

[172]. Slotine J. J. E. and Li W, Aplied nonlinear control. Prentice Hall, Englewood Cliffs, NJ, 1991.

[173] Ong, Fook Rhu, *Analysis of bone drilling characteristics for the enhancement of safety and the evaluation of bone strength.* PhD Thesis. Loughborough University, 1998.

[174] Fraucher, S., *Two Degree-of-Freedom Manipulator with Actively Constraints Joints*, MSc thesis. 2002. Loughborough University.

APPENDICES

APPENDIX A

Total Knee Replacement (TKR) procedure

A1. Traditional TKR operation [4]

Before a conventional knee replacement surgery, a standard x-ray of the whole leg (front view) is examined to determine the proper angle of the femoral component with respect to the shaft of the femur. This angle (usually about seven degrees) is chosen such that the tibia will be perpendicular to the ground and be directly under the hip joint. During surgery, a hole is drilled at the end of the femur and a rod is placed down the centre of the bone. A jig is placed on the rod, adjusted to the preoperatively determined angle, and holes are drilled into the bone where indicated by the jig. Guide pins are inserted in these holes, a cutting block is placed on the pins, and a cut is made with a powered oscillating bone saw that defines the horizontal plane of the femoral surface. A second jig is inserted on the rod and the femoral component's remaining cut locations are determined largely by inspection. The tibial component is placed in a similar manner, except that an alignment jig external to the leg is used to direct its positioning. After all cuts are made, the prosthetic components are tested in place and a polyethylene spacer is chosen to maintain the proper ligament tension and full range of joint motion. The components are then cemented in place.

It is quite probable that using this procedure a rather rough match between the bones and prosthesis is produced. This is either because of the improper alignment of the jigs, or because the oscillating saw blade flexes. This can, to some extent, be corrected using a rasp to remove any extra bone, or with extra cement to fill gaps. Ideally this should not be needed, and the bone should be shaped to match the prosthesis with the alignment of the cuts such that correct alignment of the two bones results afterwards.

A2. Robotic- Assisted TKR operation [15]

As from Davies *et al.* [15] such systems have three phases:

i) pre-operative planning.
ii) intraoperative intervention.
iii) post-operative assessment.

Pre-operatively:
-Place five landmark pins in the patient's femur and tibia that will act as fiducial points for registration of the preoperative plan to the actual bone
-Obtain a computer tomographic (CT) image or a magnetic resolution image (MRI) of the patients' leg
-Edit images and create three-dimensional model of leg
-Create three-dimensional model of prostheses
-Superimpose prostheses over three-dimensional model of leg
-Adjust and optimise location
-Plan operative procedure

Intraoperatively:
-Fix and locate patient on table
-Immobilize the bones using specially designed fixtures
-Fix and locate robot (on floor or on table)
-Input three-dimensional model of cuts into robot controller
-Datum robot to patient
-Use the robot to guide the surgical cuts

Post-operatively:
-Remove robot from vicinity
-Release patient
-Check quality of procedure

If further cuts are necessary:

- Reclamp patient
- Reposition and datum robot to patient
- Repeat robotic procedure

APPENDIX B

Actuators and Braking/Clutching methods

B1. Actuators

Table B1. Analysis of different types of actuators [91]

Type of actuator	Advantages	Disadvantages
Pneumatic	- high dynamics; - high reliability and hence safety; - good power to weight ratio; - temperature tolerant;	- limited accuracy; - noise; - backup service required; - heat dissipation requirement in supply system - requires pumps, lines and fittings.
Hydraulic	- high dynamics; - high reliability; - very high power to weight ratio; - high stiffness	- limited accuracy; - oil processing needed; - backup service required; - cooling required for oil; - leaking possible.
Electromagnetic	- flexibility; - high positional and dynamic accuracy; - good close loop control performance; - high energy conversion efficiency.	- limited power to weight ratio; - power dissipation; - temperature range limitations; - complexity.
Electric	- very simple, reliable and efficient; - easy to control; - fast and precise; - predictable dynamic response; - need little or no maintenance; - availability; - low cost;	- provide limited actuation force/torque; - poor power to weight ratio; - high continuous power dissipation; - high ripple torque.

Piezoelectric	- high rigidity; - high stability; - very fast and precise; - easy to control; - need no maintenance;	- provide limited actuation force; - small displacement; - complex dynamics; - expensive.

B2. Braking/Clutching methods

Table B2. Braking/Clutching method comparison [85]

Brake/Clutch Type	Advantages	Disadvantages
Externally and Internally Pivoted Shoe brakes (short shoe, long shoe, drum brake)	- Simple and reliable; - Requires little maintenance; - High brake factor; - Good dust and dirt resistant.	- Relatively poor heat dissipation; - May become self-locking with wear if not properly designed; - Medium stability; - Low maximum operating temperature.
Band and rim clutch/brake	- Simple and reliable; - Large force/torque ratio; - Fairly easily cooled; - Suited for controlled slip.	- Large volume; - Uneven lining wear from one end to another; - Limited materials for the band.
Cone clutch/brake	- Large force/torque ratio	- Requires greater axial length; - Small cone angles require disengagement force.
Annular disc clutch/brake	- Large torque capacity; - Oil-cooled wet clutches and brakes may dissipate large amounts of heat; - Are sealed against dirt and foreign materials.	- Requires more parts than band or drum brakes; - Time-consuming maintenance; - Require additional equipment for forced-air or fluid cooling.
Caliper disc clutch/brake	- High stability; - Good cooling; - Little fade; - Self-cleaning; - High maximum operating temperature; - Ideal for frequent repeated braking.	- Medium brake factor; - Requires relatively large disk radius.
Pneumatic and Hydraulic clutch/brake	- No metal to metal contact is necessary; - Large torque capacity.	- May be difficult to control; - Utilizes air and fluid under pressure; - Introduce oil into the workspace; - Requires pumps, lines and fittings.

Electromagnetic clutch/brake	- Large torque capacity; - Can have fast response;	- Difficult to accurately control; - Low stability; - Large delays, rise times and engagement time; - Complex dynamics.
Magnetic particle clutch/brake	- Constant torque regardless of the slip speed, which is the difference in the speed of input and output shaft; - Suitable for remote control and/or computer control; - No friction surface to wear or require replacement.	- Required to occasionally turn a full revolution to keep particle evenly distributed; - Do not perform well for back and forth motion; - Not as compact as friction clutch/brake.
Hysteresis clutch/brake	- Constant torque at low slip speeds; - Suited for remote control and/or computer control; - No friction surface to wear or require replacement.	- Hysteresis and cogging; - Constant-torque range as a function of the slip speed is limited by the cooling available; - Not as compact as friction clutch/brake; - May require cooling equipment;
Eddy-current clutch/brake	- Nearly constant torque at large slip speeds; - Easy to control at high speeds; - Suited for remote control and/or computer control; - No friction surface to wear or require replacement.	- Torque decreases as slip, or differential, speed decreases; - Not as compact as friction clutch/brake;
Centrifugal clutch/brake	- Automatically engage/disengage at specified speeds; - Mechanically simple; - No external control required; - May be designed to either engage or disengage as speed increases	- Maximum torque is speed dependent; - Very little torque transferred at initial engagement speed.
Overrunning or one way clutch	- Transmits torque only if the primary shaft turns faster than the secondary shaft; - No external control necessary; - Low friction.	- Difficult to accurately control; - Requires more parts then most of the other clutches.

Tooth clutch	- Precise, discrete positioning of the secondary shaft relative to the primary shaft; - Torque limit may be determined by the tooth profile and the axial retaining force.	- May be engaged only when the shafts are stationary or rotate at a very small speed differential.

APPENDIX C

Piezoelectricity and Piezoelectric actuators

C1. Piezoelectricity [93]

The piezoelectric effect was discovered by Jacques and Pierre Curie in 1880. They found that if certain crystals were subjected to mechanical strain, they became electrically polarised and the level of polarisation was proportional to the applied strain. The Curie also discovered that these same materials deformed when they were exposed to an electrical field. This has become known as the inverse piezoelectric effect [93].

Piezoelectric actuators are made from Lead(Pb)- Zirconium(Zr)- Titanate(Toi) oxide ceramic (PZT) and convert electrical signals like voltages or charges into mechanical displacements or forces. If a voltage is applied to an actuator there will be a displacement. When this displacement is blocked, a force will develop, named blocking force, which is a measure of the stiffness of the actuator.

The electrical behaviour of an unstressed medium under the influence of an electric field is defined by the field strength E and the dielectric displacement D. The relation is [93]:

$$D=\varepsilon E \qquad \textbf{(C0-1)}$$

In which ε is the permittivity of the medium. The mechanical behaviour of the same medium at zero electric field strength is defined by two mechanical quantities: the stress applied T and the strain S. The relation is the inverse of Hooke's law:

$$S=sT \qquad \textbf{(C0-2)}$$

where s is the compliance of the medium.

The interaction between the electrical and mechanical behaviour of the medium is described by linear relations between electrical and mechanical variables. Piezoelectric

deformation is essentially linearly dependent on the magnitude of the applied field, conforming to the equation:

$$S=sT+dE \qquad \textbf{(C0-3)}$$

The maximum travel of a PZT element is proportional to its length, so that if one doubles the length of an actuator a double travel will come out. The force produced by a PZT is dependent on two factors: electric field strength and dielectric displacement

$$D=dT+\varepsilon E \qquad \textbf{(C0-4)}$$

The blocking force of an actuator is proportional to its cross section, so that doubling the cross section the blocking force becoming double too. The produced force depends on the driving voltage and the stiffness relation between actuator and clamping mechanism. The maximum blocking force. which can be produced by an actuator, is achieved for infinite stiff clamping at maximum voltage.

To handle high tensile forces a PZT element need to be mechanical pre stressed [82]. Tensile forces are allowed as long as they are compensated by the prestress force. For dynamic operation, the prestress is necessary to compensate acceleration forces by overshooting and during the resetting of the actuator. The minimum prestress force F_{res} is given by the formula [92]:

$$F_{res}=m\Delta l/(\Delta t)^2 \qquad \textbf{(C0-5)}$$

Where, m= mass of the load;

Δl= max. travel;

Δt= min. reset time.

Piezoactuators have very high rigidity, which make them ideal for fast and precise adjustment of tools. They also show an infinitely high positioning sensitivity: an infinitely small change of the operating voltage results in an infinitely small change in position.

The piezoelectric effect is often encountered in daily life. In small butane cigarette or gas grill lighters, a lever applies pressure to a piezoelectric ceramic creating an electric field strong enough to produce a spark to ignite the gas. Furthermore, alarm clocks often use a piezoelectric element. When AC voltage is applied, the piezoelectric materials

moves at the frequency of the applied voltage producing the sound level required. The ink-jet printers are also using piezoelectric elements so that specialized individual character to be created easily [92].

Other domains where piezoactuators are being used are: smart structures (structural deformation), nano-metrology, adaptive optics, critical dimensions measurement, fast tools servos, ultrasonic vibrators, sonar transducer, etc. More applications can be found in [92].

C2. Piezoelectric actuators [92]

Stacked piezoactuators are using the shape deformation of piezoelectric ceramics under the influence of an electrical field: when a voltage of proper polarity is applied to a simple piezoceramic disc or plate, the thickness of the disc/plate increases slightly. To get a greater expansion, lots of discs are stacked together, hence adding the effect of individual components. When a voltage is applied with the specified polarity, the stack expands axially (d_{33} effect). The stroke is nearly proportional with the stacklength.

C2.1 Advantages of PZT Actuators:

- Repeatable nanometer and sub-nanometer steps at high frequency can be achieved;
- Can be designed to move heavy loads (several tons);
- Can be made to operate at very high frequencies (tens of kHz when unloaded);
- No backlash, stiction or friction;
- No wear and tear;
- No magnetic field;
- Clean-room and vacuum compatible, which make them very suitable for operating environment;
- Require no maintenance due to their solid state. Their motion is based on molecular effects within the crystalline cells.

C2.2 Piezoactuators Properties:

a) Piezostacks shows an infinitely high positioning sensitivity. An infinite small change of the operating voltage results in an infinitely small change in position. Therefore, the actuators show a continuous steady motion with no discrete "small steps".

b) Piezoactuators can generate and block high forces. This is due to their solid-state nature. These forces vary to some extent depending on the type of piezo ceramic

used, the spring clamping mechanism, load conditions, prestress, and acceleration forces during dynamic operations.

Important to remember is that force generation by an actuator is only possible at the cost of actuator's stroke. Maximum force generation results in zero strokes.

When the actuator is blocked in motion by clamping with theoretically infinitely high stiffness, the activation by a voltage is completely converted into force generation. The force generation versus stroke, depending on the activation voltage is displayed in Figure A1.

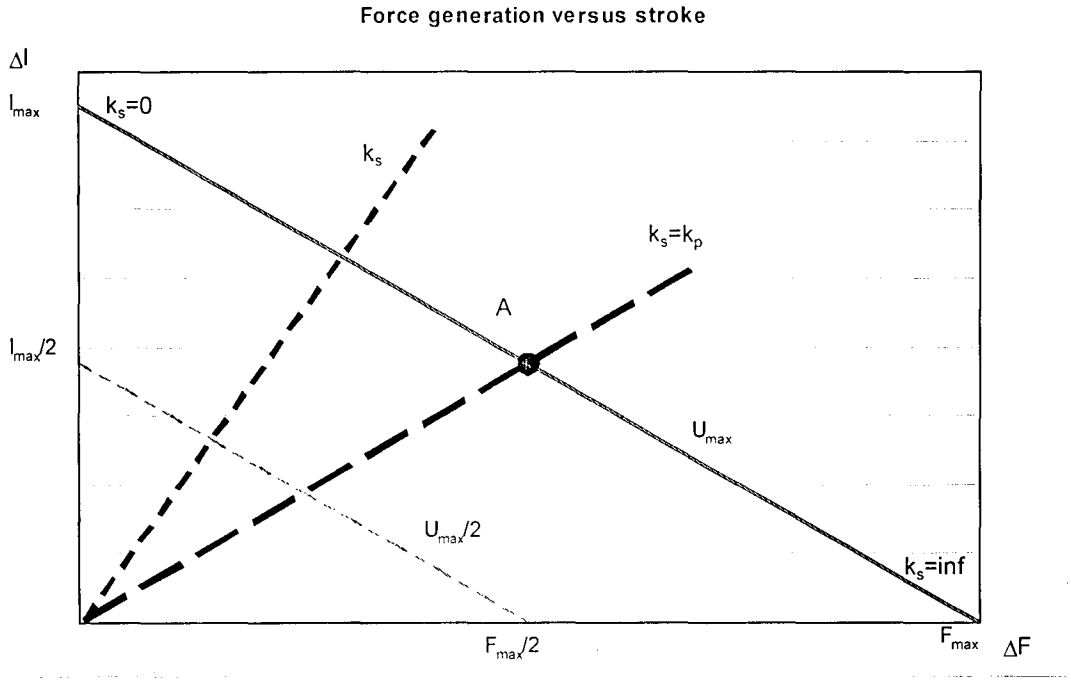

Figure A1. Force Generation v Stroke for different levels of input voltages

The operating point A of the actuator, shown in Figure A1, represents the achievable force and stroke obtained from the intersection of actuator characteristic line l_{max}-F_{max} with the stiffness line k_s of the attached mechanics. This force-stroke diagram shows three cases: (1) k_s=0, represents a negligible stiffness of the actuated system compared to actuator's stiffness. In this case the stroke is maximum while the generated force is zero; (2) k_s=inf, denotes an infinitely stiff clamping of the actuator. This is the blocking

condition. Actuator cannot produce a stroke, but only a force. However, this force can never be reached in real systems because of the limited stiffness of natural materials; (3) $k_s = k_p$ is the case for a well matched actuator system with maximum transfer of physical work from actuator to the attached system. The achieved stroke is half of the maximum stroke l_{max}, and the resulting force is half of the maximum blocking force F_{max}.

c) Stiffness: In practice, "stiffness" is used to define a distinct operating point A, shown in Figure A1, representing the force balance between two interacting elastic systems, namely the actuator (k_p) and the actuated mechanics (k_s). Stiffness of the piezoactuators is related with the stack body dimensions according to the equations:

$$S = E \cdot D/L \qquad \textbf{(C0-6)}$$

Where, S is the actuator stiffness.

E, modulus of elasticity,

D, cross section of the stack actuator,

L, length of the stack actuator.

d) Resonance frequency: The basic axial resonance frequency of a mass loaded stack actuator can be estimated according to the equation:

$$F_{res} = \frac{1}{2\pi}\sqrt{\frac{S}{m}} \qquad \textbf{(C0-7)}$$

where F_{res} is the resonance frequency,

S, actuator's stiffness,

m, attached mass.

e) Time to expand: A PZT can reach its nominal displacement in approximately 1/3 of the period of the resonant frequency.

$$T_{min} \approx \frac{1}{3 \cdot f_0} \qquad \textbf{(C0-8)}$$

f) Electrical capacitance: Piezoactuators capacitance is not constant but varies with the operating conditions due to the variation of the dielectric constant of the piezoceramic. Generally the capacity increases with:

- increase of voltage signal amplitude,
- increase of temperature,
- increase of compressive load force.

Actuator capacity is very important when designing the power/current requirements for a power supply, when piezoactuators are operated dynamically.

g) Hysteresis and creep

Definitions:

Hysteresis: Closed loop of a rate-independent relaxation phenomenon of a piezoceramic

Creep: Time dependent relaxation phenomenon of a piezoceramic. A delay that occurs when a piezoceramic is loaded mechanically or electrically. The rate of creep decreases logarithmically with time. The creep of PZT motion as a function of time is described by:

$$\Delta L(t) \approx \Delta L_{t=0.1}\left[1+\gamma \cdot \lg\left(\frac{t}{0.1}\right)\right] \qquad \textbf{(C0-9)}$$

where, $\Delta L(t)$ is the creep as a function of time;

$\Delta L_{t=0.1}$ is the displacement 0.1 seconds after the voltage change is complete;

γ is the creep factor, which is dependent on the properties of the actuator.

However, within feedback controlled systems, hysteresis and creep are not relevant as they are actively compensated.

C2.3 Low and high voltage actuators

The piezoactuators can be divided into two groups: low voltage and high voltage. The low voltage stacks are using a material that is highly dielectric ceramic with the Currie temperature of about 150 ^{o}C. The manufacture technology of these stacks is monolithic thin-layered elements/co-fired sintertechnology. The operating voltage range is (-) 30V

through (+) 150V (with possibility to go up to +200V), the operating temperature range is (–) 50 °C through (+) 100 °C.

The operating voltage ranges for a high voltage piezostack is: (-) 100V thru (+) 500V, and (-) 200V thru (+) 1000V. The materials from which they are made of, shows one of the highest strain rates together with a relatively low hysteresis. The efficiency of these actuators is much better and selfheating is reduced because of the better ratio stroke/capacitance. The Currie temperature is approx. 220 °C, optimum stack operation is up to 120 °C, and operating temperature range is (–)60 °C through (+)135 °C.

C2.4 Comparison between low and high voltage actuators

a) Stiffness, resonance frequency

Due to internal structure of the piezo stacks, low voltage actuators show a higher elastic modulus than high voltage ones. Therefore, the stiffness of high voltage actuators is usually lower than that of low voltage types of equal size. Because of that, also the resonance frequency is higher in the low voltage stacks.

b) *Electrical capacitance*

The significant difference in the electrical capacitances of low voltage and high voltage actuators is only a geometrical effect due to different thickness and quantity of the ceramic layers used to achieve a distinct actuator volume. Though, the capacity of low voltage actuators increased by a factor of 45 comparing with the high voltage actuators of same size. Therefore, the necessary current to get a distinct dynamic response is estimated to be 7 times higher for the 150 V stack.

c) *Maximum load*

Because the high voltage actuators can be manufactured with higher cross sections, they can handle much higher loads than low voltage types

d) Temperature range

High voltage actuators can achieve higher operating temperature due to the ceramic material they are made of.

e) *Lifetime*

High voltage actuators are superior to low voltage ones. One reasons for that is greater layer thickness of the high voltage elements.

C2.5 Requirements for the amplifier (piezoactuator driver):

In most cases, the original signal cannot be applied directly to the piezoactuator because voltage and power do not match the actuator's requirements. Therefore a piezoactuator driver has to be used to convert the signal to result in sufficient travel/force and dynamics of the actuator.

In a system that involves piezoactuators great attention needs to be given to the driving electronics. The most important actuator parameters that needs to be taken into account when designing the supply electronics for dynamic operations are:

- Electrical capacitance;
- Voltage supply;
- Operating frequency;
- Power dissipation.

The main applications of piezoactuators include:

a) Ultraprecise positioning;
b) Generation/handling of high forces/pressures either static (e.g. high mass load, elastic forces), or dynamic (acceleration forces);
c) Transducers, acting simultaneously as sensors and actuators.

Fast response is one of the desirable features of piezoactuators. A rapid drive voltage change results in a rapid position change. This property is necessary in applications such as switching of valves/shutters, generation of shockwaves, vibration cancellation systems, etc. Same property is used in this case to accurately control velocity.

APPENDIX D

Clutch parameters and DC Motors performance specifications

D1. Electromechanical friction clutch parameters

Table D1. Clutch parameters

Notation	Value	Description
J	0.0017 kgm^2	total moment of inertia of clutch + a mass of 0.2 kg
Rp	0.024 m	radius of pulley
r_o	0.05 m	radius of the brake disc
r_i	0.045 m	inner radius of the brake pad
r_c	0.034 m	distance between centre of the motor shaft and contact point on the disc
L	0.03 m	width of the friction pad
h	0.0055 m	height of the rectangular part of the brake pad
A_{lever}	0.032 m^2	area of a rectangular shape of the mechanical lever
A	0.040 m^2	area of the contact between the brake pad and brake disc
K_{COF}	0.14	constant of the coefficient of friction
C_d	0.001	viscous damping coefficient in the clutch system
γ	0.6 rad	angle of the segment of the proposed annular brake pad
μ_s	0.2	static coefficient of friction
μ_d	0.15	dynamic coefficient of friction
$\dot{\theta}_s$	0.001	Stribeck velocity
δ	1	Stribeck coefficient

Table D2. N9M4T Motor parameters

Notation	Value	Description
T_{DC}	4.89 Nm	motor output torque
Kt	0.0678 Nm/A	motor torque constant
La	0.03 μF	armature inductance
Ra	0.66 Ω	armature resistance
J_{DC}	$0.59x10^{-4}$ kgm^2.	inertia of the motor shaft
b	$0.8x10^{-6}$ Nsm/rad	viscous friction coefficient
K_e	$7.1x10^{-4}$ Vs/rad	back emf constant

D2. DC motor performance specification

The motor used in the experimental test-bed is N9M4T (from Kollmorgen, Motion Technologies Group). Its performance specifications are shown in Figure D1.

Performance Specifications	Symbol	Units	N9M4	N9M4T
Peak Torque	TP	oz-in	760	692
		N-cm	537	489
Rated Speed	N	RPM	3000	3000
Rated Continuous Torque @ 25°C	T	oz-in	69	57
		N-cm	49	40
Rated Continuous Torque @ 40°C	T	oz-in	63	52
		N-cm	44	37
Rated Power Output	P	Watts	153	126
Maximum Recommended Speed	NM	RPM	6000	6000
Continuous Stall torque	TS	oz-in	69	62
		N-cm	49	44
Cogging Torque	TC	oz-in	0	0
Electrical Specifications				
Rated Terminal Voltage	E	Volts	30.0	28.0
Rated Continuous Current	I	amps	7.80	7.10
Peak Current	IP	amps	79	77
Continuous Stall Current	IS	amps	7.5	7.3
Winding Specifications				
Terminal Resistance ±10%	RT	ohms	0.850	0.850
Armature Resistance ± 10%	RA	ohms	0.660	0.660
Back EMF Constant ± 10%	KE	V/kRPM	7.60	7.10
Torque Constant ± 10%	KT	oz-in/amp	10.30	9.60
		N-cm/amp	7.27	6.78
Viscous Damping Constant	KD	oz-in/kRPM	1.1	1.1
		N-cm/kRPM	0.8	0.8
Armature Inductance	L	uH	<0.03	<0.03
Temperature Coefficient of KE	C	%/°C Rise	−0.10	−0.10
Number of Commutator Bars	Z		117	117
Mechanical Specifications				
Moment of Inertia	JM	oz-in-sec²	0.0056	0.0083
		kg-cm²	0.40	0.59
Static Friction Torque	TF	oz-in	4.0	4.5
		N-cm	2.8	3.2
Weight	W	lbs	3.1	3.2
		kg	1.4	1.5
Diameter	D	in	4.37	4.37
		mm	111.0	111.0
Length	LG	in	0.94	0.95
		mm	23.9	24.1
Figures of Merit				
Peak Acceleration	AP	krad/sec²	135.7	83.3
Mechanical Time Constant	TM	ms	4.90	8.30
Electrical Time Constant	TE	ms	<0.05	<0.05
Continuous Power Rate	PC	kW/sec	6.0	2.8
Thermal Specifications				
Thermal Resistance at Rated Speed	RAAR	°C/Watt	1.50	1.70
Thermal Resistance at Stall	RAAS	°C/Watt	2.00	2.10
Tachometer Specifications				
Output Voltage	V	Volts/kRPM	–	3.50
Maximum Ripple Peak to Peak	VRH	%	–	3.0
Linearity of Output Voltage	LIN	%	–	0.06
Minimum Load Resistance	RL	ohms	–	370

Notes:

Figure D1. N9M4T Motor performance specifications

APPENDIX E

Derivation of the proposed actuators' mathematical model

E1. Piezoactuator's mathematical model

The piezoactuator equivalent diagram is shown in Figure E1.

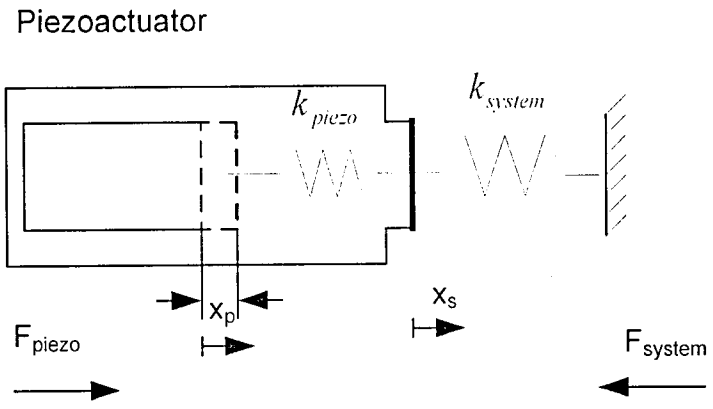

Figure E1. Piezoactuator equivalent diagram

Where F_{piezo} and F_{system} represent the forces produced by the piezoactuator and systems reaction, k_{piezo} and k_{system} denotes the stiffness of both the piezoactuator and the system, and x_p and x_s are the displacements that take place in the piezoactuator and between the piezoactuator and the external environment.

The action and reaction forces, F_{piezo} and F_{system} respectively, are given by

$$F_{system} = k_{system} \cdot x_s , \qquad \textbf{(E0-1)}$$

$$F_{piezo} = k_{piezo} \cdot (x_p - x_s) .$$

Thus, making $F_{system} = F_{piezo}$, the displacement of the system, x_s, can be written

$$x_s = \frac{k_{piezo}}{k_{system} + k_{piezo}} \cdot x_p \qquad \textbf{(E0-2)}$$

resulting the force generated by the piezoactuator with respect to the system stiffness

$$F_{piezo} = \frac{k_{system} \cdot k_{piezo}}{k_{system} + k_{piezo}} \cdot x_p \qquad \textbf{(E0-3)}$$

Consequently, if the stiffness of the external system is much greater than the stiffness of the piezoactuator, $k_{system} >> k_{piezo}$, the piezoactuator force can be approximated as

$$F_{piezo} = \frac{k_{system} \cdot k_{piezo}}{k_{system}} \cdot x_p = k_{piezo} x_p \qquad \textbf{(E0-4)}$$

and if the stiffness of the external system is much less than the stiffness of the piezoactuator, $k_{system} << k_{piezo}$, the piezoactuator force can be approximated as

$$F_{piezo} = \frac{k_{system} \cdot k_{piezo}}{k_{piezo}} \cdot x_p = k_{system} x_p \qquad \textbf{(E0-5)}$$

The displacement of the piezoactuator with respect to voltage is given as

$$x_p = K_v \, V_{piezo} \qquad \textbf{(E0-6)}$$

where V_{piezo} representes the input voltage into the actuator, and K_v is obtained at maximum displacement, $x_{p,\,max}$, and maximum voltage $V_{piezo,\,max}$.

$$K_v = x_{p,\,max} / V_{piezo,\,max} \qquad \textbf{(E0-7)}$$

Therefore, the force produced by the piezoactuator obtained in equation (E5) can be rewritten as

$$F_{piezo} = \frac{k_{system} \cdot k_{piezo}}{k_{system} + k_{piezo}} \cdot K_v \cdot V_{piezo} \qquad \textbf{(E0-8)}$$

Equation (E8) represents the mathematical model of a piezoactuator dependent on the stiffness of both the actuator and the environment on which the actuation force is exerted.

E2. DC motor's mathematical model

The diagram of a dc motor and a load is shown in Figure E2.

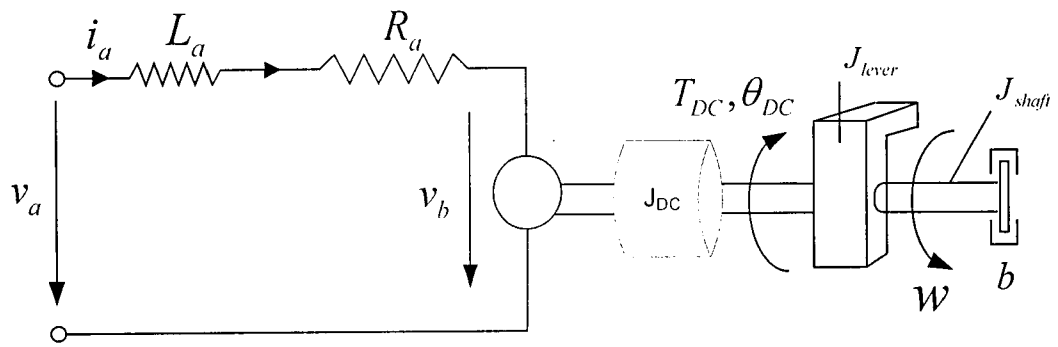

Figure E2. Actuation assembly with dc motor-equivalent diagram

The resulting moment of inertia considered is $J_T = J_{DC} + J_{shaft} + J_{lever}$. Therefore, the dynamics of the actuation assembly with a dc motor is given by:

$$J_T \ddot{\theta}_{DC} + b\dot{\theta}_{DC} + w = T_{DC} \qquad \textbf{(E0-9)}$$

$$v_b + L_a \frac{di_a}{dt} + R_a i_a = v_a \qquad \textbf{(E0-10)}$$

where, $T_{DC}(t) = K_t \cdot i_a(t)$, and $v_b(t) = K_e \cdot \dot{\theta}$. The transfer function of the motor's torque and voltage in Laplace domain is obtained in equation (E11), and the transfer function of the motor's torque and speed in Laplace domain is obtained in equation (E12):

$$\frac{T_{DC}(s)}{V_a(s) - K_e s\theta_{DC}(s)} = \frac{K_t}{L_a s + R_a} \qquad \textbf{(E0-11)}$$

$$\frac{\theta_{DC}(s)}{T_{DC}(s) - W(s)} = \frac{1}{J_T s^2 + bs} \qquad \textbf{(E0-12)}$$

The block diagram of the DC motor is illustrated in Figure E3.

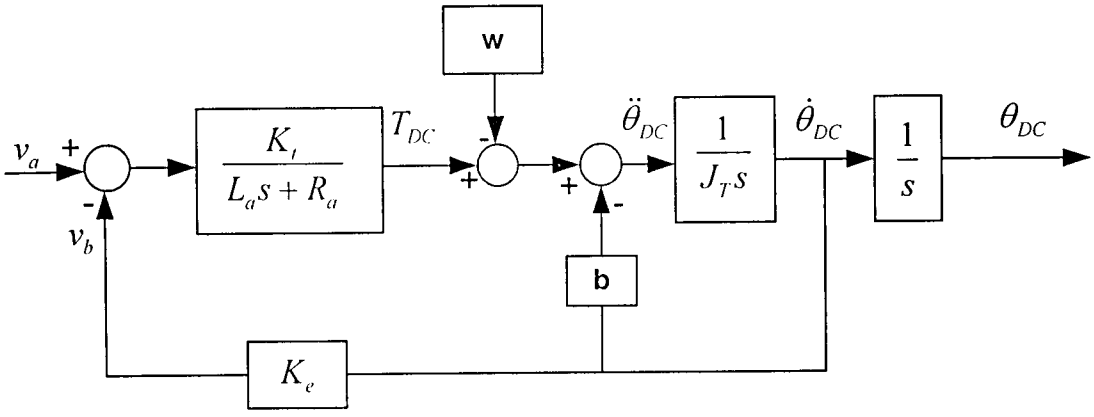

Figure E3. DC motor's block diagram

APPENDIX F

Engineering Drawings

F1. Experimental Set-up

Item #	Title	Qty for 1 item
1	Clutch's shaft	1
2	Brake disc	1
3	Pulley	1
4	Lever	1
5	Cantilever	2
6	T-shape block	1
7	Housing	1
8	Top plate DO	1
9	Side plates	2
10	Base plate	1
11	Side seals	2
12	Single row ball bearing for clutch's shaft, off the shelf (7204B)	2
13	Bush	2
14	Rectangular spacer	1
15	Adjustment shaft	1
16	Washer	1
17	Elastic coupling 6x6, off the shelf	1
18	Encoder spacer	1
19	Encoder attachment	1
20	Encoder, off the shelf	1
21	Motor's rectangular spacer	1

22	Motor's attachment	1
23	DC motor, off the shelf	1
24	Connexion shaft	1
25	Rigid coupling	1
26	Elastic coupling 8x8, off the shelf	1
27	Connexion shaft support	2
28	Single row ball bearing for connexion's shaft, off the shelf	2
29	Support plate	1
30	Support legs	2

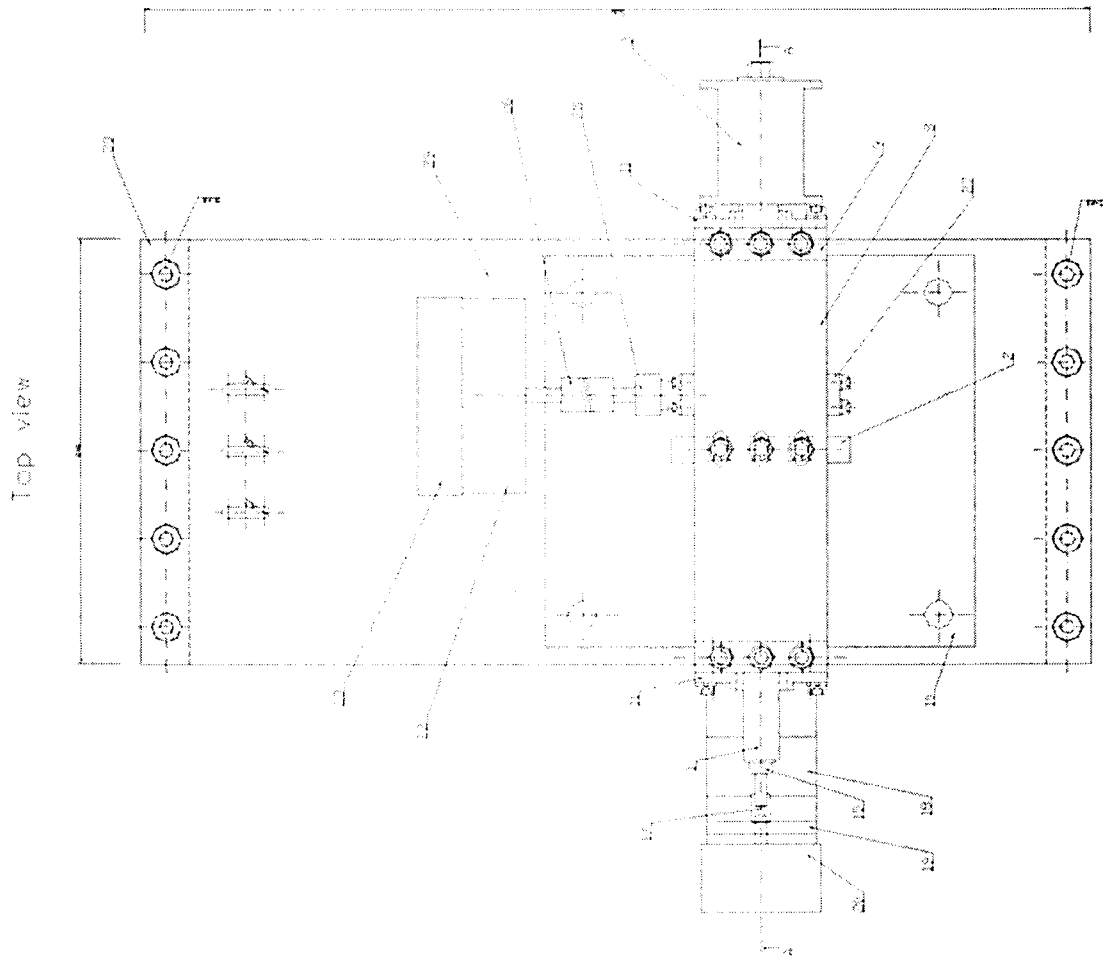
Top view

A—A
3×(M8×40)
4×(M5×25)
2×(M8×50)
3×(M10×50)
1
2
3
4
5
6
7
8
9
10
11
12
13
14
15
16
17
18
19
20
21
29
30

Right view

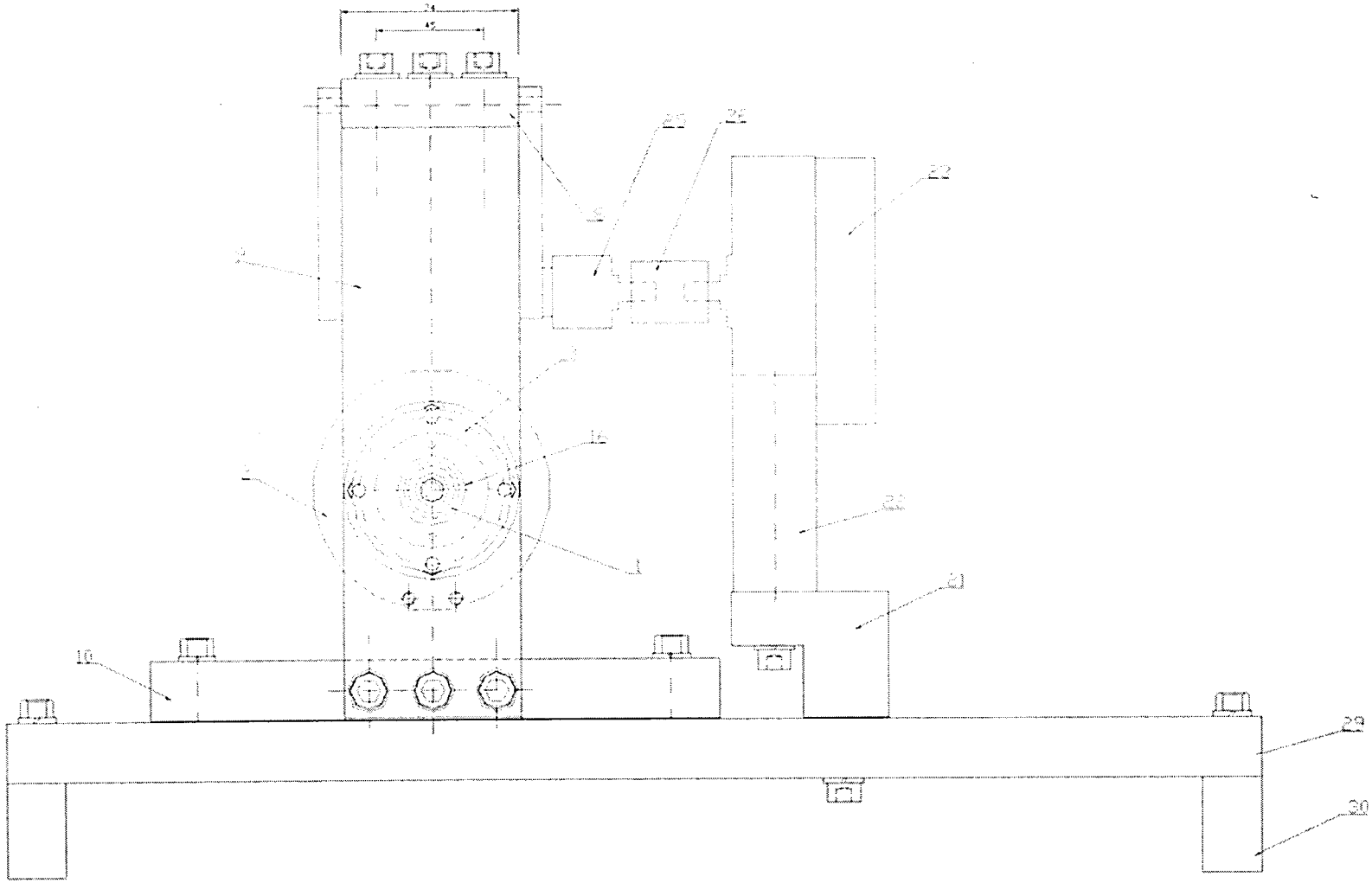

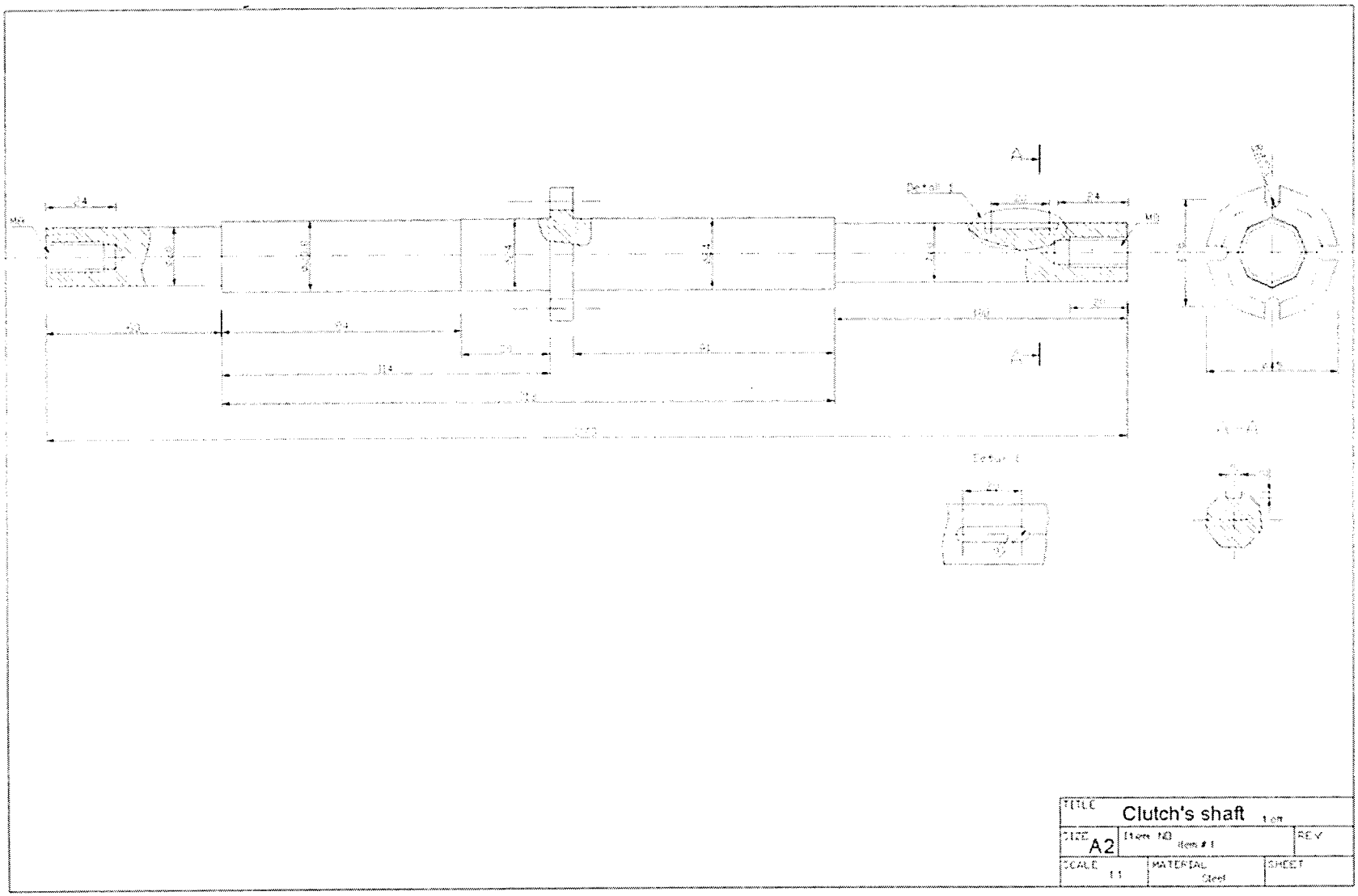
A
A
Detail E
Detail F
A-A
TITLE
Clutch's shaft
SIZE
A2
DWG NO
item # 1
REV
SCALE
1:1
MATERIAL
Steel
SHEET

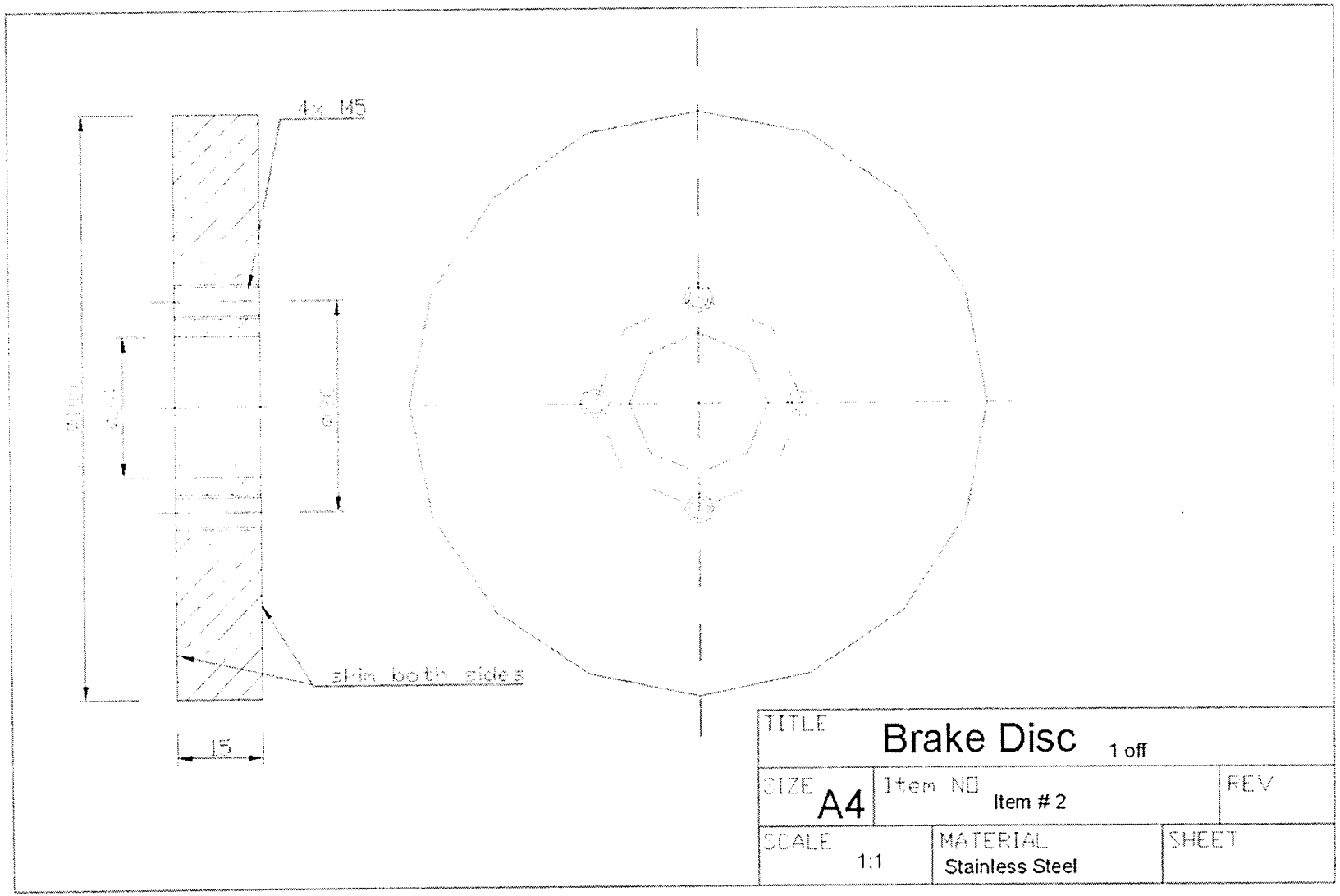

TITLE	Brake Disc 1 off		
SIZE A4	Item NO Item # 2		REV
SCALE 1:1	MATERIAL Stainless Steel		SHEET

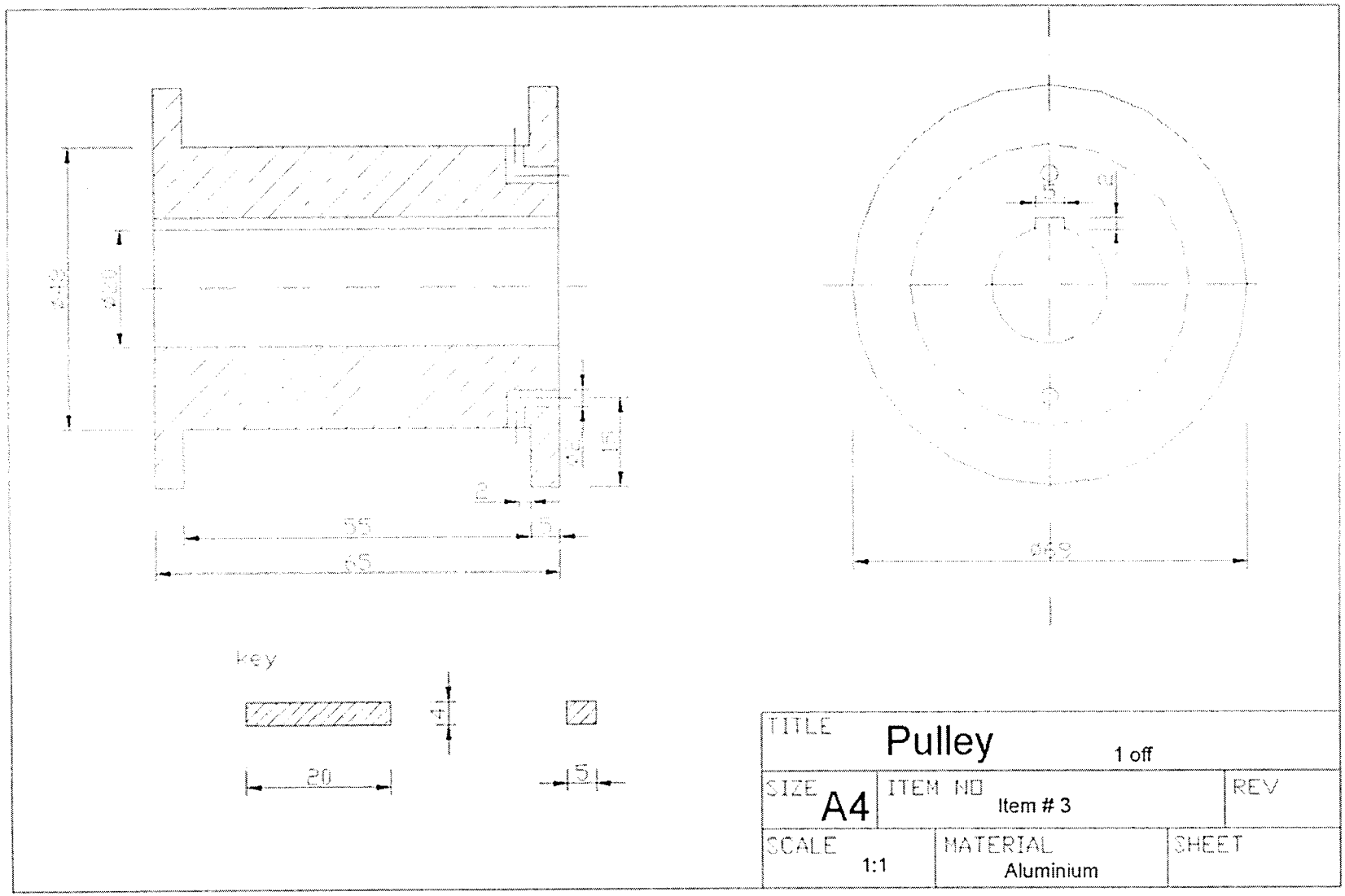
Key
20
5
55
65
2
5
Pulley
1 off
A4
Item # 3
1:1
Aluminium

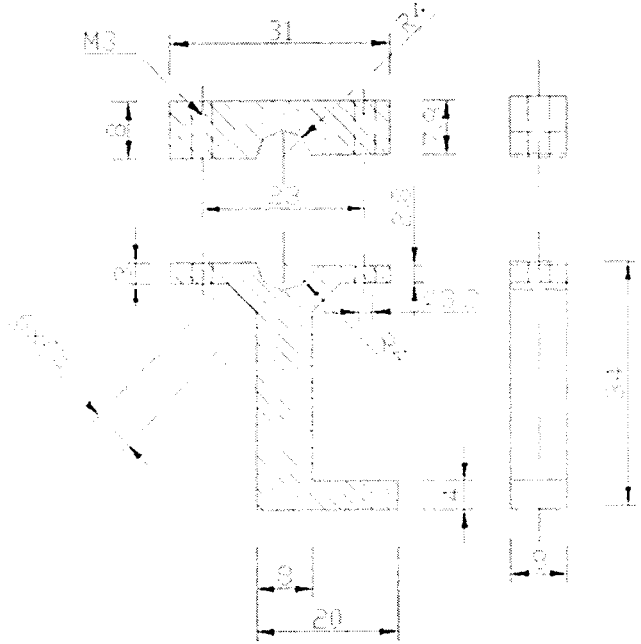

TITLE	Lever	1 off	
SIZE A4	ITEM NO Item # 4		REV
SCALE 1:1	MATERIAL Steel		SHEET

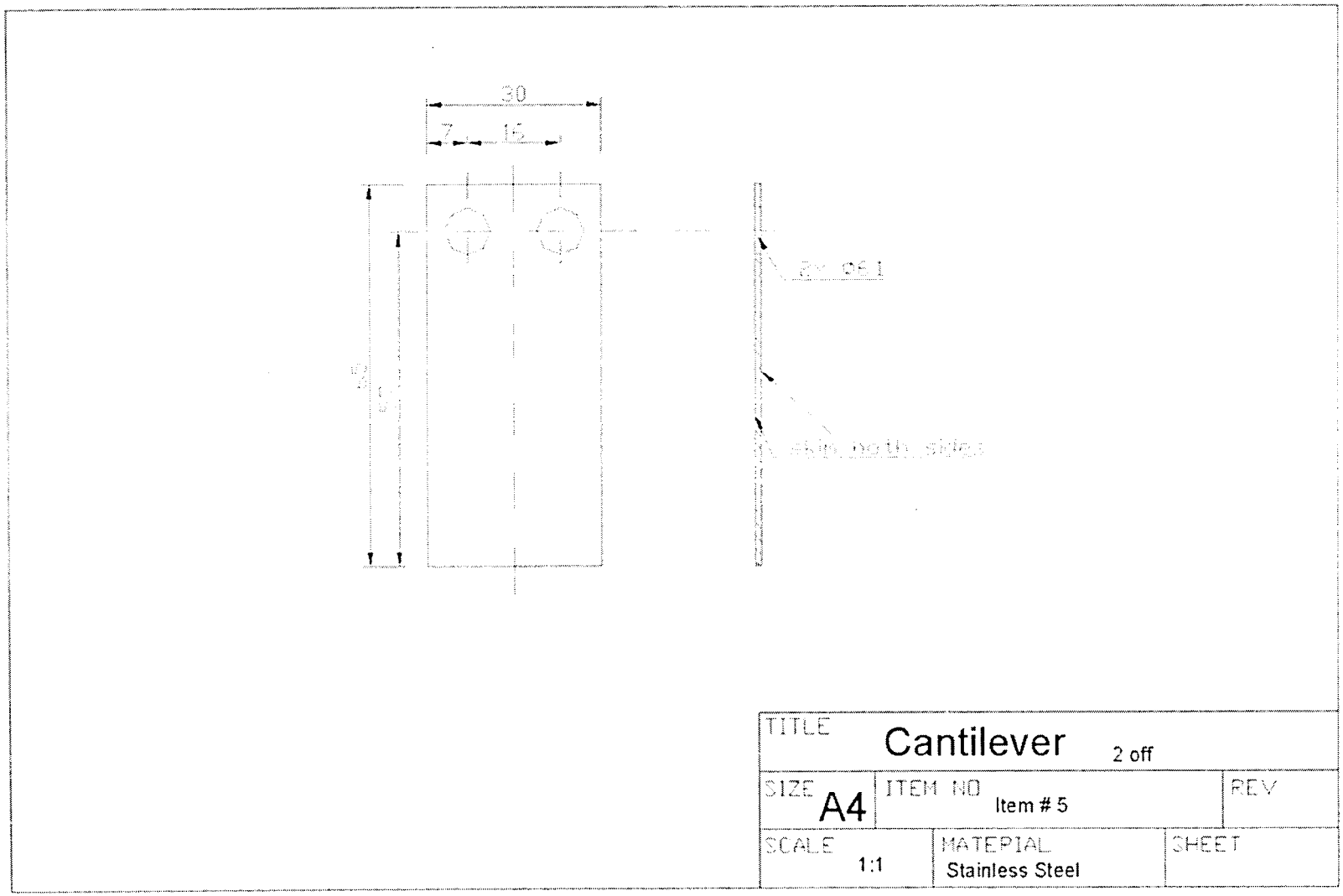

TITLE	Cantilever 2 off		
SIZE A4	ITEM NO Item # 5		REV
SCALE 1:1	MATEPIAL Stainless Steel	SHEET	

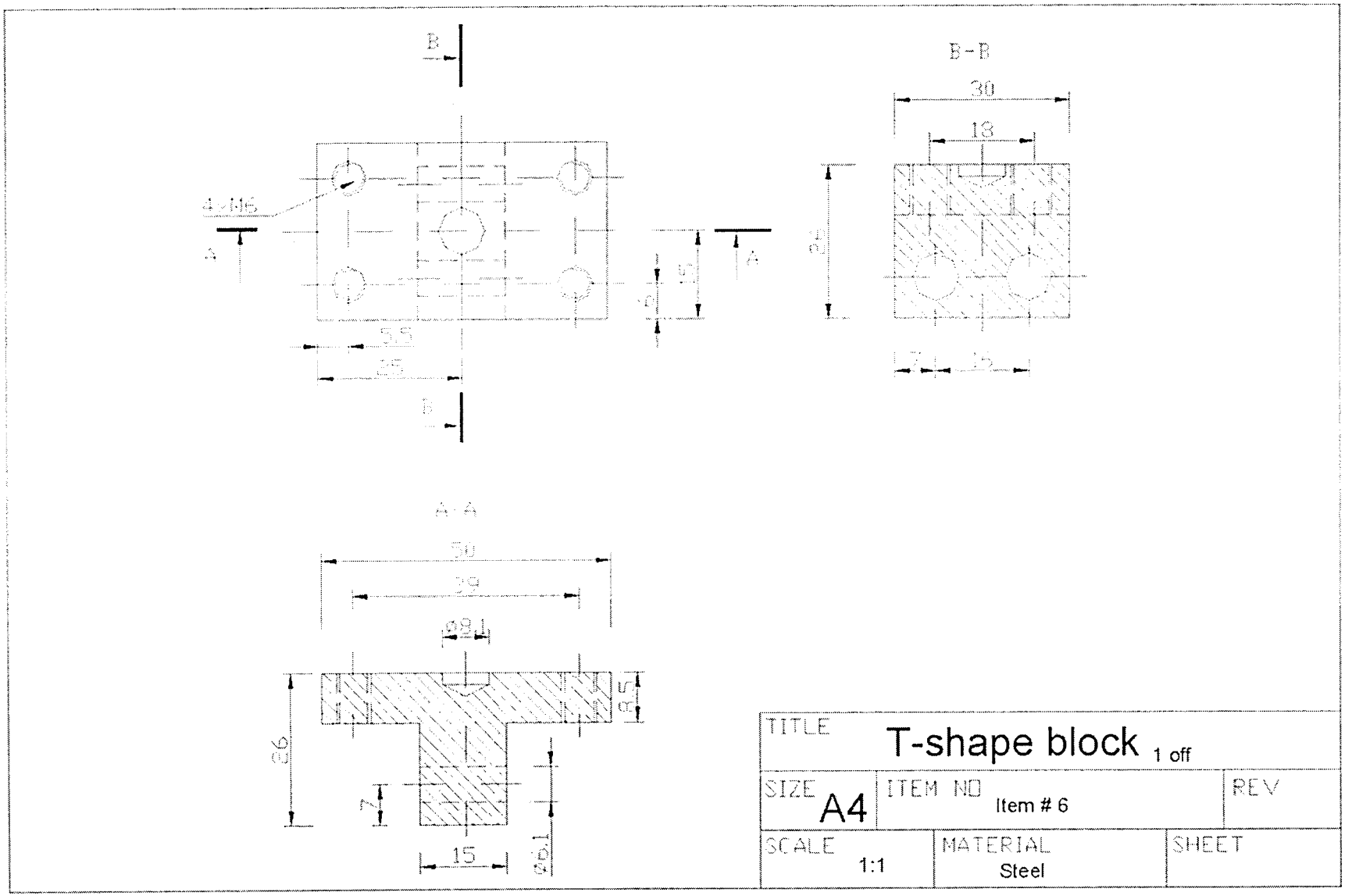
B
B-B
30
18
4×M6
A
A
35
25
B
A-A
50
36
ø8.1
ø6
7
15
ø9.1
TITLE
T-shape block 1 off
SIZE
A4
ITEM NO
Item # 6
REV
SCALE
1:1
MATERIAL
Steel
SHEET

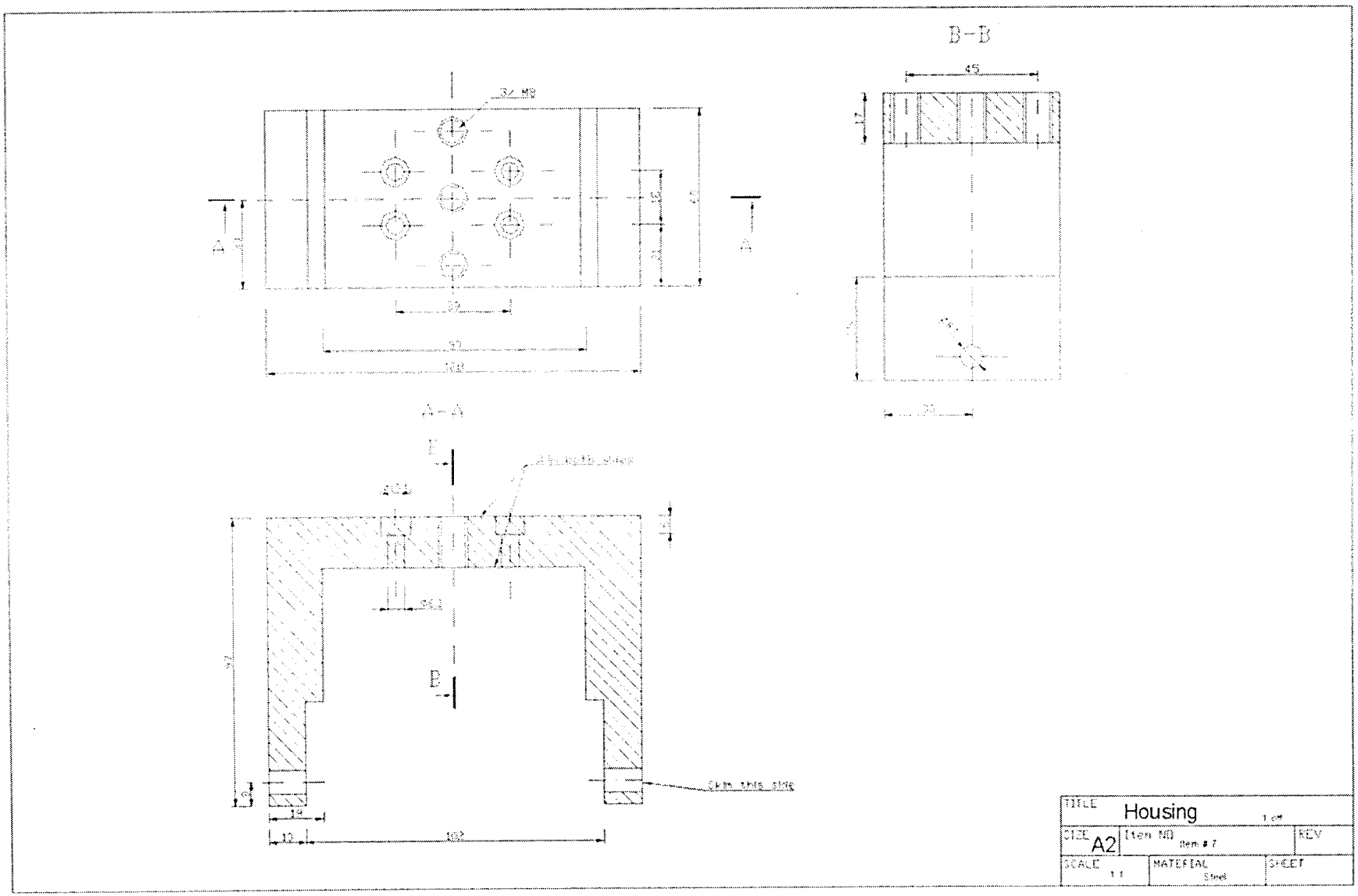
B-B
A-A
45
Housing
A2
Item NO
Item # 7
KEV
SCALE
1:1
MATERIAL
Steel
SHEET

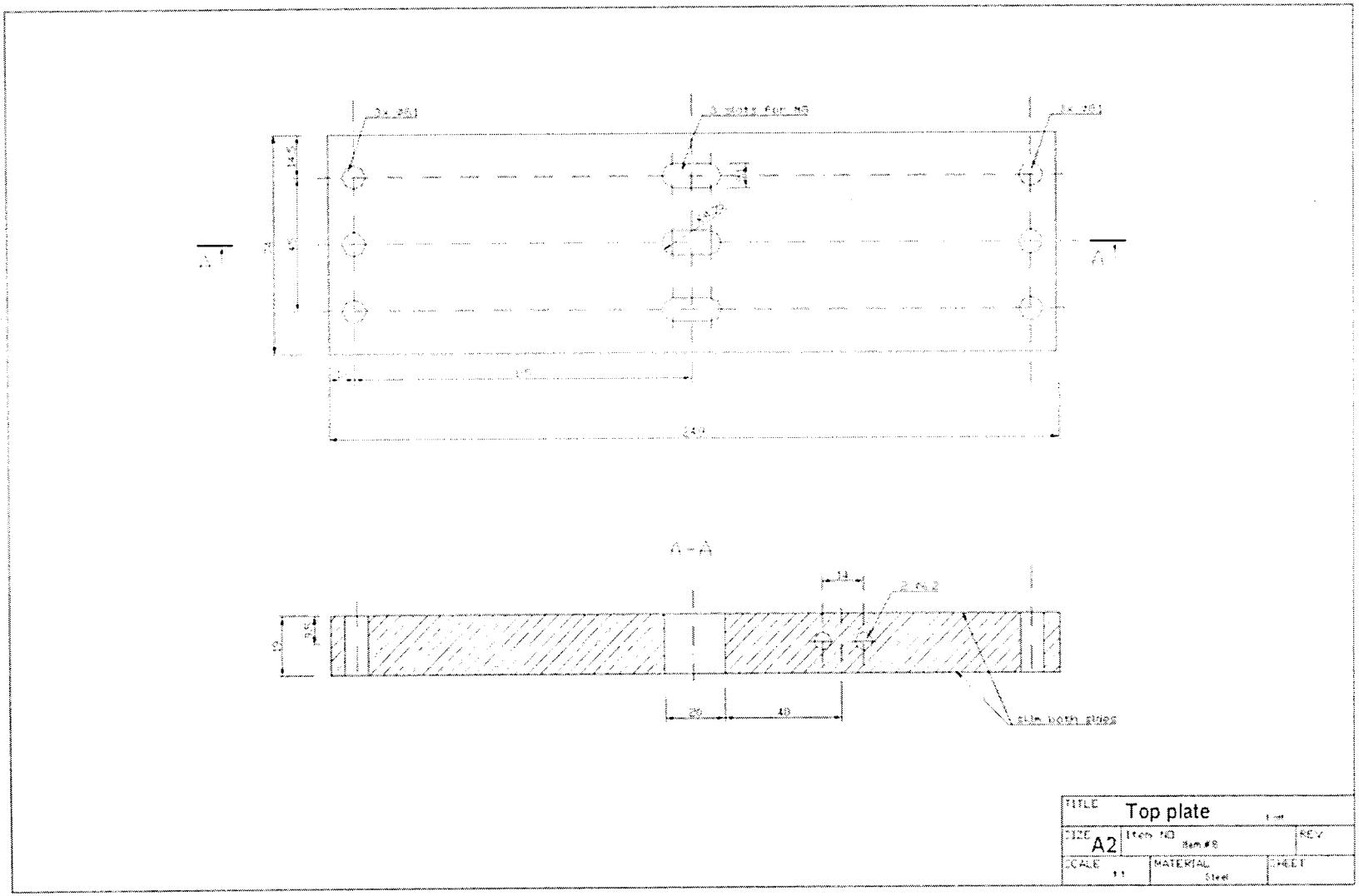
A - A
Slot both sides
TITLE
Top plate
SIZE
A2
SCALE
1:1
MATERIAL
Steel
SHEET
REV

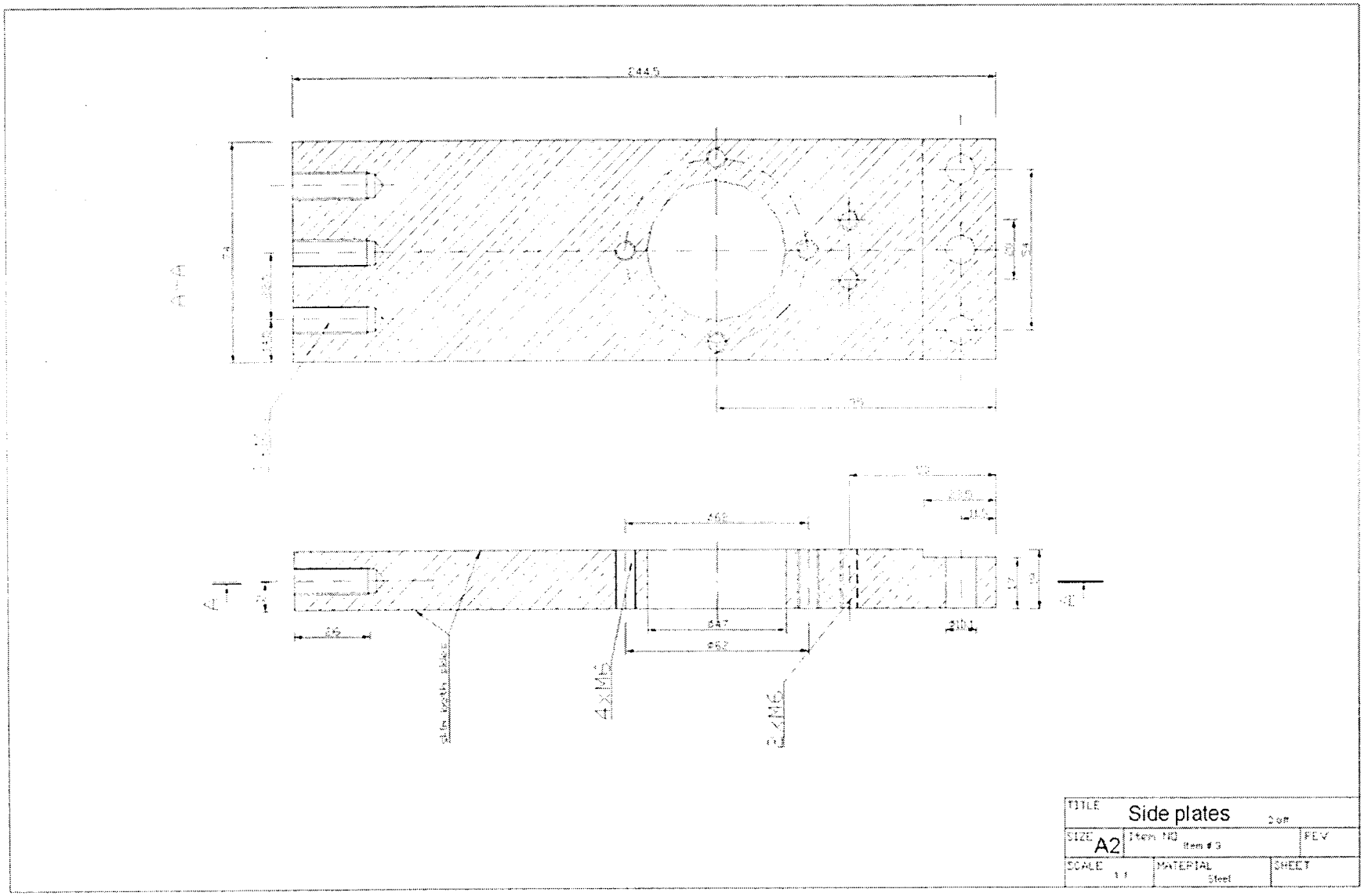
244.5
4x M6
2.4M6
TITLE
Side plates
SIZE
A2
SCALE
MATERIAL
Steel
SHEET
REV

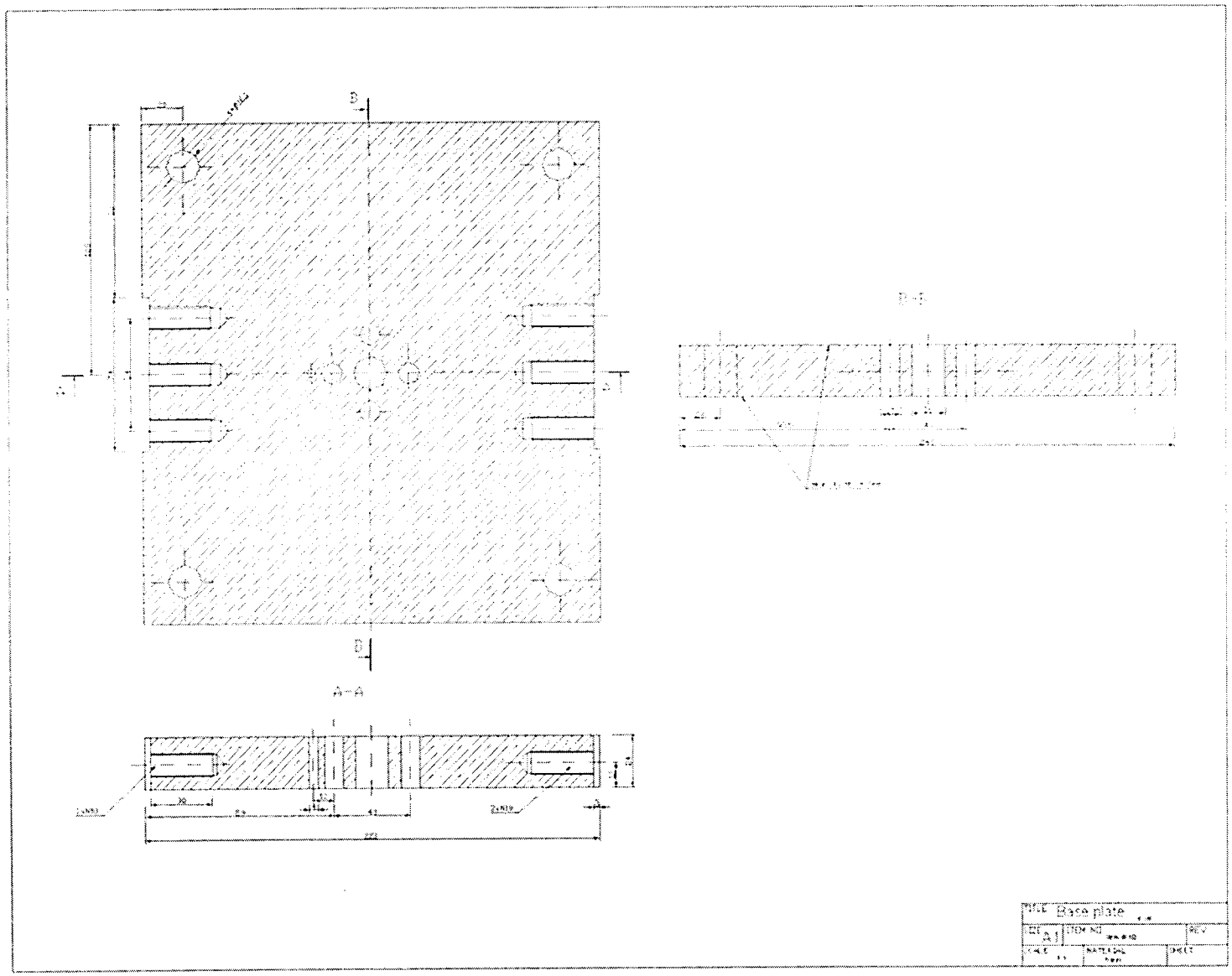
B
B
A-A
B-B
TITLE Base plate
SIZE A1
DRAWING NO.
REV.
SCALE 1:1
MATERIAL
SHEET

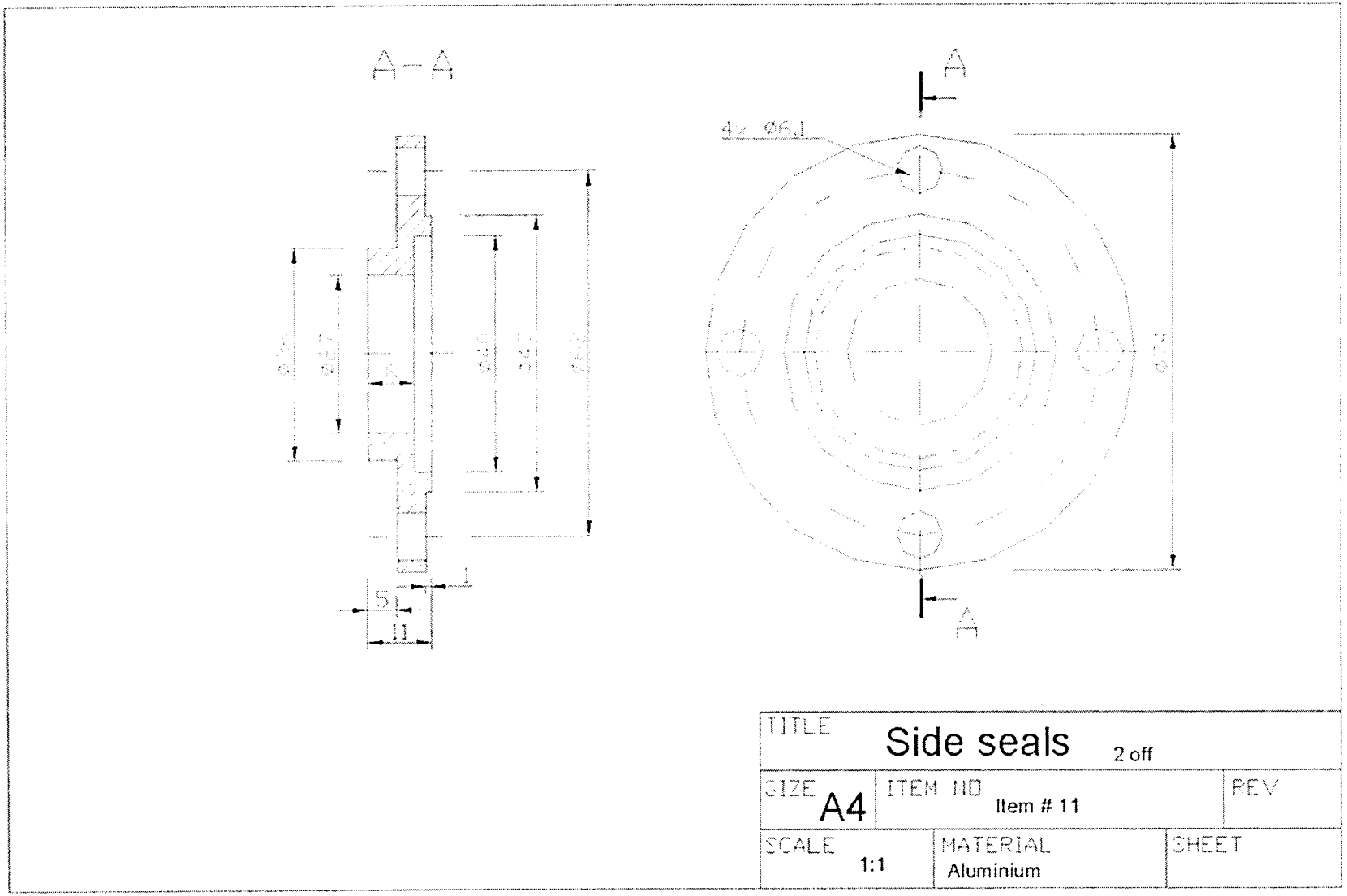

TITLE	Side seals 2 off		
SIZE A4	ITEM NO Item # 11		REV
SCALE 1:1	MATERIAL Aluminium	SHEET	

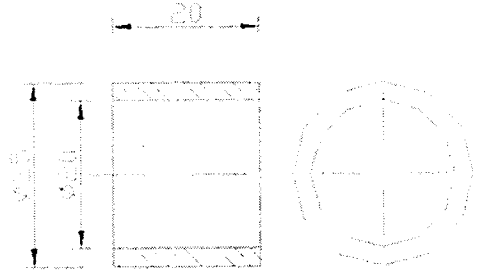

TITLE	Clutch's shaft bush 2 off	
SIZE A4	ITEM NO Item # 13	REV
SCALE 1:1	MATERIAL Steel	SHEET

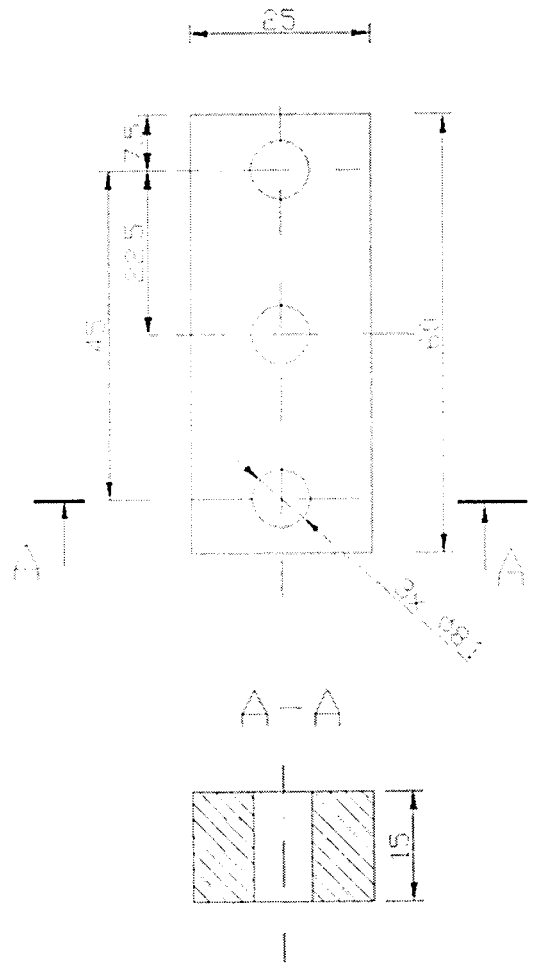

TITLE	Rectangular spacer 1 off		
SIZE A4	ITEM NO Item # 14		REV
SCALE 1:1	MATERIAL Steel	SHEET	

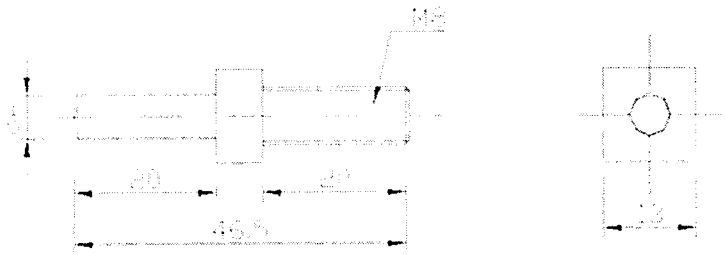

TITLE: Adjustment shaft — 1 off		
SIZE: A4	ITEM NO: Item #15	REV:
SCALE: 1:1	MATERIAL: Steel	SHEET:

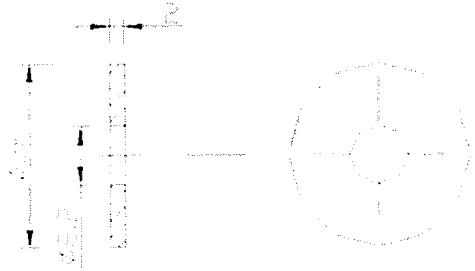

TITLE	Washer 1 off		
SIZE A4	ITEM NO Item # 16		REV
SCALE 1:1	MATERIAL Steel		SHEET

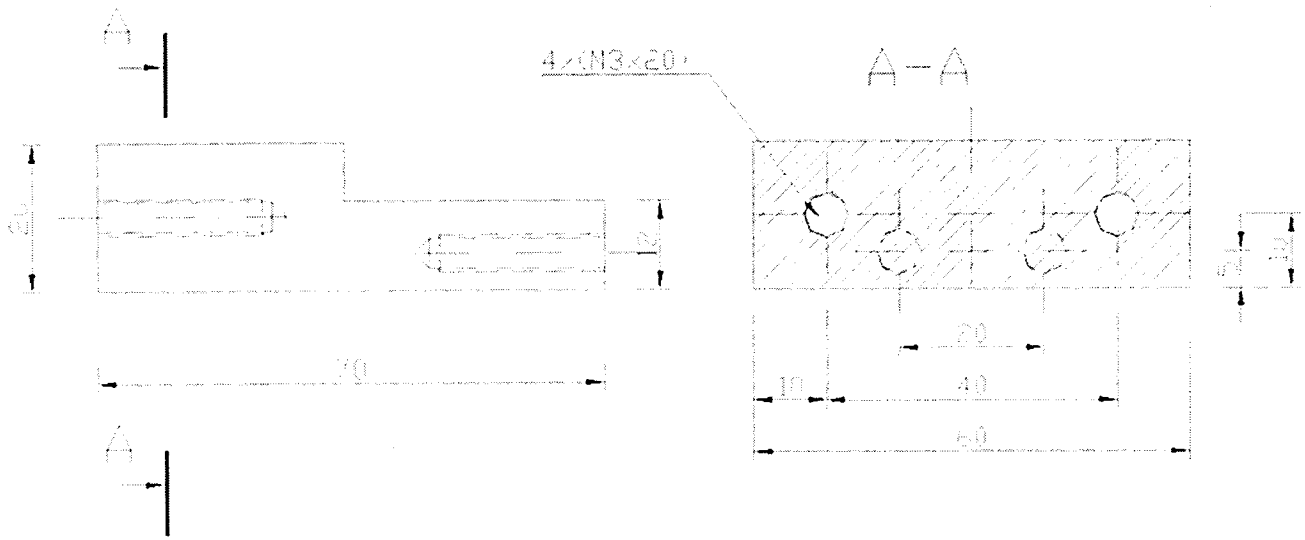

TITLE	Spacer 1 off		
SIZE A4	ITEM NO Item # 18		REV
SCALE 1:1	MATERIAL Aluminium	SHEET	

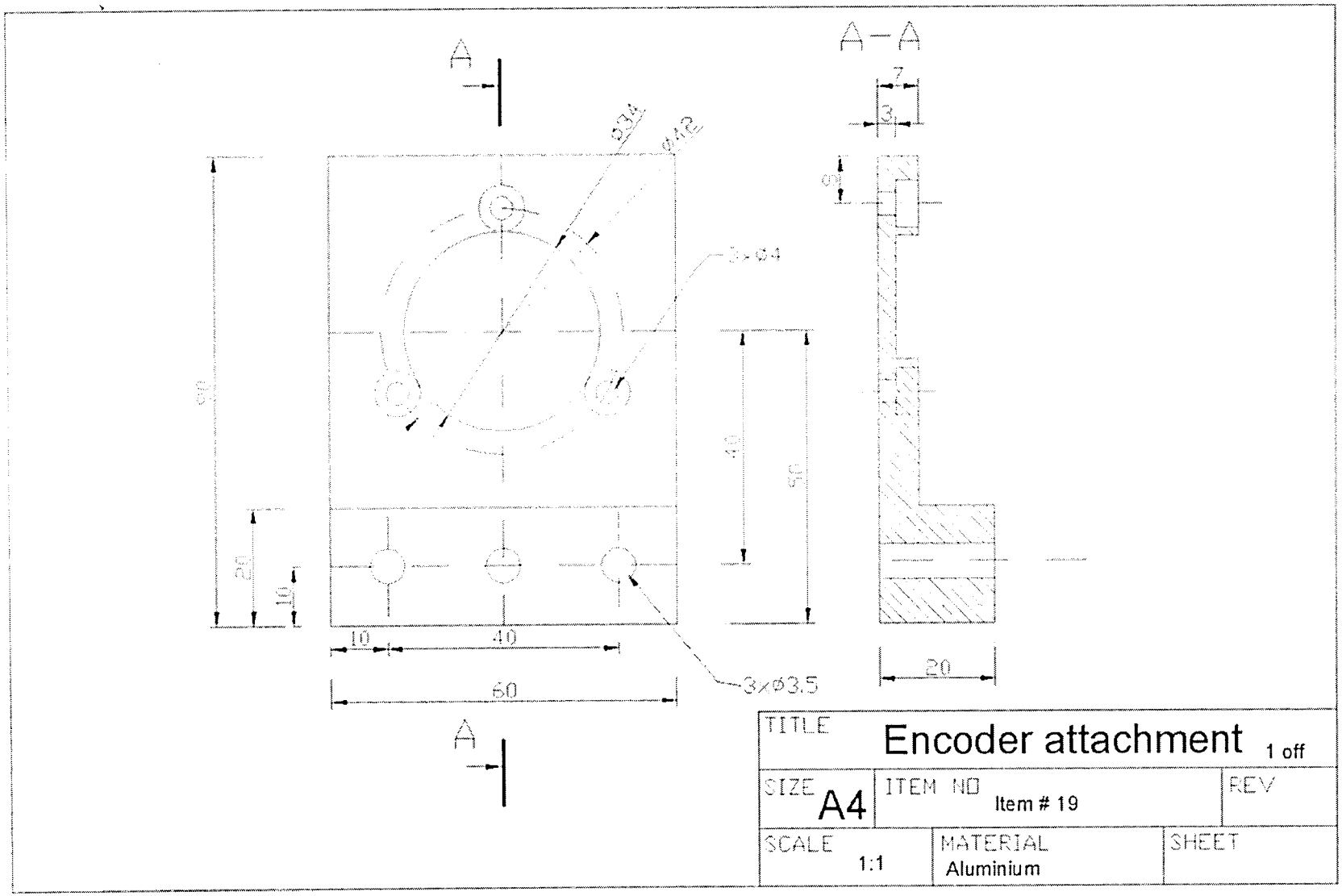

TITLE	Encoder attachment 1 off		
SIZE A4	ITEM NO Item # 19		REV
SCALE 1:1	MATERIAL Aluminium	SHEET	

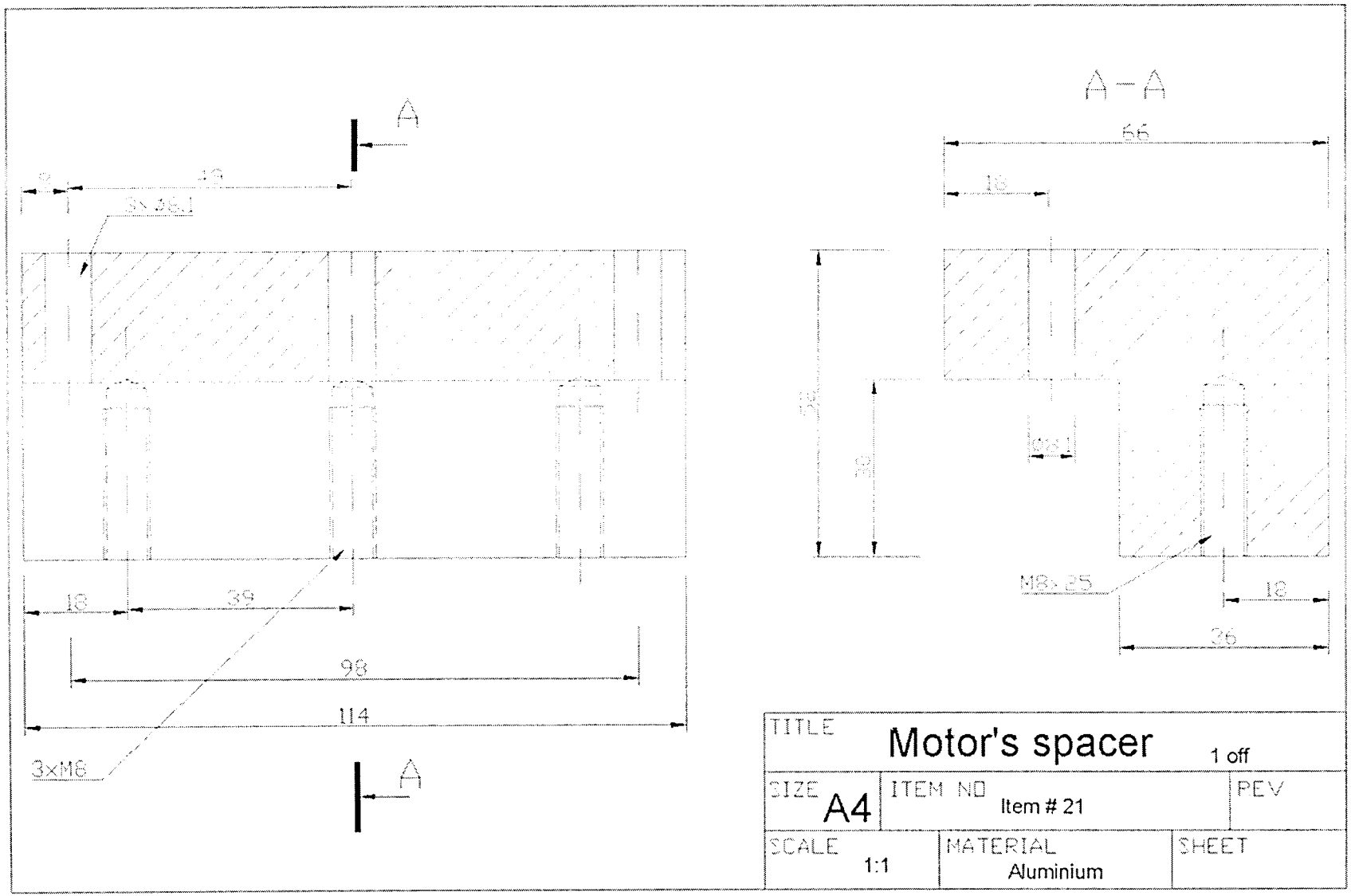

TITLE	Motor's spacer 1 off		
SIZE A4	ITEM NO Item # 21		REV
SCALE 1:1	MATERIAL Aluminium	SHEET	

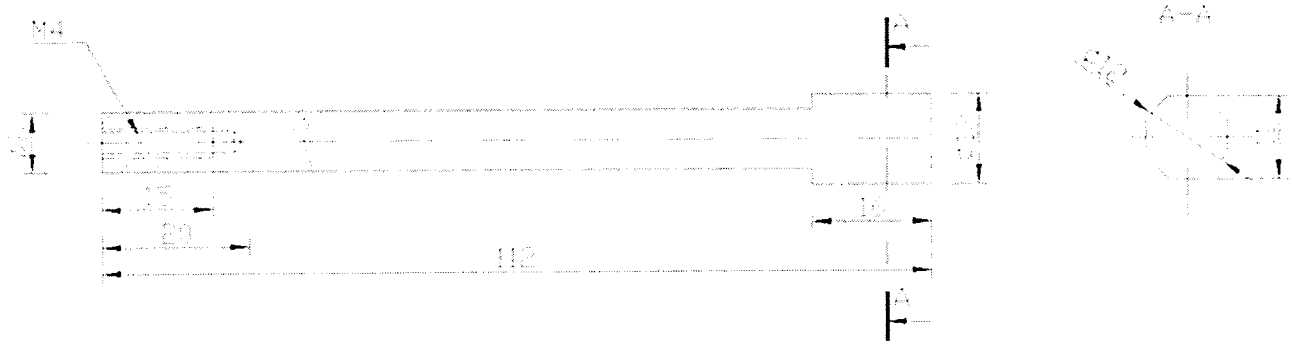

TITLE: Connexion shaft		1 off
SIZE: A4	ITEM NO: Item # 24	REV:
SCALE: 1:1	MATERIAL: Steel	SHEET:

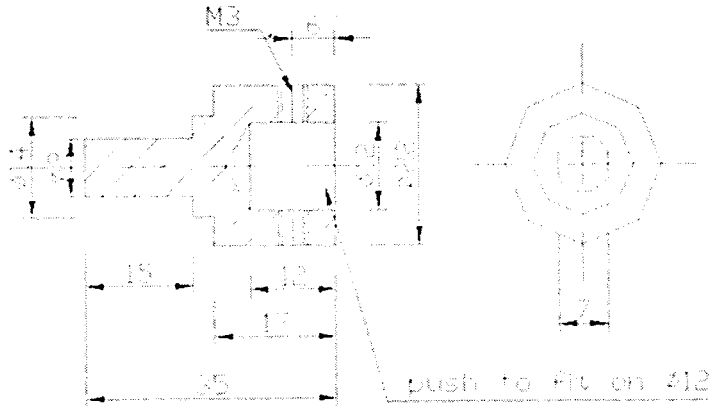

TITLE: Rigid coupling 1 off		
SIZE: A4	ITEM NO: Item # 25	REV:
SCALE: 1:1	MATERIAL: Steel	SHEET:

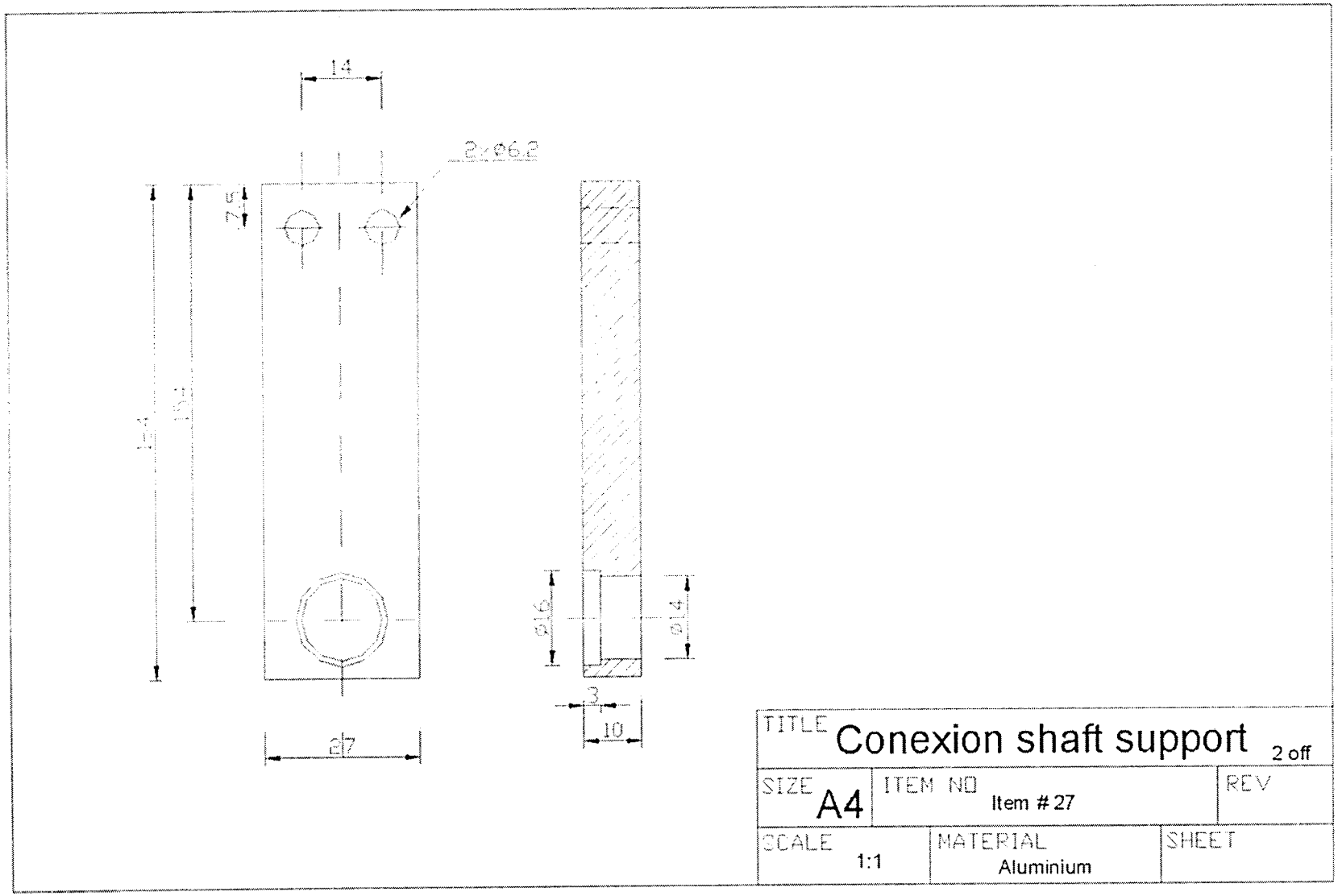

TITLE: Conexion shaft support 2 off			
SIZE: A4	ITEM NO: Item # 27		REV:
SCALE: 1:1	MATERIAL: Aluminium		SHEET:

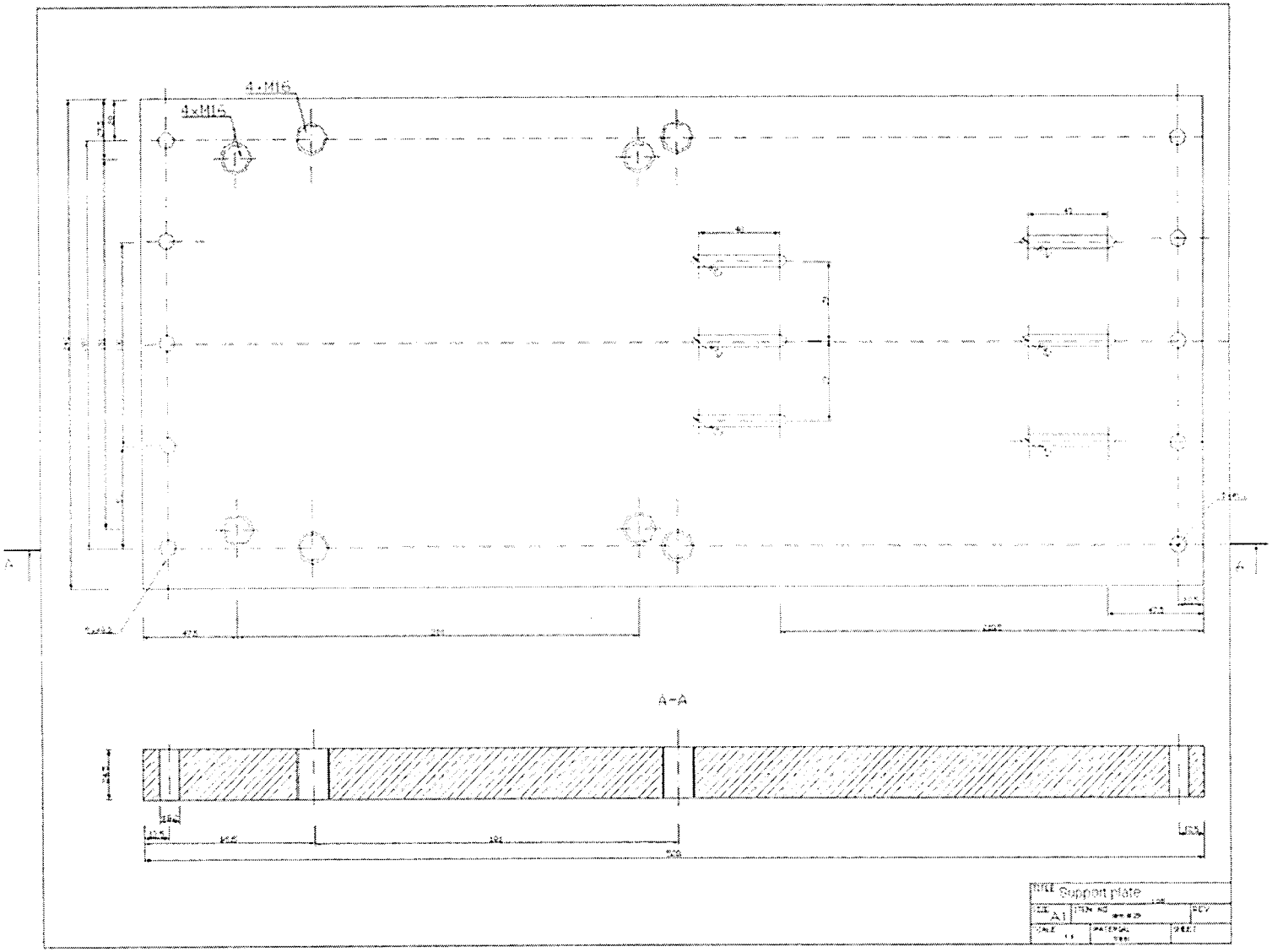
4×M16
4×M15
A
A
A–A
Support plate
A1

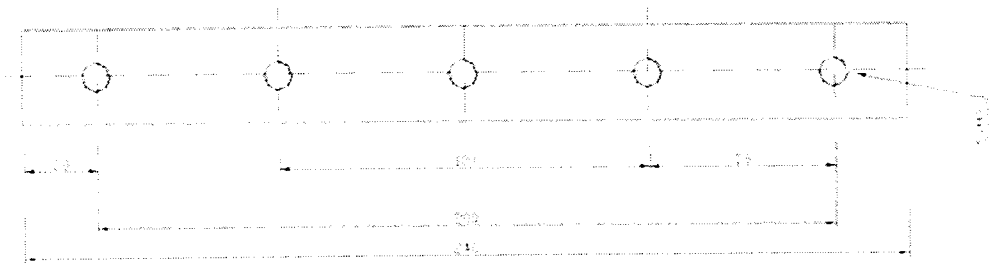

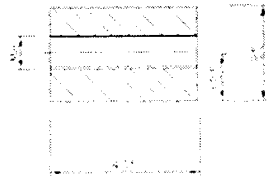

TITLE: Support legs 2 off		
SIZE: A2	Item NO: Item # 99	REV:
SCALE: 1:1	MATERIAL: Steel	SHEET:

F2. Clutch mechanism for an Actively Restrained Passive Revolute Joint with a Piezoactuator

Item #	Title	Qty for 1 item
1	Clutch's shaft	1
2	Brake disc	1
3	Pulley	1
4	Piezoelectric actuators	2
5	Cantilever	2
6	T-shape block	1
7	Housing	1
8	Top plate	1
9	Side plates	2
10	Base plate	1
11	Side seals	2
12	Single row ball bearing for clutch's shaft, off the shelf (7204B)	2
13	Bush	2
14	Rectangular spacer	1
15	Adjustment shaft	1
16	Washer	1
17	Elastic coupling 6x6. off the shelf	1
18	Encoder spacer	1
19	Encoder attachment	1
20	Encoder, off the shelf Henglster serial	1

Please note that all drawings are similar to the drawings presented for the experimental test-bed. The assembly drawings for the top, front and right views are shown in the following pages.

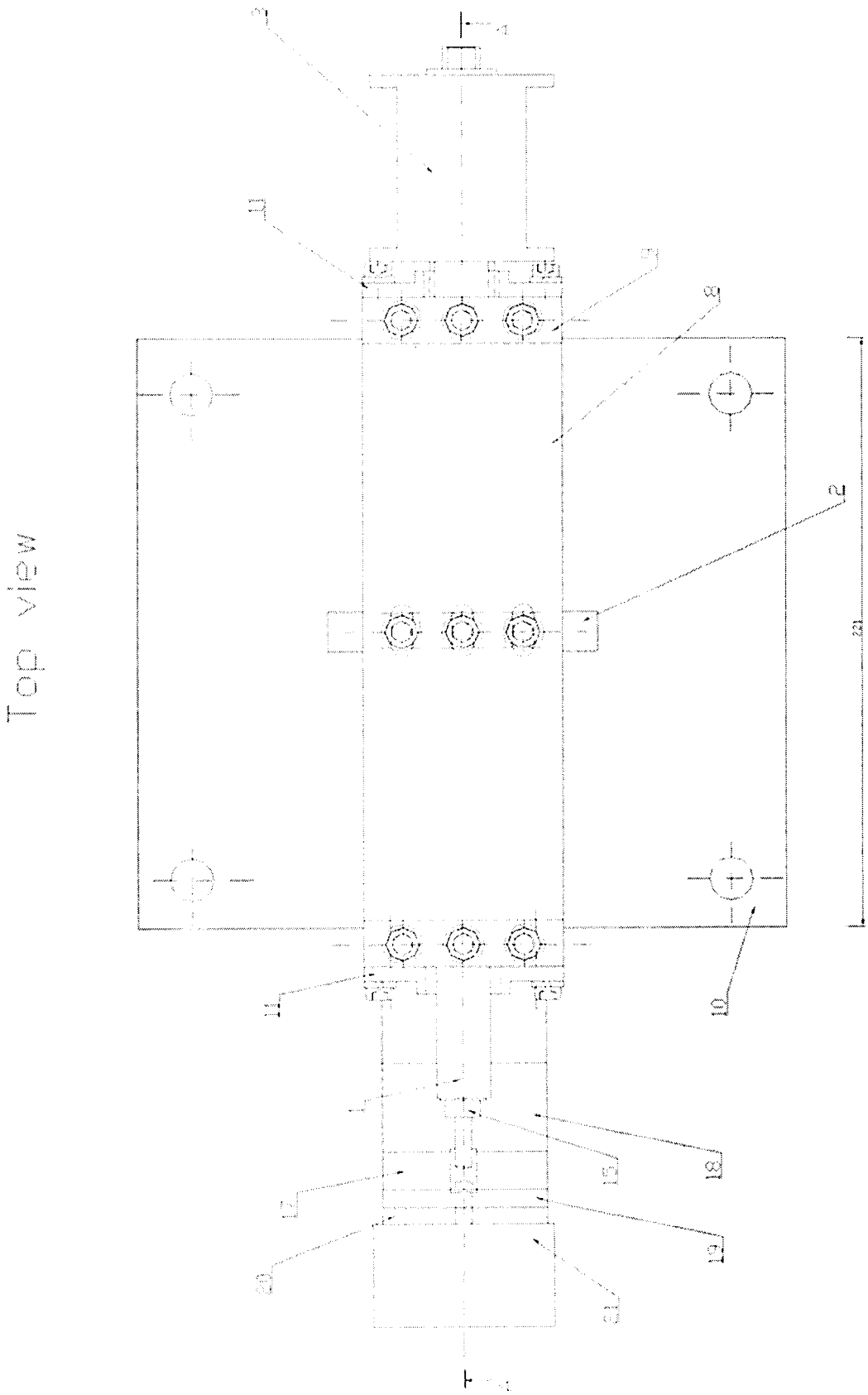
Top view

A-A

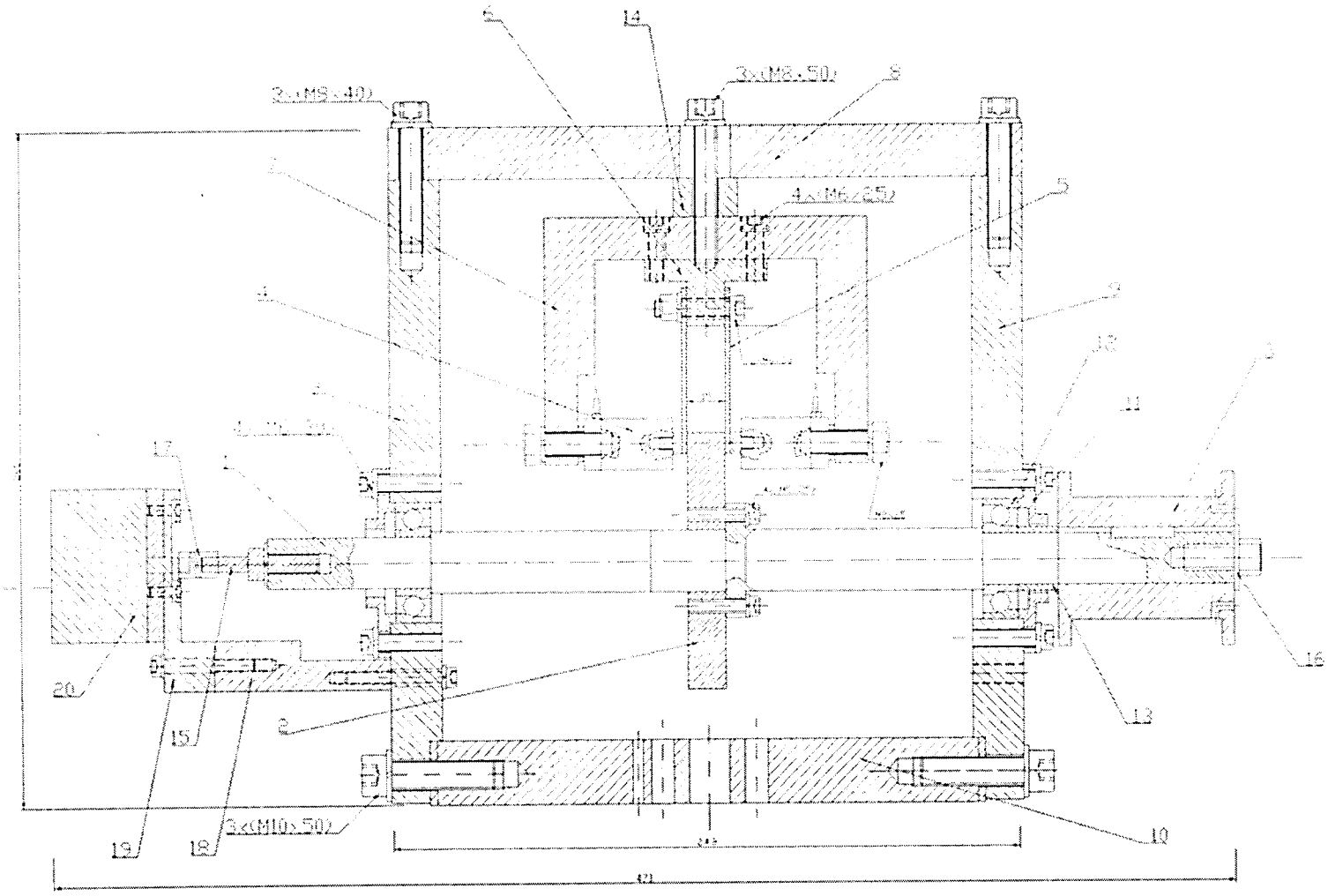

Right view

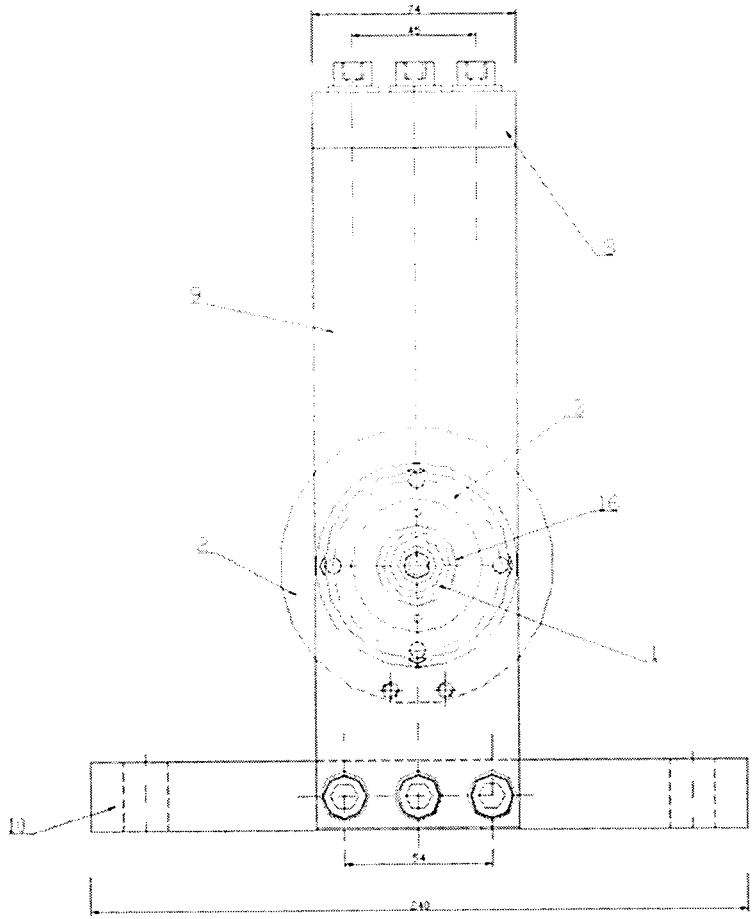

F3. Clutch mechanism for an Actively Restrained Passive Prismatic Joint

Item #	Title	Qty for 1 item
1	Rail, off the shelf	1
2	Channel beam, off the shelf	1
3	Base plate	1
4	Piezoelectric actuator, off the shelf	1
5	Actuator support	1
6	Cantilever	1
7	Cantilever support	1
8	Carriage	1

Top view

60
Assembly to produce frictional force
2, Base plate
B
B
A
A
2, Channel beam

A-A

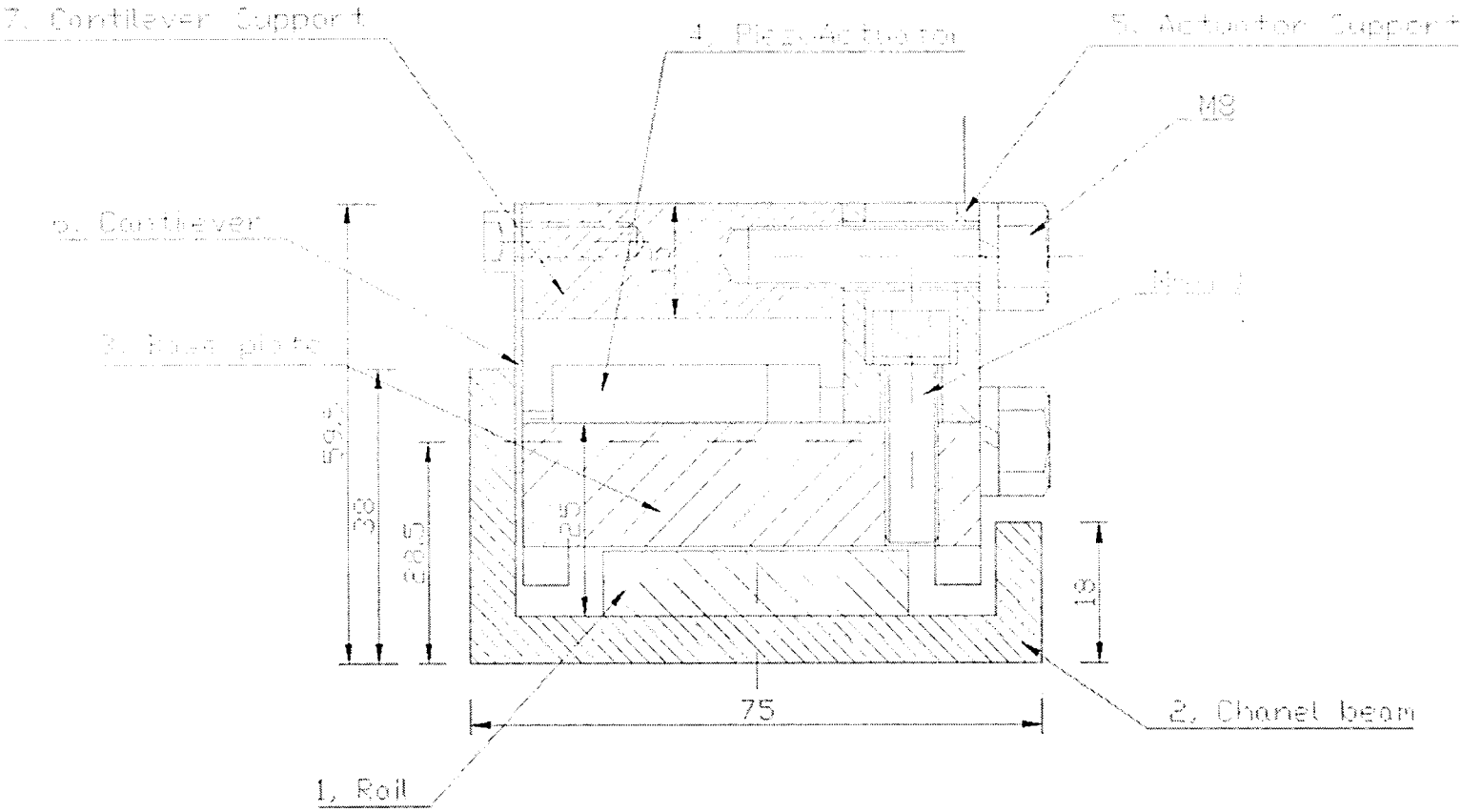
7. Cantilever Support
4. Piezo Actuator
5. Actuator Support
M8
6. Cantilever
3. Flexure plate
Shim
50.4
38
28.5
5
10
75
2. Chanel beam
1. Rail

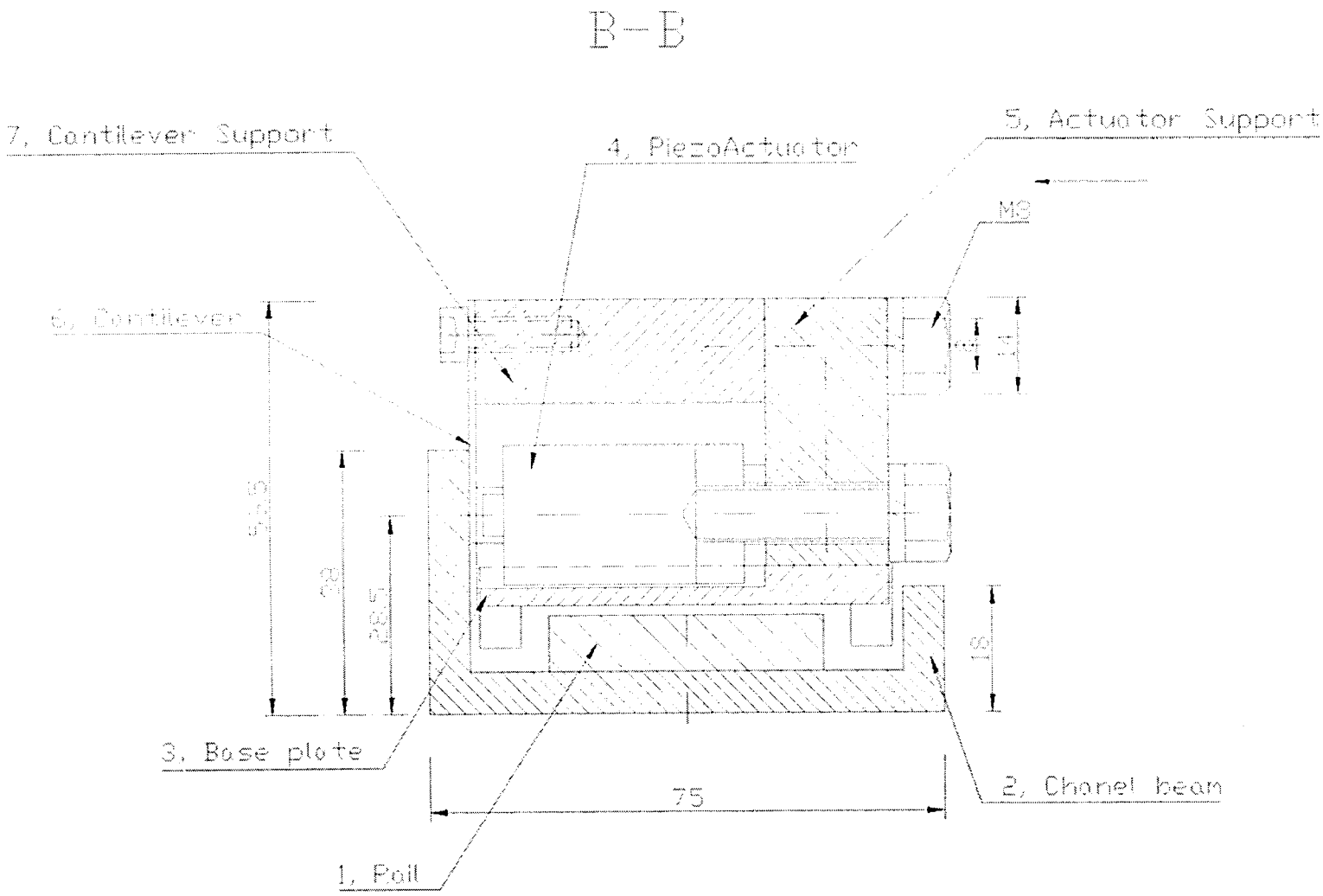
B-B
7, Cantilever Support
4, PiezoActuator
5, Actuator Support
M3
6, Cantilever
3, Base plate
2, Chanel beam
1, Foil
75

Left view
B
A
7. Cantilever Support
6xM4
5. Cantilever
3. Base plate
1. Rail
2. Chanel beam
4. Carriage
B
A

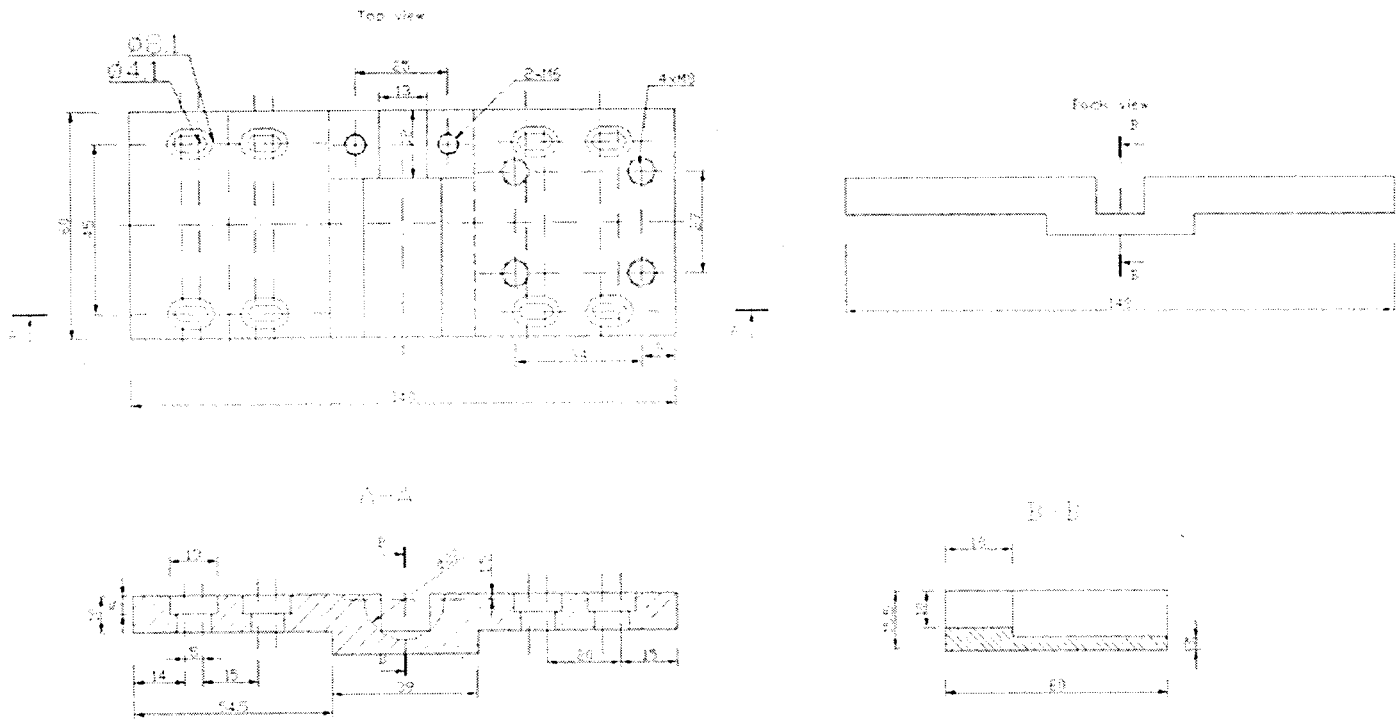

TITLE: Base plate 1 off		
SIZE: A2	Item NO Item # 3	REV
SCALE: 1:1	MATERIAL: Steel	SHEET

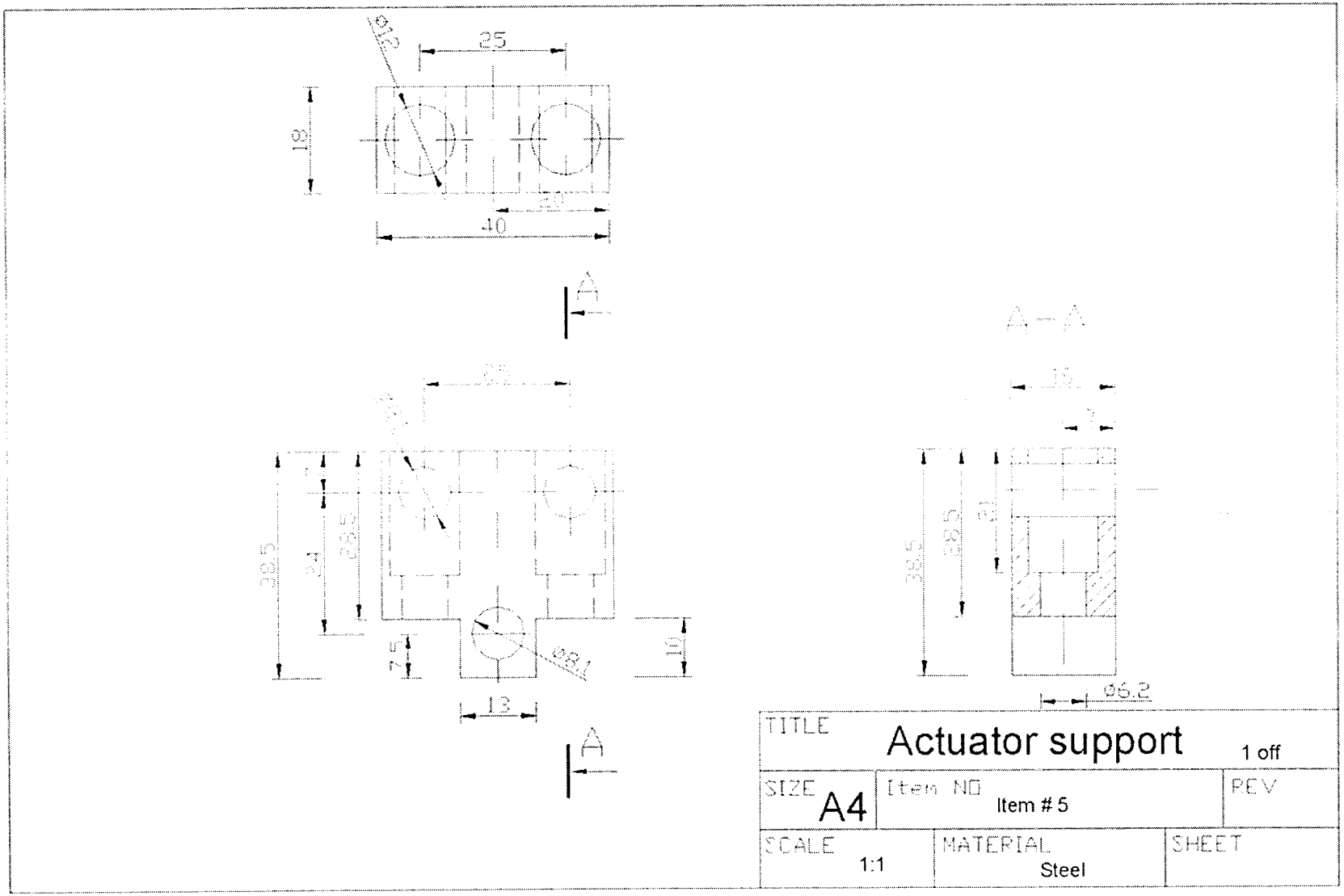
25
18
20
40
A
A
A – A
15
7
38.5
31
26.2
7.5
13
Ø6.2
TITLE
Actuator support
1 off
SIZE
A4
Item NO
Item # 5
REV
SCALE
1:1
MATERIAL
Steel
SHEET

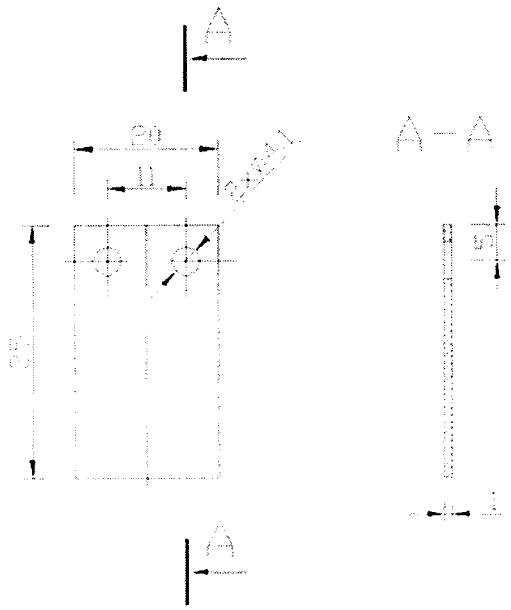

TITLE	Cantilever 1 off		
SIZE A4	Item NO Item # 6		REV
SCALE 1:1	MATERIAL Stainless Steel	SHEET	

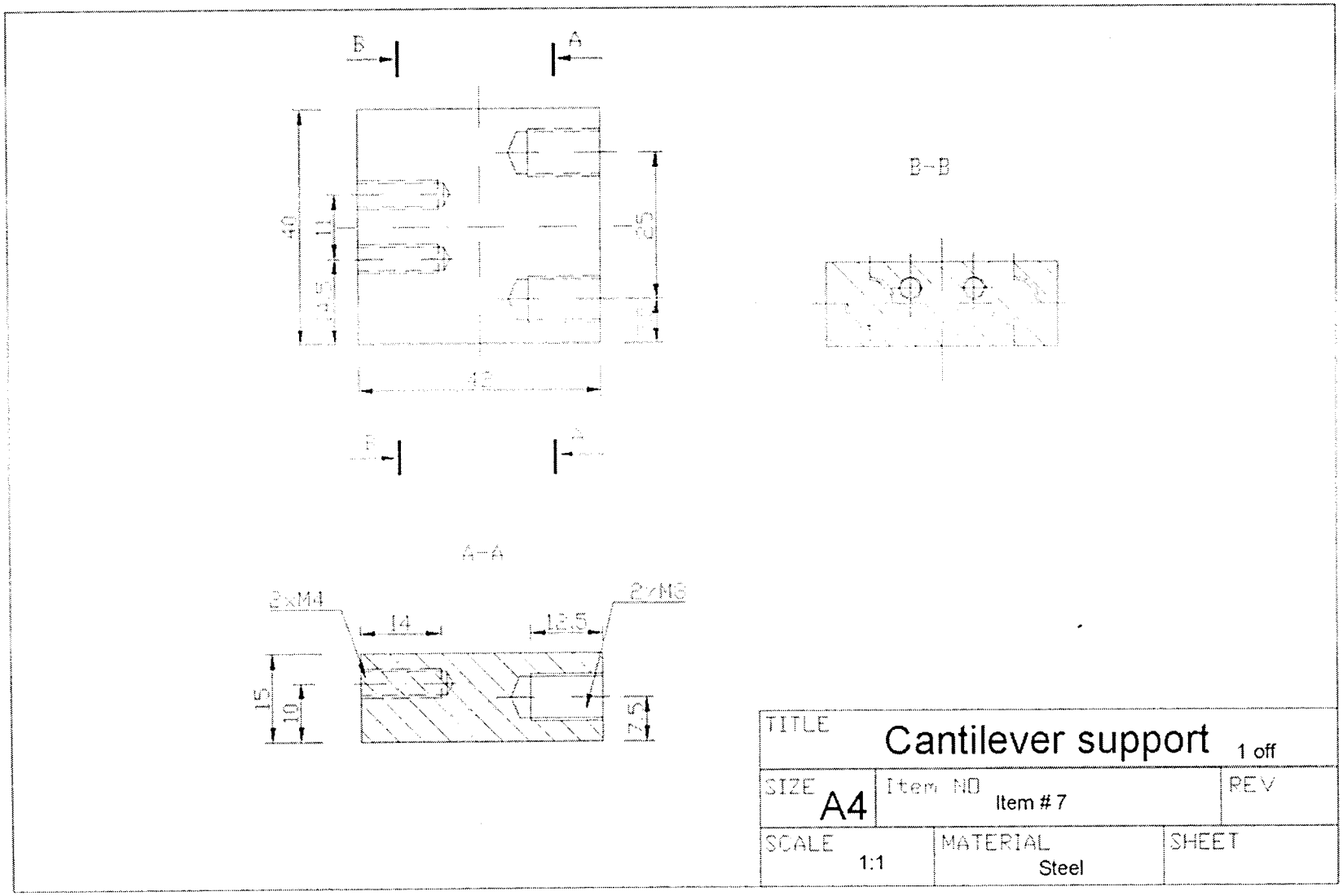
B
A
40
11
5
15
42
B-B
A-A
3xM4
14
12.5
2xM6
15
10
2.5
TITLE
Cantilever support
1 off
SIZE
A4
Item NO
Item # 7
REV
SCALE
1:1
MATERIAL
Steel
SHEET

APPENDIX G

The Computational Workstation for Real-Time Control

One of the major problems in designing control systems is implementing real-time data capture and control. The computational workstation used in this research was designed and built by Reedman [18] and is briefly described in this appendix.

The workstation is using the QNX real-time operating system (RTOS) from QNX Software Systems Ltd [53]. The RTOS runs a control development software on a Pentium 233 MHz single-board computer (SBC), from Professional Industrial Solutions, with 64Mb of RAM that guarantees a response to an externally generated interrupt in under 4μs. The SBC is housed in an industrial rack-mounted case. All of the necessary low power electronics to capture analogue/digital data, generate command signals to the motor's driver and to read the encoder positions have been designed and housed in this unit. The electronic hardware consists of:

- a PC14AT interface card from Amplicon, used to generate the interrupt signal required for the control software;
- a Single Axis Motion Card (SAMC) interface card, used to transmit the command signal to the analogue output and to read the encoder values;
- and a Power Electronics Interface used for amplification of analogue/digital signals and isolation of the low-power digital computer signals.

The control overview and actual set-up of the computational workstation used for the experimental analysis is displayed in Figure G1a and G1b respectively.

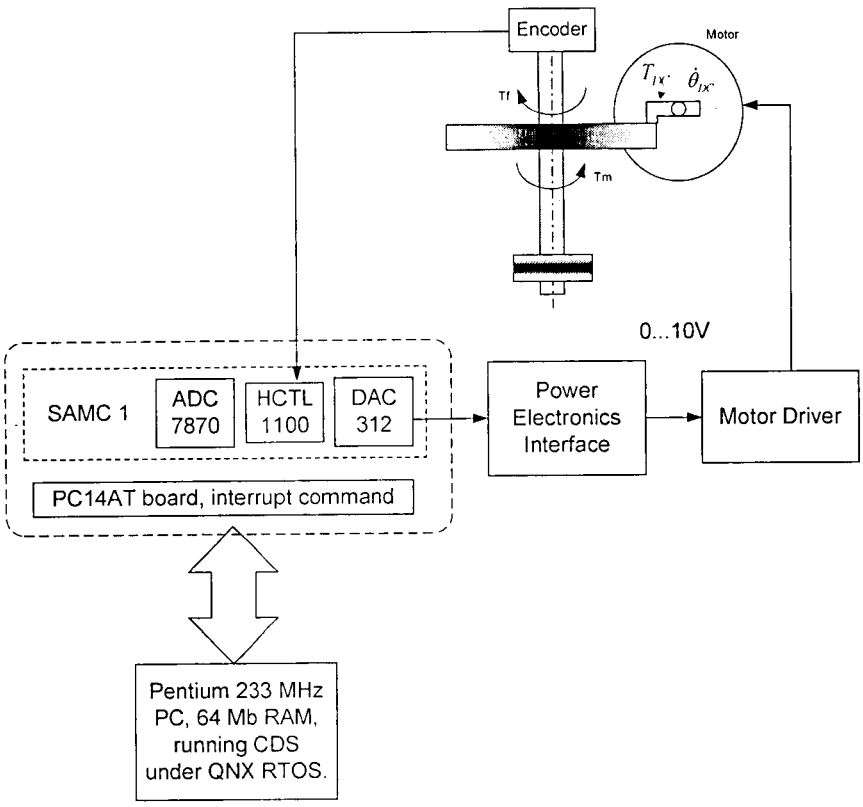

a)

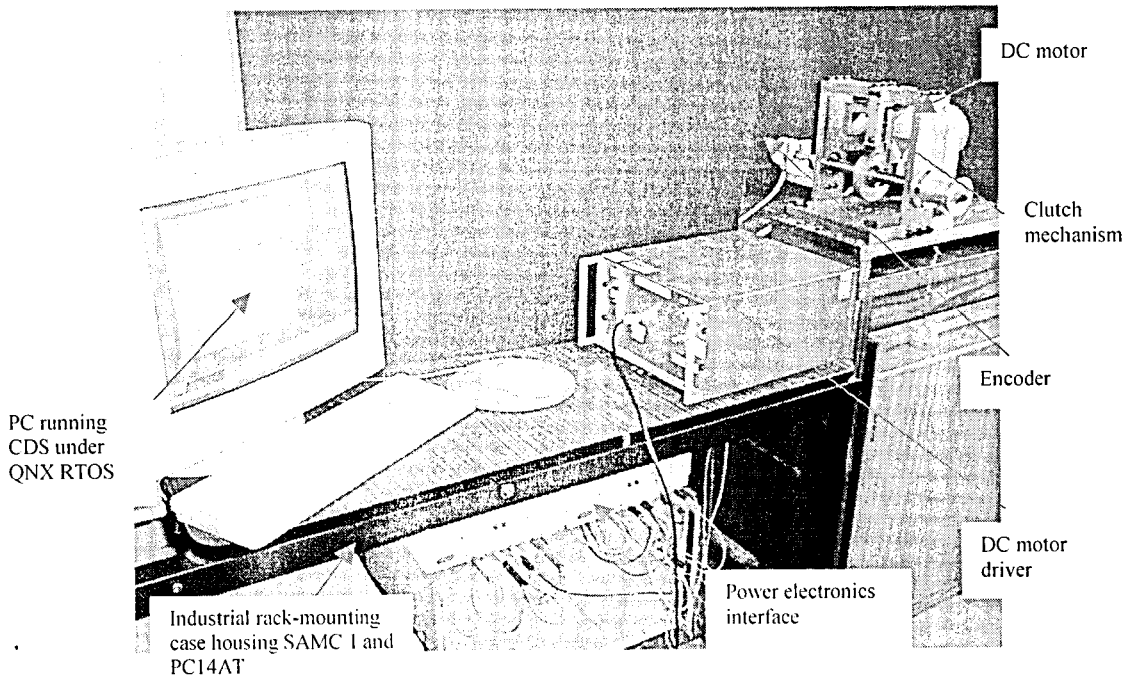

b)

Figure G1. Computational Workstation Overview: a) Diagram, b) Actual set-up

Besides generating the interrupt signal required for the control software, the PC14AT interface board supplies the following :48 programmable I/O lines compatible TTL; 3 control modes for the programmable I/O ports; 3 independent programmable counter/timers; and 6 control modes for the counter/timers.

The Single Axis Motion Control interface card has been designed to generate low power digital and analogue signals required to drive the actuator. Its block diagram and picture are displayed in Figure G2a, and G2b respectively. The SAMC interface card provides:

- 8 channel of 12-bit analogue inputs.
- 1 channel of 12-bit analogue output.
- 8 digital inputs.
- 8 digital outputs.
- HCTL-1100 interface for the control of DC/Stepper (Brushless) motors, and also interface for a position sensor (i.e. incremental encoder).

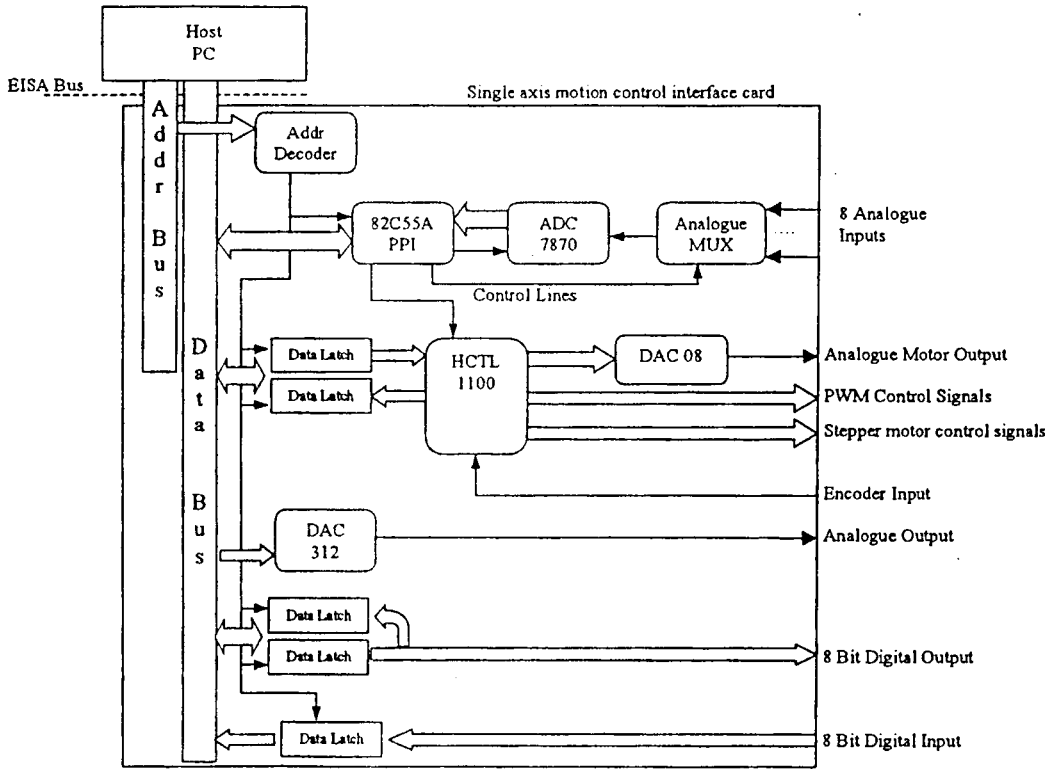

a)

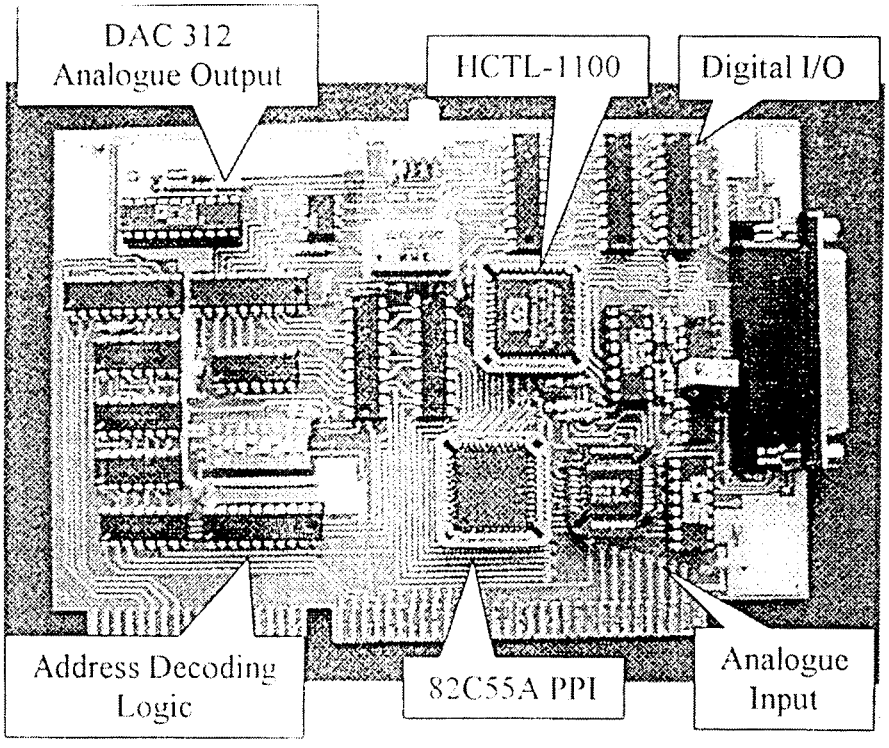

b)

Figure G2. Single Axis Motion Control Interface Card: a) Block Diagram, b) Picture [18]

Between the motion control interface card and the actuator there exist some electronic hardware for amplification of analogue/digital signals and isolation of the low-power digital computer signals. The Power Electronics Interface is housed separately from the PC to minimise the effect of noise. Its picture is shown in Figure G3.

A Control Development Studio (CDS) software, also developed by Reedman [18], was used to develop and run control algorithms. CDS loads and runs a selected control program, communicating between the user and the control program. The developer, by implementing some of the functions provided by the CDS, can allow the user to change control variables, log control data such as position, speed, error, etc, and inform the user about the state of the control program for debugging purposes. A block diagram of the processes is shown in Figure G4.

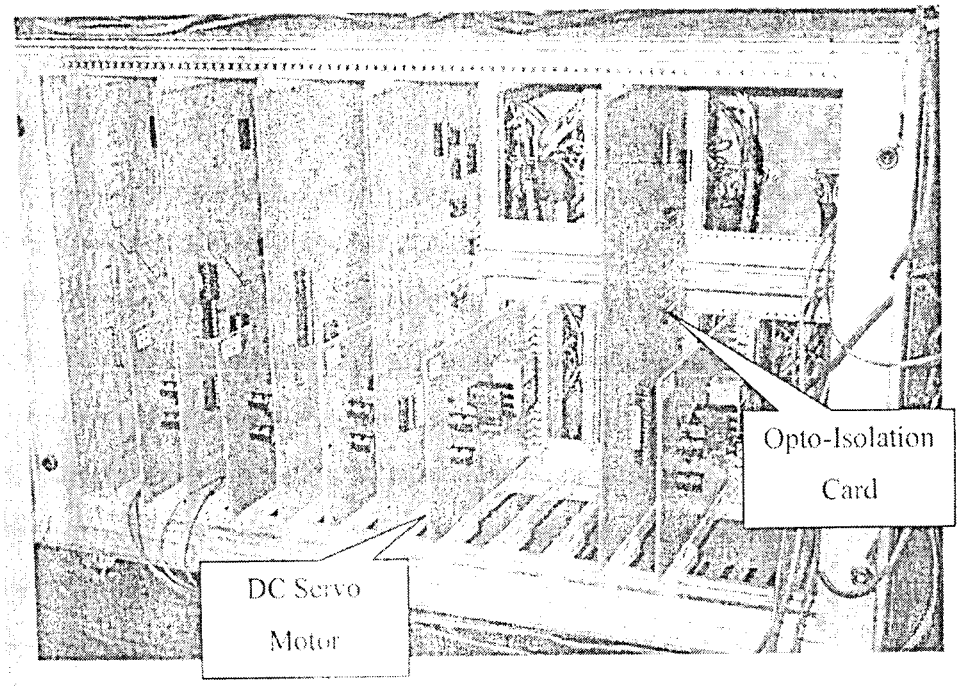

Figure G3. Power electronics and opto-isolator cards [18]

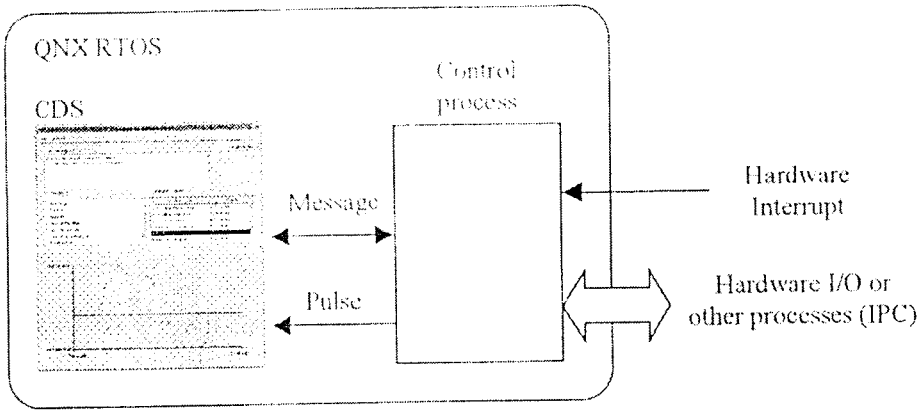

Figure G4. Control Development Studio - mode of operation [18]

More details about the real-time computational workstation and the CDS application can be found in Reedman's PhD thesis [18].

APPENDIX H

Two-DOF Polar Manipulator's Dynamics

A picture of Fraucher's two-DOF manipulator is given in Figure H1. The control handle employed in this manipulator is described in section H1, and the mathematical model is derived in section H2. The system parameters are given in section H3.

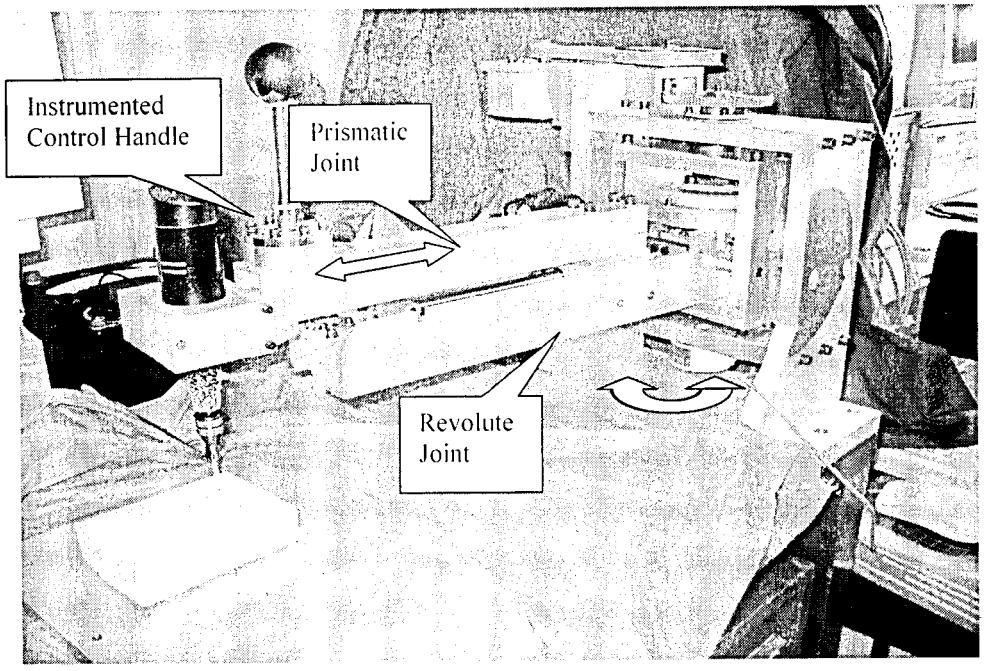

Figure H1. Fraucher's two-DOF polar manipulator [174]

H1. Two-DOF Control Handle [174]

The main advantages of using a force sensor for measuring the pulling/pushing force of the surgeons are: Firstly, the direction and force applied by the surgeon are detected, which are of a great importance for the control system as it is shown in Chapter 8. Secondly, it is possible to define a minimum required force in order to move the manipulator. This is important in order to avoid undesired movements caused by the

user when s/he does not desire to move the end-effector while holding the control handle. Thirdly, the force sensor can also be used as a safeguard against too high force levels. If the surgeon exceeds a predefined threshold force level an alarm signal is triggered and the surgeon is warned about his large force applied. Finally, the measured force can be used to calculate the surgeon's desired velocity as it is shown in Chapter 8.

A two-DOF polar robot requires a two axes force sensor for θ and r polar coordinates. The design is based on the usage of strain gauges as indirect force sensors and on a special design sensor body shown in Figure H2.

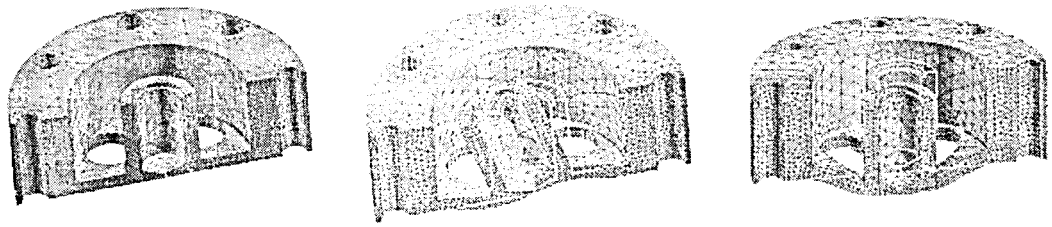

Figure H2. Sensor body: (a) cross section, (b) X/Y force input, (c) Z force input [174]

The design parameters are chosen as the length *l*, width *w* and thickness *t* of a rib and the height of the lever arm *h* of the applied user force as shown in Figure H3, which are responsible for the determined stress and strain in the sensor ribs or beams. Because of the plastic knob used on the top of the lever arm, the control handle is assumed that is always grasped by the surgeon in the same position. This is necessary for an accurate force measurement system. The control handle is shown in more detail in the assembly drawing depicted in Figure H3a, and a close-up view of the instrumented control handle mounted on the robot is shown in Figure H3b.

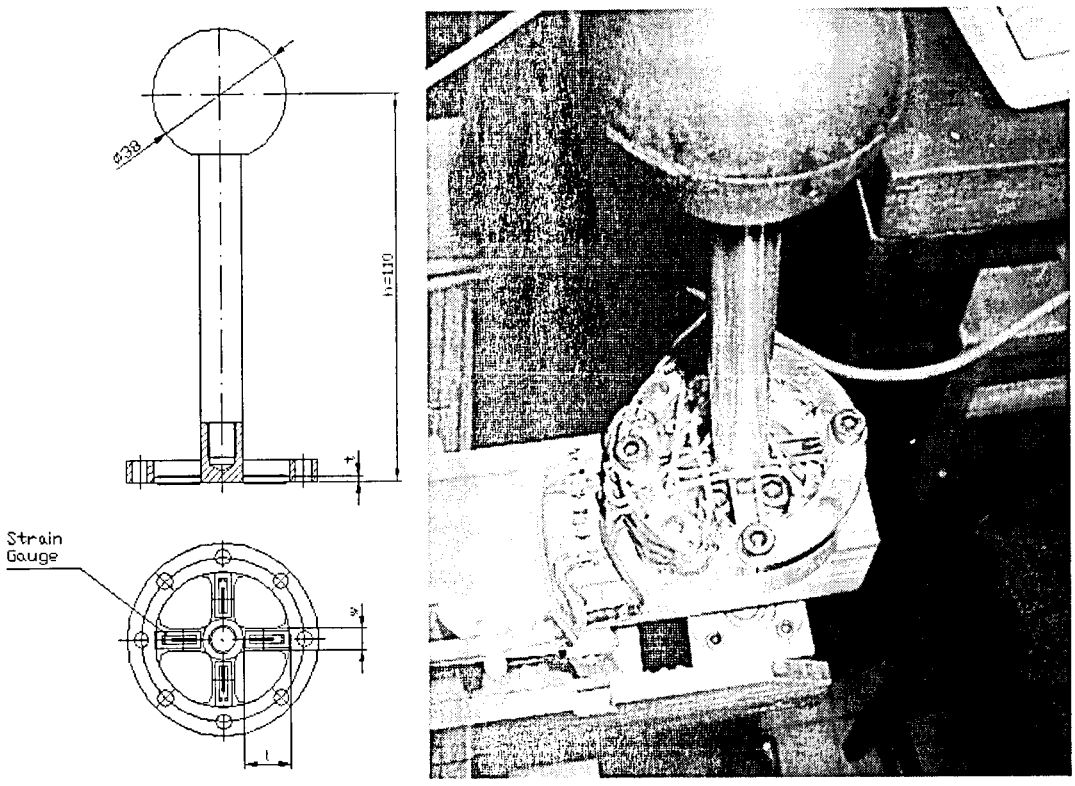

a) b)

Figure H3. Control handle: a) Drawing, b) Picture [174]

H2. Two-DOF polar manipulator's mathematical model

For the derivation of the mathematical model the manipulator is divided into three main parts as shown in Figure H4: (1) The revolute joint with inertia I_1 and mass m_1, which includes all rotational parts, excluding the translational components; (2) the prismatic joint with inertia I_2 and mass m_2, which comprises all static parts mounted, excluding the parts already considered in the first part; (3) the movable part of the prismatic joint with inertia I_3 and mass m_3, which includes also the control handle. Figure H4 shows a schematic drawing of the manipulator with the applied polar coordinate system, inertias, masses, dimensions and user-input force. The numerical values for masses and mass moments of inertia and other measurements are attached in Appendix H3.

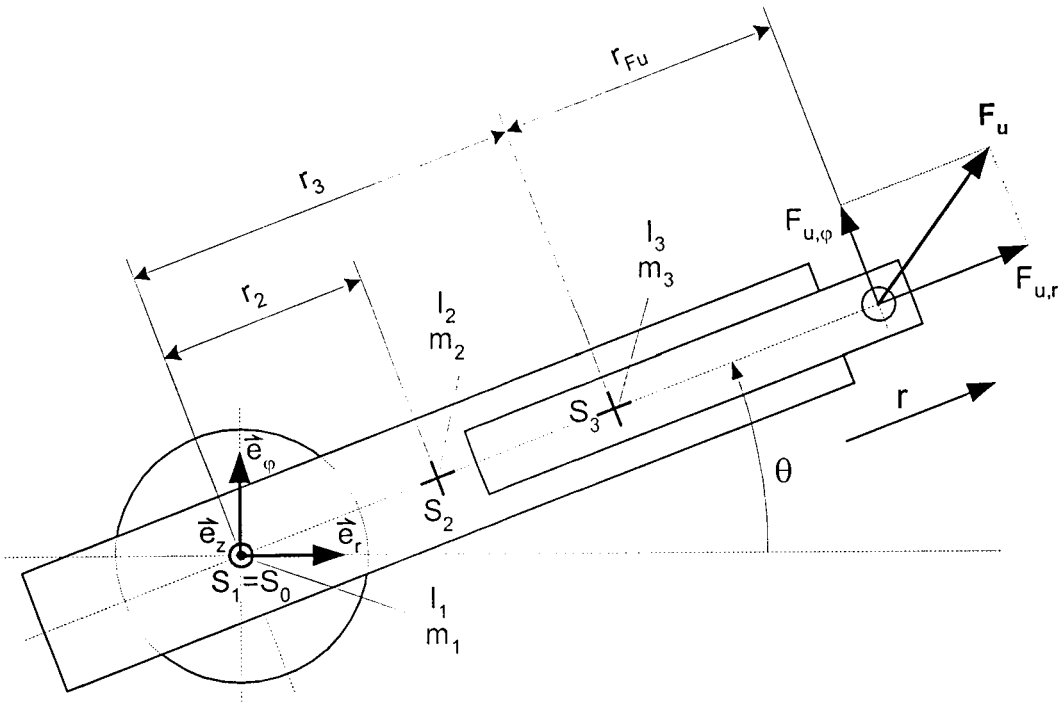

Figure H4. Schematic drawing of robot system [174]

The dynamics of the manipulator was modelled using the *Lagrangian formulation*. The Lagrange formulation describes the behaviour of the dynamic system in terms of the generalised coordinates, energy, and generalised forces. Let T and U represent the *kinematic and potential energy* of the arm, respectively, and considering that the components of q represent the joint angle of revolute joint and the joint distance of the prismatic joint, the lagrangian function is defined as the difference between the kinetic and potential energy as follows:

$$L(q.\dot{q}) = T(q.\dot{q}) - U(q) \qquad \textbf{(H0-1)}$$

where $\dot{q}$ =dq/dt denotes the vector of joint velocities. The general equation of motion of a robotic arm can be formulated in terms of the Lagrangian function as follows [174].

$$\frac{d}{dt}\frac{\partial}{\partial \dot{q}_i} L(q.\dot{q}) - \frac{\partial}{\partial q_i} L(q.\dot{q}) = F_i \qquad \textbf{(H0-2)}$$

where F_i is the generalised force acting on the ith joint. F_i represents the vector of the joint torques or forces, depending on whether the joint is revolute or prismatic. The kinetic energy for the two-DOF polar manipulator is defined as

$$T(q,\dot{q}) = \frac{1}{2} v_i^T \, m_i \, v_i \; + \; \frac{1}{2} \varpi_i^T \, I_i \, \varpi_i \qquad \textbf{(H0-3)}$$

where m_i represents the mass of the components i, where i = 1, 2, 3

v_i is the velocity of the centre of mass of component *i*,

I_i is the 3x3 inertia tensor of component *i* about its centre of mass expressed with respect to the base frame.

ω_i denotes the angular velocity about the centre of mass with respec tto the base frame.

The potential energy stored in the i^{th} component of the arm is the amount of work required to displace the centre of mass of component *i* from a horizontal reference plane in the presence of gravity. Hence.

$$U(q) = -\sum_{i=1}^{n} m_i \, g^T \, c_i(q) \qquad \textbf{(H0-4)}$$

where g is the gravitational acceleration vector with respect to the base frame, and $c_i(q)$ is the position where the components *i* is displaced with respect to the base frame coordinate.

In this case the potential energy for the manipulator components is zero because no movement takes place in z-direction due to a plane system. The generalized coordinates or the vector of the joint positions and velocities can be written as:

$$q = \begin{bmatrix} r_3 \\ \theta \end{bmatrix} \qquad \textbf{(H0-5)}$$

$$\dot{q} = \begin{bmatrix} \dot{r}_3 \\ \dot{\theta} \end{bmatrix} \qquad \textbf{(H0-6)}$$

1. Kinematic energy for part 1, the revolute joint

The derivation of the kinetic energy T_1 is based on the velocity v_{S1} of the centre of mass S_1 shown in Figure H4, the angular velocity ω_{S1} and the position vector p_{S1} of the centre of mass of the revolute joint with respect to S_0.

$$\vec{p}_{S1} = \begin{bmatrix} 0 \\ 0 \\ 0 \end{bmatrix} \qquad \textbf{(H0-7)}$$

$$\vec{\omega}_{S1} = \begin{bmatrix} 0 \\ 0 \\ \dot{\theta} \end{bmatrix} \qquad \textbf{(H0-8)}$$

From $p_{S,1}$ and $\omega_{S,1}$ the velocity of the centre of mass S_1 can be found as,

$$\vec{v}_{S1} = \dot{\vec{p}}_{S1} + \vec{\omega}_{S1} \times \vec{p}_{S1} = \begin{bmatrix} 0 \\ 0 \\ 0 \end{bmatrix}. \qquad \textbf{(H0-9)}$$

Due to $\vec{v}_{S1} = \vec{0}$ and equation (H3), just the inertia tensor in the direction of the polar coordinates is of interest.

$$I_{S1} = \begin{bmatrix} I_{r,1} & 0 & 0 \\ 0 & I_{\theta,1} & 0 \\ 0 & 0 & I_{z,1} \end{bmatrix} \qquad \textbf{(H0-10)}$$

Substituting equations (H7 to H10) in equation (H3) yields

$$T_1 = \frac{1}{2} I_{z,1} \dot{\theta}^2. \qquad \textbf{(H0-11)}$$

where $I_{z,1}$ is the moment of inertia about the z-axis.

2. Kinematic energy for part 2, the static component of the prismatic joint

The same procedure as for the revolute joint is carried out again for the prismatic joint. The necessary parameters are,

$$\bar{p}_{S,2} = \begin{bmatrix} r_2 \\ 0 \\ 0 \end{bmatrix}, \quad \bar{\varpi}_{S,2} = \begin{bmatrix} 0 \\ 0 \\ \dot{\theta} \end{bmatrix} \text{ and } \quad \bar{v}_{S,2} = \begin{bmatrix} \dot{r}_2 \\ r_2\dot{\theta} \\ 0 \end{bmatrix}. \qquad \textbf{(H0-12)}$$

Now both the mass matrix and inertia matrix are of interest:

$$m_{S2} = \begin{bmatrix} m_2 & 0 & 0 \\ 0 & m_2 & 0 \\ 0 & 0 & m_2 \end{bmatrix} \qquad I_{S2} = \begin{bmatrix} I_{r,2} & 0 & 0 \\ 0 & I_{\theta,2} & 0 \\ 0 & 0 & I_{z,2} \end{bmatrix} \qquad \textbf{(H0-13)}$$

Substituting equations (H12) and (H13) in equation (H3) yields

$$T_2 = \frac{1}{2} m_2 \left[\dot{r}_2^{\,2} + r_2^{\,2}\dot{\theta}^2 \right] + \frac{1}{2} I_{z,2}\dot{\theta}^2, \qquad \textbf{(H0-14)}$$

but with $\dot{r}_2 = 0$ because no movement takes place in $\bar{e}_r$ direction, T_2 becomes,

$$T_2 = \frac{1}{2} m_2 r_2^{\,2}\dot{\theta}^2 + \frac{1}{2} I_{z,2}\dot{\theta}^2 \qquad \textbf{(H0-15)}$$

3. Kinematic energy for part 3, the moveable component of the prismatic joint

The kinetic energy for the movable prismatic joint is calculated. The parameters are,

$$\bar{p}_{S3} = \begin{bmatrix} r_3 \\ 0 \\ 0 \end{bmatrix}, \quad \bar{\varpi}_{S2} = \begin{bmatrix} 0 \\ 0 \\ \dot{\theta} \end{bmatrix} \text{ and } \quad \bar{v}_{S2} = \begin{bmatrix} \dot{r}_3 \\ r_3\dot{\theta} \\ 0 \end{bmatrix}. \qquad \textbf{(H0-16)}$$

The mass matrix and inertia matrix are.

$$m_{S3} = \begin{bmatrix} m_3 & 0 & 0 \\ 0 & m_3 & 0 \\ 0 & 0 & m3 \end{bmatrix} \qquad I_{S3} = \begin{bmatrix} I_{r,3} & 0 & 0 \\ 0 & I_{\theta,3} & 0 \\ 0 & 0 & I_{z,3} \end{bmatrix} \qquad \textbf{(H0-17)}$$

Substituting equations (H16) and (H17) in equation (H3) yields,

$$T_3 = \frac{1}{2} m_3 \left[\dot{r}_3^{\,2} + r_3^{\,2} \dot{\theta}^2 \right] + \frac{1}{2} I_{z,3} \dot{\theta}^2 \qquad \textbf{(H0-18)}$$

Accordingly to the kinetic energy of all bodies form equations (H11), (H15) and (H18) the total kinetic energy for the two-DOF system is:

$$T_{total} = T_1 + T_2 + T_3 = \frac{1}{2} m_3 \dot{r}_3^{\,2} + \frac{1}{2} \dot{\theta}^2 \left[I_T + m_3 r_3^{\,2} \right] \qquad \textbf{(H0-19)}$$

with $I_T = I_{z,1} + I_{z,2} + I_{z,3} + m_2 r_2^{\,2}$. as the total inertia of the arm.

The equations of motion can be deduced from equation (H2) by derivation of equation (H19) according to the generalised coordinates q_i. which are r_3 and θ. Furthermore, the vector of the joint torques or forces F_i has to be determined. The generalised forces F_i act along possible degrees-of-freedom of the system. For example, translation forces along translational axes and rotational torques around axes of rotation.

Thus the derivation of T_{total} (H19) with respect to r_3 yields to,

$$\frac{d}{dt}\left(\frac{\partial T_{total}}{\partial \dot{r}_3} \right) - \frac{\partial T_{total}}{\partial r_3} = m_3 \ddot{r}_3 - m_3 \dot{\theta}^2 r_3 \qquad \textbf{(H0-20)}$$

and with respect to θ results in.

$$\frac{d}{dt}\left(\frac{\partial T_{total}}{\partial \dot{\theta}} \right) - \frac{\partial T_{total}}{\partial \theta} = \left(I_T + m_3 r_3^{\,2} \right) \ddot{\theta} + 2 m_3 r_3 \dot{r}_3 \dot{\theta} - 0. \qquad \textbf{(H0-21)}$$

The generalised force for the r-axis can be deduced from the user force component on the r-axis, $F_{u,r}$, and the constrained force $F_{f,r}$ produced by the proposed joint mechanism, which is acting opposite to the user's input force. Furthermore, the damping of the system D_r is considered to be proportional to the velocity of the joint. Thus Q_r is,

$$Q_r = F_{u,r} - F_{f,r} - D_r \dot{r}_3 \qquad \textbf{(H0-22)}$$

In the same way the generalised torque for the z-axis (revolute joint) can be deduced. Thus Q_z yields to,

$$Q_z = F_{u,\varphi}(r_3 + r_{Fu}) - T_{f,z} - D_z \dot{\theta} \qquad \textbf{(H0-23)}$$

where $F_{u,\varphi}$ is the user force component acting along the φ-axis, which generates furthermore a torque in respect to the z-axis; $T_{f,z}$ is the frictional torque produced by the clutch; the radius r_3 and r_{Fu} are shown in Figure H4. Furthermore, the term $D_z \dot{\theta}$ represents the damping proportional to velocity around the revolute joint axis, where D_z is the damping constant.

Combining equations (H20), (H21), (H22) and (H23) the Lagrange formulation yields

$$\begin{bmatrix} m_3 & 0 \\ 0 & m_3 r_3^2 + I_{sum} \end{bmatrix} \ddot{\vec{q}} + \begin{bmatrix} m_3 r_3 \dot{\theta}^2 \\ 2 m_3 r_3 \dot{r}_3 \dot{\theta} \end{bmatrix} = \begin{bmatrix} F_{u,r} - F_{f,r} - D_r \dot{r}_3 \\ F_{u,\varphi}(r_3 + r_{Fu}) - T_{f,z} - D_z \dot{\theta} \end{bmatrix} \qquad \textbf{(H0-24)}$$

or as matrix notation

$$\tilde{M}(q)\ddot{\vec{q}} + \vec{h}(q,\dot{q}) + \vec{c}(q) = \vec{Q}, \qquad \textbf{(H0-25)}$$

where: $M(q) = \begin{bmatrix} m_3 & 0 \\ 0 & m_3 r_3^2 + I_{sum} \end{bmatrix}$ represents the inertial matrix of the manipulator,

$\bar{h}(q, \dot{q}) = \begin{bmatrix} m_3 r_3 \dot{\theta}^2 \\ 2 m_3 r_3 \dot{r}_3 \dot{\theta} \end{bmatrix}$ represents the non-linear coriolis and centrifugal force vector,

$\bar{c}(q) = n \times 1$ gravity force vector, which is the zero vector for this robot,

and

$\bar{Q} = \begin{bmatrix} F_{u,r} - F_{f,r} - D_r \dot{r}_3 \\ F_{u,\varphi}(r_3 + r_{Fu}) - T_{f,z} - D_z \dot{\theta} \end{bmatrix}$ denotes the generalised force vector.

The user-input force in the direction of the polar coordinates r and φ, $F_{u,r}$ and $F_{u,\varphi}$ can be derived from Figure H5, where $F_{u,r}$ is the force acting along the prismatic joint direction and $F_{u,\varphi}$ in revolute joint direction. Thus

$$F_{u,r} = \|F_u\| \cos(\alpha - \theta) \qquad \textbf{(H0-26)}$$

$$F_{u,\varphi} = \|F_u\| \sin(\alpha - \theta) \qquad \textbf{(H0-27)}$$

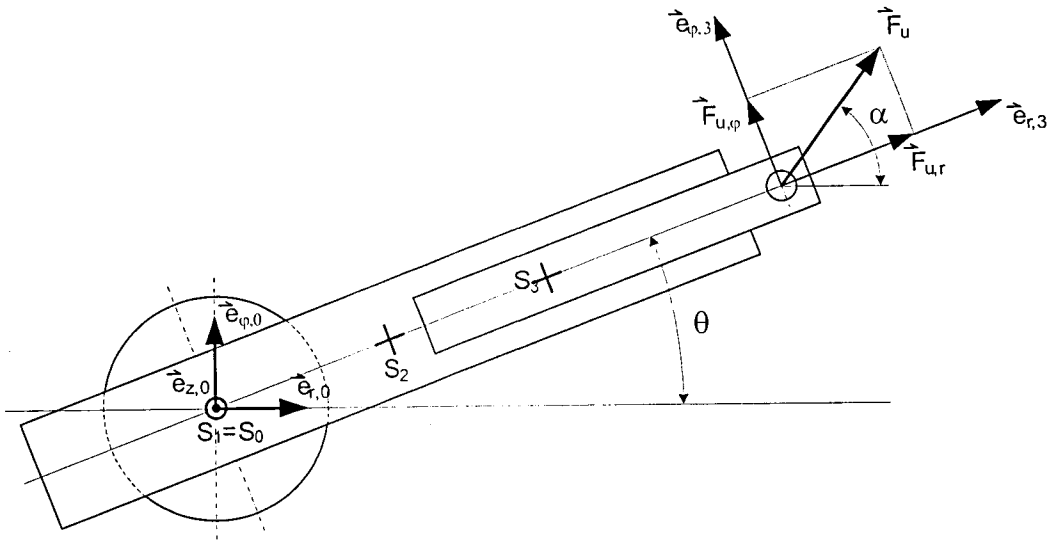

Figure H5. Magnitude and direction of user force F_u

H3. Two-DOF polar manipulator's parameters

Masses and mass moments of inertia (results)

Parameter	Value	Description
I_1	3.542 10^{-2} kgm^2	MMI* for revolute joint around joint axis
I_2	0.1359 kgm^2	MMI for static part of prismatic joint around the centre of gravity S_1 axis
I_3	2.77 10^{-2} kgm^2	MMI for movable part of prismatic joint around the centre of gravity S_3 axis
I_{sum}	0.2903 kgm^2	Simplification term in the equations of motion
$I_{m,r}$	3.88 10^{-5} kgm^2	Inertia of DC pancake motor
I_{shaft}	8.74 10^{-6} kgm^2	Inertia of all rotational parts of the prismatic joint
m_1	2.4 kg	mass of revolute joint
m_2	6.84 kg	mass of static part of prismatic joint
m_3	1.2 kg	mass of movable part of prismatic joint

* MMI = mass moment of inertia

Dimensions

Parameter	Value	Description
r_2	0.1155 m	distance between base frame and centre of gravity of static part of the prismatic joint
r_3	0.213 + r (m)	distance between base frame and centre of gravity of movable part of the prismatic joint, where *r* is the actual travel of the joint

Joint's travel and encoder resolution

Parameter	Travel	Resolution
Revolute Joint	+/- 30 deg	0.018 deg
Prismatic Joint	200 mm	0.004 mm